Aluminium Gallium Arsenide Radiation Spectrometers for Space Science Applications

Thesis submitted for the degree of
Doctor of Philosophy

Michael David Charles Whitaker
Space Research Group
Department of Engineering and Design
University of Sussex

August 2019

Abstract

Aluminium Gallium Arsenide (AlGaAs) photodiodes were investigated for their suitability as spectroscopic radiation detectors for space science applications.

$Al_{0.2}Ga_{0.8}As$ non-avalanche p^+-i-n^+ photodiodes were characterised for their response to X-ray (5.9 keV) illumination within the temperature range 20 °C to -20 °C. An energy resolution (FWHM at 5.9 keV) of 1.06 keV ± 0.04 keV was achieved at 20 °C. Improved FWHM at 5.9 keV was observed with the devices at temperatures of 0 °C (856 eV ± 30 eV) and -20 °C (827 eV ± 30 eV). The results were the first demonstration of photon counting X-ray spectroscopy with $Al_{0.2}Ga_{0.8}As$ photodiodes. The electron-hole pair creation energy was measured and found to be 4.43 eV ± 0.09 eV at 20 °C, 4.44 eV ± 0.10 eV at 0 °C, and 4.56 eV ± 0.10 eV at -20 °C. Electrical characterisation and subsequent analysis of the noise sources contributing to the measured FWHM at 5.9 keV indicated that $Al_{0.2}Ga_{0.8}As$ based X-ray spectrometers are potentially promising alternatives for space science applications.

A monolithic 2 × 2 square pixel $Al_{0.2}Ga_{0.8}As$ non-avalanche p^+-i-n^+ photodiode array was investigated for its utility as a spectroscopic X-ray (5.9 keV) and electron (β^- particle) (≤ 66 keV) detector. Each pixel's response to illumination with X-rays (5.9 keV) was investigated across the temperature range 30 °C to -20 °C. The best energy resolution (FWHM at 5.9 keV) achieved at 20 °C was 756 eV ± 30 eV. Electron (β^- particle) spectra were collected for each pixel at 20 °C. Computer simulations of electron absorption in the detectors were performed to complement the experimental work. The results demonstrated the first $Al_{0.2}Ga_{0.8}As$ pixel array suitable for X-ray and β^- particle spectroscopy. In order to direct future development, eventual use cases for such instrumentation were presented.

$Al_{0.6}Ga_{0.4}As$ p^+-i-n^+ circular mesa photodiodes were investigated for X-ray detection (5.9 keV) at 20 °C. An energy resolution (FWHM at 5.9 keV) of 626 eV ± 20 eV was measured at 20 °C, the best (lowest) energy resolution ever reported for an $Al_xGa_{1-x}As$ X-ray photodiode at room temperature. The electron-hole pair creation energy was measured and found to be 4.97 eV ± 0.12 eV at 25 °C ± 1 °C. The results were the first demonstration of photon counting X-ray spectroscopy with $Al_{0.6}Ga_{0.4}As$ and indicated promising device performance when operated uncooled.

The X-ray (5.9 keV) spectroscopic response of circular mesa GaAs/$Al_{0.8}Ga_{0.2}As$ SAM APDs at 20 °C was investigated. An energy resolution (FWHM at 5.9 keV) of 508 eV ± 5 eV was achieved at an apparent avalanche gain = 1.1. Comparisons between the GaAs/$Al_xGa_{1-x}As$ SAM

photodiodes and recently studied GaAs p^+-i-n^+ X-ray detectors indicated improved device performance through the inclusion of the avalanche layer. The measured energy resolution was the best so far reported for GaAs/$Al_xGa_{1-x}As$ SAM APD based X-ray spectrometers at room temperature.

The research presented in this thesis suggests that AlGaAs radiation detectors are promising candidates for future space science applications.

Acknowledgements

I am sincerely grateful to all those who have made the completion of this thesis possible, most notably my PhD supervisor Prof. Anna Barnett, whose guidance, encouragement, and inexhaustible knowledge has been of enormous benefit. Indeed, I could not imagine completing the amount of research undertaken throughout my PhD career without her.

Special thanks goes to Dr Andrey Krysa and Brett Harrison, who provided the devices used in this thesis, along with valuable semiconductor engineering expertise; and to Martin Nock and Kevin Brady, whose technical support throughout the PhD programme has been invaluable.

I would also like to thank my friends and colleagues in the Engineering department, whose constant support, friendship, and advice has been absolutely vital. Particular thanks goes to my colleagues in the SRG: Dr Grammatiki Lioliou; Dr Silvia Butera; Dr Shifan Zhao; Dr Nathan Gemmell; Colin Bodie; Marco Tedeschi; and Tina Gohil, all of whom contributed immeasurably to an atmosphere I will cherish forever. The research reported in this thesis could not have been achieved without them.

The financial support of the School of Engineering and Informatics, University of Sussex, in the form of a PhD scholarship is also acknowledged.

My most heartfelt thanks goes to every teacher, tutor, mentor, and author from whom I have had the pleasure of learning. They instilled in me, and continue to instil, the desire to learn, to question, and to help uncover the mysteries of our world. My love of the sciences would not exist without them, and for this I am eternally grateful.

Finally, but by no means least, I am so very thankful to my family and loved ones: to my mum and dad for their unwavering love and support; to my brother and sister for their unbreakable friendship; to my partner Dr Hannah Downer, who has kept me on the rails throughout my PhD; and to all those unmentioned who have been integral in this journey, I thank you.

Contents

Publications

Publications from work reported in this thesis

Whitaker, M.D.C., Lioliou, G., Butera, S., and Barnett, A.M., 2016, *$Al_{0.2}Ga_{0.8}As$ X-ray Photodiodes for X-ray Spectroscopy*, Nuclear Instruments and Methods in Physics Research Section A, Vol. 840, pp. 168-173.

Whitaker, M.D.C., Butera, S., Lioliou, G., and Barnett, A.M., 2017, *Temperature Dependence of $Al_{0.2}Ga_{0.8}As$ X-ray Photodiodes for X-ray Spectroscopy*, Journal of Applied Physics, Vol. 122, Art. No. 034501.

Whitaker, M.D.C., Lioliou, G., and Barnett, A.M., 2018, *$Al_{0.2}Ga_{0.8}As$ 2 × 2 Square Pixel X-ray Photodiode Array*, Nuclear Instruments and Methods in Physics Research Section A, Vol. 899, pp. 106-114.

Whitaker, M.D.C., Zhao, S., Lioliou, G., Butera, S., and Barnett, A.M., 2019, *AlGaAs Two by Two Pixel Detector for Electron (Beta Particle) Spectroscopy*, submitted to Nuclear Instruments and Methods in Physics Research Section A.

Whitaker, M.D.C., Lioliou, G., Krysa, A.B., and Barnett, A.M., 2019, *$Al_{0.6}Ga_{0.4}As$ Avalanche Photodiodes for X-ray Spectroscopy*, in preparation.

Whitaker, M.D.C., Lioliou, G., Krysa, A.B., and Barnett, A.M., GaAs/*$Al_{0.8}Ga_{0.2}As$ SAM X-ray APDs*, in preparation.

Other publications

Butera, S., **Whitaker, M.D.C.**, Lioliou, G., and Barnett, A.M., 2016, *AlGaAs ^{55}Fe X-ray Radioisotope Microbattery*, Scientific Reports, Vol. 6, Art. No. 38409.

Butera, S., **Whitaker, M.D.C.**, Krysa, A.B., and Barnett, A.M., 2017a, *Investigation of a Temperature Tolerant InGaP (GaInP) Converter Layer for a ^{63}Ni Betavoltaic Cell*, Journal of Physics D: Applied Physics, Vol. 50, Art. No. 345101.

Butera, S., **Whitaker, M.D.C.**, Krysa, A.B., and Barnett, A.M., 2017b, *Temperature Effects on an InGaP (GaInP) ^{55}Fe X-ray Photovoltaic Cell*, Scientific Reports, Vol. 7, Art. No. 4981.

Lioliou, G., **Whitaker, M.D.C.**, and Barnett, A.M., 2017, *High Temperature GaAs X-ray Detectors*, Journal of Applied Physics, Vol. 122, Art. No. 244506.

Butera, S., **Whitaker, M.D.C.**, Krysa, A.B., and Barnett, A.M., 2018, *6 μm Thick AlInP ^{55}Fe X-ray Photovoltaic and ^{63}Ni Betavoltaic Cells*, Semiconductor Science and Technology, Vol. 33, Art. No. 105003.

Lioliou, G., Butera, S., Zhao, S., **Whitaker, M.D.C.**, and Barnett, A.M., 2018, *GaAs Spectrometer for Planetary Electron Spectroscopy*, Journal of Geophysical Research: Space Physics, Vol. 123, pp. 7568-7580.

Zhao, S., Lioliou, G., Butera, S., **Whitaker, M.D.C.**, and Barnett, A.M., 2018, *Electron Spectroscopy with a Commercial 4H-SiC Photodiode*, Nuclear Instruments and Methods in Physics Research Section A, Vol. 910, pp. 35-40.

Butera, S., Lioliou, G., Zhao, S., **Whitaker, M.D.C.**, Krysa, A.B., and Barnett, A.M., 2019, *InGaP electron spectrometer for high temperature environments*, Scientific Reports, Vol. 9, Art. No. 11096.

Chapter 1
Introduction

1.1 Background

The emergence of radiation detection as a distinct field is inherently linked to the discovery of radiation and radiation effects. This began with the first detection of X-rays by Wilhelm Röntgen in 1895 (Seward & Charles, 2010), which paved the way for further observations of ionising radiation (e.g. γ-rays, electrons, positrons, neutrons, and protons). The earliest radiation detectors used around the start of the 20th century were photographic emulsions and phosphorescent screens (Owens, 2012). Such technology was famously used to take the first medical X-ray radiographs, with a range of commercial applications realised since then. A continued increase in research investment in radiation detection technology, and an improved understanding of the relevant physics, has substantially improved radiation detection instrumentation and methods. Since the days of photographic emulsion and phosphorescent screens, radiation detector technologies such as gas-filled detectors, scintillation detectors, bubble/cloud chambers, and semiconductor detectors have been developed (Tsoulfanidis & Landsberger, 2015), expanding the suitability of radiation detection across an ever-increasing range of applications.

Despite early investigations of semiconductor materials (e.g. the first construction of a light emitting diode (Round, 1907)), and the practical implementation of 'crystal counters' (van Heerden, 1945), semiconductor radiation detector development was relatively niche until the 1960s. This was primarily because of material related problems such as impurities, high defect densities, and stoichiometric imbalances, which limited their usefulness (Owens, 2012). With the advent of the microelectronics industry, which came to focus predominantly on the development of silicon (Si) and germanium (Ge), and the high demand for detector technology in nuclear research, X-ray astronomy, and military applications, rapid progress in radiation detectors made from those materials followed (Owens, 2012). Diffused junction and surface barrier detectors began to find more widespread adoption in the detection of α particles (Mayer, 1960). Ion-drifting, first demonstrated by Pell (1960), provided a method by which near-intrinsic (where the number of free electrons equals the number of holes) Si and Ge material could be made. This, in conjunction with detector geometry evolution (Brown et al., 1969) and advancements in preamplifier design (Harris & Shuler, 1967), laid the groundwork for high volume semiconductor detector development.

As of 2014, more than 99 % of X-ray and γ-ray spectrometers used semiconductor detectors (Lowe & Sareen, 2014), predominantly made from Si. The popularity of semiconductor radiation detectors is largely due to the many advantages they possess relative to other spectroscopic detectors (e.g. lower cost, smaller size, imaging array format possibilities, and better spectral resolution (Knoll, 2000)).

Si radiation detectors commonly take one of several broad structural forms, including p^+-i-n^+ photodiodes (White, 1982), charge coupled devices (CCDs) (Akimov, 2007), Si drift detectors (SDDs) (Gatti & Rehak, 1983), and depleted field effect transistors (DEPFETs) (Kemmer et al., 1990) (see **Section 1.2**). These account for the majority of semiconductor X-ray spectrometers in use today. However, despite their popularity, Si radiation detectors do have limitations. The relatively narrow* bandgap, E_g (units of eV), of Si (E_g = 1.12 eV (Owens, 2012)) means that at high temperatures (> 20 °C), thermally induced electron-hole pair concentrations (intrinsic carrier concentration, n_i (Sze, 2006)) become significant, resulting in large leakage current densities that limit the performance of Si radiation detectors. In addition, Si is prone to radiation damage, which can lead to significant increases in leakage current and charge trapping, and decreases in bulk resistivity (Li, 2008). These phenomena degrade spectroscopic performance (Lindström, 2003) (Hall & Holland, 2010). Therefore, in order to operate in environments of high temperature (> 20 °C, where Si radiation detector performance becomes poor) and intense radiation (e.g. > 5 krad, where conventional Si based electronics can lose functionality (Barth et al., 2000)), Si X-ray spectrometers require radiation shielding and cooling mechanisms.

1.2 Common Si radiation detector structures

In this section, the most common types of Si radiation detectors are introduced. Detector types covered include Si p^+-i-n^+ photodiodes, CCDs, SDDs, and DEPFETs.

1.2.1 Si p^+-i-n^+ photodiodes

Si p^+-i-n^+ photodiodes are one of the most common forms of semiconductor X-ray detector (Lowe & Sareen, 2014). The structure is an extension of the p-n junction, first created at Bell Telephone Labs by Russel Ohl in 1940 (Renker & Lorenz, 2009). There it was observed that, upon shining bright light onto adjoining regions of p type (accepter doped semiconductor with excess holes in the valence band) and n type (donor doped semiconductor with excess electrons in the conduction

* This thesis uses the convention that materials with E_g < 1.4 eV are narrow bandgap materials, and that materials with $E_g \geq$ 1.4 eV are wide bandgap materials (Owens, 2012).

band region) Si material, the photovoltaic effect could be induced (Renker & Lorenz, 2009). The p^+-i-n^+ structure differs from a p-n junction in that an intrinsic (i) layer (pure semiconductor with relatively few impurities) is situated between a p^+ layer (highly accepter doped semiconductor) and a n^+ layer (highly donor doped semiconductor) (White, 1982). The p-n and p^+-i-n^+ junctions, and their corresponding physics, are described in detail in **Section 2.3**. Si p^+-i-n^+ photodiodes, when cooled, can achieve very good energy resolutions (e.g. energy resolutions of 149 eV FWHM at 5.9 keV have been achieved at -43 °C using an Si p^+-i-n^+ photodiode (Pantazis et al., 2010)). Such energy resolutions, in combination with their low power consumption, low cost, small size, and commercial availability, form the basis of their popularity as X-ray detectors (Knoll, 2000).

1.2.2 Charge coupled devices

CCDs were originally developed by Boyle & Smith (1970) as a replacement for light-sensitive film in cameras (Lowe & Sareen, 2014). The structure consists of a two dimensional array of metal-oxide-semiconductor (MOS) capacitors upon a Si substrate (Catura & Smithson, 1979). These MOS capacitors, when electrically biased, produce an array of localised potential wells (so called pixels) that store charge generated by photo-interactions within the depletion region (see **Section 2.3**) of the MOS structure (Catura & Smithson, 1979) (Lowe & Sareen, 2014). These pixels are read out by successively transferring charge from one potential well to the next by appropriately controlling the bias upon the MOS capacitors (Catura & Smithson, 1979). In 1979, the first use of CCDs as X-ray detectors was reported by Catura & Smithson (1979), with each pixel of the CCD observed to function as a single solid state X-ray detector. Today CCDs are used for a variety of applications including X-ray spectrometry (Gruner et al., 2002), particle tracking (Damerell, 1998), and imaging (McLeod et al., 2015). It should be noted that, in addition to the MOS type CCD described here, alternative CCD architectures such as the pn-CCD (Strüder et al., 2001) have also been established. When operated at -83 °C, an energy resolution of 131 eV FWHM at 5.9 keV has been reported using a pn-CCD (Meidinger et al., 2006).

1.2.3 Si drift detectors

The Si drift detector (SDD), developed by Gatti & Rehak (1983), employs a unique metal contact configuration over an n type Si wafer such that, when reverse biased, the n type Si wafer becomes fully depleted based on the sideward depletion principle (Tsuji et al., 2004). The design enables the position of impinging radiation to be calculated and near Fano-limited (see **Section 2.4.1**) energy resolutions when cooled (Tsuji et al., 2004). For example, at -33 °C a SDD was reported to have an energy resolution of 128 eV FWHM at 5.9 keV (Redus et al., 2011). More recently, efforts have been made to permit room temperature operation of SDDs. Bertuccio et al. (2015)

reported an energy resolution of 141 eV FWHM at 5.9 keV at 21 °C, using an SDD modified to minimize n^+ anode current density, connected to an ultra low noise charge sensitive preamplifier.

1.2.4 Depleted field effect transistors

The depleted field effect transistor (DEPFET) structure was first proposed by Kemmer & Lutz (1987). Its operation was subsequently confirmed experimentally in 1990 (Kemmer et al., 1990). DEPFETs possess properties that can be extremely useful for X-ray detection; namely, they combine properties of detection, amplification, and signal charge storage, and allow for non-destructive readout (Lutz et al., 2016). The DEPFET structure includes a p type Field Effect Transistor (FET) atop a fully depleted n type Si substrate. Electrons generated through photo-interactions within the depleted n type Si substrate are collected and confined within a potential minimum underneath the FET (Tsuji et al., 2004). Mirror charges are subsequently created in the channel, increasing the FET current. This not only acts as the first amplifier stage, but also provides an opportunity for non-destructive readout, where the signal charge (electrons) can be shifted to and from a storage position repeatedly, with the resulting current step of the FET used as a measure of the signal charge (Lutz et al., 2016).

DEPFETs also possess very good energy resolutions. During the first experimental characterisation of DEPFETs, an energy resolution of 250 eV FWHM at 5.9 keV was measured at room temperature (Kemmer et al., 1990). More recently, a near Fano-limited energy resolution of 131 eV FWHM at 5.9 keV was achieved with a DEPFET operated at room temperature (Wermes et al., 2004).

1.3 Motivation

With the advent of space exploration, radiation detection applications such as in situ planetary analysis (see **Section 1.4.1**) and planetary remote sensing (see **Section 1.4.2**) have been developed in order to better understand our Solar system. These applications require radiation detectors to be sent into the harsh environment of space, often for long periods of time (multiple years) without possibility of repair or replacement. Exploration of inner planetary bodies such as Mercury and Venus give rise to extreme temperatures (e.g. the mean surface temperature of Venus = 457 °C (Taylor & Grinspoon, 2009); temperatures at Mercury can reach ≈ 400 °C (Benkhoff et al., 2010)). Missions to study the Jovian and Saturnian systems can expose spacecraft to intense radiation (e.g. radiation doses of ≈ 200 krad per day at a distance of 280 Mm from Jupiter's centre of mass, assuming an isotropic radiation environment and 4 mm of Al shielding (Atzei et al., 2007)). Even the exploration of relatively benign parts of the Solar system, such as that of the

Earth-Moon system, can result in high radiation doses over long time scales (e.g. ≈ 170 krad was measured over 971 days, including 1 mm thick Al shielding, during the Van Allen Probe mission (Maurer & Goldsten, 2016)).

Although space missions do use conventional Si radiation detectors (see **Section 1.5**), the required instrument radiation shielding and cooling systems impose financial costs and technical restrictions on the mission, potentially limiting mission objectives and rendering certain environments inaccessible. Even when adopting modern cooling and radiation shielding solutions, the spectral resolution of Si detectors can degrade over time, reducing mission lifetime.

Development of semiconductor radiation detectors that can operate in environments of high temperature and intense radiation without any (or even only reduced) cooling and radiation shielding, would enable radiation detection in environments that are currently inaccessible for reasons of financial or technical impracticability. Even in space science missions that are able to accommodate cooling and radiation shielding requirements of existing detectors, reducing such requirements would reduce costs and technical complexity, allowing radiation spectroscopy (e.g. X-ray spectroscopy and electron spectroscopy) to be deployed more widely. Therefore, if temperature tolerant, radiation hard, X-ray and electron spectrometers could be developed, they would be attractive candidates for future space science missions.

1.4 Requirements for radiation spectrometers in space applications

Analysis of planetary and related surfaces can be achieved using radiation spectrometers aboard landers/rovers (in situ analysis), or planetary orbiters and flyby spacecraft (planetary remote sensing). The specific instrumentation requirements depend on the nature of the space science mission and the environments that will be encountered by the spacecraft and instruments. This section focuses on the requirements of radiation spectrometers within in situ planetary analysis and planetary remote sensing applications.

1.4.1 In situ planetary analysis

Instrumentation designed to be landed on the surface of planetary bodies face four key driving factors: mass; volume; power; and performance (Palmer & Limero, 2001) (Potts & West, 2008). Mass, volume, and power requirements must all be minimised in order to satisfy technological and financial limitations imposed by the inherent complexity of space missions. Instrument budgets also depend on the scientific objectives and capabilities of the instrument and lander. The CheMin instrument on board the Mars Science Laboratory (MSL) Curiosity rover for example,

tasked with both X-ray diffraction (XRD) and X-ray fluorescence (XRF) analysis of drilled rock/soil samples (see **Section 1.5.1**), had a mass of ≈ 10 kg, a volume of ≈ 27×10^3 cm^3, and a power consumption of ≈ 40 W (Blake et al., 2009). The APXS instruments on board the Mars Exploration Rovers (MER) Spirit and Opportunity, responsible for in situ XRF analysis of local rocks/soils (see **Section 1.5.1**), each had a mass of ≈ 0.25 kg, a volume of ≈ 166 cm^3, and a power consumption of ≈ 0.6 W (Rieder et al., 2003).

Whilst mass, volume, and power consumption must be minimised, the performance of on board science instrumentation must be maximised and satisfy the scientific objectives/requirements of the space mission. In the case of XRF (see **Section 2.2.1**) analysis of planetary surfaces, a typical requirement is the determination of elemental compositions of rocky surfaces and soils surrounding the lander/rover. Therefore, the X-ray spectrometer must possess an energy resolution sufficient to resolve key X-ray lines that identify major rock forming elements. For example, an energy resolution of ≈ 300 eV Full Width at Half Maximum (FWHM) at 3.5 keV is necessary to distinguish between Ca (Kα = 3.69 keV (Sánchez et al., 2003)) and K (Kα = 3.31 keV (Sánchez et al., 2003)), which are common elements on Mars (Grotzinger et al., 2012). An energy detection range sufficient to encompass the fluorescence lines of the elements of interest is also necessary, such that all elements of interest can be identified (e.g. Ti (Lα = 452 eV (Sánchez et al., 2003)), Mg (Kα = 1.25 keV (Sánchez et al., 2003)), and Fe (Kα = 6.40 keV (Sánchez et al., 2003))).

In addition to these basic requirements, the environment in which a lander/rover must operate can vary dramatically, including in terms of temperature, atmospheric pressure, and weather/storms (including dust, electrical, and Solar storms). On Mars for example, surface temperatures can vary from ≈ -98 °C to ≈ 22 °C (Spanovich et al., 2006). Instruments can be constructed in order to mitigate the effects of extreme environments, but a detector that is able to cope with less protection may provide a simpler design with reduced mass, volume, and power requirements.

Radiation spectrometers can require a significant amount of time in order to accumulate a spectrum. The MSL Curiosity rover APXS instrument (see **Section 1.5.1**), for example, requires a spectrum accumulation time of ≈ 3 hours (Gellert et al., 2009). In addition, any lander/rover itself, and the chosen power supply, will have a mission lifetime. These constraints limit the amount of data that can be collected during a mission. Therefore, it is beneficial to reduce the time required to collect each spectrum. This can be achieved by improving the detector's quantum efficiency (see **Section 2.5**) and maximising the detector's area, both of which enable the detection of a larger portion of the radiated flux.

1.4.2 Planetary remote sensing

As is the case for in situ planetary analysis, mass, volume, power, and performance are the four key factors for instruments designed for orbiting/close-encounter satellites/spacecraft. However, unlike in situ X-ray spectroscopy, remote sensing X-ray spectroscopy does not use internal radioisotope X-ray sources as the exciting source. Instead, external sources such as Solar X-rays are used; these can fluoresce the surfaces of airless planetary bodies. This method is limited to bodies sufficiently close to the external source, where the corresponding X-ray flux produces sufficient fluorescence X-rays to be detected.

Aside from the Sun, remote observations from Chandra and XMM-Newton have shown that the Jovian system (Elsner et al., 2005) and the Saturnian system (Branduardi-Raymont et al., 2010) are sources of X-rays. X-ray emissions have been observed from the Galilean moons, attributed to surface bombardment from highly energetic magnetospheric protons and ions (Elsner et al., 2005). Jupiter itself has X-ray aurorae, emitting both periodic (Gladstone et al., 2002) and irregular (Branduardi-Raymont et al., 2007) X-ray pulses at the northern pole. The origin of such X-rays is thought to be high charge state ions undergoing charge exchange (Dunn et al., 2017). Saturn has complex X-ray aurorae (Branduardi-Raymont et al., 2010), with current observations revealing significant variance between the Saturnian X-ray emission processes and aurorae observed at Jupiter and Earth (Branduardi-Raymont et al., 2010). Remote sensing X-ray spectroscopy is therefore suitable for airless bodies near the Sun (e.g. Mercury, Earth's Moon, and near-Sun (less than about 1 AU distant) objects such as asteroids or comets), the Jovian system, and the Saturnian system. These environments are some of the most aggressive in terms of ionising radiation in the Solar system (Atzei et al., 2007), and in the case of objects close to the Sun, experience large temperature variations. An appropriately radiation hard and temperature tolerant X-ray detector would therefore be beneficial for planetary remote sensing instruments, reducing the mass, volume, and power requirements of instrument radiation shielding and temperature control units.

Unlike in situ planetary analysis, the sample of interest in remote sensing is typically moving relative to the instrument. X-ray spectra must therefore be accumulated quickly in order to map surface elemental composition to spatial position. Maximising the quantum efficiency of the detector and the detector area are important in order to ensure fast accumulation times. Alternatively, spacecraft/instrument pointing capabilities can be used, at the expense of increased propulsion and power demands.

Planetary remote sensing also provides the opportunity to study the magnetospheres of planets and the interactions between planetary surfaces, atmospheres, and magnetospheres, with the Solar

wind and other forms of ionising radiation. In order to characterise these interactions, the electron and ion populations, including the energy and angular distributions, must be studied. Missions such as Cassini/Huygens (Matson et al., 2002), Galileo (Johnson et al., 1992), and JUNO (Stephens, 2018) all use or used spectrometers to analyse in situ electrons and ions. Despite the success of previous missions to the Jovian and Saturnian systems, many questions still remain. For example: the interactions between local environments of the Galilean moons, such as Ganymede and the Jovian magnetosphere, are still not fully understood; the stability and dynamics of the Jovian magnetodisks, including angular momentum exchange and dissipation of rotational energy, still require investigation; the middle magnetosphere of Jupiter contains a warm plasma, for which the responsible processes are not yet known (Grasset et al., 2013). Financial cost and technical complexity impose limits on the frequency of missions to these systems, as well as restricting mission objectives. Reducing instrument radiation shielding and temperature control requirements by using radiation hard and temperature tolerant semiconductor detectors would help alleviate these restrictions.

1.5 Space missions employing Si X-ray and electron detectors

1.5.1 X-ray detectors

Progress in the development of XRF (see **Section 2.2.1**) instrumentation has led to an increased adoption of X-ray spectrometers within space science missions. Examples of Si X-ray spectrometers employed within the fields of in situ planetary analysis and planetary remote sensing are presented below.

SMART-1, launched in 2003, was used to perform scientific observations of the Moon (Foing et al., 2001). The D-CIXS (Demonstration of a Compact Imaging X-ray Spectrometer) instrument, carried by SMART-1, produced the first global XRF map of the Lunar surface, expanding upon the XRF measurements of the Lunar surface conducted by the Apollo 15 and 16 missions (Foing et al., 2001). D-CIXS consisted of 24 swept charge device (SCD) Si X-ray detectors (each 107 mm^2 (Holland et al., 2004)) in order to perform spatially localised XRF (Grande et al., 2003). The exciting source for XRF of the Lunar surface was Solar X-rays emitted by the Sun. A 500 μm thick Si p^+-i-n^+ photodiode based X-ray spectrometer was used for Solar X-ray monitoring (Huovelin et al., 2002). At launch, the energy resolution of D-CIXS was better than 250 eV FWHM at Mg Kα = 1.25 keV, Al Kα = 1.48 keV, and Si Kα = 1.74 keV (Thompson et al., 2009). However, after the 15 month journey to the required Lunar orbit, the energy resolution had degraded to ≈ 420 eV due to radiation damage (Swinyard et al., 2009), thus emphasising the need for radiation hard detectors even for space science missions to relatively benign environments such as the Moon. D-CIXS measurements revealed the absolute elemental

abundances of Fe, Mg, Al, and Si, across the entire Lunar surface (Dunkin et al., 2003). This was a significant improvement over the elemental ratios derived from the Apollo XRF measurements (Foing et al., 2001). D-CIXS also provided the first Lunar XRF observations of the Ti Kα line (Swinyard et al., 2009). Additionally, D-CIXS successfully demonstrated that even X-ray spectrometers of modest energy resolution can return valuable scientific data.

MESSENGER, the first spacecraft to enter orbit around Mercury (McAdams et al., 2007), was launched in 2004 to investigate the planet's composition and magnetic field structure. The study of Mercury, especially its chemical composition, is important not least due to the potential clues offered regarding the formation of the Solar system (Solomen et al., 2001). The X-ray spectrometer (XRS) aboard MESSENGER was used to measure the elemental composition of Mercury's surface (Schlemm et al., 2007), using Solar X-rays as the exciting source. A 500 µm thick Si p^+-i-n^+ photodiode, cooled to temperatures lower than -20 °C, was used to measure incident Solar X-rays over a range of 1 keV to 10 keV, with an energy resolution of 589 eV FWHM at 5.9 keV. The Si detector provided similar functionality to that of the X-ray Solar monitoring system aboard SMART-1. It should be noted that XRF measurements of Mercury's surface were not achieved using semiconductor based detectors. Instead, three gas proportional counters (GPCs) were used. This design decision was based on the requirements of the space science mission, where the large geometric factor of GPCs were unmatched relative to available semiconductor detectors at the time (Solomen et al., 2001). As was the case with D-CIXS, the Si Solar X-ray detector within XRS experienced radiation damage during the 6.6 year interplanetary cruise to Mercury and throughout its lifetime, which reduced the detectors maximum operating temperature (Starr et al., 2016).

BepiColombo, a mission consisting of two spacecraft (the Mercury Planetary Orbiter (MPO) and the Mercury Magnetospheric Orbiter (MMO)) will be the next mission to arrive at Mercury. The scientific objectives of BepiColombo include: understanding the origins and evolution of the planet; examining its form, interior, geology, and structure; investigating the composition and dynamics of the vestigial atmosphere; determining the origins of its magnetic field (Benkhoff et al., 2010). Aboard MPO is the Mercury Imaging X-ray Spectrometer (MIXS), which will measure fluorescence X-ray emissions from the surface of Mercury in the energy range 0.5 keV – 7.5 keV (Fraser et al., 2010), using Solar X-rays as the exciting source. MIXS is a two component instrument, comprising a collimated channel (MIXS-C) providing 70 km – 270 km per pixel spatial resolution, and an imaging X-ray telescope (MIXS-T) providing < 10 km per pixel spatial resolution (Fraser et al., 2010). MIXS-T will be the first imaging X-ray telescope used for planetary remote sensing, providing a unique opportunity in the study of elemental compositions of specific landforms such as crater peaks (Fraser et al., 2010). Both MIXS-C and

MIXS-T will use Si Macropixel DEPFET arrays (Zhang et al., 2006), operated at temperatures ≈ -40 °C. At this temperature, the spectrometers can achieve energy resolutions of ≈ 126 eV FWHM at 5.9 keV (Treis et al., 2010). Due to radiation damage throughout the 6 year cruise to Mercury, the energy resolution of the spectrometer is anticipated to degrade from ≈ 100 eV FWHM at 1 keV (the energy of interest) to ≈ 200 eV FWHM at 1 keV, at an operating temperature of -40 °C (Treis et al., 2010).

The Hayabusa spacecraft, launched in 2003, was used to acquire samples from the surface of the near-Earth asteroid Itokawa (arrived in 2005) (Fujiwara et al., 2006), and return them to Earth (arrived in 2010) (Yada et al., 2013). A suite of on board instruments performed in situ observations of the asteroid, including the analysis of major surface elements (Arai et al., 2008). The study of primitive asteroids is considered important not least because they provide key information regarding the early planetary system evolution process (Fujiwara et al., 2006). The Hayabusa spacecraft included an X-ray fluorescence spectrometer (XRS) which used four Si CCDs (1024 × 1024 pixels per CCD, each pixel 24 μm^2) (Arai et al., 2008). The exciting source for XRF was Solar X-rays emitted by the Sun. Three CCDs were used to observe fluorescence X-rays from the surface of the asteroid, while one CCD observed fluorescence X-rays from an on board sample which acted as an indirect Solar X-ray monitor. The energy resolution of each Si CCD X-ray detector was 160 eV at 5.9 keV, when cooled to -60 °C (Okada et al., 2006). XRS enabled the successful determination of Mg, Si, Al, and S elemental abundances in 10 areas of Itokawa, the results of which suggested that the asteroid was an ordinary chondrite (Arai et al., 2008).

The primary purpose of Mars Pathfinder (MPF), launched in 1996, was to demonstrate low-cost cruise, entry, descent, and safe landing of a payload on the Martian surface (Golombek, 1997). MPF also included the deployment and operation of the first rover (Sojourner) on Mars (Golombek, 1997). On board Sojourner was the Alpha Proton X-ray Spectrometer (APXS). APXS was used, in conjunction with other scientific instrumentation, to identify rock petrology and mineralogy across the Ares Vallis landing area (Golombek et al., 1999), thus providing a calibration point for orbital remote sensing observations (Golombek, 1997). The APXS instrument used 9 ^{244}Cm radioisotope α particle sources (emitting 5.8 MeV α particles, total activity = 1.7 GBq), installed within the instrument head, as the exciting source for XRF of the Martian surface (Brückner et al., 2003). The X-ray detector was a Si p^+-i-n^+ photodiode (300 µm thick), operated within the ambient Martian environment without any cooling. An energy resolution of ≈ 250 eV FWHM at 5.9 keV was achieved during Martian nights, where APXS operating temperatures were between -50 °C and -90 °C (Economou, 2001). Measurements

during the Martian days were not possible due to increased noise in X-ray spectra from the higher daytime temperatures (> -50 °C) (Brückner et al., 2003).

The Mars Exploration Rovers (MER), launched in 2003, were developed to determine whether Mars ever provided the conditions necessary for the formation and preservation of life (Crisp et al., 2003). The two rovers, Spirit and Opportunity, landed in 2004 and investigated their respective landing sites (Gusev crater and Meridiani Planum) for evidence of action of liquid water. This involved the characterisation of local rocks and soils, which could provide evidence of past water activity (Crisp et al., 2003). Each rover contained an Alpha Particle X-ray Spectrometer (APXS) for this purpose, with technology derived from the Sojourner rover APXS instrument. Six ^{244}Cm radioisotope α particle sources were used as the excitation sources for XRF (emitting 5.8 MeV α particles, with a total activity of 1.1 GBq) (Rieder et al., 2003). The measurement geometry was improved relative to the Sojourner APXS (30 mm mean distance between sources/detectors and sample, cf. 50 mm for the Sojourner APXS) such that X-ray count rate was improved (Rieder et al., 2003). An SDD (10 mm^2) was used as the spectrometer's X-ray detector; the spectrometer had an improved energy resolution compared to its predecessor: 160 eV FWHM at 5.9 keV at temperatures ≈ -35 °C cf. 250 eV FWHM at 5.9 keV for the Sojourner APXS at temperatures ≈ -50 °C (Rieder et al., 2003). The MER APXS instruments were able to measure the elemental abundances of Na, Mg, Al, Si, P, S, Cl, K, Ca, Ti, Cr, Mn, Fe, Ni, Zn, and Br from over 100 samples of soils and rocks within the first 470 sols on Mars (Martian days) (Gellert et al., 2006). The chemical data revealed alteration in rocks and soils from an acidic and aqueous environment (Gellert et al., 2006).

Mars Science Laboratory (MSL), launched in 2011, was designed in order to explore the habitability of Mars (Vasavada et al., 2014). The MSL curiosity rover was successfully delivered to the surface of Mars in 2012 (Vasavada et al., 2014). The science payload of Curiosity included an X-ray diffractometer (CheMin) and an Alpha Particle X-ray Spectrometer (APXS); both have been used to analyse the chemical composition of surrounding rock and soil samples (Grotzinger et al., 2012). The CheMin instrument combined XRF and XRD measurements in order to provide information about the chemistry and crystal structure of collected drill samples (< 150 μm diameter grains) (Blake et al., 2012). A Co X-ray tube (emitting Kα = 6.93 keV and Kβ = 7.65 keV X-rays) was used as the exciting source for XRF and XRD. The X-ray detector was an E2V Si CCD array (600 × 1182 pixels, 40 μm^2 per pixel) with a 600 × 582 pixel data collection area (Blake et al., 2012). This arrangement was chosen such that data collection could take place continuously (Blake et al., 2012). The detector was cooled via a cryocooler to temperatures between -22 °C and -48 °C (Blake et al., 2012). An energy resolution of ≈ 250 eV FWHM at 6.93 keV was reported within this temperature range (Blake et al., 2012). The APXS

instrument, with technology derived from the previous rovers (MPF and MER), was used to analyse unprepared rock and soil samples, as well as providing support for the CheMin instrument (Blake et al., 2012). The X-ray detector was the same as that used for the MER APXS instruments, but an internal Peltier cooler was installed which provided a constant detector temperature of -35 °C. This improved Martian day time operation relative to the MER APXS instruments (Gellert et al., 2009). The APXS instruments measurement geometry was further improved (19 mm mean distance between sources/detectors and sample cf. 30 mm for the Spirit & Opportunity APXS instruments), thus providing better (higher) X-ray count rates (Gellert et al., 2009). Other changes to the APXS instrument included the elimination of α particle detectors and the use of conventional sealed ^{244}Cm radioisotope α particle sources (Gellert et al., 2009).

1.5.2 Electron detectors

Electron spectroscopy can be used to study interactions between the Solar wind and planetary atmospheres, magnetospheres, and surfaces (Livi et al., 2003). In cases of sufficiently strong dipole moments, interactions with the Solar wind can result in space plasma activity (Schindler, 2007). Understanding the complex phenomena behind such interactions has spurred considerable research efforts and has formed part of the science objectives for various space missions. Some examples of Si based electron spectrometers used within space science missions are presented below.

The Galileo mission to Jupiter, launched in 1989, was developed in order to: determine the chemical composition and dynamics of the Jovian atmosphere; characterise the morphology, geology, atmospheres, and ionospheres of the Jovian satellites; investigate the composition and angular distribution of energetic particles throughout the magnetosphere (Johnson et al., 1992). The Energetic Particle Detector (EPD), on board the Galileo spacecraft, was used to characterise ions (20 keV to 55 MeV), electrons (15 keV to 11 MeV), and elemental species (He to Fe) (10 keV nucl^{-1} to 15 MeV nucl^{-1}) important in determining the size, shape, and dynamics of the Jovian magnetosphere (Williams et al., 1992). The instrument comprised two bi-directional solid-state detector telescopes: the Low-Energy Magnetospheric Measurements System (LEMMS) and the Composition Measurement System (CMS) (Williams et al., 1992). LEMMS was responsible for measuring the characteristics of incoming electrons and housed 8 Si detectors of varying surface area and thickness, see Williams et al. (1992) for details. The omni-directional electron environment about Jupiter, mapped by LEMMS, has been used in order to model the effects of the radiation environment on Jupiter's moons and their corresponding atmospheres (Jun et al., 2005). In addition, LEMMS measurements identified intense, magnetic field-aligned,

energetic electron beams (> 20 keV) flowing along Io's flux tube (a ring of charged particles connecting Io with Jupiter) (Mauk et al., 2001).

JUNO, launched in 2011 and arrived in 2016, became the second spacecraft to orbit Jupiter. The goal of the mission is to improve our understanding of the Solar system by investigating the origin, evolution, and structure of Jupiter (Stephens, 2018). The Jupiter Energetic Particle Detector Instrument (JEDI), on board JUNO, is being used to investigate the generation of Jupiter's aurorae by measuring the incoming angle and energy of ions (50 keV to 1 MeV) and electrons (40 keV to 500 keV) (Mauk et al., 2017). JEDI consists of three near-identical instruments mounted at three different locations on the JUNO spacecraft. Each instrument houses 6 Si detector arrays to measure the energy of ions and electrons (Mauk et al., 2017). Each Si detector array consists of four pixels: two large pixels (0.40 cm^2) and two small pixels (0.02 cm^2). One large and one small pixel are dedicated to electron detection whilst the other pixel set are dedicated to ion detection (Mauk et al., 2017). The electron pixels are covered with a 2 μm Al layer such that < 250 keV protons would not be absorbed (Mauk et al., 2017). The estimated total ionising dose experienced by JUNO (100 krad with 13 mm thick Al shielding) will be four times greater than that of Galileo (Bolten et al., 2017). In an effort to protect the various scientific instruments, including the Si based electron/ion spectrometers, a highly elliptical orbit was chosen (closest approach to Jupiter every 53 days) and significant radiation shielding was implemented (Bolten et al., 2017). The radiation shielding requirements increased the mass of each JEDI instrument to ≈ 6.4 kg from ≈ 2 kg (Mauk et al., 2017).

The MESSENGER mission, in addition to the XRS instrument (see **Section 1.5.1**), also housed the Energetic Particle and Plasma Spectrometer (EPPS) instrument (Andrews et al., 2007). The EPPS instrument was used to determine: the structure of Mercury's magnetic field; the configuration of Mercury's extended magnetospheric environment; the nature of Mercury's sparse atmosphere (Andrews et al., 2007). EPPS was composed of two parts: the Energetic Particle Spectrometer (EPS) and the Fast Imaging Plasma Spectrometer (FIPS). EPS measured the particle composition and energy spectra of in situ H to Fe ions (≈ 15 keV $nucl^{-1}$ to ≈ 3 MeV $nucl^{-1}$) and electrons (15 keV to 1 MeV), with a $160° \times 12°$ field of view (Andrews et al., 2007). A combination of 6 Si detector arrays were used for particle energy determination. Each array consisted of four, 500 μm thick pixels: two pixels for ion detection and two pixels for electron detection. The electron detecting pixels were covered with a thin Al layer in order to stop < 110 keV ions from entering the pixels (Andrews et al., 2007).

The New Horizons mission, launched in 2006, was the first spacecraft to explore the icy dwarf planets that dominate the third outer portion of our Solar system (Young et al., 2008). The

spacecraft flew past Pluto in 2015, providing information regarding the dwarf planets geology, composition, and atmosphere (Stern et al., 2015). The flyby also provided the first direct observations of Pluto's interactions with the Solar wind (McComas et al., 2016). The Pluto Energetic Particle Spectrometer Science Investigation (PEPSSI), on the New Horizons spacecraft, was tasked with measuring ions (15 keV to 1 MeV) and electrons (25 keV to 500 keV) in the near-Pluto environment (McNutt et al., 2008). The detector within PEPSSI consisted of a 12 pixel, 500 μm thick, SSD array. Three pixels were dedicated to energetic electron detection and coated with an Al layer in order to block < 100 keV ions. The detector operated uncooled, with operating temperature limits between 35 °C and -35 °C. The electron energy resolution was 5 keV over the energy range of interest (McNutt et al., 2008). It was also possible to determine the electron particle direction, where incoming electrons could travel through three separate 25 ° × 12 ° windows (McNutt et al., 2008). The New Horizons radiation environment included exposure to Solar protons, Jovian high energy particles, galactic cosmic rays, and neutrons and γ-rays emitted from the on-board radioisotope thermoelectric generator (RTG) (McNutt et al., 2008). Appropriate radiation shielding was implemented in order to ensure a total ionising dose of < 15 krad, the radiation dose limit of PEPSSI (McNutt et al., 2008).

1.6 Compound semiconductor materials for radiation detection

1.6.1 An introduction to compound semiconductors

Compound semiconductors provide the opportunity to engineer materials with specific properties suitable for radiation detectors within space science applications. By adjusting the elements used, and at what ratios, it is possible to modify the bandgap energy and stopping power of the resultant compound semiconductor. To date, a wide variety of compound semiconductor materials have been studied and their suitability as radiation detectors reported. These include GaAs, AlGaAs, GaN, InGaP, AlInP, SiC, CdTe, and CdZnTe. This thesis concentrates on AlGaAs detectors. Owens (2012) provides an introduction to compound semiconductors and associated detecting systems. The reader is referred to the work of Lioliou & Barnett (2018), Gohil et al. (2016), Butera et al. (2017), Auckloo et al. (2016), Zhao et al. (2018a), Ishikawa et al. (2016), and Hansson et al. (2014) for more recent work on GaAs, cubic-GaN, InGaP, AlInP, SiC, CdTe, and CdZnTe detectors, respectively.

1.6.2 $Al_xGa_{1-x}As$ photodiode radiation detectors

$Al_xGa_{1-x}As$ has received particular attention as a promising material for X-ray and beta particle detection for space applications. The bandgap of $Al_xGa_{1-x}As$ changes rapidly with x (e.g. 2.17 eV for AlAs cf. 1.42 eV for GaAs (Adachi, 1985)), enabling the device engineer to balance

improvements in intrinsic resolution (see **Section 2.4.1**) resulting from a reduced bandgap, with the reduction of temperature dependent noise (see **Section 2.8**) derived from an increased bandgap. The larger X-ray linear attenuation coefficients of $Al_xGa_{1-x}As$ relative to Si (e.g. 787.8 cm^{-1} for $Al_{0.2}Ga_{0.8}As$ cf. 346.4 cm^{-1} for Si, at 5.9 keV, see Fig. 1.1) (Henke et al., 1993) allows for use of thinner detectors, potentially reducing performance degradation in extreme radiation environments. The expected better radiation hardness of $Al_xGa_{1-x}As$ relative to Si (Walker et al., 2017) (Yamaguchi et al., 1995) (Yoshida et al., 1982) is anticipated to improve detector durability and alleviate detector shielding requirements within intense radiation environments, such as those encountered in space.

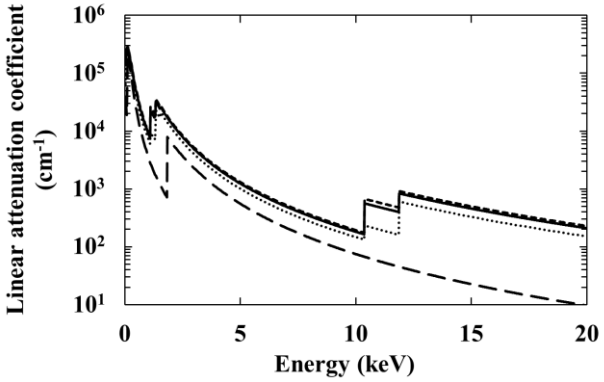

Fig. 1.1. Linear attenuation coefficient as a function of energy for GaAs (short dashed line), $Al_{0.2}Ga_{0.8}As$ (solid line), $Al_{0.8}Ga_{0.2}As$ (dotted line), and Si (long dashed line). The discontinuities are the associated Al, Ga, As, and Si absorption edges (see **Section 2.2.2.1**).

Prior to the results reported in this thesis, research had been conducted for $Al_xGa_{1-x}As$ radiation detectors with a variety of x. The first use of $Al_xGa_{1-x}As$ for X-ray detection was demonstrated in 1995, using $Al_xGa_{1-x}As$/GaAs separate absorption and multiplication (SAM) avalanche photodiodes (APDs) (Lauter et al., 1995). The devices included a staircase multiplication region structure incorporating linearly graded $Al_xGa_{1-x}As$ material (x = 0.1 – 0.45). The following year, results were published using 2 × 2 monolithic arrays of detectors of similar design (Lauter et al., 1996). Those initial investigations were very promising; energy resolutions of 1.95 keV FWHM at 13.96 keV without avalanche gain, and 0.9 keV FWHM at 13.96 keV at the optimal working point of the detector, were measured. Dark leakage currents < 100 pA were also reported (Lauter et al., 1995). The findings clearly established that AlGaAs was a suitable candidate for further investigation as an X-ray detecting material.

In 2002, current mode X-ray flux detection results were reported for graded-gap $Al_xGa_{1-x}As$/GaAs (x = 0 – 0.4) devices (Silenas et al., 2002) (Silenas et al., 2006), using thicker $Al_xGa_{1-x}As$ layers

when compared to those devices previously reported by Lauter et al. (1995). Silenas et al. (2002 & 2006) claimed a charge collection efficiency of 100 % without the application of bias. It should be noted however, that neither X-ray spectroscopy or photon counting were demonstrated with these detectors.

In 2008, $Al_{0.8}Ga_{0.2}As$ p^+-p^--n^+ photodiodes, intended for use in telecommunications, were successfully demonstrated as X-ray photon counting and spectroscopic detectors at room temperature (Lees et al., 2008). The extensive study of $Al_{0.8}Ga_{0.2}As$ for X-ray detection followed, with results reported for varied device structures, thicknesses, and diameters (Barnett et al., 2010) (Barnett, 2011) (Barnett et al., 2012a) (Gomes et al., 2014) (Barnett et al., 2015). In 2010, 1 µm thick i layer $Al_{0.8}Ga_{0.2}As$ p^+-i-n^+ (200 µm diameter) photodiodes were reported as soft X-ray photon counting detectors. At room temperature, the devices had energy resolutions of ≈ 1.1 keV FWHM at 5.9 keV (Barnett et al., 2010). Thicker i layer $Al_{0.8}Ga_{0.2}As$ p^+-i-n^+ devices were subsequently investigated as material development improved. The X-ray response of $Al_{0.8}Ga_{0.2}As$ p^+-i-n^+ (400 µm diameter) photodiodes with 1.7 µm thick i layers was reported in 2015 (Barnett et al., 2015). Prior to the work in this thesis, the devices were the thickest AlGaAs X-ray spectroscopic mesa photodiodes reported to date, and had better energy resolutions than any previously investigated non-avalanche AlGaAs X-ray detector of the same area (≈ 1.27 keV FWHM at 5.9 keV) (Barnett et al., 2015).

Aside from X-ray detection, initial results characterising 1 µm i layer thick $Al_{0.8}Ga_{0.2}As$ p^+-i-n^+ photodiodes (400 µm diameter) as electron detectors has been reported (Barnet et al., 2013). The devices were shown to be spectroscopically sensitive to β^- particles with energies > 21 keV when operated at room temperature (20 °C). This early work indicated that AlGaAs was suitable for both X-ray and electron spectroscopy.

1.7 Thesis organisation

Chapter 2 reviews the relevant detector physics associated with compound semiconductor X-ray and electron spectrometers. The different radiation production processes are discussed, with a focus on those most important to this thesis. The noise components associated with the spectrometers reported in this thesis are described, and the theory of impact ionisation introduced. **Chapter 3** presents measurements and analysis characterising the performance of non-avalanche $Al_{0.2}Ga_{0.8}As$ p^+-i-n^+ photodiodes as spectroscopic X-ray detectors in the temperature range 20 °C to -20 °C. Electrical characterisation of these devices is also reported, at temperatures 60 °C to -20 °C. **Chapter 4** reports the electrical characterisation (20 °C to -20 °C) and the spectroscopic performance (X-rays and β^- particles) (30 °C to -20 °C) of a prototype multi pixel

non-avalanche $Al_{0.2}Ga_{0.8}As$ p^+-i-n^+ photodiode array. **Chapter 5** presents room temperature (20 °C) electrical characterisation and X-ray detection measurements of $Al_{0.6}Ga_{0.4}As$ p^+-i-n^+ photodiodes, operating in avalanche mode. **Chapter 6** reports measurements and analysis characterising the performance of GaAs/$Al_{0.8}Ga_{0.2}As$ separate absorption and multiplication avalanche photodiodes (SAM APDs) at room temperature (20 °C). Improvements in performance, attributed to the inclusion of an avalanche layer, are discussed. **Chapter 7** offers overarching conclusions on the work reported in this thesis. Possible future research is considered.

Chapter 2
Detector physics

2.1 Introduction

This thesis concentrates on the detection of soft X-rays within the energy range 5.9 keV to 6.5 keV and β^- particles (fast electrons) within the energy range 1 keV to 66 keV, using photon counting non-avalanche photodiodes and photon counting avalanche photodiodes (APDs). The physical principles and production mechanisms concerning such radiation, in addition to the associated interactions with matter and relevant detector physics are reviewed in this chapter. The factors affecting the energy resolution of semiconductor detectors are discussed, and the impact ionisation process for avalanche photodiodes is reviewed.

For further detail, comprehensive introductions to X-ray detection with semiconductor devices include Fraser (1989), Jenkins et al. (1995), Owens (2012), and Owens (2019). Comprehensive introductions to β^- particle detection with semiconductor devices include Knoll (2000) and Ahmed (2014).

2.2 X-ray and electron interaction with matter

2.2.1 X-ray production

X-ray radiation from an X-ray source (e.g. the Sun, active galaxies, neutron stars, or radioisotopes) can be classified as either continuous X-ray radiation (i.e. emission of X-rays within a range of energies) or characteristic X-ray radiation (i.e. emission of X-rays with discrete energies) (van Grieken & Markowicz, 2002). The type of X-ray radiation produced depends on the physics of the emitting X-ray source. For example, a Mo target X-ray tube operated at an electric potential difference of 35 kV produces a continuous X-ray spectra of energy $\leq$ 35 keV (by virtue of there being an electric potential of 35 kV across the tube), while also producing characteristic Mo Kα (17.4 keV) and Mo Kβ (19.6 keV) X-rays (Sánchez et al., 2003). The ^{55}Fe radioisotope X-ray source, used in this thesis, produces only characteristic Mn Kα 5.9 keV and Mn Kβ 6.49 keV X-rays via electron capture (Sánchez et al., 2003). It should be noted that the ^{55}Fe radioisotope X-ray source used in this thesis also emits electrons; however these electrons are fully attenuated by the included Be window and subsequently not observed.

Continuous X-ray emission occurs when charged particles (e.g. electrons, protons, and ions) of sufficiently high energy are accelerated at relativistic velocities due to passing through a magnetic

field (synchrotron radiation) (Ahmed, 2014), or decelerated due to passing through the Coulomb field of an atomic nucleus (bremsstrahlung radiation) (van Grieken & Markowicz, 2002). Bremsstrahlung radiation is the origin of the X-ray continuum produced by conventional X-ray tubes (Knoll, 2000). In this case, electrons are emitted via a heated cathode and accelerated into an anode; the accelerated electrons are then scattered by the atomic nuclei of the anode material, producing a bremsstrahlung X-ray continuum with energies extending up to the kinetic energy of the moving charged particle (Tsoulfanidis & Landsberger, 2015). Characteristic X-rays at defined energies are also emitted from the X-ray tube's target. Whilst not an X-ray source used in this thesis, synchrotron radiation can be, in contrast with bremsstrahlung radiation, extremely intense, highly collimated, and polarized (Ahmed, 2014). As such, synchrotron radiation is very useful (Knoll, 2000).

The production of characteristic X-rays involves the ionisation of electrons in atomic shells and the subsequent rearrangement of remaining electrons in order to return the atom to its lowest energy state (van Grieken & Markowicz, 2002) (Knoll, 2000). Ionisation of atomic shells can occur by radioactive decay, electron capture, internal conversion, or by charged particles/photons with energies greater than or equal to the binding energy of inner shell electrons interacting with the atom (Knoll, 2000) (Jenkins et al., 1995). Should an electron be ejected, electrons of higher energy states will attempt to fill the inner atomic shell vacancy (Knoll, 2000). This process requires the release of energy, which can occur through the emission of a photon whose energy equals the difference between the two orbit states (Knoll, 2000), as well as by other mechanisms. Since there are a limited number of possible atomic shell transitions, such photons are characteristic in nature. If, for example, an electron from the K shell (inner most shell) was to be ejected, then an electron from the L shell (next inner most shell) may fill the K shell vacancy. In this case, a so called Kα photon would be emitted, whose energy is equal to the difference in binding energy between the K and L shells (Knoll, 2000). Alternatively, the K shell vacancy could be filled by an M shell electron, resulting in the emission of a Kβ photon whose energy is slightly greater than that of a Kα photon. Vacancies created in outer shells by the filling of a K shell vacancy are subsequently filled by yet higher energy state electrons, inducing the emission of L, M, … etc. series characteristic photons (Knoll, 2000). Since the allowed energy levels in an atom are unique to each individual element, the emitted characteristic photons are correspondingly unique. For example, Kα X-rays of sodium (Na; Z (proton number) = 11) have an energy of ≈ 1.04 keV, Kα X-rays of iron (Fe; Z = 26) have an energy of ≈ 6.40 keV, and Kα X-rays of gold (Au; Z = 79) have an energy of ≈ 68.80 keV. K series X-ray energies increase with increasing atomic number of the element (Knoll, 2000). As such, this phenomenon can be used in order to analyse the elemental composition of samples, a technique called X-ray

fluorescence spectroscopy (XRF). A thorough examination of characteristic X-ray production is given by van Grieken & Markowicz (2002).

It should be noted that following the ionisation of an inner atomic shell there are alternative processes that may occur in order to return the atom to a lower energy state. For example, instead of emitting a photon, an excited atom may eject an additional electron that is less tightly bound, subsequently reducing the atom's energy state (van Grieken & Markowicz, 2002). This transition is called the Auger effect, and the ejected electron is called an Auger electron (van Grieken & Markowicz, 2002). Two special cases of the Auger effect are known: the Coster-Kronig transition, where the transitioning electron (that which occupies the vacancy) and the ejected electron originate from the same shell, but from differing sub shells; the super Coster-Kronig transition, where the transitioning electron and ejected electron originate from the same shell and subsequent sub shell (Bambynek et al., 1972) (Howell, 2008). These phenomena result in fewer X-ray photons produced for a given quantity of material than would otherwise be expected (van Grieken & Markowicz, 2002). A thorough examination of these processes is given by Stoneham (1981).

2.2.2 X-ray attenuation

Monochromatic X-rays interact with matter through a number of processes, of which, contribute to the incident X-rays attenuation when passing through a given material. This attenuation is described by the Beer-Lambert law,

$$I = I_0 \exp[-\mu_m \rho x_t], \tag{2.1}$$

where I (units of W cm^{-2}) is the final intensity of X-rays transmitted through the material, I_0 (units of W cm^{-2}) is the initial intensity of X-rays just before entering the material, μ_m (units of cm^2 g^{-1}) is the mass attenuation coefficient of the material at the specific monochromatic X-ray energy, ρ (units of g cm^{-3}) is the material density, and x_t (units of cm) is the material thickness (Jenkins et al., 1995). The mass attenuation coefficient, μ_m, can be expressed as

$$\mu_m = \frac{\mu}{\rho}, \tag{2.2}$$

where μ (units of cm^{-1}) is the linear attenuation coefficient, and accounts for the various interactions that can occur between the monochromatic X-rays and the material (Jenkins et al., 1995). These interactions include: photoelectric absorption; Compton scattering; pair production;

coherent scattering (Knoll, 2000). It should be noted that μ, as defined here, is broader in scope when compared to the absorption coefficient, μ_{abs} (units of cm^{-1}); the linear attenuation coefficient includes purely elastic processes, where photons are deflected but do not give up any initial energy to the material (van Grieken & Markowicz, 2002).

2.2.2.1 Absorption edges

Generally, the linear attenuation coefficient decreases with increasing incident X-ray energy for the same material. However, there are abrupt discontinuities in this trend (see Fig. 3.5), known as absorption edges (Jenkins et al., 1995). Absorption edges occur at energies equal to the electron binding energies of the material (Knoll, 2000). At these energies the probability of photon absorption occurring increases, resulting in an increased linear attenuation coefficient relative to energies slightly below the absorption edges (Knoll, 2000).

2.2.2.2 Photoelectric absorption

Photoelectric absorption is the predominant mechanism of interaction between photons of relatively low energy and atoms (Evans, 1955). Consequently, it is the most important mode of interaction for X-ray (≈ 5.9 keV) detection. No single analytic expression is valid for the probability of photoelectric absorption per atom over all photon energies and atomic numbers (Knoll, 2000). However, for photons of energy < 100 keV, the probability of photoelectric absorption can be approximately expressed by the proportionality

$$\tau_{abs} \cong \propto \frac{Z^4}{E^3}, \tag{2.3}$$

where τ_{abs} (units of cm^2) is the total photoelectric absorption cross section per atom (the probability of photoelectric absorption occurring) and E (units of eV) is the energy of the incident photon (Evans, 1955). From this proportionality, it is evident that photoelectric absorption becomes far more likely with increased atomic number and less likely with increased photon energy (van Grieken & Markowicz, 2002).

In the photoelectric absorption process, the interacting photon, providing its energy is equal to or greater than the binding energy of the most loosely bound electron within a given atom, is completely absorbed by the atom. In its place, an electron is ejected from the atom (Knoll, 2000). This ejected electron is called a photoelectron, and appears with an energy, E_{pe} (units of eV), given by

$$E_{pe} = E - E_b, \tag{2.4}$$

where E_b (units of eV) is the binding energy of the photoelectron in its original shell (Knoll, 2000). Given an incident photon of sufficient energy, the K shell (containing the most tightly bound electrons) of an atom is the most probable origin of photoelectrons (Knoll, 2000).

Upon ejection of a photoelectron, a vacancy in an inner shell of the atom is left, leading to characteristic X-ray emission or the ejection of an Auger electron (see **Section 2.2.1**). This possibly emitted X-ray photon, in addition to other photons emitted via the rearrangement of higher shell electrons, can itself also interact with other atoms in the material, repeating the photoelectric absorption process. The result is a large production of X-rays, Auger electrons, and photoelectrons. In this thesis, the range of photoelectrons and Auger electrons created by photoelectric absorption is sufficiently short that they can be considered to be localised to the point of X-ray absorption which caused their emission.

2.2.2.3 Compton scattering

Compton scattering is described as the interaction between a photon and a free electron considered to be at rest (van Grieken & Markowicz, 2002). In contrast with photoelectric absorption, the incident photon does not get absorbed. Instead, the incident photon is deflected through an angle, θ, with respect to its original direction, and transfers a portion of its energy to the electron (Knoll, 2000). Should energy be transferred to the electron, it is then known as a recoil electron (Knoll, 2000).

The probability of Compton scattering occurring per atom of the material depends on the number of electrons available as scattering targets (Knoll, 2000), thus increases linearly with Z. The probability dependence upon incident photon energy is rather complex, but generally reduces with increasing photon energy (Knoll, 2000). It should be noted that Compton scattering is of minimal consequence for the work in this thesis. The reader is referred to van Grieken & Markowicz (2002) for a more detailed review of Compton scattering.

2.2.2.4 Pair production

Pair production is another possible interaction between a photon and an atomic nucleus (Tsoulfanidis & Landsberger, 2015). As a result of the interaction, the incident photon disappears and an electron-positron pair is created (Tsoulfanidis & Landsberger, 2015). For pair production to occur, the incident photon must have an energy equal to or greater than twice the rest mass

energy of an electron (i.e. $E \geq 1.02$ MeV) (Knoll, 2000); consequently, this interaction is impossible for the X-ray photons of interest in this thesis.

2.2.2.5 Coherent scattering

Coherent scattering, or Rayleigh scattering, is a process that can occur between a photon and the electrons of an atom (Nikjoo et al., 2012). The scattering event is a response to the oscillating electric field of an incoming electromagnetic wave (photon), where an atom's electron population oscillates at the same frequency as the incoming photon's electric field vector. This mode of acceleration causes the emission of radiation at the same frequency of the incoming photon (Nikjoo et al., 2012). Since virtually no energy is transferred within the coherent scattering process, it is often neglected in basic discussion (Knoll, 2000). However, for photon energies < 100 keV, coherent scattering can cause small deviances in μ relative to μ_{abs} (see **Section 2.2.2**).

2.2.3 Fast electron production

Laboratory fast electron sources include electron guns (e.g. thermionic and field-emission sources) (Williams & Carter, 2009) and radioisotope sources that produce energetic electrons (Knoll, 2000). The fast electron source used in this thesis was an ^{63}Ni radioisotope β^- particle (electron) source, producing a continuous spectrum of β^- particles with energies up to 66 keV (the ^{63}Ni radioisotope endpoint energy). In the case of radioisotope β^- particle sources, there are two processes that lead to fast electron emission: electron (β^- particle) decay and internal conversion (Knoll, 2000).

Electron (β^- particle) decay occurs when a neutron of an atomic nucleus transforms into a proton, resulting in the emission of an electron and an antineutrino (Nikjoo et al., 2012). Each β^- decay transition is characterised by a fixed decay energy, which is shared between the emitted electron and antineutrino. The emitted electron can therefore range in energy up to the characteristic endpoint energy for that radioisotope (Knoll, 2000). In the case of ^{63}Ni, the endpoint energy is 66 keV.

Internal conversion begins with an excited nuclear state (Knoll, 2000). The nuclear excitation energy is transferred to a bound electron and is subsequently ejected. The kinetic energy of the ejected electron is equal to the difference between the nuclear excitation energy and the electrons binding energy (Knoll, 2000).

Neutron bombardment of stable materials (e.g. with a nuclear reactor or particle accelerator) has led to a wide variety of β^- particle emitting radioisotopes of various half-lives and endpoint energies (Knoll, 2000). Many laboratory radioisotope β^- particle sources are made in nuclear reactors or particle accelerators. Naturally occurring radioisotope β^- particle sources also exist; the most abundant isotopes are ^{238}U, ^{235}U, and ^{232}Th (Lottermoser, 2010). Other natural sources of fast electrons include cosmic-rays (electrons emitted from astrophysical objects such as pulsars) (Adriani et al., 2011) and the Sun (Gershman et al., 2015).

2.2.4 Coulomb and nuclear interactions

As charged particles, fast electrons are subject to Coulomb and nuclear interactions as they pass through matter (Ahmed, 2014). Fast electrons do not typically lose all their energy in a single interaction. Instead, they lose energy through multiple interactions, forming a path (sometimes called a track or trajectory) through the medium (Knoll, 2000). Large deviations in the path are possible, as the incident fast electron's mass is equivalent to orbital electrons with which they interact (Knoll, 2000). These deviations result in a much shorter penetration depth into the material when compared to the total path length of the incident fast electron.

Coulomb interactions between incident fast electrons and matter can result in elastic scattering events, excitation of atoms, and the ionisation of atoms. The type of event is largely dependent on the fast electron's energy (Ahmed, 2014). If the incident electron's energy is equal to or greater than the binding energy of the most loosely bound electron within a given atom, ionisation may take place, causing the ejection of an electron (Ahmed, 2014). The energy of the ejected electron depends on its binding energy and the energy of the incident fast electron (Ahmed, 2014). The ejected electron, should it have sufficient energy, can induce further ionisation events, resulting in additional free electrons (Ahmed, 2014). If the energy of an incident fast electron is not sufficient to cause ionisation, the interacting atom can still be excited, raising an orbiting electron's energy level (Nikjoo et al., 2012).

Nuclear interactions between an incident fast electron and an atomic nucleus can result in scattering which significantly alters the trajectory of the fast electron (Nikjoo et al., 2012). Any change in trajectory is a result of a change in acceleration, thus fast electrons can cause bremsstrahlung radiation as a consequence of their scattering, and experience a reduction in energy (Nikjoo et al., 2012).

2.3 Photodiode structure

In order to efficiently collect the charge carriers generated by the absorption of X-ray photons and β^- particles (see **Section 2.2**) within a semiconductor detector, the application of an electric field is common (Barnett, 2011). Applying an electric field across simple crystals of intrinsic semiconductor material induces high device leakage currents (Fraser, 1989) and unacceptable levels of parallel white noise (see **Section 2.8.2.1**). Instead, reverse biased semiconductor junctions can be used to achieve low leakage current regions even at high electric field strengths (Spieler, 2005). Such junctions are created by the deliberate (or otherwise) introduction of impurities into the semiconducting crystal, a process known as doping (Spieler, 2005).

Semiconductors can have n type doping (introduced impurities that create an excess of electrons in the semiconductor (donor)) and p type doping (introduced impurities that create an excess of holes in the semiconductor (accepter)) (Spieler, 2005). If the impurity concentration within a semiconductor changes abruptly from p type to n type, a p-n junction is formed (Sze, 2006). In practice this is achieved by starting with a semiconductor of one type (e.g. p type), and either transforming an existing section into the opposing type (n type), or growing an additional section of the opposing type (n type) (Tsoulfanidis & Landsberger, 2015).

A p-n junction causes electrons to diffuse from the n type region to the p type region, resulting in an electrostatic potential difference (built-in potential, V_{bi} (units of V)) between the p and n layers (Renker & Lorenz, 2009). In addition to a built-in potential, the diffusion of holes and electrons across the junction leads to a region greatly reduced of mobile carriers (depletion region) (Spieler, 2005). The width of this region, W_D (units of cm), is defined by

$$W_D = \left[\frac{2\varepsilon V_0}{\mathrm{q}}\left(\frac{N_A+N_D}{N_A N_D}\right)\right]^{\frac{1}{2}}, \tag{2.5}$$

where ε (units of $A^2\ s^4\ cm^{-3}\ kg^{-1}$) is the permittivity of the photodiode material, V_0 (units of V) is the potential difference across the junction, q (units of C) is the charge of an electron, and N_A (units of cm^{-3}) and N_D (units of cm^{-3}) are the acceptor and donor doping densities (Ahmed, 2014). Absent of an externally applied potential difference,

$$V_0 = V_{bi}. \tag{2.6}$$

The potential difference across the junction can be increased through the application of an external reverse bias, V_R (units of V), such that

$$V_0 = V_{bi} + V_R \, . \tag{2.7}$$

This has the effect of increasing the depletion region width and increasing the electric field strength across the junction.

The $Al_xGa_{1-x}As$ diodes described in this thesis are based on p^+-i-n^+ junction and separate absorption and multiplication (SAM) layer architectures (see Tables 3.1, 4.1, 5.1, and 6.1 for layer properties). The separate absorption and multiplication layer structure, and its principle of operation, is described in detail in **Section 2.9.1**. In the case of a p^+-i-n^+ junction, heavily doped p (p^+) and heavily doped n (n^+) layers are separated by an intrinsic (i) (or near intrinsic) layer. This i layer provides unique properties when compared to a p-n junction (Sze, 2006). For example, if the i layer is of sufficiently high resistivity, at zero applied reverse bias the depletion region will extend across the entire thickness of the intrinsic region (i layer), W_i (units of cm) (White, 1982). Given this assumption, the total thickness of the depletion region in a p^+-i-n^+ diode as a function of potential difference across the junction, V_0, is given by

$$W_D = \sqrt{W_i + \frac{2\varepsilon V_0}{\mathrm{q}}\left(\frac{N_A + N_D}{N_A N_D}\right)}. \tag{2.8}$$

Increasing the thickness of a sufficiently high resistivity i layer can improve the quantum efficiency (see **Section 2.5**) of the detector (Sze, 2006), and reduce the capacitance across the junction, reducing series white noise (see **Section 2.8.2.2**) (White, 1982). Thus p^+-i-n^+ diodes are often preferable to p-n diodes for radiation detection (Sze, 2006).

2.4 Charge creation and transport

2.4.1 Charge creation

The charge generation mechanisms of interest in this thesis are photoelectric absorption as a result of X-ray photon interactions and ionisation events induced by β^- particles interactions (see **Section 2.2**). Both processes generate a distribution of electron-hole pairs within the semiconductor material (Knoll, 2000). The average number of electron-hole pairs, N_{EHP}, created by the absorption of an interacting radiation quantum of energy E, can be expressed as

$$N_{EHP} = \frac{E}{\omega_{EHP}}, \tag{2.9}$$

where ω_{EHP} (units of eV) is the average energy consumed in the generation of an electron-hole pair (commonly referred to as the electron-hole pair creation energy) (Rizzi et al., 2010). The

electron-hole pair creation energy depends on the temperature and the semiconductor material. Table 2.1 presents the electron-hole pair creation energy of Si, GaAs, $Al_{0.2}Ga_{0.8}As$, $Al_{0.6}Ga_{0.4}As$, and $Al_{0.8}Ga_{0.2}As$.

It should be noted that while Eq. 2.9 gives the average number of electron-hole pairs generated by interacting radiation quanta, the energy deposited by incident radiation within a semiconducting material is subject to random variation from one interaction event to the next (Lowe & Sareen, 2014). If the process of creating electron-hole pairs was Poissonian, then the standard deviation, σ, of the N_{EHP} distribution would be $\sqrt{N_{EHP}}$ (Knoll, 2000). As the average number of created electron-hole pairs is typically large upon X-ray photon interactions (see Eq. 2.9 and Table 2.1), a Gaussian distribution results (Jenkins et al., 1995). The FWHM of this Gaussian distribution, assuming no other factors affect the fluctuations in measured charge, can be described by

$$\text{FWHM [electron-hole pairs]} = 2\sqrt{2\ln(2)N_{EHP}}. \tag{2.10}$$

However, it has been shown experimentally that the processes by which individual electron-hole pairs are generated are not independent of each other (Fano, 1947). Fano (1947) observed, in the case of a Hydrogen gas, that the variance (σ^2) in the number of generated electron-hole pairs was smaller than expected by Poissonian statistics. This deviation is quantified by the Fano factor (Fano, 1947), F, such that

$$F = \frac{\text{Observed variance in } N_{EHP}}{\text{Poisson distribution variance in } N_{EHP}}, \tag{2.11}$$

where F is bounded by 0 and 1. Typical values of F in semiconductors are ≈ 0.12 (see Table 2.1). The Fano factor modifies Eq. 2.10 such that

$$\text{FWHM [electron-hole pairs]} = 2\sqrt{2\ln(2)FN_{EHP}}. \tag{2.12}$$

Substituting Eq. 2.9 into Eq. 2.12 gives

$$\text{FWHM [electron-hole pairs]} = 2\sqrt{\frac{2\ln(2)FE}{\omega_{EHP}}}, \tag{2.13a}$$

and subsequently

$$\text{FWHM [eV]} = 2\omega_{EHP}\sqrt{\frac{2\ln(2)FE}{\omega_{EHP}}}, \quad (2.13b)$$

the fundamental energy resolution limit for a semiconductor radiation detecting system (so called the Fano noise) (Lowe & Sareen, 2014).

From Eq. 2.13b it is clear that a small ω_{EHP} and a small F are favourable characteristics for an improved fundamental energy resolution (i.e. low fundamental FWHM). However, the Fano noise is not the only source of noise within a semiconductor radiation detection system. Additional noise sources will be discussed in **Section 2.8**.

Parameter	Si	GaAs	$Al_{0.2}Ga_{0.8}As$	$Al_{0.6}Ga_{0.4}As$	$Al_{0.8}Ga_{0.2}As$
Atomic number	14	31, 33	13, 31, 33	13, 31, 33	13, 31, 33
Density (g cm^{-3})	2.33	5.32	5.04	4.40	4.08
Bandgap (eV)	1.12	1.43	1.67	2.03	2.09
Electron-hole pair creation energy (eV)	3.65	4.18	4.43	4.97	5.10
Fano factor	0.12	0.12	-	-	-

Table 2.1. Values of some key parameters for Si, GaAs, $Al_{0.2}Ga_{0.8}As$, $Al_{0.6}Ga_{0.4}As$, and $Al_{0.8}Ga_{0.2}As$, at room temperature. The values were obtained from Bertuccio & Maiocchi (2002), Lowe & Sareen (2007), Owens (2012), Barnett et al. (2012b), Adachi (1985), **Section 3.8**, and **Section 5.7**. Reliable measurements of the Fano factor for $Al_{0.2}Ga_{0.8}As$, $Al_{0.6}Ga_{0.4}As$, and $Al_{0.8}Ga_{0.2}As$ are yet to be reported.

2.4.2 Charge transport

Charge carriers generated within a semiconductor as a consequence of radiation quanta interactions can move under the influence of an electric field. In a uniform electric field of strength E_f (units of V cm^{-1}), providing that E_f is sufficiently small (see **Section 2.9**), the associated electron and hole velocities, V_e and V_h (each in units of cm s^{-1}) respectively, are given by

$$V_e = \mu_e E_f, \quad (2.14a)$$

and

$$V_h = \mu_h E_f, \quad (2.14b)$$

where μ_e (units of $cm^2\ V^{-1}\ s^{-1}$) and μ_h (units of $cm^2\ V^{-1}\ s^{-1}$) are the electron and hole mobility constants, whose values depend on the semiconducting material (Ahmed, 2014). Real semiconductor crystals suffer from defects introduced during crystal growth, device fabrication, and radiation damage (Spieler, 2005). These defects can take the form of impurities, vacancies, and dislocations, which can impede the motion of charge carriers through the semiconductor by trapping and recombination (Spieler, 2005). Trapping centres may immobilise charge carriers, sometimes for longer than the read out time of the detector (Knoll, 2000). Recombination centres may annihilate charge carriers entirely. These processes limit the lifetimes of electrons, τ_e (units of s), and holes, τ_h (units of s), and consequently the average distances of which they travel. The associated recombination lengths, R_e (units of cm) and R_h (units of cm), are the average distances that the carriers can travel before being lost, and are given by

$$R_e = \mu_e E \tau_e, \tag{2.15a}$$

and

$$R_h = \mu_h E \tau_h\ . \tag{2.15b}$$

The recombination lengths set an upper limit upon the useful thickness of a detector, since any charge carriers generated beyond one recombination length from an electrode do not contribute to the total detected charge.

2.5 Quantum detection efficiency

For photodiodes, the quantum detection efficiency determines the number of photons absorbed within the active layer of the detector relative to the number of photons available. The quantum detection efficiency, *QE*, can be defined as

$$QE = \frac{Number\ of\ photons\ absorbed\ in\ active\ layer}{Number\ of\ photons\ incident\ on\ detector\ face}. \tag{2.16}$$

In order to calculate the *QE* of a semiconductor photodiode of a known geometry and at a given photon energy, the Beer-Lambert law can be used (see **Section 2.2.2**), such that

$$QE = [\prod_d \exp(-\mu_d x_d)][1 - \exp(-\mu_a x_a)], \tag{2.17}$$

where μ_d is the linear attenuation coefficient and x_d is the thickness of each d dead layer before the active layer, and μ_a is the linear attenuation coefficient and x_a is the thickness of the active layer (Fraser, 1989). Dead layers in front of the active layer of a semiconductor photodiode may include the top metal contact and any layers between the surface of the detector and the depletion layer (active layer). It should be noted that photons absorbed just outside of the active layer can generate charge carriers that diffuse into the active layer of a semiconductor photodiode, also contributing to recorded pulses in a spectroscopic system (Sze, 2006).

In the case of electron detection, for the avoidance of confusion due to multiple possible definitions for quantum efficiency when applied to electron detectors, the equilivant parameter is defined here as the percentage of electron energy absorbed in the active layer of the photodiode, E_{abs}. The percentage of electron energy absorbed in the active layer can be calculated by

$$E_{abs} = \frac{Total\ electron\ energy\ absorbed\ in\ active\ layer}{Total\ electron\ energy\ incident\ on\ detector\ face}. \quad (2.18)$$

2.6 Photodiode radiation detecting system

A block diagram of the spectroscopic system used in this thesis can be seen in Fig. 2.2. Incident X-ray photons and β^- particles interact with the semiconductor photodiode, creating electron-hole pairs (charge carriers) via the photoelectric effect (see **Section 2.2.2.2**). The charge carriers, created within the depletion region (assumed to be the active region, unless otherwise specified) of the photodiode, are swept out via an electric field towards their respective electrode (see **Section 2.4.2**). The movement of these charge carriers induces charge on the contacts of the semiconductor photodiode as per the Shockley-Ramo theorem (Shockley, 1938) (Ramo, 1939). The resulting charge generated by each radiation quantum, Q_d, is then transferred to the charge-sensitive preamplifier. The preamplifier converts Q_d into a proportional voltage step by integrating the current pulse (see **Section 2.7**). The output of the charge-sensitive preamplifier takes the form of a tail pulse, with a rapidly rising signal which slowly returns to baseline (Knoll, 2000). This tail pulse is sent to a shaping amplifier, which modifies the tail pulse shape to improve the signal-to-noise ratio and enable a pulse height measurement (Spieler, 2005). Shaping amplifiers may also provide other functions, such as pile-up rejection, baseline restoration, and pole-zero cancellation (Gilmore, 2008). The shaping amplifier used in this thesis was an Ortec 572A shaping amplifier (Ortec, 2004). The multi-channel analyser (MCA) measures the peak height of the shaped pulse and, through a process of digitization, the measurement (commonly referred to as a count) is allocated to a channel representing the appropriate voltage range (Gilmore, 2008). Subsequent radiation quantum interactions result in a stream of pulses which,

when allocated to the appropriate channels, results in a histogram of counts (a spectrum). Information regarding the incident radiation may then be deduced from the recorded spectrum. Two MCA's were used in this thesis: an Ortec 927 ASPEC MCA (Ortec, 2014a) (see **Chapters 3**, **4**, and **5**) and an Ortec Easy-MCA-8K (Ortec, 2014b) (see **Chapter 6**).

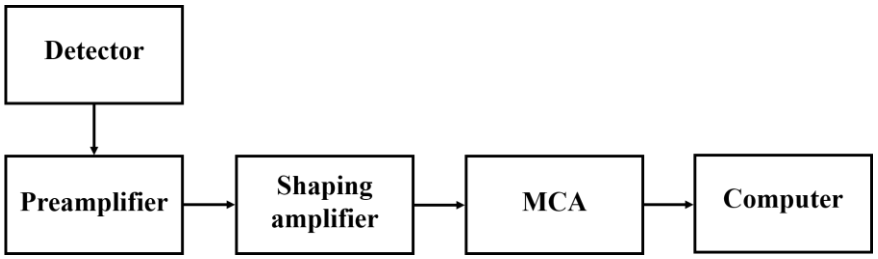

Fig. 2.2. Block diagram of a semiconductor photodiode spectrometer.

2.7 The charge sensitive preamplifier

The custom-made low-noise charge-sensitive preamplifier used to obtain spectra reported in this thesis was of a feedback-resistorless design similar to that described by Bertuccio et al. (1993). The elimination of the feedback resistor, used to continually discharge the feedback capacitor in conventional charge-sensitive preamplifier circuits, reduces the noise associated with the readout electronics (Bertuccio et al., 1993). This elimination was achieved using an additional feedback loop for stabilising the working point of the preamplifier and by using a slightly forward biased n type junction field effect transistor (JFET) (2N4416A Si JFET (Siliconix, 2001)) as a path for the feedback capacitor to discharge (Bertuccio et al., 1993).

In the charge-sensitive feedback-resistorless preamplifier reported here, the semiconductor photodiode detector is connected to the input (gate) of the JFET such that the detected charge, Q_d, generated by interacting radiation quanta, enters the preamplifier input (Bertuccio et al., 1993). It should be noted that alternative input transistors (e.g. bipolar transistors (BJTs) or metal oxide semiconductor field effect transistors (MOSFETs)) can be used. However, JFETs are often the preferred choice of input transistor for low-noise charge-sensitive preamplifiers for X-ray spectroscopy as they minimise preamplifier noise relative to other input transistors, given the resistance of semiconductor detectors (> 1 kΩ) (Levinzon & Vandamme, 2011) (Bertuccio, 2012).

The gate (input) to source (ground) junction of the input JFET provides a path for the leakage current of the detector, whilst Q_d is subsequently converted into a proportional voltage step by integrating the current pulse onto the feedback capacitor, which is then amplified by a cascade voltage amplifier (Bertuccio et al., 1993). The reader is referred to Bertuccio et al. (1993) for a

detailed description of the type of charge-sensitive feedback-resistorless preamplifier used in this thesis.

2.8 Noise processes in photodiode radiation spectrometers

2.8.1 Introduction to noise components

Three independent terms constitute the total noise present within a non-avalanche semiconductor photodiode X-ray or electron spectrometer. The first is the statistically limited energy resolution of a semiconductor X-ray detector (Eq. 2.13b), as described in **Section 2.4.1**. The second term, R (units of e^- rms), is the equivalent noise charge introduced by incomplete charge collection within the detector (Owens, 2012). Incomplete charge collection is a result of charge carrier trapping and recombination processes, as described in **Section 2.4.2**. The third term, A (units of e^- rms), is the equivalent noise charge representing the broadening of the photopeak due to electronic noise (Bertuccio et al., 1996). The electrical characteristics of the semiconductor detector, the charge-sensitive preamplifier, and the shaping amplifier all effect the electronic noise (Lioliou & Barnett, 2015).

The energy resolution (FWHM in units of eV) of a non-avalanche semiconductor photodiode X-ray or electron spectrometer is defined by the quadratic sum of these three independent terms, such that,

$$FWHM\ [\text{eV}] = 2\omega_{EHP}\sqrt{\frac{2\ln(2)FE}{\omega_{EHP}} + R^2 + A^2}\ . \tag{2.19}$$

2.8.2 Electronic noise components

Five components constitute the electronic noise, A, of a semiconductor photodiode spectroscopic system. These are: parallel white noise; series white noise; $1/f$ series noise; dielectric noise; induced gate current noise. Each of which are summarised below.

2.8.2.1 Parallel white noise

Parallel white noise arises from the shot noise of the currents which flow through the input of the charge-sensitive preamplifier (Bertuccio et al., 1996). It is primarily dependent upon the leakage currents of the semiconductor detector, I_d (units of A), and the preamplifier input field effect transistor (JFET), I_{JFET} (units of A) (Bertuccio et al., 1996). An additional source of parallel white

noise is the feedback resistor, R_f (units of Ω), in preamplifiers that have them (Bertuccio et al., 1996). The parallel white noise equivalent noise charge, ENC_{pw}, is given by

$$ENC_{pw} = \frac{1}{\mathrm{q}}\sqrt{\frac{A_3}{2}S_{pw}\tau}, \tag{2.20}$$

where A_3 is a constant depending on the shape of the pulse determined by the type of shaping amplifier (Gatti et al., 1990), S_{pw} (units of V^2 Hz^{-1}) is the parallel white noise power spectral density (also known as the spectral current noise density of shot noise), and τ is the shaping time of the shaping amplifier (units of s). For the RC-CR shaping amplifier used in this thesis, A_3 = 1.85 (Gatti et al., 1990), and τ can be adjusted between (0.5 µs, 2 µs, 3 µs, 6 µs, and 10 µs). S_{pw} is given by

$$S_{pw} = 2\mathrm{q}\left(I_d + I_{JFET}\right) + \frac{4\mathrm{k}T}{R_f}, \tag{2.21}$$

where k is Boltzman's constant (units of m^2 kg s^{-2} K^{-1}) and T is the temperature (units of K). From Eq. 2.21, it can be seen that I_d and I_{JFET} are important in determining the limits of spectral resolution of the semiconductor spectroscopic system.

2.8.2.2 Series white noise

Series white noise arises primarily from the thermal noise affecting the current of the preamplifier input JFET (Bertuccio et al., 1996). The series white noise equivalent noise charge, ENC_{sw}, is given by

$$ENC_{sw} = \frac{1}{\mathrm{q}}\sqrt{\frac{A_1}{2}S_{sw}{C_T}^2\frac{1}{\tau}}, \tag{2.22}$$

where A_1 is a constant depending on the type of shaping amplifier (A_1 = 1.85 for an RC-CR shaping amplifier) (Gatti et al., 1990), S_{sw} (units of V^2 Hz^{-1}) is the series white noise power spectral density (also known as the spectral voltage noise density of thermal noise), and C_T (units of F) is the total capacitance at the preamplifier input (Bertuccio et al., 1996). C_T includes the detector capacitance, C_d, the input JFET capacitance, C_{JFET}, the feedback capacitance, C_f (arising from the feedback capacitor used to integrate the detector charge pulse (see **Section 2.7**)), the test capacitance, C_t (arising from the test capacitor used to inject charge at the input of the preamplifier in order to simulate a charge pulse of a detector (Lioliou, 2017)), and the stray capacitance, C_s (arising from unknown stray capacitances within the system (Glisson, 2011)). When secondary

noise sources (e.g. stray resistance in series with the input JFET's gate) are negligible (Barnett, 2011), S_{sw} can be approximated to the thermal noise of the JFET (Bertuccio et al., 1996) such that

$$S_{sw} = \gamma \frac{4\mathrm{k}T}{g_m}. \tag{2.23}$$

The parameter γ is a constant and depends on the JFET characteristics (γ = 0.85 for the JFET's used in this thesis), g_m (units of A V^{-1}) is the transconductance of the JFET (g_m = 0.006 A V^{-1} for the JFETs used in this thesis).

2.8.2.3 1/*f* series noise

The 1/*f* series noise arises from lattice defects and impurities within the depleted regions of the JFET. These cause charge carrier generation and recombination fluctuations, resulting in current fluctuations from the JFET (Vasilescu, 2005). The 1/*f* series noise equivalent noise charge, $ENC_{1/f}$, is given by

$$ENC_{1/f} = \frac{1}{\mathrm{q}}\sqrt{A_2 \pi A_f {C_T}^2}, \tag{2.24}$$

where A_2 is a constant depending on the type of shaping amplifier (A_2 = 1.18 for an RC-CR shaping amplifier) (Gatti et al., 1990), and A_f is a constant depending on the JFET (Bertuccio et al., 1996) which can be expressed as

$$A_f = \frac{(\gamma 2\mathrm{k}T/\pi)(f_c/f_T)}{C_{JFET}}. \tag{2.25}$$

The parameters f_c (units of Hz) and f_T (units of Hz), are the corner frequency and transition frequency of the JFET (f_c = 1 × 10^3 Hz, f_T = 4.77 × 10^8 Hz, for the JFETs used in this thesis), respectively (Lioliou & Barnett, 2015).

2.8.2.4 Dielectric noise

Dielectric noise arises from thermal fluctuations in insulators that are close to, or in contact with, the preamplifier's input. Such insulators include the packaging of the JFET and detector, as well as the JFET and detector themselves (Bertuccio et al., 1996). The dielectric noise equivalent noise charge, ENC_{die}, is given by

$$ENC_{die} = \frac{1}{\mathrm{q}}\sqrt{A_2 2\mathrm{k}TD_{die}C_{die}}\,, \tag{2.26}$$

where C_{die} (units of F) is the capacitance of the dielectrics and D_{die} is the dissipation factor of the dielectrics (Radeka, 1968). Noise from lossy dielectrics can degrade the energy resolution of a spectrometer substantially (see **Section 3.7.2**). Consequently, it is desirable to design the input JFET and detector packaging such that exposure to dielectrics is minimised (Barnett, 2011) (Bertuccio et al., 1996).

2.8.2.5 Induced gate current noise

Induced gate current noise arises from charge fluctuations in the JFET gate current (Vasilescu, 2005). Experimental investigation has shown that Eq. 2.22 can be modified in order to account for the induced gate current noise via the introduction of a correction factor, G_{gc}, which either enhances or reduces the contribution of white series noise depending on its value (Bertuccio et al., 1996) ($G_{gc} = 0.8^2$ for the JFETs used in this thesis). The equivalent noise charge of the series white noise modified to include induced gate current noise, ENC_{swgc}, is given by

$$ENC_{swgc} = \frac{1}{\mathrm{q}}\sqrt{\frac{A_1}{2}S_{sw}G_{gc}{C_T}^2\frac{1}{\tau}}\,. \tag{2.27}$$

2.9 Impact ionisation

2.9.1 Introduction

Photodiodes in which impact ionisation occurs are widely used in radiation detection systems (notably telecommunications equipment (Campbell, 2007)) in order to improve the performance (Tsang, 1985) (David & Tan, 2008). The improved performance is due to avalanche multiplication, where the charge generated by each radiation quantum, Q_d, is multiplied by a multiplication factor, M, of the detector (see **Section 2.9.3**).

Avalanche multiplication occurs when an electric field applied across a semiconductor p-n or p^+-i-n^+ junction is sufficiently great that charge carriers can gain sufficient kinetic energy that they can cause impact ionisation upon interaction with lattice atoms (Sze, 2006).

In the case of an electron generated by a radiation quantum interaction within the active region of a p^+-i-n^+ device (see **Section 2.3**), the electron is accelerated toward the n^+ contact. If this energetic electron interacts with a lattice atom, some of the electron's energy can be transferred such that a valence band electron of the atom is promoted into the conduction band (Tsang, 1985).

This necessarily creates a hole in the valence band position. The electrons (and holes) generated by a radiation quantum interaction, together with the created (by impact ionisation) electrons and holes, are then accelerated in the same manner as before by the electric field (electrons toward the n^+ contact, holes toward the p^+ contact). Both the electrons and holes can interact with lattice atoms and, upon gaining sufficient energy, can generate more charge carriers. This process can be repeated many times, with many impact ionisation events taking place before the charge carriers reach their respective destination boundaries. The result is an appreciable multiplication of charge carriers, and hence, a greater amount of charge is induced on the contacts, in accordance with the Shockley-Ramo theorem (Shockley, 1938) (Ramo, 1939) (Tsang, 1985).

A photodiode that operates in this way is called an avalanche photodiode (APD). There are various structural forms of APD, including p^+-i-n^+ devices and separate absorption and multiplication region devices (both of which are APD structures considered in this thesis, see **Chapters 5** and **6**, respectively). A separate absorption and multiplication region avalanche photodiode (SAM APD) contains two regions: a low-field drift region, in which the interacting radiation quanta is absorbed (absorption region); a high-field region, in which avalanche multiplication takes place (multiplication region) (Campbell et al., 1983) (Lauter et al., 1995). The absorption region is typically much thicker (ideally of sufficient thickness to completely absorb the incident radiation (Lauter et al., 1995)) than the multiplication region, such that the majority of incident radiation is absorbed within the drift region. In the case of the p^+-i-p-i-n^+ SAM APD reported in this thesis, electrons move toward the n^+ contact and subsequently enter the multiplication region at the same position, thus they receive the same multiplication factor (although with the natural variation that would be expected from such a stochastic process) (see **Section 2.9.3**). Holes move toward the p^+ contact, and thus do not enter the multiplication region (Gomes et al., 2014). This is in contrast to a regular p^+-i-n^+ APD, where the absorption region is also the multiplication region. In this case, the multiplication factor depends on the position at which electron-hole pairs are created by incident radiation quanta (see **Section 2.9.3**).

2.9.2 Ionisation coefficients

The distance that charge carriers travel between impact ionisation events (ionisation path length), due to the stochastic nature of the impact ionisation process, is not constant. The number of charge carriers generated by impact ionisation is commonly different for electron and hole initiated avalanche multiplication. The reciprocal of the average distance that charge carriers travel between impact ionisation events is called the ionisation coefficient, where the electron ionisation coefficient and hole ionisation coefficient are individually defined as α (units cm^{-1}) and β (units of cm^{-1}), respectively. The ionisation coefficients α and β, for a given material, are

assumed in the local model (McIntyre, 1966) to remain constant, depending only on the electric field and temperature within the device. Stronger electric fields within the device result in charge carriers achieving the energy required to impact ionise in a shorter distance, increasing the respective ionisation coefficients. It is assumed that any differences in multiplication experienced by the same charge carrier type is due only to the starting position of the initiating charge carrier (McIntyre, 1966), although this is actually a simplification.

2.9.3 Multiplication factors

Assuming a local model (McIntyre, 1966), for a given temperature, the multiplication factor, M, as a function of photon absorption position, x_p (units of cm), in the i layer of an ideal p^+-i-n^+ diode can be expressed as

$$M(x_p) = \frac{(\alpha-\beta)\exp[-(\alpha-\beta)x_p]}{\alpha\exp[-(\alpha-\beta)W_i]-\beta}. \tag{2.28}$$

For pure electron initiated mean average multiplication, M_e, which occurs when $x_p = 0$ cm (i.e. photons are absorbed at the p^+-i boundary), Eq. 2.28 becomes

$$M_e = \frac{(\alpha-\beta)}{\alpha\exp[-(\alpha-\beta)W_i]-\beta}. \tag{2.29a}$$

For pure hole initiated mean average multiplication, M_h, which occurs when $x_p = W_i$ (i.e. photons are absorbed at the i-n^+ boundary), Eq. 2.28 becomes

$$M_h = \frac{(\alpha-\beta)\exp[-(\alpha-\beta)W_i]}{\alpha\exp[-(\alpha-\beta)W_i]-\beta}. \tag{2.29b}$$

From Eq. 2.28 it can be seen that α and β are the only two variables needed to characterise M within the local model. Conversely, α and β can be deduced from experimentally measured multiplication characteristics. The combination of Eqs. 2.29a and 2.29b yields

$$\alpha = \frac{1}{W_i}\left(\frac{M_e-1}{M_e-M_h}\right)\ln\left(\frac{M_e}{M_h}\right), \tag{2.30a}$$

and

$$\beta = \frac{1}{W_i}\left(\frac{M_h-1}{M_h-M_e}\right)\ln\left(\frac{M_h}{M_e}\right). \tag{2.30b}$$

2.9.4 Excess noise factor

If single electron-hole pairs are injected one at a time into an APD, where the avalanche region has a constant electric field, the distribution in ionisation path lengths (see **Section 2.9.2**) leads to different values of multiplication factors, *m*, produced by each trial (Hakim et al., 1990). This variation in multiplication factor is quantified by the excess noise factor, N_x, defined by

$$N_x = \frac{\langle m^2 \rangle}{\langle m \rangle^2} = \frac{\langle m^2 \rangle}{M^2}, \tag{2.31}$$

where <*m*> is the mean average multiplication factor, *M* (Hakim et al., 1990).

Until recently, the excess noise factors for pure electron initiated mean average multiplication, N_{xe}, and pure hole initiated mean average multiplication, N_{xh}, were thought to be well described by McIntyre (1966), such that

$$N_{xe} = kM_e + (2 - \frac{1}{M_e})(1 - k), \tag{2.32a}$$

and

$$N_{xh} = \frac{M_h}{k} + (2 - \frac{1}{M_h})(1 - \frac{1}{k}), \tag{2.32b}$$

where $k = \beta/\alpha$. In most compound semiconductors *k* ranges from 0.3 to 1.0 (Tan et al., 2011), hence Eqs. 2.32a and 2.32b predict poor energy resolutions when the gain is appreciable in X-ray compound semiconductor APDs (Tan et al., 2011). For this reason, it was originally thought that the use of APDs would degrade the resolution of X-ray spectrometers and thus were not extensively investigated (Fraser, 1989). However, recent studies have improved the understanding of APDs (Tan et al., 2011) (David & Tan, 2008) (Barnett et al., 2011a) (Tan et al., 2001). Notably, David & Tan (2008) showed that thin avalanche layers could be used to reduce excess noise, and Tan et al. (2011) showed that the common model of excess noise is not directly applicable at X-ray energies, since the distribution of avalanche gains tightens as the initiating photon energy, *E*, is increased; this leads to significantly lower additional noise for X-rays than would be expected for infrared, visible, or UV photons (Tan et al., 2011).

Chapter 3

3 µm i layer $Al_{0.2}Ga_{0.8}As$ mesa p^+-i-n^+ single pixel detectors

3.1 Introduction

In this chapter, work characterising the X-ray spectroscopic performance of custom-made $Al_{0.2}Ga_{0.8}As$ p^+-i-n^+ circular mesa non-avalanche photodiodes (200 µm diameter) at room temperature and as a function of temperature is presented. The AlGaAs photodiodes were shown to be suitable for photon counting X-ray spectroscopy across the temperature range 20 °C to -20 °C. The best energy resolution (FWHM at 5.9 keV) achieved at 20 °C was 1.06 keV ± 0.04 keV (with 10 V reverse bias applied to the detector). Improved FWHM was observed with the devices at temperatures of 0 °C (856 eV ± 30 eV) and -20 °C (827 eV ± 30 eV) with the photodiodes reverse biased at 30 V. The average electron hole pair creation energy was experimentally measured and determined to be 4.43 eV ± 0.09 eV at 20 °C, 4.44 eV ± 0.10 eV at 0 °C, and 4.56 eV ± 0.10 eV at -20 °C. The experimental methods and techniques, along with the findings of the experimental work, are discussed.

3.2 Background

Previous investigation of $Al_{0.8}Ga_{0.2}As$ photodiodes for soft X-ray photon counting spectroscopy has shown that such devices can operate with promising spectral resolutions (≈ 1.1 keV FWHM at 5.9 keV (Barnett et al., 2010)) at room temperature and above (see **Section 1.6.2**). However, depending on the operating environment, lower Al fractions of $Al_xGa_{1-x}As$ could be more beneficial. Varying the Al fraction adjusts the material's bandgap (e.g. 2.17 eV for AlAs cf. 1.42 eV for GaAs (Adachi, 1985)), where a reduction in Al fraction reduces the bandgap. Since the optimal bandgap for room temperature X-ray detection is ≈ 1.5 eV (Swierkowski & Armantrout, 1975) (Armantrout et al., 1977), relatively close to the bandgap of $Al_{0.2}Ga_{0.8}As$ (1.67 eV (Adachi, 1985)), $Al_{0.2}Ga_{0.8}As$ may provide a better solution than $Al_{0.8}Ga_{0.2}As$ for operation at temperatures ≈ 20 °C.

Furthermore, previous work on $Al_{0.8}Ga_{0.2}As$ for photon counting X-ray spectroscopy detectors has focused on thin i layers, e.g. 1.0 µm (Barnett et al., 2010) (Barnett et al., 2013b) and 1.7 µm (Barnett et al., 2015), due to the lattice mismatch between $Al_{0.8}Ga_{0.2}As$ and GaAs (the substrate material typically used for AlGaAs growth). Whilst virtual substrate technology, in which graded Al fraction AlGaAs is grown on a GaAs substrate to provide a virtual $Al_{0.8}Ga_{0.2}As$ substrate, may enable the production of thick and high quality $Al_{0.8}Ga_{0.2}As$ epilayers, comparatively thicker

$Al_{0.2}Ga_{0.8}As$ layers can be grown on a commercial GaAs substrate directly. Prior to the work reported in this thesis, there had been no report of $Al_{0.2}Ga_{0.8}As$ photodiodes used for soft X-ray photon counting spectroscopy.

3.3 Device structure

The wafer from which the $Al_{0.2}Ga_{0.8}As$ p^+-i-n^+ mesa X-ray photodiodes (200 µm diameter, 3 µm i layer) were fabricated was grown by metalorganic vapour phase epitaxy (MOVPE) on a commercial 2 inch GaAs n^+ substrate at the EPSRC National Centre for III-V Technologies, Sheffield, UK. The layer details are summarised in Table 3.1. Circular mesa structures (200 µm diameter) were formed using 1:1:1 H_3PO_4:H_2O_2:H_2O solution followed by 10 s in 1:8:80 H_2SO_4:H_2O_2:H_2O solution. An Ohmic contact consisting of 20 nm InGe and 200 nm Au was evaporated onto the rear substrate, and an Ohmic top contact of 20 nm Ti and 200 nm Au was evaporated onto the p^+ side of the mesa devices; the devices were unpassivated. Fabrication occurred at the National Centre. The top contact covered 45 % of the diode's faces; its geometry is shown in Fig. 3.1.

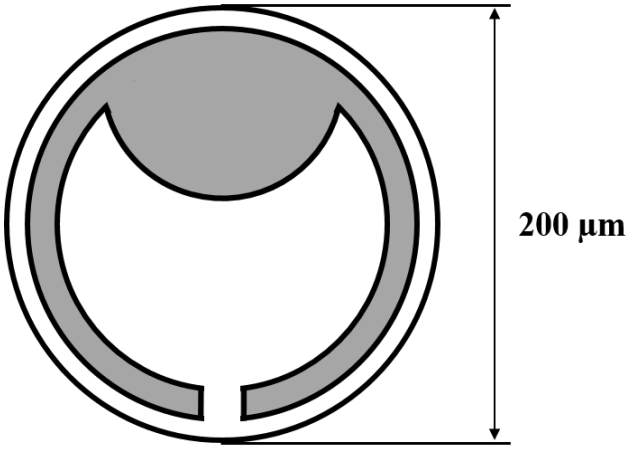

Fig. 3.1. Top-view of the $Al_{0.2}Ga_{0.8}As$ p^+-i-n^+ mesa structure.

Material	Dopant	Dopant type	Thickness (µm)	Doping density (cm^{-3})
GaAs	C	p	0.01	1×10^{19}
$Al_{0.2}Ga_{0.8}As$	C	p	0.5	2×10^{18}
$Al_{0.2}Ga_{0.8}As$		i	3	Undoped
$Al_{0.2}Ga_{0.8}As$	Si	n	1	2×10^{18}
GaAs n^+ substrate				

Table 3.1. Layer details of the $Al_{0.2}Ga_{0.8}As$ p^+-i-n^+ mesa X-ray photodiodes.

3.4 Room temperature electrical characterisation

3.4.1 Current measurements as a function of applied reverse bias

In order to establish the electrical characteristics of the $Al_{0.2}Ga_{0.8}As$ p^+-i-n^+ mesa X-ray photodiodes such that comparisons could be made between available devices, leakage current as a function of applied reverse bias measurements were made for each of the three 200 µm diameter $Al_{0.2}Ga_{0.8}As$ p^+-i-n^+ mesa X-ray photodiodes (D1 – D3). The devices were housed within a custom, electromagnetically screened, light tight test fixture and connected, in turn, to a Keithley 6487 Picoammeter/Voltage Source, at room temperature. National Instruments LabVIEW software was used to automate the characterisation routine.

Reverse bias was applied in increments of 0.1 V at a rate of one increment per 2 s up to a maximum reverse bias of 30 V. The measurements were made in a dry N_2 environment (< 5 % relative humidity) to eliminate any humidity related effects (Barnett et al., 2013b). All three diodes had comparable leakage currents across the measurement range. Fig. 3.2 presents the leakage current as a function of applied reverse bias for one representative device (D1). At 30 V, the reverse bias at which the detectors were fully depleted (see **Section 3.4.2**), the mean leakage current was 15.4 pA ± 0.4 pA (rms deviance), corresponding to a leakage current density of 49.0 nA cm^{-2} ± 1.3 nA cm^{-2} (rms deviance). Device D2 recorded the lowest leakage current: 15.1 pA ± 0.4 pA, corresponding to 48.0 nA cm^{-2} ± 1.4 nA cm^{-2}.

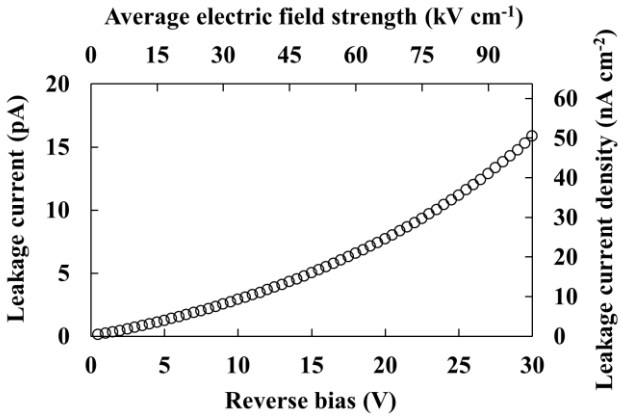

Fig. 3.2. Measured leakage current for one representative $Al_{0.2}Ga_{0.8}As$ X-ray p^+-i-n^+ mesa photodiode, D1, at room temperature, in a dry N_2 atmosphere (< 5 % relative humidity), as a function of reverse bias. Leakage current density and average electric field strength are also shown. The associated uncertainties were omitted for clarity.

Recently reported $Al_{0.8}Ga_{0.2}As$ X-ray detectors (400 µm diameter; 1.7 µm i layer) had a leakage current density of 4.72 nA cm^{-2} ± 1.67 nA cm^{-2} at an average electric field strength of 29.4 kV cm^{-1} (Barnett et al., 2015). The presently reported $Al_{0.2}Ga_{0.8}As$ detectors had a larger

leakage current density of 9.1 nA cm^{-2} ± 2.1 nA cm^{-2} (a leakage current of 2.8 pA ± 0.7 pA) at the same average electric field strength (equivalent to a reverse bias of 8.8 V for the present detectors). It is also interesting to compare to GaAs mesa photodiodes: recently two 200 µm diameter, 7 µm i layer mesa photodiodes were reported which had leakage current densities of 17.4 nA cm^{-2} and 1.08 nA cm^{-2} respectively, at an average electric field strength of 22 kV cm^{-1} (Lioliou et al., 2016a). At this field strength (equivalent to an applied reverse bias of 6.6 V for the present devices), the $Al_{0.2}Ga_{0.8}As$ detectors had a mean leakage current density of 7.1 nA cm^{-2} ± 2.7 nA cm^{-2} (rms deviance); device D1 exhibited the lowest leakage current density of the three measured $Al_{0.2}Ga_{0.8}As$ detectors (5.5 nA cm^{-2} ± 1.3 nA cm^{-2}).

3.4.2 Capacitance measurements as a function of applied reverse bias

Capacitance as a function of applied reverse bias was measured for each $Al_{0.2}Ga_{0.8}As$ photodiode (D1 – D3) at room temperature, using an HP 4275A LCR Meter and an HP 16065A EXT Voltage Bias Fixture. A Keithley 6487 picoammeter/voltage source was used to bias the detectors. National Instruments Labview software was used to automate the characterisation routine. The LCR meter test signal was sinusoidal with a 50 mV rms magnitude and 1 MHz frequency.

The measured capacitances were consistent across all devices. Fig. 3.3 presents the capacitance as a function of applied reverse bias for one representative diode (D1); comparable results were found for the other devices. As the devices were measured after packaging, the capacitance of the package was removed by measuring the capacitance of four empty connections on the same package (0.65 pF ± 0.04 pF (rms deviance)) and deducting this from the total capacitance obtained for each diode. The capacitance of the bond wire of each detector was not individually separated from the packaging capacitance, but the subsequent analysis suggests that the bond wire capacitances were insignificant compared with the other system capacitances. The capacitances of the devices at 10V and 30V were 1.81 pF ± 0.02 pF and 1.14 pF ± 0.02 pF, respectively.

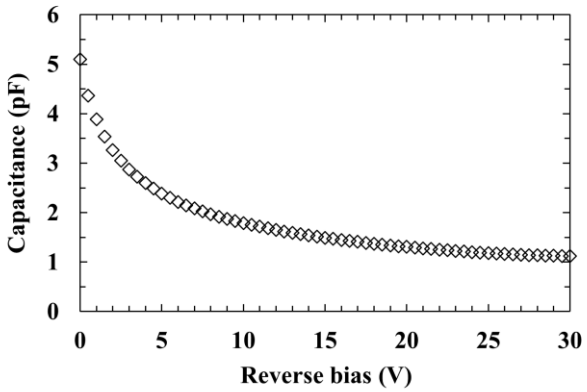

Fig. 3.3. Measured capacitance as a function of applied reverse bias for one representative $Al_{0.2}Ga_{0.8}As$ X-ray p^+-i-n^+ mesa photodiode, D1, at room temperature. Comparable results were obtained for the other devices. The associated uncertainties were smaller than the symbols.

When reverse biased, the junction capacitance is predominantly defined by the depletion layer capacitance, C_{DL} (units of F) (Sze, 2006). From C_{DL}, the depletion width, W_D, of the diodes as a function of applied reverse bias was calculated using

$$C_{DL} = \frac{\varepsilon_0 \varepsilon_r A_d}{W_D}, \tag{3.1}$$

where ε_0 is the permittivity of free space (units of $A^2\ s^4\ cm^{-3}\ kg^{-1}$), ε_r is the relative permittivity of the material (12.332 for $Al_{0.2}Ga_{0.8}As$ (Adachi, 1993)), and A_d is the area of the device (units of cm^2) (Sze, 2006). From the measured depletion layer capacitance of the $Al_{0.2}Ga_{0.8}As$ photodiode D1 shown in Fig. 3.3, depletion widths of 1.92 µm ± 0.05 µm and 3.06 µm ± 0.12 µm were calculated at reverse biases of 10 V and 30 V, respectively. The Debye length of $Al_{0.2}Ga_{0.8}As$ (0.07 µm) was calculated as per Stradling & Klipstein (1991), and was taken into account when calculating the depletion width uncertainty. Fig. 3.4 shows the calculated depletion width as a function of applied reverse bias for D1; comparable results were obtained for the other devices. Beyond 30 V, the measured depletion layer capacitance and consequently the depletion width, remained constant, suggesting that the diodes were fully depleted at a reverse bias of 30 V.

The effective doping density of the i layer, N_{eff} (units of cm^{-3}), was calculated using the equation for general nonuniform distributions (Sze, 2006),

$$\frac{\mathrm{d}\left(1/C_{DL}^2\right)}{\mathrm{d}V_R} = \frac{2}{\mathrm{q}\varepsilon_0 \varepsilon N_{eff}}, \tag{3.2}$$

where V_R (units of V) is the applied reverse bias. The effective doping density throughout the intrinsic region of each diode was determined from the capacitance measurements to be $\approx 4 \times 10^{15}$ cm^{-3}. Further refinement and optimisation of the growth process may improve (reduce) the unintentional doping concentration in the i layer, which may lead to performance improvements.

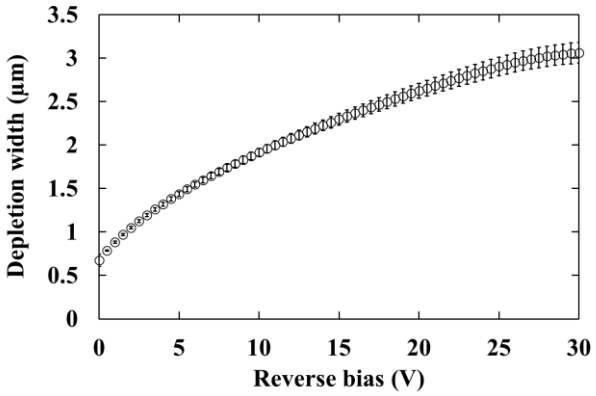

Fig. 3.4. Calculated depletion width as a function of applied reverse bias for D1 $Al_{0.2}Ga_{0.8}As$ (200 µm diameter, 3 µm i layer). Comparable results were obtained for the other devices.

The implied detection efficiency of the $Al_{0.2}Ga_{0.8}As$ diodes when reverse biased at 10 V (mean depletion width of 1.90 µm ± 0.05 µm (rms deviance)) and 30 V (mean depletion width of 3.02 µm ± 0.12 µm (rms deviance)) as functions of energy are shown in Fig. 3.5. The detection efficiencies of two previously reported $Al_{0.8}Ga_{0.2}As$ devices (Barnett et al., 2015) (Barnett et al., 2013b) are also plotted for reference. Spectra acquired by two recent space science missions (see Fig. 3.6) are shown in order to illustrate the typical detectable energy range requirements of in situ planetary analysis (see **Section 1.4.1**) and planetary remote sensing (see **Section 1.4.2**).

The detection efficiency (0.134 in areas not covered by the top contact cf. 0.123 in areas covered by the top contact at 5.9 keV) has been calculated under the conservative assumption that the only active region of the detector is the i layer. The greater X-ray linear attenuation coefficients of $Al_{0.2}Ga_{0.8}As$ (e.g. 787.8 cm^{-1} at 5.9 keV) compared with $Al_{0.8}Ga_{0.2}As$ (e.g. 638.8 cm^{-1} at 5.9 keV), together with the thicker i layer for the presently reported detectors, resulted in greater efficiency of the detectors compared with previous photon counting spectroscopic AlGaAs X-ray detectors. The attenuation due to device top contacts has not been included in the calculated detection efficiencies presented in Fig. 3.5.

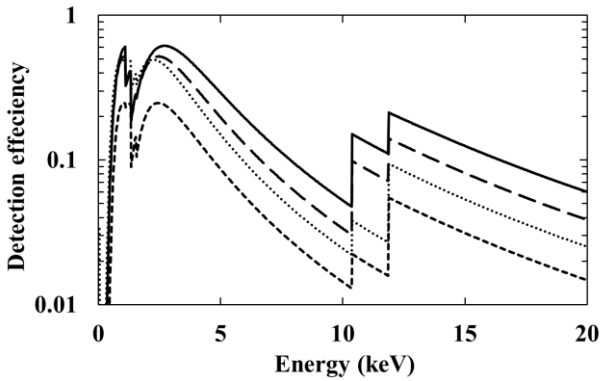

Fig. 3.5. Calculated detection efficiency as a function of energy for the $Al_{0.2}Ga_{0.8}As$ X-ray p^+-i-n^+ mesa photodiodes when operated at 30 V (solid line) and 10 V (long dashed line) reverse bias, respectively. For comparison, the detection efficiencies of $Al_{0.8}Ga_{0.2}As$ photodiodes used by Barnett et al. (2015) and Barnett et al. (2013b) are also shown (dotted and short dashed lines respectively). The discontinuities are the associated Al, Ga, and As X-ray absorption edges (see **Section 2.2.2.1**).

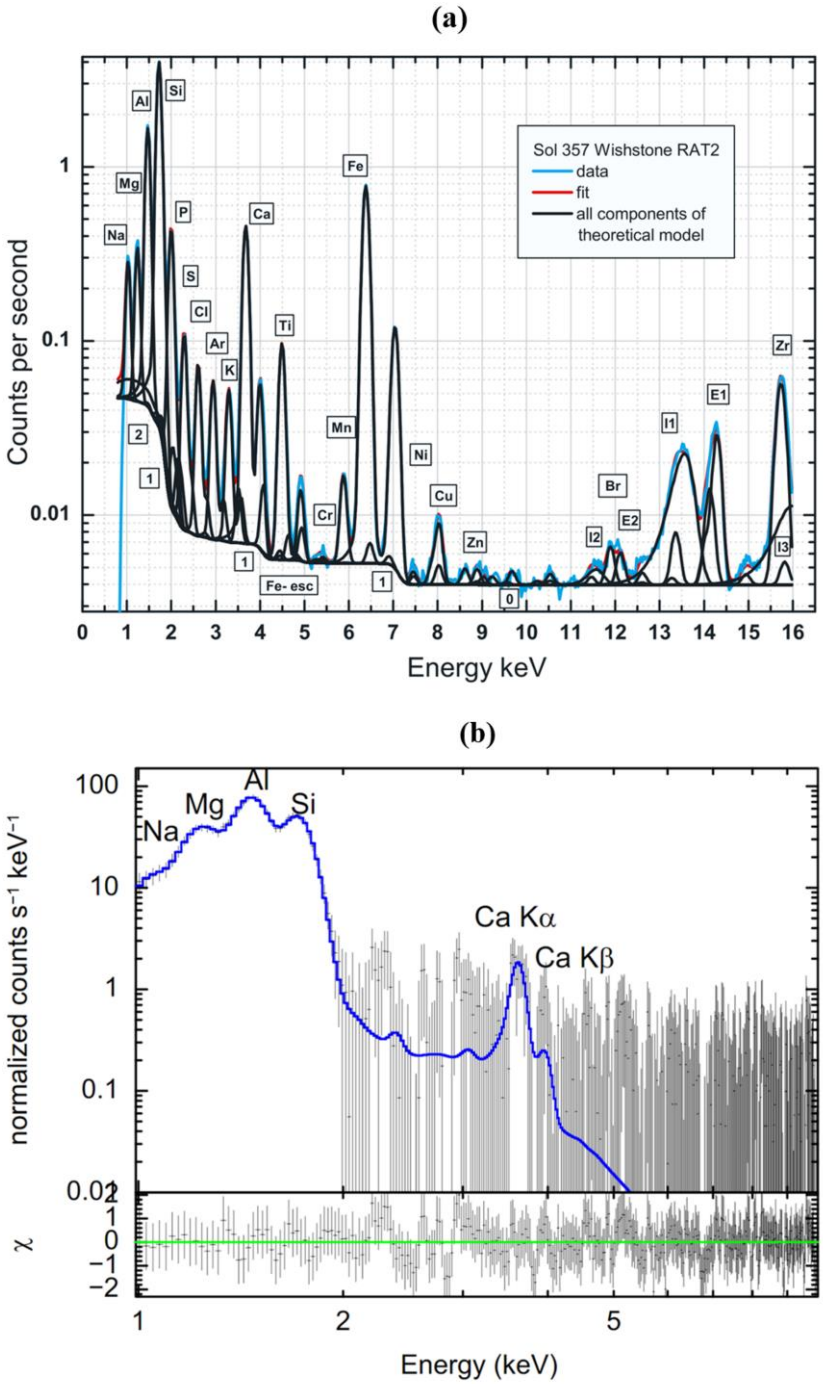

Fig. 3.6. (a) X-ray spectrum obtained by the Mars Exploration Spirit Rover APXS instrument (see **Section 1.5.1**) on Mars, together with the deconvolution model components, as reported by Gellert et al. (2006). The reader is referred to Gellert et al. (2006) for an in-depth discussion on the presented spectrum. (b) X-ray spectrum of the Lunar surface, obtained by the Chandrayaan-1 X-ray spectrometer, as reported by Athiray et al. (2014). The reader is referred to Athiray et al. (2014) for further information on the presented spectrum.

3.5 Room temperature X-ray spectroscopy

3.5.1 Measurements with an ^{55}Fe radioisotope X-ray source

To investigate the performance of the photodiodes (D1 – D3) as detectors of soft X-rays, each diode was connected in turn to a custom-made low-noise charge-sensitive single channel preamplifier of feedback-resistorless design (see **Section 2.7**). The preamplifier used a silicon JFET (2N4416A, capacitance = 2 pF) as the input transistor. The preamplifier was connected to an Ortec 571A shaping amplifier (shaping time = 1 μs, the optimum for the system used) and an Ortec 927 ASPEC multi-channel analyser (MCA). An ^{55}Fe radioisotope X-ray source (225 MBq) emitting characteristic Mn Kα (5.9 keV) and Mn Kβ (6.49 keV) X-rays was placed above the AlGaAs diodes. The diodes and preamplifier were operated at room temperature (22 °C) in a dry N_2 environment (< 5 % relative humidity). Spectra were accumulated with the photodiodes reverse biased at 0 V, 5 V, 10 V, 15 V, 20 V, and 30 V. The live time limit for each spectrum was 1,000 s. The spectra were energy calibrated using the positions of the zero energy noise peak and the fitted Mn Kα 5.9 keV peak, with the assumption of a linear variation of detected charge with energy. A representative spectrum accumulated with device, D1, reverse biased at 10 V is presented in Fig. 3.7. To minimise counts from the noise peak, a low energy discriminator threshold (3.1 keV) was set. The dashed lines are the Mn Kα and Mn Kβ peaks fitted to the observed peak in the accepted ratio (Schötzig, 2000), accounting for the relative efficiency of the detector at the respective energies. The FWHM at 5.9 keV measured with D1 under these conditions was 1.28 keV ± 0.05 keV. A FWHM at 5.9 keV of 1.24 keV ± 0.04 keV were measured for both D2 and D3. The impact ionisation coefficients (see **Section 2.9.2**) of $Al_{0.2}Ga_{0.8}As$ as a function of average electric field were calculated and indicated that the diodes were operating within the non-avalanche regime (Zheng et al., 2000). In addition, no shift in channel number of the Mn Kα 5.9 keV peak as a function of reverse bias was observed (see **Section 5.5.1**).

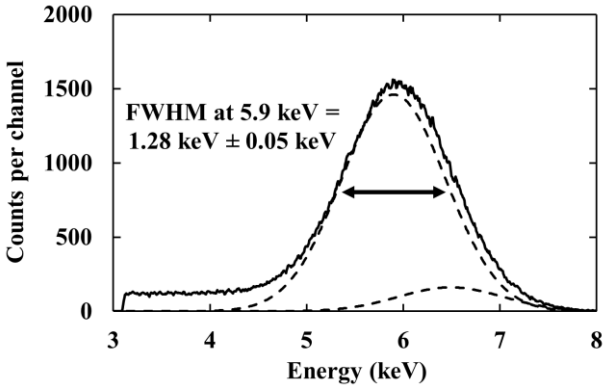

Fig. 3.7. Spectrum accumulated with the $Al_{0.2}Ga_{0.8}As$ device D1 at an applied reverse bias of 10 V when illuminated with an ^{55}Fe radioisotope X-ray source. The dashed lines are the fitted Mn Kα and Mn Kβ peaks.

From Fig. 3.7, low energy tailing can be seen in the accumulated spectrum. This tailing was attributed to the partial collection of charge created by X-ray photons absorbed in the low-field regions of the photodiode (Barnett et al., 2015). The valley-to-peak ratio, R_{VtoP}, can be used to quantify the amount of low energy tailing (Barnett et al., 2015). For the $Al_{0.2}Ga_{0.8}As$ X-ray p^+-i-n^+ mesa photodiodes reported, the mean R_{VtoP} at a reverse bias of 10 V was 0.08. This was comparable to that previously reported for $Al_{0.8}Ga_{0.2}As$ devices (0.08) (Barnett et al., 2015). For previously reported GaAs devices (Lioliou et al., 2016a), at room temperature, an improved R_{VtoP} (0.05) was calculated. As thicker i layer devices are produced, assuming that non-uniformities in the charge collection efficiency, especially at the device edges, are small, it is likely that R_{VtoP} will improve due to a greater fraction of the X-ray photons, illuminating the devices, being absorbed in the active region compared with the low-field layers.

The FWHM at 5.9 keV observed with each diode reverse biased at 0 V, 5 V, 10 V, 15 V, 20 V, and 30 V is presented in Fig. 3.8. The best mean FWHM at 5.9 keV (= 1.24 keV ± 0.04 keV) was observed when the diodes were operated at 10 V and 20 V. An improving trend in FWHM from 0 V to 10 V was attributed to a reduction in capacitance and associated series white noise, in combination with a decrease in charge trapping noise (see **Section 3.5.2**). Between 20 V and 30 V, an increase in FWHM indicated that the leakage current and associated parallel white noise outweighed any positive aspects brought from operation at higher reverse bias.

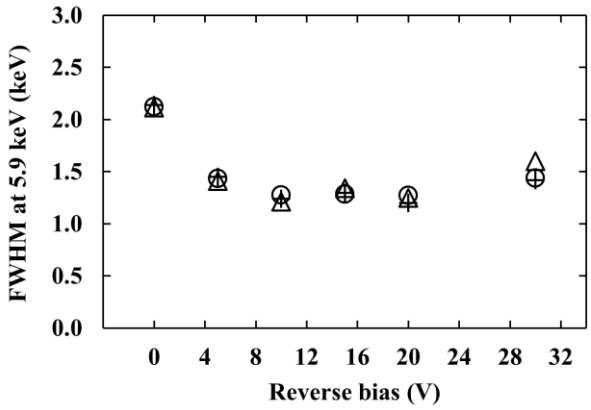

Fig. 3.8. Measured FWHM at 5.9 keV as a function of applied reverse bias for D1 (circles), D2 (+ symbol), and D3 (triangles). The associated uncertainties were omitted for clarity.

3.5.2 Noise analysis

The energy resolution of a non-avalanche semiconductor detector coupled to a charge sensitive preamplifier is influenced by three sources of noise (see **Section 2.8**). Assuming a Fano factor of 0.12, and an electron hole pair creation energy of 4.4 eV (assuming a linear variation of ω_{EHP} with Al fraction between GaAs (ω_{EHP} = 4.18 eV (Bertuccio & Maiocchi, 2002)) and $Al_{0.8}Ga_{0.2}As$ (ω_{EHP} = 5.10 (Barnett et al., 2012b)), the expected Fano limited energy resolution (FWHM) at 5.9 keV would be 131 eV for $Al_{0.2}Ga_{0.8}As$ at room temperature. Given that the experimentally observed energy resolutions (FWHM at 5.9 keV) of the diodes were much greater than the Fano-limit energy resolution at 5.9 keV, it was important to consider the relative contributions of the additional noise sources.

Electronic noise contributions include parallel white noise, series white noise (including induced gate drain current noise), 1/*f* series noise, and dielectric noise (see **Section 2.8.2**). Fig. 3.9 presents the calculated values of these noise contributions, as per **Section 2.8.2**, for each diode (D1 – D3) when reverse biased at 10 V.

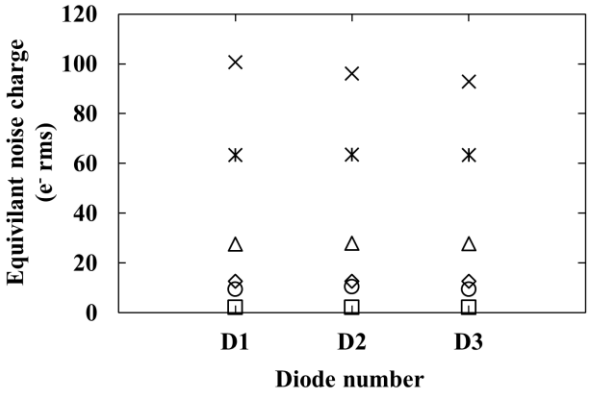

Fig. 3.9. Calculated remaining noise contributions of each $Al_{0.2}Ga_{0.8}As$ diode at an applied reverse bias of 10 V and a shaping time of 1 μs: combined unknown dielectric noise, incomplete charge collection noise and any additional stray series white noise (crosses); known dielectric noise (stars); series white noise (triangles); Fano noise (diamonds); parallel white noise (circles); 1/*f* series noise (squares).

In addition to the parallel white noise of the detector (calculated using the measured leakage current as shown in Fig. 3.2), the parallel white noise contribution from the JFET was also included within the total parallel white noise contribution, assuming that the leakage current of the JFET at room temperature was 1 pA (Siliconix, 2001). As the contribution from series white noise depends on the total capacitance load at the gate of the input transistor of the preamplifier, only a minimum estimate could be calculated. This was due to the prototype nature of the preamplifier, where, in addition to estimable capacitances, stray capacitances with unknown values were present. Similarly, dielectric noise contributions arising from the detector, JFET, and feedback capacitor were readily estimated (Barnett et al., 2015) (Lioliou et al., 2015), but additional noise from other lossy dielectrics in proximity to the preamplifier would also have added to the noise. Subtracting the expected Fano noise (the statistically limited resolution) and the electronic noise contributions (parallel white noise, known series white noise (including induced gate drain current noise), known dielectric noise, and 1/*f* noise) from the measured FWHM at 5.9 keV in quadrature, the remainder can be attributed to incomplete charge collection noise and the unknown dielectric and stray series white noises (Barnett et al., 2015).

From Fig. 3.9, the dominant source of noise across all diodes was this remaining noise. Assuming the remaining noise from unknown lossy dielectrics and stray series white noise was independent of reverse bias (Bertuccio et al., 1996) (Barnett et al., 2012a), the reduction of this remaining noise as the reverse bias was increased from 0 V to 10 V can be attributed to a reduction in charge trapping noise (the prime constituent of incomplete charge collection noise broadening the energy resolution).

Given this assumption, a quantitative estimate of the reduction of charge trapping noise as a function of increased applied bias can be made by subtracting the known noise contributions that vary with applied reverse bias from the equivalent noise charge of the measured FWHM at 5.9 keV at each reverse bias in quadrature, and examining the change in the remainder as a function of applied reverse bias (Bertuccio et al., 1996). Therefore, it can be said that there was a mean additional charge trapping noise of 146 e^- rms equivalent noise charge at 5.9 keV when the detectors were operated at 0 V in comparison to 5 V reverse bias. Similarly, a mean additional charge trapping noise of 67 e^- rms at 5.9 keV was calculated at 5 V in comparison to 10 V. Beyond this reverse bias, any remaining charge trapping noise became insignificant compared with the other noise components. The calculated charge trapping noise was then subtracted from the unknown dielectrics, incomplete charge collection, and additional series white noise in quadrature. The various noise components are presented in Fig. 3.10 for one representative diode (D1). The $Al_{0.8}Ga_{0.2}As$ (400 µm diameter, 1.7 µm i layer) photodiodes reported by Barnett et al. (2015), had 26 e^- rms charge trapping noise at 5.9 keV at 5 V reverse bias; significantly less than the presently reported detectors (67 e^- rms at 5 V reverse bias). This is not surprising given the maturity of $Al_{0.8}Ga_{0.2}As$ as a material for X-ray spectroscopy compared with that of $Al_{0.2}Ga_{0.8}As$. Additionally, as can be seen in Fig. 3.10, an apparent increase in the noise attributed to unknown lossy dielectrics and stray series white noise occurred between 20 V and 30 V reverse bias. One possible explanation for this is that rather than an increase in these particular noise components, there may have been an increase in parallel white noise from the preamplifier's input JFET as a result of the larger leakage current of the detector at 30 V compared with 20 V reverse bias. Such dependence of the JFET's performance was negligible at lower detector leakage currents, but could have had a small effect at higher leakage currents due to the bias condition of the JFET being controlled, in part, by the leakage current of the detector in feedback-resistorless preamplifiers (Bertuccio et al., 1993).

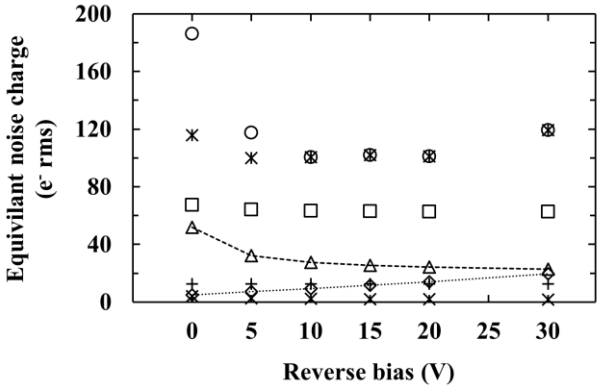

Fig. 3.10. Calculated remaining noise contributions (unknown dielectric noise, incomplete charge collection noise and additional series white noise) (circles), remaining noise contributions with charge trapping noise subtracted (stars), known dielectric noise (squares), series white noise (triangles), Fano noise (plus sign), parallel white noise (diamonds), and 1/*f* series noise (crosses) as a function of applied reverse bias, at a shaping time of 1 μs, for one representative $Al_{0.2}Ga_{0.8}As$ X-ray p^+-i-n^+ mesa photodiode, D1, at room temperature. The dashed lines are guides for the eyes only.

3.6 Temperature dependent electrical characterisation

3.6.1 Current measurements as a function of applied bias

Current as a function of applied forward and reverse bias, across the temperature range 60 °C to -20 °C, was measured for two devices (D1 and D2) previously investigated in **Section 3.4**, using a Keithley 6487 Picoammeter/Voltage Source. The package and the associated diodes of interest (D1 and D2) were connected within a custom, electromagnetically screened, light tight test fixture, and installed within a TAS Micro MT climatic cabinet for temperature control. A thermocouple was appropriately positioned in order to monitor the temperature and ensure that thermal equilibrium was reached and maintained between the climatic cabinet and the detectors at each temperature. The custom test fixture was initially purged with dry N_2, then sealed and the climatic cabinet shut. The climatic cabinet was continually purged with dry N_2 for the duration of the measurement in order to maintain a dry N_2 environment (< 5 % relative humidity) to eliminate any humidity related effects (Barnett et al., 2013b). National Instruments LabVIEW software was used to automate the characterisation routine. The temperature was initially set to 60 °C and decreased in 20 °C increments to -20 °C, the minimum recorded temperature. The diodes were left to stabilise for 30 minutes at each temperature before measuring to ensure thermal equilibrium. Fig. 3.11 presents the dark current as a function of applied forward bias for diode,

D1, with dark current decreasing as a function of decreasing temperature. Comparable results were obtained for D2.

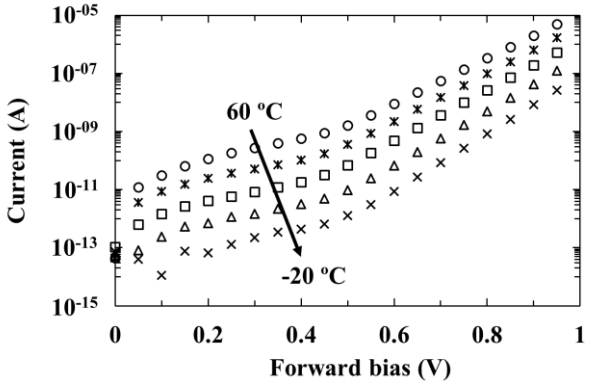

Fig. 3.11. Current as a function of applied forward bias in the temperature range 60 °C to -20 °C for D1. Comparable results were obtained for D2. The associated uncertainties were omitted for clarity.

The forward current, I_F (units of A), of a p^+-i-n^+ diode can be approximated by the recombination current, I_{rec} (units of A), arising from the generation-recombination of carriers within the depletion layer (see **Section 2.4.2**), and the diffusion current, I_{diff} (units of A), arising from the diffusion of carriers within the neutral region (see **Section 2.3**) such that

$$I_F = A_d \mathrm{q} {n_i}^2 \left(\frac{1}{N_D}\sqrt{\frac{D_h}{\tau_h}} + \frac{1}{N_A}\sqrt{\frac{D_e}{\tau_e}}\right) \exp\left(\frac{\mathrm{q}V_F}{\mathrm{k}T}\right) + A_d \mathrm{q} \frac{n_i}{2\tau_g} W_D \exp\left(\frac{\mathrm{q}V_F}{2\mathrm{k}T}\right), \qquad (3.3)$$

where I_{diff} is the first term and I_{rec} is the second term. D_h and D_e are the diffusion coefficients for holes and electrons respectively (units of $cm^2\ s^{-1}$), V_F is the applied forward bias (units of V), and τ_g is the carrier generation lifetime (units of s) (Schötzig, 2000). Other current generating processes, such as tunnelling of carriers between states in the bandgap, surface effects, and parasitic series resistances, are considered negligible.

I_{rec} and I_{diff} have the temperature dependencies

$$I_{rec} \propto n_i \exp\left(\frac{\mathrm{q}V_F}{2\mathrm{k}T}\right) \qquad (3.4)$$

and

$$I_{diff} \propto n_i^2 \exp\left(\frac{\mathrm{q}V_F}{\mathrm{k}T}\right), \qquad (3.5)$$

respectively, which can be directly compared to the profiles of I_F as a function of temperature for the investigated devices D1 and D2. Over the investigated temperature range, the forward current was found to be better described by Eq. 3.4 for both diodes, suggesting that recombination current was dominant.

From Eq. 3.3, the forward current of a p^+-i-n^+ diode can be defined by

$$I_F = I_{sat} \exp\left(\frac{qV_F}{nkT}\right), \tag{3.6}$$

where I_{sat} (units of A) is the saturation current (the expected leakage current, I_d, of a p^+-i-n^+ diode) and n is the ideality factor. The ideality factor determines the dominant current mechanism occurring within the diode; a value of 1 suggests that the diffusion current dominates, whilst a value of 2 suggests that the recombination current dominates (Sze, 2006). The saturation current and the ideality factor were calculated at each temperature based on the linear region of the semi-logarithm I-V characteristics as described by Lioliou et al. (2016b). Eq. 3.6 is valid only when $V_F > 3kT/q$; in addition, ideal diode behaviour was not exhibited until approximately $V_F >$ 0.5 V for both diodes where, at lower applied forward bias, parallel or shunt resistances were present. Such shunt resistance can be caused by defects in the form of diffusion paths along dislocations in the semiconductor, or leakage around the edge of the diode walls (Luque & Hegedus, 2003). A linear least squares fit was therefore applied to the region 0.65 V $\leq V_F \leq$ 0.95 V. The saturation current was found to decrease as a function of temperature, from 195 fA ± 1 fA and 199 fA ± 1 fA at 60 °C, to 8.70 aA ± 0.03 aA and 7.99 aA ± 0.03 aA at -20 °C, for D1 and D2 respectively. Fig. 3.12 presents the ideality factor as a function of temperature.

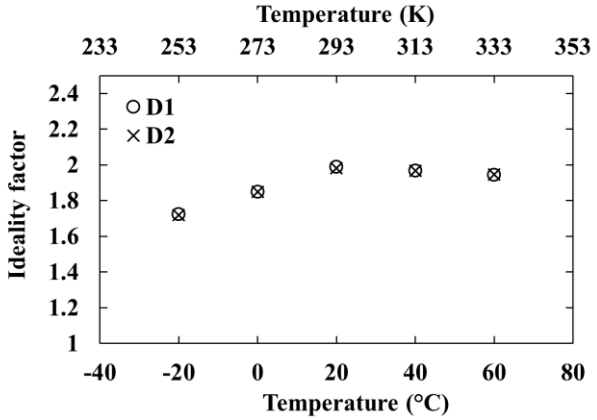

Fig. 3.12. Ideality factor as a function of temperature, extracted from the measured current as a function of applied forward bias (0.65 V $\leq V_F \leq$ 0.95 V) for D1 (circles) and D2 (crosses). The associated uncertainties were smaller than the symbols.

At 20 °C and above, the ideality factor was ≈ 2 for both D1 and D2. This suggests that recombination within the depletion region is the dominant limiting factor of current (Luque & Hegedus, 2003). Below 20 °C however, the ideality factor decreased; this suggests that fewer thermally stimulated crystal lattice defects were present within the detecting material at temperatures < 20 °C.

The leakage current, I_d, as a function of applied reverse bias for D1 is shown in Fig. 3.13. The leakage current for both devices, D1 and D2, decreased as a function of decreasing temperature. At the maximum applied reverse bias (30 V), the leakage current was measured to be 300 pA ± 1 pA at 60 °C and 1.1 pA ± 0.4 pA at -20 °C for D1, and 242 pA ± 1 pA at 60 °C and 1.0 pA ± 0.4 pA at -20 °C for D2.

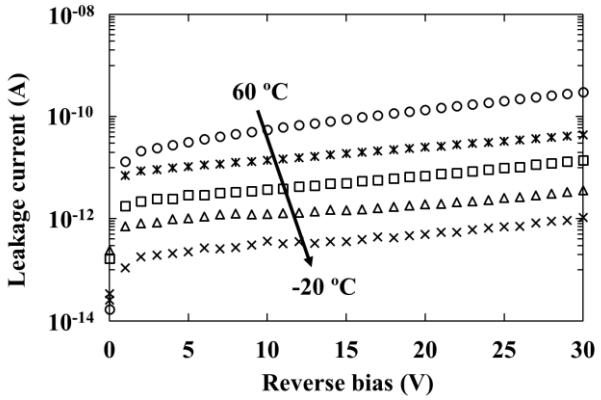

Fig. 3.13. Leakage current as a function of applied reverse bias in the temperature range 60 °C to -20 °C for D1. Comparable results were obtained for D2. The associated uncertainties were omitted for clarity.

The leakage current, I_d, of a p^+-i-n^+ diode can be approximated to the saturation current, I_{sat}, such that

$$I_d \approx I_{sat} = A_d \mathrm{q} {n_i}^2 \left(\frac{1}{N_D} \sqrt{\frac{D_h}{\tau_h}} + \frac{1}{N_A} \sqrt{\frac{D_e}{\tau_e}} \right) + A_d \mathrm{q} \frac{n_i}{2\tau_g} W_D, \qquad (3.7)$$

where diffusion current, I_{diff}, is the first term and generation current, I_{gen} (units of A), is the second term (Lioliou et al., 2016b). Unlike Eq. 3.3, other current generating processes, such as tunnelling of carriers between states in the bandgap, surface effects, and parasitic series resistances, can cause significant departures in experimental measurements of p^+-i-n^+ devices from Eq. 3.7 (Sze, 2006). As a result, Eq. 3.7 only yields a qualitative agreement for certain semiconducting p^+-i-n^+ junctions (Sze, 2006).

When a reverse bias, V_R, is applied across a semiconducting p^+-i-n^+ diode at a fixed temperature T (units of °C), the detected current can change as a function of time beyond that expected by fluctuations in charge carrier generation (see **Section 2.4.1**). The measured current can initially decrease or increase over time, eventually stabilising at some time, t (units of s). Or, the measured current may continually increase until the diode is permanently damaged. The source of such leakage current instability is related to conduction mechanisms and greatly depends on the semiconducting material (Street, 2000).

Leakage current stability with time was measured for both diodes, D1 and D2, where the leakage current at the maximum applied reverse bias (30 V) was found to be stable at 20 °C and below. At temperatures > 20 °C, the leakage currents of both devices were found to increase. Fig. 3.14 shows the measured leakage current as a function of time for D1 at 60 °C and 20 °C. Similar results were obtained for D2.

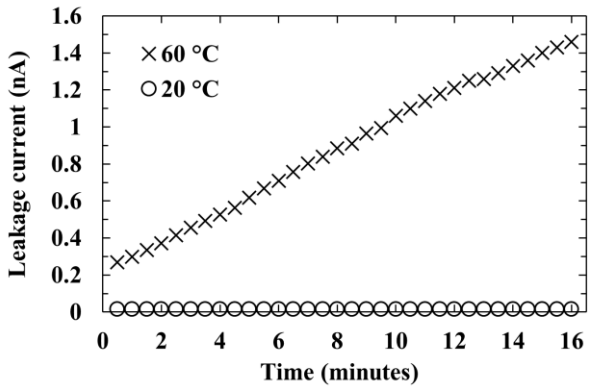

Fig. 3.14. Leakage current as a function of time for D1 at an applied reverse bias of 30 V, and a temperature of 60 °C (crosses) and 20 °C (circles). The associated uncertainties were smaller than the symbols.

Fig. 3.15 presents the leakage current density, J_d (units of A cm^{-2}), at the maximum applied reverse bias (30 V, 100 kV cm^{-1}) as a function of temperature for D1. Within the temperature range 40 °C to -20 °C the leakage current density, J_d, increased exponentially with increasing temperature. Beyond 40 °C, the trend changed, which suggested that the leakage current mechanism was different at higher temperatures (Lioliou et al., 2016b). Near identical results were obtained with D2, where the exponential fit coefficients over the temperature range 40 °C to -20 °C were calculated to be: a = $1.11 \times 10^{-8} \pm 0.02 \times 10^{-8}$ and b = 0.063 ± 0.001, given J_d = aexp(bT).

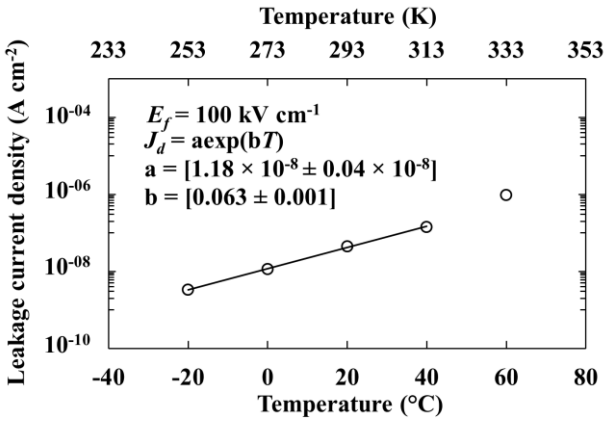

Fig. 3.15. Measured leakage current density, J_d, at a 100 kV cm^{-1} average internal electric field strength, E_f, as a function of temperature for D1. A linear least squares fitting has been applied, with the line of best fit plotted. The associated uncertainties were smaller than the symbols.

From Eq. 3.7, the leakage current density can be expressed as

$$J_d = \mathrm{q}{n_i}^2 \left(\frac{1}{N_D}\sqrt{\frac{D_h}{\tau_h}} + \frac{1}{N_A}\sqrt{\frac{D_e}{\tau_e}}\right) + \mathrm{q}\frac{n_i}{2\tau_g}W_D. \tag{3.8}$$

The first and second term represents the diffusion and generation current respectively, where the diffusion current scales with n_i^2 whilst the generation current scales with n_i (Sze, 2006). Since the intrinsic carrier concentration is also a function of the bandgap energy, E_g, of the semiconducting material, such that

$$n_i^2 \propto \exp\left(-\frac{E_g}{\mathrm{k}T}\right), \tag{3.9}$$

and

$$n_i \propto \exp\left(-\frac{E_g}{2\mathrm{k}T}\right), \tag{3.10}$$

a plot of ln(J_d) as a function of 1/kT yields a relationship whose slope determines the activation energy, E_A (units of eV), and the dominant leakage current mechanism. A gradient of -E_g/2, suggests that the generation current is dominant, whilst a gradient of E_g suggests that the diffusion current is dominant (Lioliou et al., 2016b) (Sze, 2006) (Spieler, 2005). Fig. 3.16 shows ln(J_d) as a function of 1/kT plotted for the device, D1.

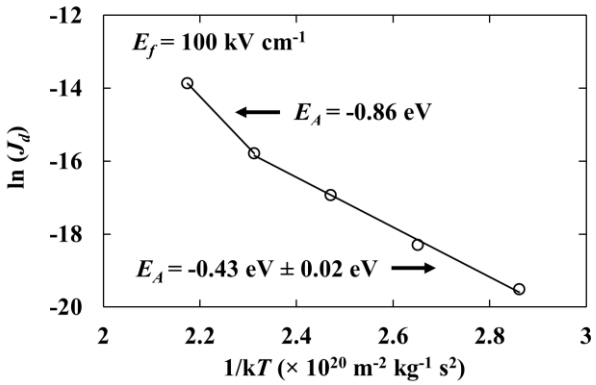

Fig. 3.16. Natural logarithm of leakage current density, ln(J_d), as a function of 1/kT at an average internal electric field, E, of 100 kV cm^{-1} for the $Al_{0.2}Ga_{0.8}As$ p^+-i-n^+ photodiode, D1. Linear least squares fitting was applied to the temperature ranges: 60 °C to 40 °C and 40 °C to -20 °C. The lines of best fit and respective activation energies, E_A, are shown.

Two linear regions (E_A = -0.86 eV; E_A = -0.43 eV ± 0.02 eV) are apparent in Fig. 3.16. D2 exhibited comparable performance (E_A = -0.79 eV; E_A = -0.43 eV ± 0.02 eV) over the same temperature ranges. Within the temperature range 60 °C to 40 °C, the slope was approximately -E_g/2 for both D1 and D2, where the bandgap of $Al_{0.2}Ga_{0.8}As$ is 1.67 eV (Adachi, 1985). This corresponded to a generation dominant leakage current mechanism. Below 40 °C, the slope gradient was reduced (-0.43 eV). Growth of Si doped n^+ type $Al_xGa_{1-x}As$ layers has been reported to cause deep donor traps (often called DX centers), with an activation energy of 0.43 eV (Mooney et al., 1990) (Kumagai et al., 1984). Growth of Be doped p^+ type $Al_xGa_{1-x}As$ layers has also been found to create 0.40 eV and 0.46 eV traps within the temperature ranges of 225 – 200 K and 300 – 250 K respectively (Szatkowski et al., 1999) (Mari et al., 2011). Such DX centres residing in the Si doped n^+ type $Al_xGa_{1-x}As$ layer, or possible traps within the C doped p^+ type $Al_xGa_{1-x}As$ layer, may be responsible for the activation energy presently reported (E_A = -0.43 eV at 313.15 K – 253.15 K).

At sufficiently high temperatures, diffusion current will always dominate (Spieler, 2005), therefore Fig. 3.16 suggests that the diffusion current must dominate at a temperature beyond 60 °C for the photodiodes measured. Due to the high leakage currents which were observed at temperatures greater than 60 °C, a greater temperature range was not investigated.

3.6.2 Capacitance measurements as a function of applied bias

Capacitance as a function of applied forward and reverse bias was measured for the two $Al_{0.2}Ga_{0.8}As$ p^+-i-n^+ photodiodes D1 and D2, across the temperature range 60 °C to -20 °C, using

an HP 4275A LCR Meter (signal magnitude 50 mV rms; frequency 1 MHz) and a Keithley 6487 picoammeter/voltage source to bias the detectors. The custom made, electromagnetically screened, light tight test harness in which the $Al_{0.2}Ga_{0.8}As$ package was installed, was placed within a TAS Micro MT climatic cabinet for temperature control as per **Section 3.6.1**. National Instruments LabVIEW software was used to automate the characterisation routine. The temperature was initially set to 60 °C, and then decreased in 20 °C steps to -20 °C. The diodes were left for 30 minutes after reaching each temperature before measuring to ensure thermal equilibrium and stabilisation. Fig. 3.17 presents the capacitance as a function of applied forward bias at each measured temperature for the $Al_{0.2}Ga_{0.8}As$ p^+-i-n^+ photodiode, D1. Comparable results were found for D2. Since the devices were measured after packaging, the capacitance of the package was removed by measuring the capacitance of an empty connection on the same package across the same applied bias range, and at each temperature, with each packaging capacitance value deducted from the respective total capacitance obtained for the detectors. This procedure also removed any additional unknown capacitances of the system, with exception to the capacitance of the bond wires of each detector; however, subsequent analysis suggested that the bond wire capacitances were negligible when compared with the other associated capacitances. Temperatures greater than 60 °C were not measured due to the high leakage currents (> 40 nA at 10 V at 80 °C) being observed at such temperatures.

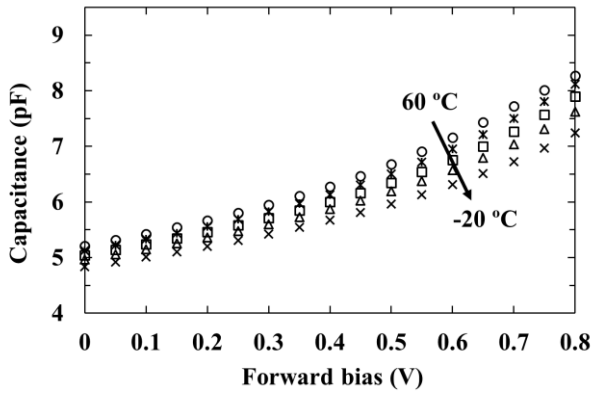

Fig. 3.17. Capacitance as a function of applied forward bias in the temperature range 60 °C to -20 °C, for D1; comparable results were obtained for D2. The associated uncertainties were smaller than the symbols.

As the temperature was decreased from 60 °C to -20 °C, the forward capacitance, which is proportional to the forward current, of both devices decreased at each applied forward bias. At low applied reverse biases (< 4 V), the measured capacitances increased as the temperature decreased for both diodes: without application of reverse bias (i.e. 0 V), at 60 °C, capacitances of 5.20 pF ± 0.04 pF and 5.26 pF ± 0.04 pF were measured for D1 and D2, respectively; at -20 °C

capacitances of 4.83 pF ± 0.04 pF and 4.90 pF ± 0.04 pF were measured. As applied reverse bias was increased, the temperature dependence of the capacitance reduced, as shown by Fig. 3.18. At applied reverse bias ≥ 4 V, the variation in capacitance as a function of temperature became indiscernible i.e. the change in capacitance remained within the uncertainty of the measurement.

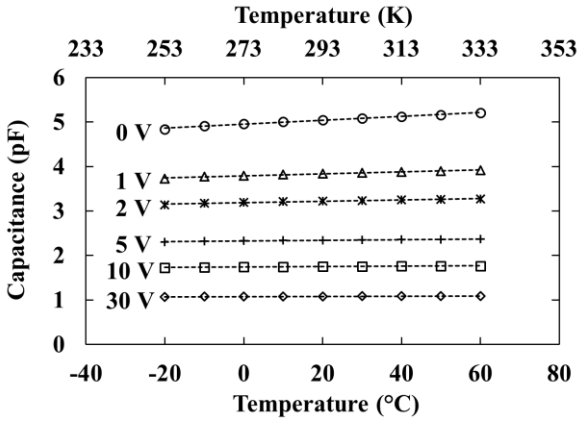

Fig. 3.18. Capacitance as a function of temperature for D1, in the temperature range 60 °C to -20 °C at 6 reverse bias values: 0 V (circles); 1 V (triangles); 2 V (stars); 5 V (plus signs); 10 V (squares); and 30 V (diamonds). Linear least squares fitting was applied to each data set in order to determine the capacitance per degree Celsius: 4.38 fF $°C^{-1}$ ± 0.18 fF $°C^{-1}$ for 0 V; 2.24 fF $°C^{-1}$ ± 0.13 fF $°C^{-1}$ for 1 V; 1.51 fF $°C^{-1}$ ± 0.11 fF $°C^{-1}$ for 2 V; 0.79 fF $°C^{-1}$ ± 0.07 fF $°C^{-1}$ for 5 V; 0.47 fF $°C^{-1}$ ± 0.04 fF $°C^{-1}$ for 10 V; 0.24 fF $°C^{-1}$ ± 0.01 fF $°C^{-1}$ for 30 V. Comparable results were obtained for D2, with calculated gradients falling within the uncertainty of those calculated for D1.

When reverse biased, the junction capacitance is predominantly defined by the depletion layer capacitance, C_{DL} (see **Section 3.4.2**). Thus, from the measured depletion layer capacitance, the depletion width as a function of applied reverse bias was calculated using Eq. 3.1. The depletion width of each diode increased as a function of applied reverse bias for all temperatures until reaching an applied reverse bias of 30 V, where the measured depletion layer capacitance, and consequently the depletion width, remained constant. This suggested that the diodes were fully depleted at an applied reverse bias of 30 V (3.20 µm ± 0.15 µm and 3.01 µm ± 0.14 µm at -20 °C, 3.14 µm ± 0.14 µm and 2.96 µm ± 0.13 µm at 60 °C, for D1 and D2 respectively, at an applied reverse bias of 30 V). The calculated depletion width as a function of applied reverse bias at -20 °C and 60 °C for diode D1 can be seen in Fig. 3.19. The depletion width of both diodes was found to be temperature independent, where the change in calculated depletion width as a function of temperature lay within the measurement uncertainty.

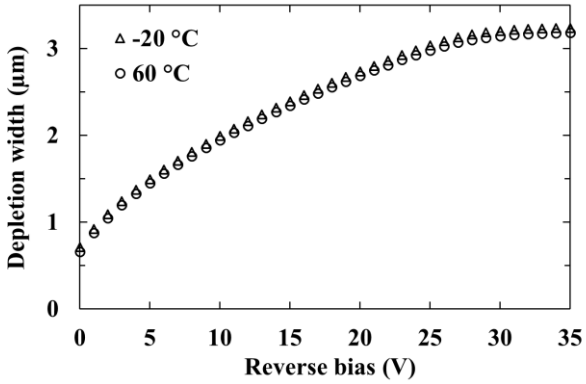

Fig. 3.19. Calculated depletion width as a function of reverse bias for D1, at -20 °C (triangles) and 60 °C (circles). Comparable results were obtained for D2. The associated uncertainties were omitted for clarity.

The effective doping density of the i layer, N_{eff}, was calculated using the equation for general nonuniform distributions (see **Section 3.4.2**). The effective doping density throughout the intrinsic region was calculated to be $\approx 4.0\times10^{15}$ cm^{-3} and $\approx 4.4\times10^{15}$ cm^{-3} for D1 and D2, respectively. The variation of the effective doping density as a consequence of change in temperature fell well within the calculated uncertainty of the measurement. At the i-n$^+$ interface, the effective doping density increased to $\approx 5\times10^{16}$ cm^{-3} for both D1 and D2. The effective doping density as a function of distance below the p$^+$-i junction for D1 has been plotted in Fig. 3.20.

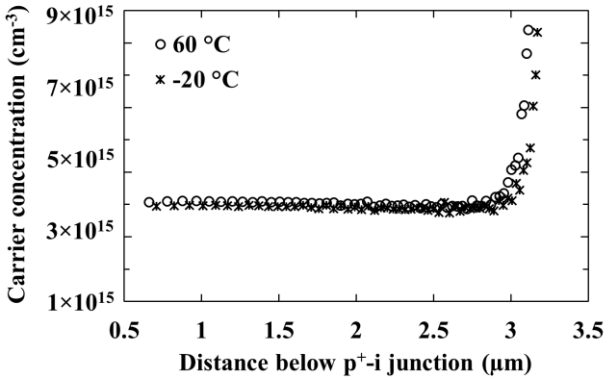

Fig. 3.20. Effective doping density profile for D1, at 60 °C (circles) and -20 °C (stars). Comparable results were obtained for D2. The associated uncertainties were omitted for clarity.

3.7 Temperature dependent X-ray spectroscopy

3.7.1 Measurements with an ^{55}Fe radioisotope X-ray source

X-ray spectra were obtained using the $Al_{0.2}Ga_{0.8}As$ p$^+$-i-n$^+$ photodiode, D1, to characterise the X-ray detection performance as a function of temperature. The diode was connected to a

custom-made low-noise charge-sensitive single channel preamplifier of feedback-resistorless design, similar to Bertuccio et al. (1993), and composing of slight modifications relative to that used in **Section 3.5**. The preamplifier was connected to an Ortec 571A shaping amplifier (shaping time = 0.5 μs, the optimum available for the system used) and an Ortec 927 ASPEC multi-channel analyser (MCA). An ^{55}Fe radioisotope X-ray source (193 MBq) emitting characteristic Mn Kα (5.9 keV) and Mn Kβ (6.49 keV) X-rays was placed 3 mm above the $Al_{0.2}Ga_{0.8}As$ p^+-i-n^+ photodiode, housed within the preamplifier. The detector and preamplifier were installed inside a TAS Micro MT climatic cabinet throughout the measurements for temperature control, and a thermocouple was placed close to the detecting system to ensure temperature agreement between the climatic cabinet and the detecting system. The climatic cabinet was continually purged with dry N_2 (< 5 % relative humidity) in order to reduce humidity related effects (Barnett et al., 2013b).

The temperature was initially set to 20 °C, and was decreased to a minimum temperature of -20 °C, in steps of 20 °C, where the device was allowed to stabilise for 30 minutes upon reaching the desired temperature in order to ensure thermal equilibrium. A maximum temperature of 20 °C was set due to diode instability at greater temperatures over the time used to accumulate the spectra. Spectra were accumulated at each temperature, with the photodiode reverse biased at 0 V, 10 V, 20 V, and 30 V. The live time limit for each spectrum was 1,000 s. Gaussian fitting was applied to the detected photopeak from the ^{55}Fe radioisotope X-ray source (Mn Kα = 5.9 keV; Mn Kβ = 6.49 keV) taking into account the relative emission ratio and the relative efficiency of the detector at these respective energies (Schötzig, 2000). The spectra were energy calibrated using the positions of the zero energy noise peak and the fitted Mn Kα 5.9 keV peak, with the assumption of a linear variation of detected charge with energy. The impact ionisation coefficients of $Al_{0.2}Ga_{0.8}As$ as a function of average internal electric field, within the investigated temperature range, were calculated and indicated that the diodes were operating within the non-avalanche regime (Zheng et al., 2000). The FWHM was measured for all obtained spectra, and have been plotted as a function of reverse bias in Fig. 3.21.

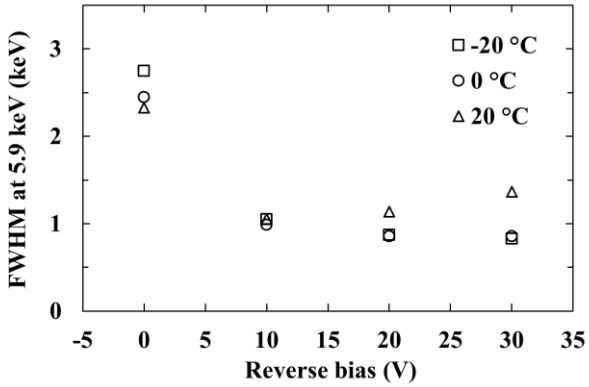

Fig. 3.21. Measured FWHM at 5.9 keV as a function of applied reverse bias for the $Al_{0.2}Ga_{0.8}As$ p^+-i-n^+ photodiode, D1, in the temperature range 20 °C to -20 °C at a shaping time of 0.5 µs. The associated uncertainties were omitted for clarity.

Room temperature device performance was found to be better than that previously reported for the $Al_{0.2}Ga_{0.8}As$ X-ray photodiode, where a FWHM at 5.9 keV of 1.24 keV ± 0.04 keV was measured at an average internal electric field strength of 33 kV cm^{-1} (see **Section 3.5.1**). Using the presently reported spectrometer, a FWHM at 5.9 keV of 1.06 keV ± 0.04 keV was measured at the same applied electric field. Fig. 3.22 shows spectra accumulated of the ^{55}Fe radioisotope X-ray source, at 20 °C and -20 °C, with a detector applied reverse bias of 20 V; the reduction of the FWHM due to decreasing temperature can be seen. The low energy tailing in the accumulated spectra was attributed to the partial collection of charge created by X-ray photons absorbed in the low-field regions of the photodiode/substrate (Barnett et al., 2015).

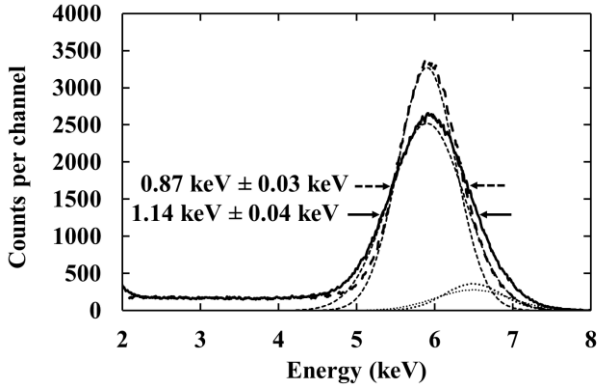

Fig. 3.22. ^{55}Fe X-ray spectra accumulated with the $Al_{0.2}Ga_{0.8}As$ p^+-i-n^+ photodiode D1 at a shaping time of 0.5 µs and an applied reverse bias of 20 V at two operating temperatures: -20 °C (dashed line) and 20 °C (solid line). The Mn Kα (narrow dashed line) and Mn Kβ (dotted line) Gaussian fitted peaks have also been plotted. The total number of counts under the Gaussian associated with the ^{55}Fe Mn Kα peak was ≈ 360,000 in each case.

3.7.2 Noise analysis

Assuming a Fano-limited energy resolution (FWHM) at 5.9 keV of 131 eV for $Al_{0.2}Ga_{0.8}As$ at room temperature (see **Section 3.5.2**), it was possible to conclude that a significant noise contribution from either the electronics noise or incomplete charge collection noise was present. The electronic noise components: parallel white noise; series white noise; induced gate drain current noise; 1/*f* series noise; dielectric noise, were calculated as per **Section 2.8.2**. Fig. 3.23 presents the calculated values of these noise contributions.

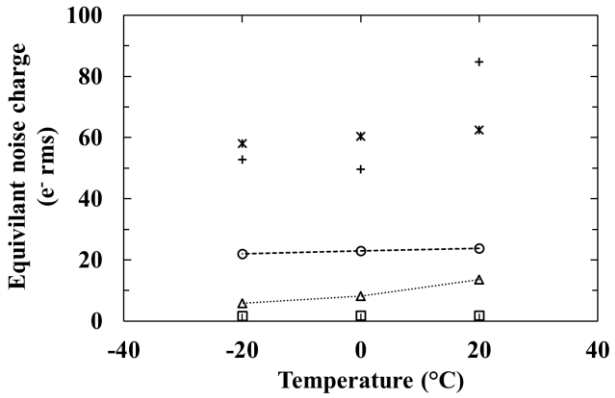

Fig. 3.23. Calculated remaining noise contributions of the $Al_{0.2}Ga_{0.8}As$ p^+-i-n^+ photodiode, D1, at an applied reverse bias of 20 V and a shaping time of 0.5 µs as a function of temperature: combined unknown dielectric noise, incomplete charge collection noise and any additional stray series white noise (plus signs); known dielectric noise (stars); series white noise (circles); parallel white noise (triangles); 1/*f* series noise (squares).

The parallel white noise component was calculated based on the measured leakage current of the detector at different temperatures (Fig. 3.13) and on the estimated leakage current of the input JFET as a function of temperature (1 pA for the investigated temperature range 20 °C to -20 °C (Siliconix, 2001)). The series white noise, due to the capacitance of the detector and the input JFET, was calculated based on the measured capacitance of the detector at different temperatures and on the estimated input capacitance of the input JFET (2 pF for the investigated temperature range 20 °C to -20 °C (Siliconix, 2001)). The known dielectric noise was calculated by taking the quadratic sum of the known individual dielectric noise of the detector and JFET. The quadratic sum of the noise components (series white noise, parallel white noise, 1/*f* series noise, the expected Fano noise, and the known dielectric noise) was subtracted from the total FWHM at 5.9 keV (see Fig. 3.21), and was attributed to unknown dielectric noise and stray series white noise, since incomplete charge collection noise has been previously shown to be insignificant in these devices at this operation condition (20 V) (see **Section 3.5.2**).

At no applied bias, the FWHM at 5.9 keV ranged from 2.33 keV ± 0.08 keV at 20 °C to 2.75 keV ± 0.10 keV at -20 °C. Since the quadratic sum of the known noise contributions with no applied bias decreased from 551 eV at 20 °C to 501 eV at -20 °C, the unknown dielectric noise, stray series white noise, and incomplete charge collection accounted for the increase in FWHM as the temperature was reduced (2.24 keV ± 0.08 keV at 20 °C and 2.47 keV ± 0.09 keV at -20 °C). The optimal operating reverse bias for the $Al_{0.2}Ga_{0.8}As$ detector was found to be 10 V at room temperature (1.06 keV ± 0.04 keV FWHM at 5.9 keV), and 30 V for 0 °C (856 eV ± 30 eV FWHM at 5.9 keV) and -20 °C (827 eV ± 30 eV FWHM at 5.9 keV). The variation in operating bias dependence of the energy resolution as a function of decreasing temperature was a result of the interplay between the noise driven by the detector's capacitance (series white noise) and the detector's leakage current (parallel white noise) contributions. At 20 °C, and at an applied reverse bias of 30 V, the increased parallel white noise (192 eV) relative to 10 V (108 eV) exceeded the benefits of a reduced series white noise contribution (232 eV) relative to an applied reverse bias of 10 V (283 eV). At lower temperatures (e.g. -20 °C), the reduction in parallel white noise (71 eV) relative to 10 V (58 eV), in addition to a lower series white noise contribution (215 eV) relative to 10 V (261 eV), reduced the FWHM at 5.9 keV accordingly (1.36 keV ± 0.05 keV at 20 °C and 827 eV ± 30 eV at -20 °C for an applied reverse bias of 30 V, and 1.06 keV ± 0.04 keV at 20 °C and 1.05 keV ± 0.04 keV at -20 °C for an applied reverse bias of 10 V).

3.8 Electron-hole pair creation energy measurements

3.8.1 Room temperature

The electron-hole pair creation energy (the average energy consumed in the generation of an electron-hole pair, see **Section 2.4.1**) at room temperature was determined for $Al_{0.2}Ga_{0.8}As$ (ω_{EHP} = 4.43 eV ± 0.09 eV for $Al_{0.2}Ga_{0.8}As$) relative to that of GaAs (ω_{EHP} = 4.18 eV ± 0.03 eV for GaAs (Bertuccio & Maiocchi, 2002)). The following method was previously used to determine the electron-hole pair creation energy for SiC (ω_{EHP} = 7.8 eV for SiC (Bertuccio & Casiraghi, 2003)) and GaAs (Bertuccio & Maiocchi, 2002) using a Si reference detector, and in $Al_{0.8}Ga_{0.2}As$ (ω_{EHP} = 5.10 eV ± 0.08 eV for $Al_{0.8}Ga_{0.2}As$ (Barnett et al., 2012b)) using a GaAs reference detector. The well characterised (Lioliou & Barnett, 2016) GaAs p^+-i-n^+ mesa X-ray photodiode (200 µm diameter, 10 µm i layer) structure is shown in Table 3.2.

Material	Dopant	Dopant type	Thickness (nm)	Doping density (cm^{-3})
GaAs	C	p	10	1×10^{19}
GaAs	C	p	500	2×10^{18}
GaAs		i	10000	Undoped
GaAs	Si	n	1000	2×10^{18}
GaAs n^+ substrate				

Table 3.2. Layer details of the GaAs reference diode.

The two detectors (the $Al_{0.2}Ga_{0.8}As$ photodiode, D1, and the GaAs reference photodiode) were connected in parallel to similar readout electronics used in **Section 3.5**, but with a modified preamplifier, as to appropriately accommodate two detectors. The detectors and preamplifier were kept at room temperature (20 °C) during the experiment. The ^{55}Fe radioisotope X-ray source was positioned above each detector in turn, taking great care not to disturb any other aspect of the apparatus (American National Standards Institute, 1989). The live time limit for each spectrum was 1,000 s. X-ray spectra were accumulated as a function of applied reverse bias (10 V, 15 V, and 20 V) of the $Al_{0.2}Ga_{0.8}As$ diode, D1, in order to ensure that no electric field dependencies (e.g. charge collection losses) affected the electron-hole pair creation energy results. The GaAs reference detector was kept at its optimum reverse bias of 10 V for each accumulated spectra. The shaping time of the shaping amplifier was set to 1 μs (the optimal shaping time for the dual detector configuration). The experimental system differs only slightly from that used by Bertuccio & Casiraghi (2003), Bertuccio & Maiocchi (2002), and Barnett et al. (2012b), in that although the detectors were connected in parallel, they were illuminated individually. This adjusted method was used in order to prevent any possible additional distortion (undershoot) within the preamplifier output caused as a consequence of two detectors being connected in parallel (American National Standards Institute, 1989). Although such an undershoot can typically be resolved by implementing a pole-zero cancellation (American National Standards Institute, 1989), the preamplifier response to the pulse would not be a simple exponential in this case, and consequently, it would be impractical to perform pole-zero cancellation in the amplifier (American National Standards Institute, 1989). Thus, the improved experimental method was used to eliminate the problem. Whilst obtaining measurements in this way can introduce the possibility of detector or input JFET leakage current instabilities over time, preliminary measurements of these parameters indicated that no such effects were present over the experiment's duration when the set up was operated in the described condition, and thus they did not affect the measurements. Fig. 3.24 presents representative spectra obtained with the $Al_{0.2}Ga_{0.8}As$ and GaAs detectors when they were connected in parallel and illuminated separately; the spectra are presented within the same figure for the convenience of the reader. Charge calibration was achieved using the positions of the zero energy noise peak of the preamplifier and

the 5.9 keV Mn Kα peak observed with the reference GaAs diode, together with the accepted electron-hole pair creation energy value of GaAs. The dashed and dotted lines are the fitted Mn Kα peaks for the $Al_{0.2}Ga_{0.8}As$ and GaAs detectors respectively.

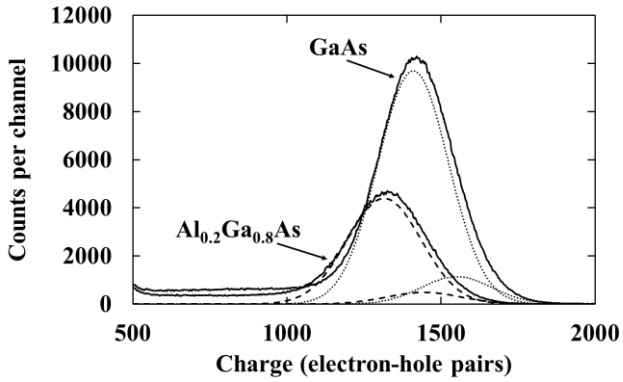

Fig. 3.24. Accumulated spectra at room temperature with an ^{55}Fe radioisotope X-ray source placed above the $Al_{0.2}Ga_{0.8}As$ detector, D1, (solid line as indicated) and the GaAs reference detector (solid line as indicated) at an applied reverse bias of 10 V and a shaping time of 1 μs. The detectors were connected in parallel but illuminated individually in turn; their spectra have been overlaid on the same calibrated charge scale. The Mn Kα and Mn Kβ Gaussian fitted peaks of the $Al_{0.2}Ga_{0.8}As$ detector (dashed lines), and the GaAs reference detector (dotted lines) have also been plotted.

As shown by the different positions of the peaks' centroids in Fig. 3.24, the average number of charge carriers created by the absorption of a photon of energy, *E*, in each material ($Al_{0.2}Ga_{0.8}As$ and GaAs) differs (Barnett et al., 2012b). Therefore, the electron-hole pair creation energy of $Al_{0.2}Ga_{0.8}As$ and GaAs must also differ, as illustrated by Eq. 2.9 (see **Section 2.4.1**). Since previous investigations of the $Al_{0.2}Ga_{0.8}As$ detector and the GaAs reference detector have shown charge trapping to be negligible (see **Section 3.5.2**) (Lioliou & Barnett, 2016), i.e. a unity charge collection efficiency (CCE = 1) can be assumed for both devices, the ratio of the average numbers of charge carriers, N_{EHP}, created by the absorption of a photon of energy, *E*, in conjunction with the known electron-hole pair creation energy of GaAs (ω_{EHP} = 4.18 eV ± 0.03 eV (Bertuccio & Maiocchi, 2002)), can be used to determine the unknown electron-hole pair creation energy of $Al_{0.2}Ga_{0.8}As$.

The above derivation can be understood through the rearrangement of Eq. 2.9 (see **Section 2.4.1**), and defining ω_{GaAs} and ω_{AlGaAs} as the electron-hole pair creation energies of GaAs and $Al_{0.2}Ga_{0.8}As$ respectively, and N_{GaAs} and N_{AlGaAs} as the average number of charge carriers created by the absorption of a photon of energy, *E*, for GaAs and $Al_{0.2}Ga_{0.8}As$, respectively, such that

$$E = N_{GaAs}\omega_{GaAs} = N_{AlGaAs}\omega_{AlGaAs}. \quad (3.11)$$

The spectra obtained with the $Al_{0.2}Ga_{0.8}As$ and GaAs photodetectors were fitted with the Mn Kα (5.9 keV) and Mn Kβ (6.49 keV) peaks in the accepted ratio (Schötzig, 2000), taking into account the detectors' relative detection efficiencies for the Mn Kα and Mn Kβ emissions, as shown in Fig. 3.24. With the $Al_{0.2}Ga_{0.8}As$ detector biased at 10 V, 15 V, and 20 V, the electron-hole pair creation energy of $Al_{0.2}Ga_{0.8}As$ was found to be 4.48 eV ± 0.09 eV, 4.42 eV ± 0.09 eV, and 4.40 eV ± 0.09 eV, respectively. All determined values were within the estimated uncertainties of each other. The mean of these measurements was 4.43 eV ± 0.09 eV (rms deviance), which agreed with the value predicted at room temperature (4.4 eV) when assuming a linear variation of electron-hole pair creation energy with Al fraction between GaAs (Bertuccio & Maiocchi, 2002) and $Al_{0.8}Ga_{0.2}As$ (Barnett et al., 2012b).

Since the electron-hole pair creation energy of $Al_{0.2}Ga_{0.8}As$ did not significantly reduce with increasing reverse bias of the $Al_{0.2}Ga_{0.8}As$ device, the assumption that the determined value was not significantly influenced by charge trapping within the i layer appears valid. Had charge losses been significant at low reverse biases, it would have been expected that at higher reverse biases a significantly reduced value of ω_{EHP} for $Al_{0.2}Ga_{0.8}As$ would have resulted. However, because complete charge collection within the i layer cannot be absolutely guaranteed, the value of 4.43 eV ± 0.09 eV should still be taken as an upper limit, which may decrease in future as higher quality material is grown (Barnett et al., 2013a).

3.8.2 Temperature dependence

The $Al_{0.2}Ga_{0.8}As$ electron-hole pair creation energy was then studied across the temperature range 20 °C to -20 °C. The GaAs reference detector was removed from the experimental setup; thus the $Al_{0.2}Ga_{0.8}As$ p^+-i-n^+ photodiode, D1, was individually connected to a custom-made low-noise charge-sensitive preamplifier. The ^{55}Fe radioisotope X-ray source was positioned 3 mm above the $Al_{0.2}Ga_{0.8}As$ diode, and the detector and preamplifier were installed inside the TAS Micro MT climatic cabinet as per **Section 3.7.1**. A stabilised pulse generator (Berkeley Nucleonics Corporation model BH-1) was connected to the test signal input of the custom preamplifier, such that the change in conversion factor of the preamplifier as a result of change in temperature could be measured, and its effects taken into account in the subsequent analysis (Barnett et al., 2013a). The preamplifier was connected to the same shaping amplifier and MCA used in **Section 3.8.1**. Spectra were accumulated at each temperature, decreasing from 20 °C to -20 °C, in steps of 20 °C. The photodiode was reverse biased to 0 V, 10 V, 20 V, and 30 V at each temperature, with a live time limit of 1,000 s and a shaping time of 0.5 μs (the optimal shaping time for this set up) set for

each spectrum. For each spectrum, the photopeak was fitted with Gaussians corresponding to the Mn Kα and Kβ peaks and the peak from the pulse generator. The positions of the peak centroids, with respect to the zero noise peak, were calculated. The relative change in position of the Mn Kα peak on the MCA's charge scale, taking into account the preamplifier's change in conversion factor with temperature (determined from the pulser peak) and the change in test capacitance as a function of temperature, enabled the determination of the change in ω_{EHP} of $Al_{0.2}Ga_{0.8}As$ with temperature (Barnett et al., 2013a). Knowing ω_{EHP} of $Al_{0.2}Ga_{0.8}As$ at 20 °C (4.43 eV ± 0.09 eV) enabled the calculation of the absolute value of ω_{EHP} for $Al_{0.2}Ga_{0.8}As$ at the other temperatures. Fig. 3.25 presents the electron-hole pair creation energy as a function of temperature for $Al_{0.2}Ga_{0.8}As$.

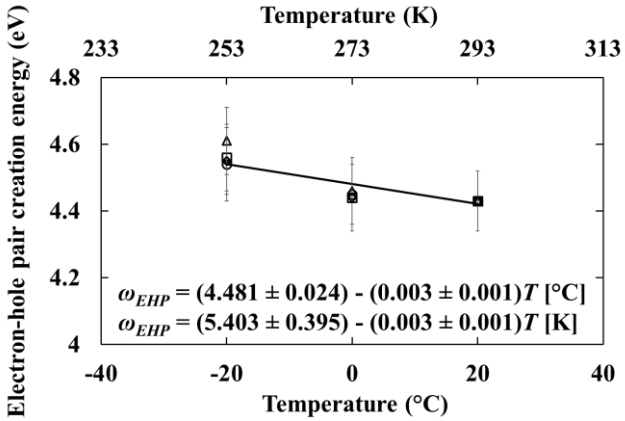

Fig. 3.25. The average energy required to produce an electron-hole pair in $Al_{0.2}Ga_{0.8}As$ at an applied reverse bias of 0 V (circles), 10 V (triangles), 20 V (squares), and 30 V (diamonds) as a function of temperature, with the line of best fit plotted.

For each applied reverse bias investigated, the average energy required to produce an electron-hole pair decreased with increasing temperature. Variations in the calculated electron-hole pair creation energy as a function of reverse bias at each temperature fell within the uncertainty of the measurement. A linear relationship between the electron-hole pair creation energy and temperature can be seen in Fig. 3.25, and has been evaluated using linear least squares fitting such that: $\omega_{EHP} = aT + b$, where a = (-0.003 ± 0.001) eV K^{-1}, and b = (5.403 ± 0.395) eV. The calculated gradient defining the relationship between the electron-hole pair creation energy and temperature in $Al_{0.2}Ga_{0.8}As$, was found to be shallower than for $Al_{0.8}Ga_{0.8}As$ (-0.0077 eV K^{-1} (Barnett et al., 2013a)), and steeper than for GaAs (-0.00122 eV K^{-1} (Bertuccio & Maiocchi, 2002)).

The relationship between the electron-hole pair creation energy and the physical parameters of semiconductor materials has been subject to study using a variety of incident radiation types

(Pehl et al., 1968). According to Shockley (1961), and later revised by Klein (1968), the relationship between the electron-hole pair creation energy and the bandgap energy of a given semiconductor can be expressed as

$$\omega_{EHP} = \left(\frac{9}{5}\right) E_g + E_g + r(\hbar\omega_r), \tag{3.12}$$

where r is the average number of optical phonons emitted between impact ionisations, $\hbar$ (units of m^2 kg s^{-1}) is the reduced Planck's constant, and ω_r (units of s^{-1}) is the frequency of an optical photon (Klein, 1968). The (9/5) E_g term is the residual kinetic energy, and $r(\hbar\omega_r)$ accounts for the optical phonon losses which, according to Klein, lies within the range 0.5 eV $\leq$ $r(\hbar\omega_r)$ $\leq$ 1.0 eV (Klein, 1968).

The Klein model was derived on the premise that the average energy consumed in the generation of an electron-hole pair (the electron-hole pair creation energy) is accounted for by the sum of three contributions: the intrinsic bandgap energy; optical phonon losses; and the residual kinetic energy (Klein, 1968). At the time, experimentally measured electron-hole pair creation energies of a variety of materials appeared to corroborate these assumptions (Klein, 1968), however, it should be noted that such measurements were made using different radiation types and at different energies, which were later found to induce variation in electron-hole pair creation energy measurements.

Experimentally measured electron-hole pair creation energies of many materials, and their associated bandgap energies, have since been presented by Owens & Peacock (2004) and subsequently, by Owens (2012). A traditional "main" Klein function branch (ω_{EHP} = (14/5)E_g + 0.6) was identified in the data set, along with a number of materials including diamond, AlN, 4H-SiC, PbI_2, and HgI_2, which were displaced from the main branch and lay on an apparent secondary Klein function branch, where $r(\hbar\omega_r)$ = -1.5 eV, which was identified as unphysical within the Klein model (Owens & Peacock, 2004). Additionally, for the data compiled by Owens & Peacock (2004), it is difficult to determine the temperatures at which the measurements of bandgap and electron-hole pair creation energy included in the Klein plots were made (Owens & Peacock, 2004). Since the electron-hole pair creation energy is a temperature dependent parameter, knowledge of the temperature at which the measurements were made is critical to interpretation of the data. Likewise, the material qualities of many of the semiconductors used to make the measurements which were collated and summarised by Owens & Peacock (2004) are also questionable in most cases.

Considering only the well characterised materials Ge, Si, and GaAs, at room temperature, Bertuccio & Maiocchi (2002) reported a linear relationship between bandgap and electron-hole pair creation energy which differed from the "main" and "secondary" Klein branches. Barnett et al. (2012b) and Barnett et al. (2013a) subsequently extended this dataset with measurements for $Al_{0.8}Ga_{0.2}As$, refining the Bertuccio & Maiocchi linear fit, and additionally demonstrating that $Al_{0.8}Ga_{0.2}As$ fitted neither the main nor secondary Klein branch.

The electron-hole pair creation energy measurements reported here show that $Al_{0.2}Ga_{0.8}As$ is another material that does not fit either of the Klein branches. If $Al_{0.2}Ga_{0.8}As$ were to lie on the main Klein function branch, a value of ω_{EHP} = 5.28 eV at room temperature would have been expected. If $Al_{0.2}Ga_{0.8}As$ were situated on the secondary Klein function branch, a value of ω_{EHP} = 3.18 eV at room temperature would have been expected. The measured value (ω_{EHP} = 4.43 eV ± 0.09 eV for $Al_{0.2}Ga_{0.8}As$ at room temperature) was between those predicted by the Klein functions. However, ω_{EHP} = 4.43 eV ± 0.09 eV is in remarkable agreement with the Bertuccio-Maiocchi-Barnett (BMB) relationship, which predicted ω_{EHP} = 4.47 eV ± 0.29 eV for $Al_{0.2}Ga_{0.8}As$. Refining the BMB relationship with the new experimental data for $Al_{0.2}Ga_{0.8}As$ yields a linear least squares fit, where at room temperature $\omega_{EHP} = (1.58 \pm 0.09)\, E_g + (1.83 \pm 0.13)$, as shown in Fig. 3.26. This linear fit lies within the uncertainties calculated by Barnett et al. (2013a).

Since this work was performed, electron-hole pair creation energy measurements for $Al_{0.52}In_{0.48}P$ (Butera et al., 2018a) and $In_{0.5}Ga_{0.5}P$ (Butera et al., 2018b) have been reported. These results are subsequently discussed and considered in **Chapter 6**, along with electron-hole pair creation energy measurements for $Al_{0.6}Ga_{0.4}As$.

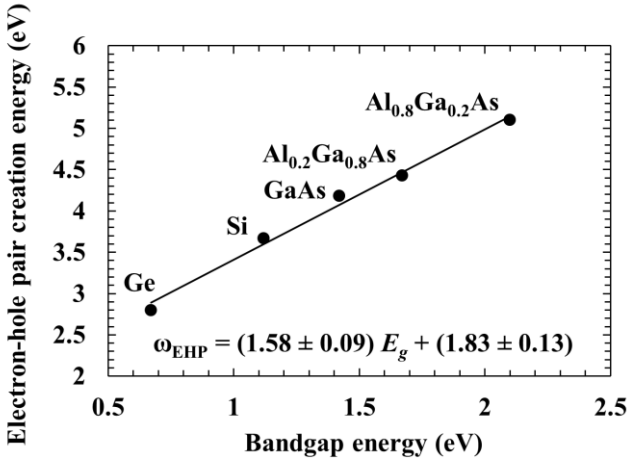

Fig. 3.26. Electron-hole pair creation energies for Ge, Si, GaAs, $Al_{0.2}Ga_{0.8}As$, and $Al_{0.8}Ga_{0.2}As$ plotted as a function of their respective bandgap energies at room temperature.

3.9 Conclusion

For the first time, $Al_{0.2}Ga_{0.8}As$ p^+-i-n^+ mesa X-ray photodiodes (200 µm diameter, 3 µm i layer) have been shown to operate as photon counting spectroscopic X-ray detectors in non-avalanche mode at room temperature, and as a function of temperature (20 °C to -20 °C), with promising spectral resolutions (FWHM at 5.9 keV) reported. Initial room temperature spectral measurements reported energy resolutions of 1.24 keV ± 0.04 keV FWHM at 5.9 keV for the devices studied (see **Section 3.5.1**). Although such energy resolutions were already impressive, and comparable to recent reports using $Al_{0.8}Ga_{0.2}As$ (1.27 keV ± 0.04 keV FWHM at 5.9 keV (Barnett et al., 2015)), subsequent noise analysis results showed that the systems performance was primarily limited by the performance of the preamplifier electronics rather than the material's inherent properties (see **Section 3.5.2**). This suggested that improvements to the front-end electronics alone could significantly improve the spectral energy resolution of the system.

Subsequent spectral measurements as a function of temperature (see **Section 3.7.1**) reported a spectral resolution of 1.06 keV ± 0.04 keV FWHM at 5.9 keV at 20 °C, whilst also reporting spectral resolutions of 856 eV ± 30 eV FWHM at 5.9 keV and 827 eV ± 30 eV FWHM at 5.9 keV at 0 °C and -20 °C respectively. The improved energy resolution relative to the preceding room temperature measurements was attributed to a reduced unknown dielectric noise contribution through slight changes to the preamplifier (see **Section 3.7.2**). The performance was comparable to the best previously reported energy resolution for non-avalanche AlGaAs X-ray detectors (1.07 keV FWHM at 5.9 keV at room temperature (Barnett et al., 2010)).

It should be noted that the reported energy resolutions achieved with the $Al_{0.2}Ga_{0.8}As$ X-ray photodiodes were modest compared with those achieved using state-of-the-art Silicon Drift Detectors (SDDs) coupled to state-of-the-art ultra-low-noise CMOS readout electronics, even at room temperature (FWHM = 141 eV at 5.9 keV (Bertuccio et al., 2015)). Other wide band gap materials such as GaAs, SiC, and AlInP have also shown promising results for photon counting X-ray detection. GaAs detectors of thicker i layer (e.g. 10 µm (Lioliou et al., 2017) and 40 µm (Owens et al., 2001)) and better energy resolution (690 eV (Lioliou et al., 2017) and 266 eV (Owens et al., 2001)) have been demonstrated. SiC has been shown to possess excellent energy resolution at room temperature (196 eV FWHM at 5.9 keV (Bertuccio et al., 2011)), and despite its significantly lower linear attenuation coefficients (e.g. 348.2 cm^{-1} at 5.9 keV (Henke et al., 1993)) compared to those of AlGaAs (e.g. 787.8 cm^{-1} at 5.9 keV (Henke et al., 1993) for $Al_{0.2}Ga_{0.8}As$) and GaAs (e.g. 836.7 cm^{-1} at 5.9 keV (Henke et al., 1993)), SiC is still a highly competitive technology for soft X-ray spectroscopy, with the availability of thicker structures offsetting the lower linear attenuation coefficients. $Al_{0.52}In_{0.48}P$ (6 µm i layer) was recently characterised at room temperature, where an energy resolution of 890 eV FWHM at 5.9 keV was

reported (Zhao et al., 2019). The increasing research in X-ray detection employing ternary semiconducting structures will undoubtedly yield further materials suitable for replacing Si photon counting X-ray detectors, better equipped to handle intense radiation and high temperature conditions.

Despite competition from other materials, the results indicate that $Al_{0.2}Ga_{0.8}As$ is a potentially promising material for uncooled photon counting X-ray spectroscopy at room temperature and below. Should the detection efficiency (thickness) be increased, and the energy resolution improved, the development of $Al_{0.2}Ga_{0.8}As$ radiation detectors could prove suitable for soft X-ray detection aboard space science missions (e.g. in situ planetary analysis on the Martian and Lunar surface, or planetary remote sensing within the Jovian system), where temperature control systems, required for conventional Si radiation detectors, could be reduced or removed entirely, reducing the financial costs and technological complexity of future space science missions.

Refinements to the design of the preamplifier, reductions to the photodiode leakage current through improved material quality, and increases in intrinsic layer thicknesses, will all potentially enable improvement upon the currently achieved energy resolutions, facilitating further progress towards the expected Fano limited energy resolution of $Al_{0.2}Ga_{0.8}As$ (131 eV at 5.9 keV).

Parameter	Value
FWHM at 5.9 keV at 20 °C	1.06 keV ± 0.04 keV
FWHM at 5.9 keV at 0 °C	856 eV ± 30 eV
FWHM at 5.9 keV at -20 °C	827 eV ± 30 eV
ω_{EHP} at 20 °C	4.43 eV ± 0.09 eV
Detector leakage current density at full depletion (30 V, 100 kV cm^{-1}) at 20 °C	49.0 nA cm^{-2} ± 1.3 nA cm^{-2}
Detector capacitance density at full depletion (30 V, 100 kV cm^{-1}) at 20 °C	3.56 nF cm^{-2} ± 0.14 nF cm^{-2}
Intrinsic carrier concentration at 20 °C	$\approx 4 \times 10^{15}$ cm^{-3}

Table 3.3. Key results of **Chapter 3** $Al_{0.2}Ga_{0.8}As$ p^+-i-n^+ circular mesa X-ray photodiode (200 µm diameter, 3 µm i layer) measurements.

Chapter 4

3 µm i layer $Al_{0.2}Ga_{0.8}As$ Mesa p^+-i-n^+ multi pixel array

4.1 Introduction

In this chapter, work characterising the spectroscopic performance of a prototype 2 × 2 square pixel $Al_{0.2}Ga_{0.8}As$ p^+-i-n^+ mesa photodiode array (each photodiode area 200 µm by 200 µm), under illumination of soft X-rays and β^- particles, is reported. An energy resolution (FWHM at 5.9 keV) of 756 eV ± 30 eV (with 30 V reverse bias applied to the detector) was achieved at 20 °C. The results demonstrated, for the first time, that device yields are now sufficient such that small (2 × 2) $Al_{0.2}Ga_{0.8}As$ mesa pixel arrays can be produced at a quality suitable for radiation spectroscopy. The experimental methods and techniques used to characterise the devices are presented, along with the findings of the experimental work performed.

4.2 Background

As reported in this thesis (see **Chapter 3**), single pixel $Al_{0.2}Ga_{0.8}As$ p^+-i-n^+ photodiodes have been demonstrated as promising X-ray photon counting detectors with energy resolutions (1.06 keV ± 0.04 keV FWHM at 5.9 keV (see **Section 3.7.1**)) similar to those reported for single pixel $Al_{0.8}Ga_{0.2}As$ p^+-i-n^+ photodiodes (1.07 keV FWHM at 5.9 keV (Barnett et al., 2010)) at room temperature. Although single pixel detectors are useful for many applications (e.g. Solar X-ray monitoring), for applications that require spatial resolution (e.g. imaging), pixel arrays are more desirable. Prior to the results reported in this thesis, due to poor quality material and low device yields, there have been no reports of multi pixel $Al_xGa_{1-x}As$ detectors for X-ray photon counting spectroscopy. Therefore, the successful demonstration of a multi pixel $Al_xGa_{1-x}As$ X-ray detector, even if composed of only a few pixels, represents a significant milestone in material quality.

The reports in the literature demonstrating $Al_xGa_{1-x}As$ as a suitable material for β^- particle spectroscopy are also very few. Barnett et al. (2013b) successfully demonstrated β^- particle spectroscopy using an $Al_{0.8}Ga_{0.2}As$ p^+-i-n^+ photodiode. Current-mode (i.e. not spectroscopic photon-counting) measurements have been reported with a graded-gap $Al_xGa_{1-x}As$ detector exposed to high energy electron beams (Silenas et al., 2011). Prior to the results reported in this thesis, there have been no reports of β^- particle spectroscopy using a single pixel or multi pixel $Al_{0.2}Ga_{0.8}As$ device.

4.3 Device structure

An $Al_{0.2}Ga_{0.8}As$ p^+-i-n^+ structure was grown by MOVPE on a commercial 2 inch GaAs n^+ substrate. The layer details are summarised in Table 4.1. Square, 200 µm × 200 µm, mesa structures were formed using 1:1:1 H_3PO_4:H_2O_2:H_2O solution followed by 10 s in 1:8:80 H_2SO_4:H_2O_2:H_2O solution. An Ohmic contact consisting of 20 nm InGe and 200 nm Au was evaporated onto the rear of the substrate, and an Ohmic top contact of 20 nm Ti and 200 nm Au was evaporated onto the p^+ side of the mesa devices; the devices were unpassivated. Fig. 4.1 illustrates the geometry of the pixels. The p^+ metal contact is represented by the shaded area, it covers 50 % of each pixel's surface. The devices were packaged in a TO-5 can.

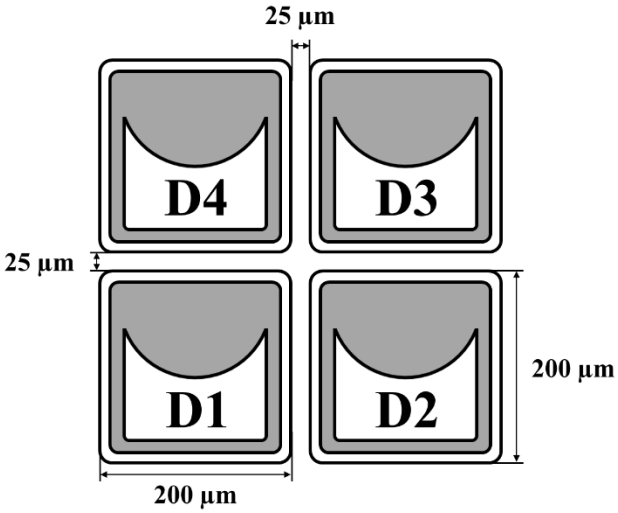

Fig. 4.1. Layout of the $Al_{0.2}Ga_{0.8}As$ p^+-i-n^+ mesa X-ray photodiode 2 × 2 array, where the shaded area is the top contact/bondpad.

Material	Dopant	Dopant type	Thickness (nm)	Doping density (cm^{-3})
GaAs	C	p	10	1×10^{19}
$Al_{0.2}Ga_{0.8}As$	C	p	500	2×10^{18}
$Al_{0.2}Ga_{0.8}As$			3000	Undoped
$Al_{0.2}Ga_{0.8}As$	Si	n	1000	2×10^{18}
GaAs n^+ substrate				

Table 4.1. Layer details of the $Al_{0.2}Ga_{0.8}As$ p^+-i-n^+ structure from which the devices were fabricated.

4.4 Temperature dependent electrical characterisation

4.4.1 Current measurements as a function of applied bias

Current as a function of applied forward and reverse bias across the temperature range 100 °C to -20 °C was measured using a Keithley 6487 Picoammeter/Voltage Source. Each diode was housed in a custom light-tight electromagnetically screened test harness and installed within a TAS Micro MT climatic cabinet for temperature control as per **Section 3.6.1**. The temperature was initially set to 100 °C and decreased in 10 °C increments to -20 °C. The diodes were left to stabilise for 30 minutes at each temperature before measuring to ensure thermal equilibrium. Fig. 4.2 presents the dark forward current, I_F, as a function of applied forward bias, V_F, for diode D1. At each bias, the dark current decreased as the temperature was decreased. Comparable results were obtained for D2, D3, and D4.

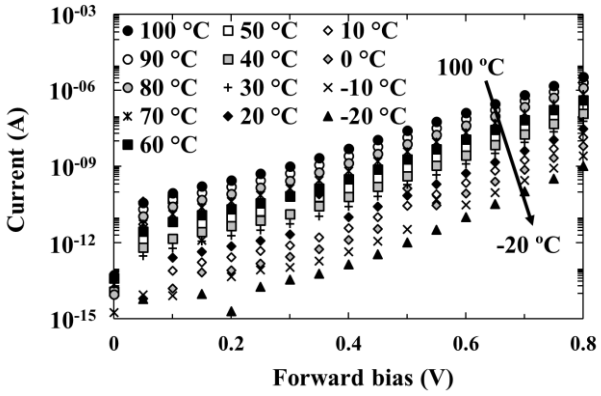

Fig. 4.2. Current as a function of applied forward bias in the temperature range 100 °C to -20 °C for pixel D1. Comparable results were obtained for pixels D2, D3, and D4. The associated uncertainties were omitted for clarity.

The saturation current, I_{sat}, and ideality factor, n, were calculated at each temperature as per **Section 3.6.1**. Ideal diode behaviour was not exhibited until approximately $V_F > 0.4$ V for each diode, at each temperature, where at lower applied forward bias, parallel resistances, or shunt resistance, was present. This shunt resistance may have been caused by defects, which can be in the form of diffusion paths along dislocations in the semiconductor (Luque & Hegedus, 2003), or leakage around the edge of the diode walls (Soga, 2006). As a result, a linear least squares fit was applied to the region $0.5 \leq V_F \leq 0.8$. The saturation current was found to decrease as a function of temperature, from 7.97 pA, 8.05 pA, 8.03 pA, and 7.93 pA (each ± 0.04 pA) at 100 °C, to 10.11 aA ± 0.04 aA, 94.12 aA ± 100.32 aA, 10.12 aA ± 0.06 aA, and 11.80 aA ± 6.96 aA at -20 °C, for D1, D2, D3, and D4 respectively. Fig. 4.3 presents the ideality factor as a function of temperature.

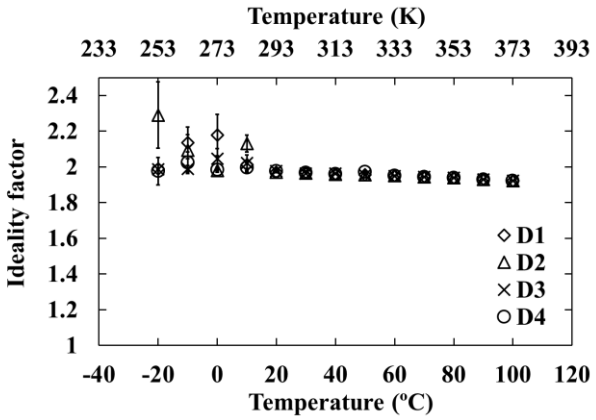

Fig. 4.3. Ideality factor as a function of temperature, extracted from the measured current as a function of applied forward bias ($0.5 \leq V_F \leq 0.8$) for pixels D1 (diamonds), D2 (triangles), D3 (crosses), and D4 (circles).

Across the temperature range 100 °C to 20 °C, the ideality factor was ≈ 2 for each diode. This suggested that recombination within the depletion region was the dominant limiting factor for current between 100 °C and 20 °C (Luque & Hegedus, 2003). Below 20 °C, the ideality factor of two diodes (D1 and D2) were calculated to be slightly > 2, which exceeds the expected value from the Sah-Noyce-Shockley model (Sah et al., 1957). The values > 2 in the present case are not thought to be significant but rather a consequence of noise affecting the current measurements at low temperatures and biases. The calculated ideality factors indicated that recombination current defined the forward current, and such a small temperature dependence excluded tunnelling from significant contribution to the forward current (Lioliou et al., 2016b).

The measured leakage current, I_d, as a function of applied reverse bias for D1 is shown in Fig. 4.4. The leakage current for each pixel decreased as a function of decreasing temperature. At the maximum applied reverse bias (35 V), the leakage current was measured to be 712.00 pA ± 2.54 pA, 596.19 pA ± 2.19 pA, 591.87 pA ± 2.18 pA, and 671.61 pA ± 2.41 pA at 100 °C; 0.31 pA, 0.37 pA, 0.36 pA, and 0.33 pA (each ± 0.40 pA) at -20 °C, for D1, D2, D3, and D4 respectively. Fig. 4.5 presents the leakage current density at an applied reverse bias of 30 V (E_f = 100 kV cm^{-1}) as a function of temperature for D1, with comparable results obtained for D2, D3, and D4. The leakage current density, J_d, increased exponentially with increasing temperature (-20 °C to 100 °C). The leakage current densities of each pixel at room temperature were smaller than recently characterised circular $Al_{0.2}Ga_{0.8}As$ (200 µm diameter, 3 µm i layer) devices, where leakage current densities of 40.0 nA cm^{-2} ± 1.4 nA cm^{-2} have been reported at an electric field strength of 100 kV cm^{-1} (see **Section 3.6.1**). At the same field strength (equivalent to an applied reverse bias of 30 V for the present devices), and at room temperature, the presently reported $Al_{0.2}Ga_{0.8}As$ 2 × 2 array had a mean pixel leakage current density of 9.0 nA cm^{-2} ± 1.0 nA cm^{-2}

(rms deviance). The best leakage current density reported for AlGaAs X-ray photodiodes at room temperature and at an average internal electric field of 100 kV cm^{-1} is 2.2 nA cm^{-2} (Barnett et al., 2013b); for comparison, the leakage current density for high quality 4H-SiC Schottky devices can be $\approx$ 1 pA cm^{-2} (Bertuccio et al., 2011).

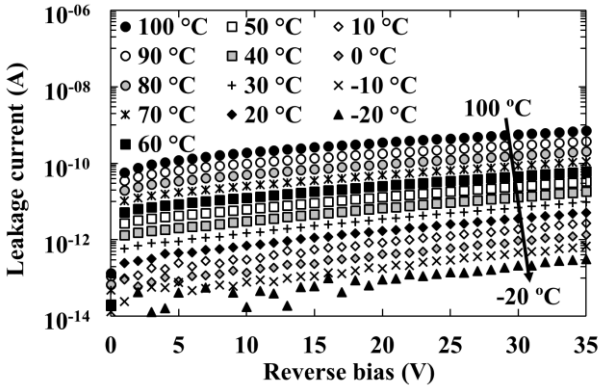

Fig. 4.4. Leakage current as a function of applied reverse bias in the temperature range 100 °C to -20 °C for D1. Comparable results were obtained for D2, D3, and D4. The associated uncertainties were omitted for clarity.

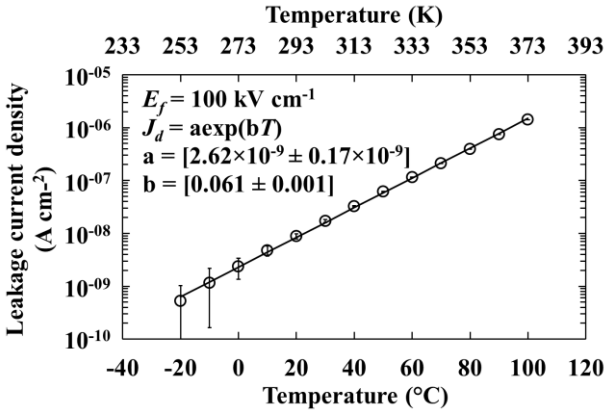

Fig. 4.5. Measured leakage current density, J_d, at a 100 kV cm^{-1} average internal electric field, E_f, as a function of temperature for D1. A linear least squared fit has been applied, with the line of best fit plotted of the form $J_d = aT + c$, where a has the units of A cm^{-2}, and b units of ^{o}C^{-1}.

Leakage current stability with time was measured for each diode as a function of temperature in order to identify the maximum temperature suitable for the X-ray photon counting measurements (see **Section 4.5**). Each pixel was reverse biased at 30 V and its leakage current was measured every 30 seconds for 1020 seconds. The applied reverse bias was then reduced to 0 V for a 1 minute resting period, and the process repeated 5 times; the results for D1 can be seen in Fig. 4.6. The devices were found to be stable at temperatures $\leq$ 30 °C, but at hotter temperatures,

the devices became increasingly unstable with repeated applied reverse bias measurements, as shown in Fig. 4.6.

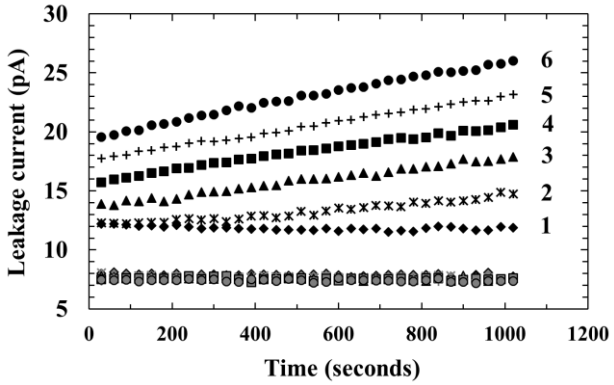

Fig. 4.6. Leakage current as a function of time for D1 at an applied reverse bias of 30 V and a temperature of 40 °C (black shapes) and 30 °C (grey shapes). Comparable results were obtained for D2, D3, and D4. The measurements made at 40 °C are numbered in accordance with each repetition of the measurement. The associated uncertainties were omitted for clarity.

4.4.2 Capacitance measurements as a function of applied bias

Capacitance as a function of applied forward and reverse bias was measured for each $Al_{0.2}Ga_{0.8}As$ p^+-i-n^+ pixel (D1, D2, D3, and D4) across the temperature range 100 °C to -20 °C, using an HP 4275A LCR Meter (signal magnitude 50 mV rms; frequency 1 MHz) and a Keithley 6487 picoammeter/voltage source to bias the detectors. The light-tight dark electromagnetically screened test harness, in which the $Al_{0.2}Ga_{0.8}As$ detectors were installed, was placed inside a TAS Micro MT climatic cabinet for temperature control as per **Section 3.6.1**. National Instruments LabVIEW software was used to automate the characterisation routine. The temperature was initially set to 100 °C, and then decreased in 10 °C steps to -20 °C, with measurements made at each step. The diodes were left for 30 minutes after reaching each temperature before measuring in order to ensure thermal equilibrium and stabilisation. Since the devices were measured after packaging, the capacitance of the package was estimated and removed by measuring the capacitance of an empty connection from an identical package across the same applied bias range and at each temperature. The packaging capacitance values were then deducted from the respective packaged device capacitances obtained for the detectors. Temperatures greater than 100 °C were not measured due to the high leakage currents (> 1 nA at 15 V at 120 °C) observed at such temperatures. Fig. 4.7 presents the capacitance of photodiode, D1, with the packaging

capacitance subtracted, as a function of applied forward bias; comparable results were found for D2, D3, and D4.

As the temperature was decreased from 100 °C to -20 °C, the forward capacitance decreased at each applied forward bias. At 100 °C and at an applied forward bias of 0.8 V, capacitances of 10.45 pF, 10.60 pF, 10.62 pF, 10.41 pF (each ± 0.05 pF) were measured for D1, D2, D3, and D4 respectively. At -20 °C and at the same applied forward bias, capacitances of 9.29 pF, 9.40 pF, 9.43 pF, 9.26 pF (each ± 0.05 pF) were measured. The diffusion capacitance, a consequence of the change in minority carrier density, significantly contributed to the diode forward capacitance. Since the diffusion capacitance is directly proportional to the forward current (Sze, 2006), the observed dependency of the forward capacitance with temperature (Fig. 4.7) was attributed to the same temperature dependence of the forward current.

The capacitance for D1 as a function of applied reverse bias in the temperature range 100 °C to -20 °C can be seen in Fig. 4.8. Comparable results were found for D2, D3, and D4. At low applied reverse biases, the measured capacitances decreased as the temperature decreased: without application of reverse bias (i.e. at 0 V applied bias) and at 100 °C, capacitances of 6.77 pF, 6.85 pF, 6.88 pF, and 6.73 pF (each ± 0.04 pF) were measured for D1, D2, D3, and D4, respectively; at -20 °C, capacitances of 6.19 pF, 6.26 pF , 6.29 pF, and 6.14 pF (each ± 0.04 pF) were measured. As the applied reverse bias was increased in magnitude, the temperature dependence of the capacitance reduced at that applied reverse bias; at applied reverse biases ≥ 7 V, any variation in capacitance as a function of temperature became indiscernible i.e. the change in capacitance remained within the uncertainty of the measurement, as shown by Fig. 4.8.

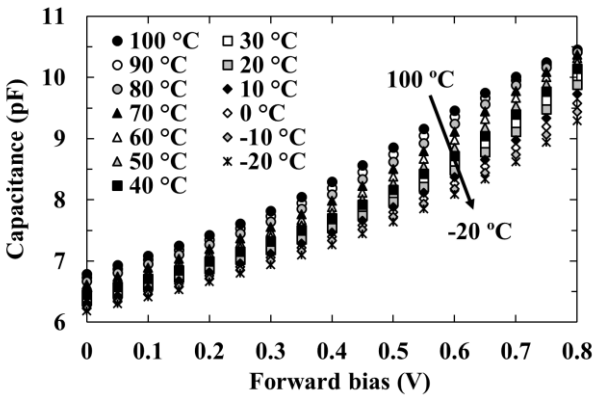

Fig. 4.7. Capacitance as a function of applied forward bias for pixel D1 in the temperature range 100 °C to -20 °C. Comparable results were obtained for pixels D2, D3, and D4. The associated uncertainties were omitted for clarity.

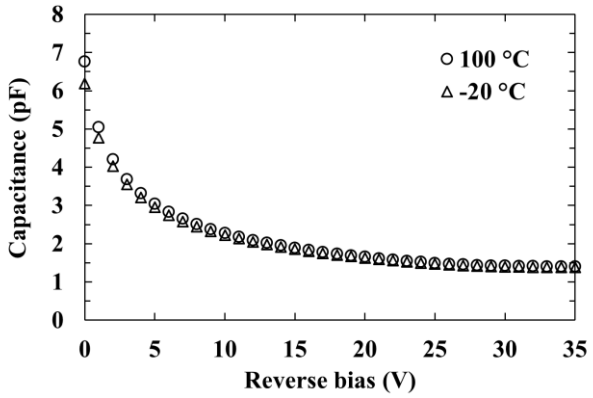

Fig. 4.8. Capacitance as a function of reverse bias for pixel D1, at 100 °C (circles) and -20 °C (triangles). Comparable results were obtained for pixels D2, D3, and D4. The associated uncertainties were smaller than the symbols.

The depletion width, W_D, as a function of applied reverse bias was calculated as per **Section 3.4.2**. The Debye length of $Al_{0.2}Ga_{0.8}As$ (0.07 μm) was calculated as per Stradling & Klipstein (1991) and was taken into account when calculating the depletion width uncertainty. The depletion width of each diode increased as a function of applied reverse bias at all temperatures until a reverse bias of 26 V, at which the i layer of each pixel was fully depleted. At high reverse biases (≥ 26 V), the depletion width of each pixel was found to be temperature independent; any apparent variation in calculated depletion width as a function of temperature lay within the measurement uncertainty. For D1, at the hottest investigated temperature (100 °C), the depletion width was 0.65 μm ± 0.07 μm at 0 V, and 3.11 μm ± 0.10 μm at 35 V. Comparable results were obtained for the other pixels. The calculated depletion width as a function of applied reverse bias at -20 °C and 100 °C for pixel D1, and the quantum detection efficiency implied by this width assuming that the active region of the photodiodes was solely confined to the depletion region, and that only the depleted part of the i layer was active, can be seen in Fig. 4.9. The quantum detection efficiency of the $Al_{0.2}Ga_{0.8}As$ X-ray p-i-n mesa pixels at an applied reverse bias of 30 V was 0.21 at 5.9 keV and 0.17 at 6.49 keV in areas not covered by the top contact, and 0.17 at 5.9 keV and 0.14 at 6.49 keV in areas covered by the top contact. It should be noted that this is a conservative assumption since it is likely that at least some of the charge carriers created in the non-depleted part of the i layer also contributed to the collected charge at lower reverse biases. Furthermore, previous investigations have shown that electrons from electron-hole pairs created in the p region and within 0.16 μm of the p-i interface in $Al_{0.8}Ga_{0.2}As$ X-ray photodiodes, also contribute to the detected signals (Barnett et al., 2011a).

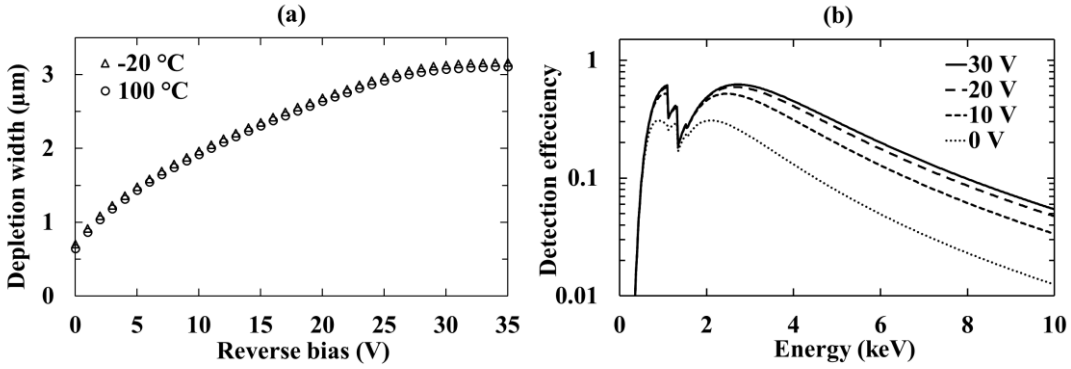

Fig. 4.9. (a) Calculated depletion width as a function of reverse bias for D1, at -20 °C (triangles) and 100 °C (circles). Comparable results were obtained for D2, D3, and D4. The associated uncertainties were omitted for clarity. (b) Calculated detection efficiency as a function of energy for the $Al_{0.2}Ga_{0.8}As$ X-ray p-i-n mesa pixels when operated at: 30 V (solid line); 20 V (long dashed line); 10 V (short dashed line); and 0 V (dotted line) reverse bias, respectively, assuming that the active region of the photodiodes in each case was confined solely to the depletion region and that only the depleted part of the i layer was active. It should be noted that this is a conservative assumption, since it is likely that charge carriers created in the non-depleted part of the i layer also contribute to the collected charge. The p^+ layer was considered to be inactive and the top contact was excluded from the *QE* calculations. The discontinuities are the Al K, Ga L, and As L X-ray absorption edges (see **Section 2.2.2.1**).

The carrier concentration of the i layer, N_{eff}, was calculated using the equation for general nonuniform distributions (see **Section 3.4.2**). The carrier concentration throughout the intrinsic region was calculated to be 4×10^{15} cm^{-3} for each pixel. At the i-n^+ interface, the carrier concentration increased to 2×10^{18} cm^{-3} for each pixel. The carrier concentration as a function of distance below the p^+-i junction for D1 has been plotted in Fig. 4.10. Although there appears to be some carrier concentration variation with temperature, this was within the calculated uncertainty of the measurements.

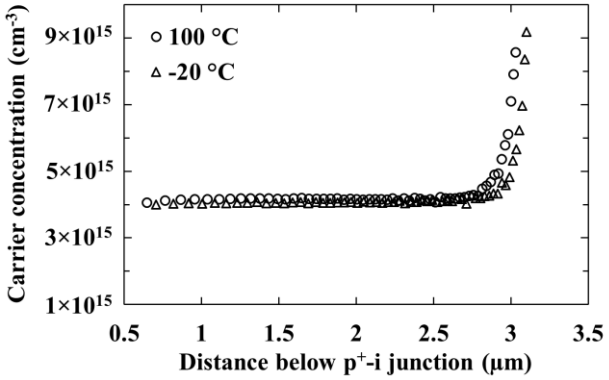

Fig. 4.10. Doping profile for D1, at 100 °C (circles) and -20 °C (triangles). Comparable results were obtained for D2, D3, and D4. The variation of the carrier concentration between 100 °C and -20 °C fell within the calculated uncertainty of the measurements. The associated uncertainties were omitted for clarity.

4.5 Temperature dependent X-ray spectroscopy

4.5.1 Measurements with an ^{55}Fe radioisotope X-ray source

^{55}Fe X-ray spectra were obtained using the X-ray spectrometer S1 (employing detector D1), S2 (employing detector D2), S3 (employing detector D3), and S4 (employing detector D4), to characterise the X-ray detection performance as a function of temperature for the $Al_{0.2}Ga_{0.8}As$ 2 × 2 array. Each diode was connected, in turn, to the same custom-made low-noise charge-sensitive preamplifier of feedback-resistorless design (see **Section 2.7**). The preamplifier used a Vishay 2N4416A Si JFET as the input transistor. In each case, the preamplifier was connected to an Ortec 571A shaping amplifier and an Ortec 927 ASPEC multi-channel analyser (MCA). An ^{55}Fe radioisotope X-ray source (≈ 176 MBq) emitting characteristic Mn Kα (5.9 keV) and Mn Kβ (6.49 keV) X-rays was placed 5 mm above the $Al_{0.2}Ga_{0.8}As$ array. S1, S2, S3, and S4 were installed inside a TAS Micro MT climatic cabinet throughout the measurements for temperature control as per **Section 3.7.1** and characterised in turn.

The temperature was initially set to 30 °C. It was then decreased to a minimum temperature of -20 °C, in steps of 10 °C. The spectrometer was allowed to stabilise for 30 minutes upon reaching each desired temperature in order to ensure thermal equilibrium. A maximum temperature of 30 °C was set due to the diodes' leakage current instability at higher temperatures (see Fig. 4.6). Spectra were accumulated with S1, S2, S3, and S4 at each temperature, and at each shaping time, τ (0.5 µs, 1 µs, 2 µs, 3 µs, 6 µs, and 10 µs), with each detector reverse biased (V_R) at 0 V, 10 V, 20 V, and 30 V. The live time limit for each spectrum was 200 s. Gaussian fitting was applied to the detected photopeak from the ^{55}Fe radioisotope X-ray source (Mn Kα = 5.9 keV;

Mn Kβ = 6.49 keV), taking into account the relative emission ratio (Schötzig, 2000) and the relative efficiency of the detector at these energies. The spectra were energy calibrated using the positions of the so called zero energy noise peak and the fitted Mn Kα (5.9 keV) peak, with the assumption of a linear variation of detected and output charge with energy. The impact ionisation coefficients of $Al_{0.2}Ga_{0.8}As$ as a function of average internal electric field were calculated and indicated that the diodes were operating within the non-avalanche regime (Zheng et al., 2000). The FWHM at 5.9 keV was measured for all obtained spectra and the associated uncertainty of the fitting calculated; Fig. 4.11 presents obtained spectra at the maximum (30 °C) and minimum (-20 °C) investigated temperatures for the X-ray spectrometer, S1, at the maximum investigated applied reverse bias (30 V) of the detector, D1.

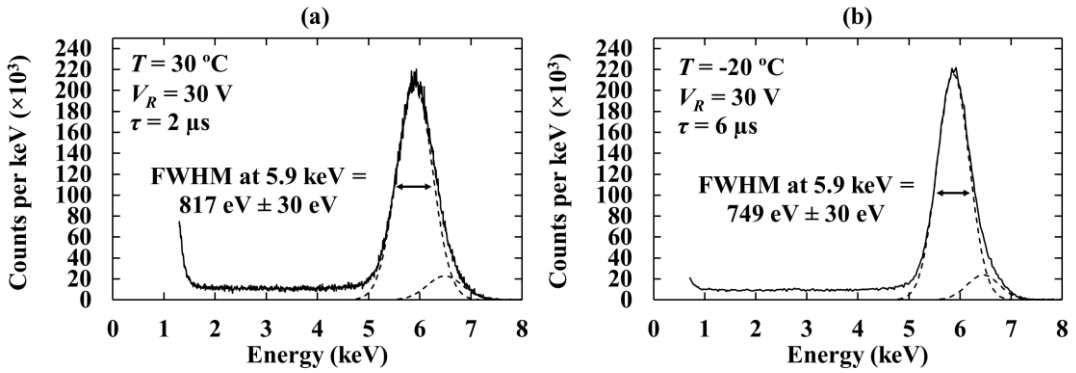

Fig. 4.11. ^{55}Fe X-ray spectra accumulated with the $Al_{0.2}Ga_{0.8}As$ p^+-i-n^+ mesa photodiode, D1, based X-ray spectrometer, S1, at 30 °C (a) (30 V applied reverse bias and 2 µs shaping time) and -20 °C (b) (30 V applied reverse bias and 6 µs shaping time). The fitted Mn Kα (5.9 keV) and Mn Kβ (6.49 keV) peaks have been plotted (dashed lines). The accumulated spectra have been normalised into counts per 1 keV in order to account for the differing channel widths.

The low energy tailing seen in Fig. 4.11 was attributed to partial charge collection of charge created in the non-active layers of the detector (Kalinka, 1994). The amount of low energy tailing can be quantified by the valley-to-peak ratio, R_{VtoP}, which was calculated for each X-ray spectrometer across the investigated temperature range (30 °C to -20 °C), using the ratio between the number of counts at 3.5 keV and 5.9 keV. R_{VtoP} was found to improve (i.e. decrease) as a function of applied reverse bias of the detector for each spectrometer investigated. For the spectrometer S1 (detector D1), at the maximum temperature investigated (30 °C), R_{VtoP} was calculated to be 0.15 ± 0.02 with no reverse bias (0 V) applied to the detector, and 0.05 ± 0.01 with 30 V applied reverse bias, at a shaping time of 2 µs. Comparable results were obtained for the spectrometers S2, S3, and S4. The valley-to-peak ratio reported here, was better than that previously reported for AlGaAs devices (0.08 at room temperature (see **Section 3.5.1**)), but not as good when compared to recently reported GaAs 10 µm i layer devices (0.03 at -20 ºC

(Lioliou et al., 2017)). R_{VtoP} for each detector bias did not change as a function of temperature within the measured uncertainty, this was likely due to the small temperature range investigated (30 °C to -20 °C).

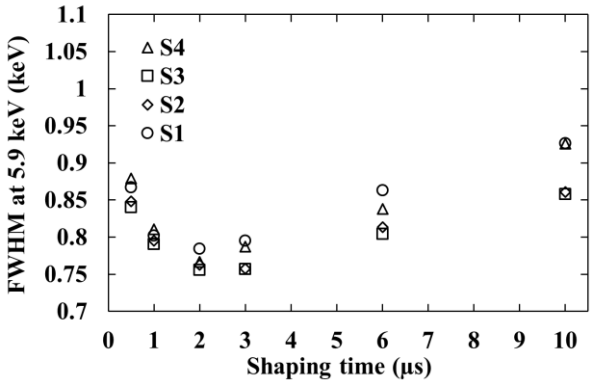

Fig. 4.12. Measured FWHM at 5.9 keV as a function of shaping time for the $Al_{0.2}Ga_{0.8}As$ based spectrometers S1 (circles), S2 (diamonds), S3 (squares), and S4 (triangles), at room temperature (20 °C) at an applied reverse bias of 30 V. The associated uncertainties were omitted for clarity.

Fig. 4.12 presents the measured FWHM at 5.9 keV as a function of shaping time for each spectrometer at 20 °C. The measured energy resolution (FWHM at 5.9 keV) was better than previously reported $Al_{0.2}Ga_{0.8}As$ X-ray photodiodes at room temperature. The best previously reported energy resolution for non-avalanche $Al_{0.2}Ga_{0.8}As$ X-ray detectors (200 µm diameter; 3 µm i layer) was 1.06 keV ± 0.04 keV FWHM at 5.9 keV at room temperature at an average internal electric field strength of 33 kV cm^{-1} (see **Section 3.7.1**). Using the presently reported devices, a FWHM at 5.9 keV = 863 eV ± 30 eV was measured under the same conditions with the best performing spectrometer, S2. Additionally, an improved energy resolution (FWHM at 5.9 keV) was measured across the entire temperature range. The best energy resolution (FWHM at 5.9 keV) achieved in **Section 3.7.1** at 0 °C was 856 eV ± 30 eV and the best at -20 °C was 827 eV ± 30 eV, at an average electric field strength of 100 kV cm^{-1}. Under the same conditions, the best energy resolution measured with the present detectors was 716 eV ± 30 eV (741 eV, 732 eV, and 766 eV for S1, S3, and S4 respectively, each ± 30 eV) at 0 °C and 722 eV ± 30 eV (749 eV, 743 eV, and 762 eV for S1, S3, and S4 respectively, each ± 30 eV) at -20 °C, for the best performing spectrometer reported here, S2. As the epitaxial wafer material of the $Al_{0.2}Ga_{0.8}As$ array used in the present work was the same as that used for the single pixels in **Chapter 3**, the improved energy resolution now reported is thus attributable to subtle improvements in device fabrication and processing techniques, as well as in the front-end of the preamplifier (which may have resulted from the detectors that were connected). Fig. 4.13 presents the measured FWHM at 5.9 keV at the optimum shaping time as a function of temperature for the

spectrometer, S1, with the photodiode, D1, operated at a reverse bias of 30 V (100 kV cm^{-1}) at the best shaping time investigated. The energy resolutions (FWHM at 5.9 keV) achieved at a fixed shaping time of 2 μs across the reverse bias range investigated are presented in Fig. 4.14 at both 30 °C and -20 °C. Comparable results were obtained for the spectrometers S2, S3, and S4.

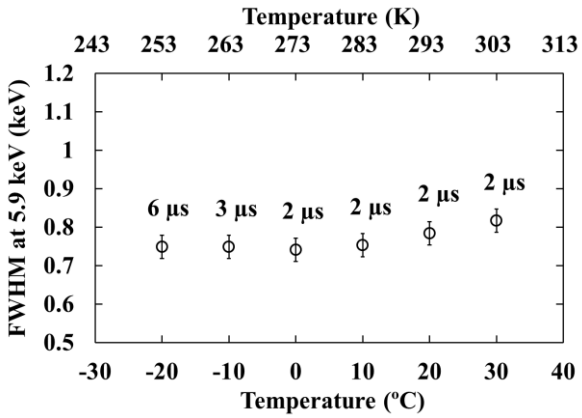

Fig. 4.13. Measured FWHM at 5.9 keV as a function of temperature for the spectrometer S1. ^{55}Fe X-ray spectra were accumulated with the detector D1 at an applied reverse bias of 30 V, with the optimal shaping time at each temperature plotted.

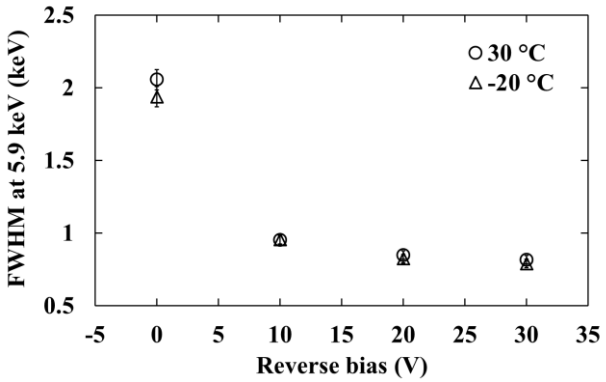

Fig. 4.14. Measured FWHM at 5.9 keV for S1 as a function of applied reverse bias for the detector, D1, at 30 °C (circles) and -20 °C (triangles) at a shaping time of 2 μs. Comparable results were obtained for S2, S3, and S4.

4.5.2 Noise analysis

The energy resolution of a non-avalanche semiconductor detector coupled to a charge sensitive preamplifier is influenced by three sources of noise (see **Section 2.8**). The fundamental Fano-limited energy resolution (FWHM) at 5.9 keV was calculated to be 132 eV for $Al_{0.2}Ga_{0.8}As$ at room temperature, assuming a Fano factor of 0.12 and an electron hole pair creation energy of 4.43 eV (see **Section 3.8**). Since the measured energy resolution of the spectrometer was greater

than the calculated fundamental Fano-limited energy resolution, there were clearly significant noise contributions beyond the statistical generation of charge carries termed the Fano noise.

In a photon counting photodiode X-ray spectrometer the electronic noise, due to the preamplifier and the detector itself, consists of parallel white noise, series white noise (including the induced gate drain current noise), 1/*f* series noise, and dielectric noise (see **Section 2.8.2**). Parallel white noise is proportional to the shaping time, τ (see **Section 2.8.2.1**). Series white noise is inversely proportional to τ (see **Section 2.8.2.2**). Fano noise, 1/*f* series noise, and dielectric noise, are τ invariant (see **Sections 2.8.2.3, 2.8.2.4, 2.4.1** respectively). Incomplete charge collection noise is also considered to be τ invariant, except in extreme cases (Owens, 2012). The noise contributions can be calculated by applying a multidimensional least squares estimation method to the FWHM at 5.9 keV measured as a function of shaping time (Bertuccio & Pullia, 1993). The different noise contributions of each spectrometer (S1, S2, S3, and S4) were investigated as a function of reverse bias applied to the detector and as a function of temperature, in the temperature range 30 °C to -20 °C. Fig. 4.15 presents the noise contributions as a function of detector applied reverse bias, at 20 °C, and at the optimum shaping time, for the $Al_{0.2}Ga_{0.8}As$ based spectrometer S1 (employing detector D1). It is useful to consider the dielectric noise in two parts: known origin dielectric noise (e.g. contributions arising from the detector and JFET themselves); and unknown origin dielectric noise (e.g. arising from the dielectrics of stray capacitances in proximity to the preamplifier input). The combined contribution of the unknown origin dielectric noise and incomplete charge collection noise at 5.9 keV was calculated by subtracting in quadrature the calculated Fano noise at 5.9 keV, 1/*f* noise, and known dielectric noise from the total shaping time invariant noise contribution.

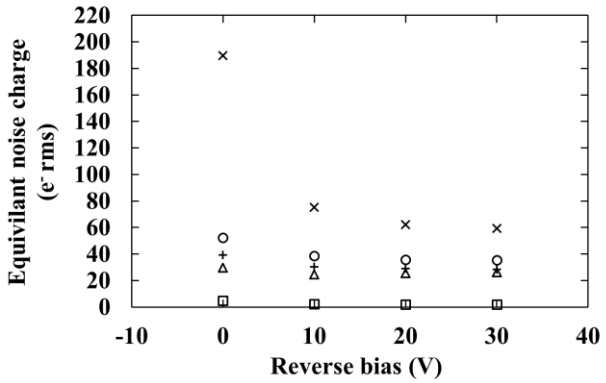

Fig. 4.15. Equivalent remaining noise contributions of the $Al_{0.2}Ga_{0.8}As$ detector spectrometer, S1, as a function of applied reverse bias of the detector, D1, at the optimum shaping time (2 μs), and at 20 °C. Quadratic sum of the unknown dielectric noise (e.g. stray dielectrics) and any incomplete charge collection noise (crosses); series white noise (circles); known dielectric noise (plus signs); parallel white noise (triangles); 1/*f* series noise (squares). Comparable results were obtained for S2, S3, and S4.

The quadratic sum of the unknown (e.g. stray) dielectric noise and incomplete charge collection noise decreased as a function of increased applied reverse bias of the detector, from 190 e^- rms at 5.9 keV at 0 V, to 60 e^- rms at 5.9 keV at 30 V. This decrease in noise contribution as a function of increased applied reverse bias, assuming the noise from unknown lossy dielectrics was independent of reverse bias (Barnett et al., 2012a), was attributed to the reduction in charge trapping noise (the prime constituent of incomplete charge collection noise broadening the energy resolution). The change in the detector's known dielectric noise as a consequence of the changing detector capacitance was taken into account in calculating the known dielectric noise contributions, and was thus also taken into account in the calculation of the unknown (e.g. stray) dielectric noise.

A quantitative estimate of the reduction of charge trapping noise as a function of increased applied bias was made by subtracting, in quadrature, the unknown dielectric noise and incomplete charge collection noise at an applied reverse bias of 30 V, from the unknown dielectric noise and incomplete charge collection noise at no applied reverse bias (0 V). The incomplete charge collection noise was reduced by 180 e^- rms at 5.9 keV when the detector, D1, was operated at 30 V in comparison to 0 V reverse bias at 20 °C. The majority of this reduction occurred at low magnitude (< 20 V) reverse biases; increasing the reverse bias from 20 V to 30 V reduced the incomplete charge collection noise by only 18 e^- rms at 5.9 keV at 20 °C. As an applied reverse bias > 30 V was not investigated, a definite value for the incomplete charge collection noise at 30 V cannot be established. However, the rapid decrease in incomplete charge collection noise

which occurred as the applied reverse bias was increased in magnitude towards 30 V, suggests that any incomplete charge collection noise at 30 V was small compared with the total dielectric noise in this condition. The calculated equivalent noise contributions present in S1 as a function of temperature, at an applied reverse bias of 30 V, and at a shaping time of 2 μs, are presented in Fig. 4.16. The quadratic sum of the unknown dielectric noise and incomplete charge collection noise was the largest noise contribution across all temperatures investigated, and remained approximately constant with temperature (60 e^- rms at 5.9 keV and 58 e^- rms at 5.9 keV, at 30 °C and -20 °C respectively, with the detector reverse biased at 30V in each case). The parallel white noise decreased with decreasing temperature (from 35 e^- rms at 5.9 keV at 30 °C, to 18 e^- rms at 5.9 keV at -20 °C, with the detector reverse biased at 30V in each case), resulting from the decreased JFET and detector leakage current with decreasing temperature (see Fig. 4.4). The series white noise contribution increased with decreasing temperature (35 e^- rms at 5.9 keV to 46 e^- rms at 5.9 keV at 30 °C and -20 °C respectively, with the detector reverse biased at 30 V in each case); this could not be explained solely by the detector's depletion capacitance, which remained approximately constant within the temperature range (100 °C to -20 °C). However, the series white noise not only depends on the total capacitance, but also the capacitive matching between the input JFET and the input load (Bertuccio et al., 1996). Therefore, the decreased series white noise with increased temperature may be attributed to a better capacitive match between the input JFET and the input load at higher temperatures.

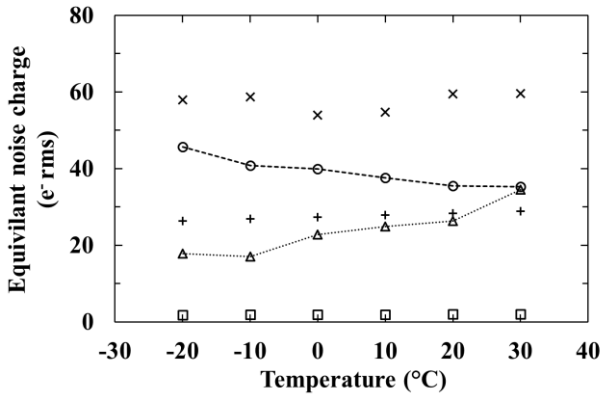

Fig. 4.16. Calculated remaining noise contributions of the $Al_{0.2}Ga_{0.8}As$ based spectrometer S1 at an applied reverse bias of 30 V and at a shaping time of 2 μs, as a function of temperature: quadratic sum of the unknown dielectric noise and incomplete charge collection noise (crosses); series white noise (circles); known dielectric noise (plus signs); parallel white noise (triangles); 1/*f* series noise (squares). Comparable results were obtained for S2, S3, and S4. The dashed lines are guides for the eyes only.

4.6 ^{63}Ni β^- particle spectroscopy

4.6.1 Percentage of electron energy absorbed by the detector

The Monte Carlo simulation program CASINO (Hovington et al., 1997) (Drouin et al., 1997), with which electron trajectories in solids can be simulated, was used to predict the percentage of electron energy absorbed in the active layer (i layer), E_{abs}, of the photodiodes across the incident electron energy range 1 keV to 66 keV in 1 keV steps (see **Section 2.5**).

CASINO was configured to use its Mott by Interpolation model; the ionisation potential was set as per Joy & Luo (1989); the random number generator was set as per Press et al. (1986); the effective section ionisation was set as per Casnati et al. (1982); the direction cosine was set as per Hovington et al. (1997). The same CASINO settings and presently reported methodology were used in Lioliou et al. (2018), Zhao et al. (2018b), and Butera et al. (2019). One computer, with an Intel i7-6700 (4 cores, 3.40 GHz) processor and 32 GB of random access memory, was used to perform the simulations. The CASINO simulations included backscattered electron emission, secondary electron emission, and X-ray emission from incident electron interactions (Hovington et al., 1997). Energy lost due to secondary electron emission and X-ray emission was considered to be localised, and in each set of simulations the GaAs p^+ layer, the p^+ layer, the n^+ layer, and the substrate of the $Al_{0.2}Ga_{0.8}As$ p^+-i-n^+ mesa structure were considered to be inactive. Therefore, only charge created by electrons (β^- particles) in the undoped region (i layer) was assumed to usefully contribute to the E_{abs}.

Two sets of simulations, each using 4000 electrons, were performed at each electron energy. The first set was simulated as incident upon a portion of a pixel's face which was not covered by the top metal contact (the so called window). The second set was simulated as incident upon a portion of a pixel's face which was covered by the top metal contact. The results of the simulations were then combined in the appropriate proportions according to the areas covered and uncovered by the contact. Fig. 4.17 presents the percentage of electron energy absorbed in the i layer as a function of incident electron energy, as predicted by these simulations.

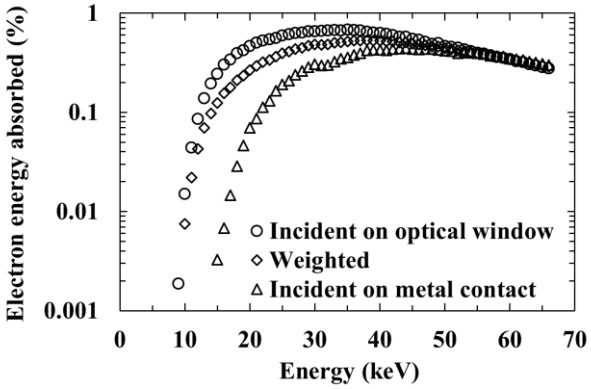

Fig. 4.17. Percentage of electron energy absorbed in the active layer (i layer), E_{abs}, of the $Al_{0.2}Ga_{0.8}As$ p^+-i-n^+ mesa photodiode structure for electrons incident on the window (circles), weighted case for actual contact coverage of the pixel (diamonds), and electrons incident on the metal contact (triangles), as a function of electron energy, at 20 °C, as determined by Monte Carlo simulations.

When electrons were incident upon the window of a pixel, the E_{abs} increased with increasing electron energy up to ≈ 33 keV (E_{abs} = 0.68). When electrons were incident upon the top metal contact of the detector, the E_{abs} increased with increasing electron energy up to ≈ 44 keV (E_{abs} = 0.44). The weighted E_{abs} (i.e. assuming uniform illumination of the $Al_{0.2}Ga_{0.8}As$ p^+-i-n^+ mesa structure from the top) reached a maximum of 0.53 at 38 keV. The increase of the weighted E_{abs} with increasing electron energy up to 38 keV suggested that the absorption of electrons at low energies was limited by the absorption of electrons within the inactive top layers of the detector (top metal contacts and p^+ layers). Beyond an electron energy of 38 keV, the weighted E_{abs} decreased, falling to 0.29 at 66 keV. This suggested that the absorption of electrons with high energies (> 38 keV) was limited by the relative thinness (3 µm) of the active i layer, although losses in the inactive overlayers also played a part. A thicker i layer would be required for the optimal absorption of electrons with energies > 38 keV; for example, it was found that ≈ 5 µm and ≈ 13 µm thick $Al_{0.2}Ga_{0.8}As$ would fully absorb 95 % of electrons with energies up to 38 keV and 66 keV respectively.

4.6.2 Expected measurements of ^{63}Ni β^- particle spectra

The β^- particle spectrum expected to be incident on the detector array as a result of illumination with the ^{63}Ni radioisotope β^- particle source was also simulated using the Monte Carlo simulation program CASINO (Hovington et al., 1997) (Drouin et al., 1997). Included in these simulations were the effects of self-absorption within the ^{63}Ni itself, as well as attenuation of β^- particles as they passed through the radioisotope β^- particle source's inactive Ni overlayer (1 µm thick,

density of 8.9 g cm^{-3} (Lide, 2005)) and the dry N_2 atmosphere (7 mm thick, density of 1.16 g cm^{-3} (Younglove & Olien, 1985)) separating the ^{63}Ni radioisotope β^- particle source and the detector array. A total of 66 independent simulations were conducted, in steps of 1 keV, from 1 keV to 66 keV (the ^{63}Ni endpoint energy). The number of electrons simulated at each energy was dependent on the relative emission probability, P_i, of each β^- particle energy from ^{63}Ni as corrected for self-absorption in a 3 μm thick layer (Liu et al., 2015). A total of 18,199,200 electrons were simulated. This number was selected to ensure sufficiently good statistics for interpretation of the data rather than to directly reflect the number of β^- particles which would be emitted from the source during the experimental accumulation of spectra reported in **Section 4.6.3**. A bank of 14 computers, each with an Intel i7-6700 (4 cores, 3.40 GHz) processor and 32 GB of random access memory, was used to perform the simulations. The same CASINO settings as per **Section 4.6.1** were used. The presently reported methodology was the same as that used in Lioliou et al. (2018), Zhao et al. (2018b), and Butera et al. (2019).

The computed trajectories of the simulated electrons were used to calculate the remaining energy of each electron after passing out of the ^{63}Ni itself and through the Ni overlayer and N_2 layer. The remaining energies of each of the 18,199,200 electrons were then binned into channels each of 1 keV width, thus providing the spectrum expected to be incident on the top face of the detector array. This spectrum is presented in Fig. 4.18. Particles which lost all of their energy before reaching the detector have been excluded from the spectrum.

The ^{63}Ni β^- particle spectrum predicted to be detected by each pixel was then calculated by combining the weighted percentage of electron energy absorbed in the active layer (see Fig. 4.17) with the spectrum expected to be incident upon the detector. This is shown in Fig. 4.18, alongside the emitted spectrum and the spectrum incident on the detector. The spectrum predicted to be detected does not include the effects of Fano noise, spectrometer electronic noise, incomplete charge collection, or pixel edge effects. A key outcome of the simulations was the prediction of the spectrum's apparent endpoint energy, which would be detected during the subsequent experimental measurements.

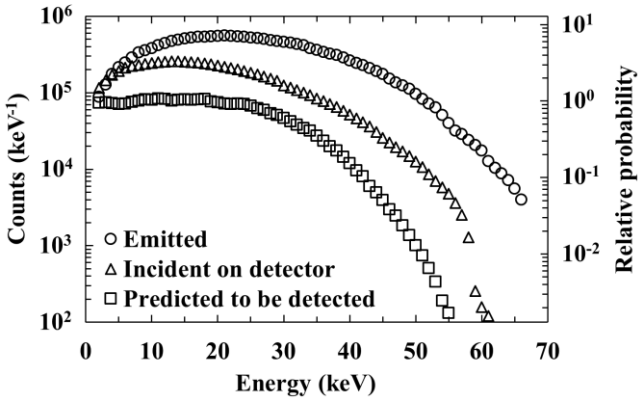

Fig. 4.18. Simulated ^{63}Ni β^- particle spectrum as emitted from the active material of the source including self-absorption (circles), incident on the top face of the detector (triangles) thus including attenuation in the inactive Ni overlayer and N_2 atmosphere, and predicted to be detected (squares). The relative probability axis refers to the predicted to be detected (squares) data series only. A relative probability of 1 was assigned to the mean number of counts detected per channel within the broadly flat region (1 keV $\leq E \leq$ 20 keV) within the spectrum predicted to be detected.

4.6.3 Experimental measurements of ^{63}Ni β^- particle spectra

Each pixel of the array was connected, in turn, to a single channel custom-made low-noise charge-sensitive preamplifier of feedback-resistorless design (see **Section 2.7**). The output signal of the preamplifier was shaped using an Ortec 572A shaping amplifier, which was then connected to a multi-channel analyser (MCA) for digitisation. The temperature of the detector array and the preamplifier was 20 °C throughout the experiment. The detector array was operated in a dry N_2 environment for the duration of the measurements to eliminate any humidity related effects (Barnett et al., 2013b). The ^{63}Ni radioisotope β^- particle source was placed 7 mm ± 1 mm above the detectors in the same dry N_2 environment. A spectrum accumulation live time of 1000 s and a shaping amplifier shaping time of 2 μs (optimal available shaping time for this detector array at 20 °C) were used for each ^{63}Ni β^- particle spectrum, with a reverse bias of 30 V applied to each pixel. The pixels were fully depleted when operated in this bias condition. The spectra accumulated using each pixel are presented in Fig. 4.19. Each ^{63}Ni β^- particle spectrum has been energy calibrated using the apparent endpoint energy determined from the simulations (see **Section 4.6.2**), taking into account the number of detected counts and as such, the relative probability of detection and the position of the zero energy noise peaks (not shown in the figures). It was assumed that there was a linear variation of spectrometer output as a function of detected energy between the zero energy noise peak and the endpoint energy.

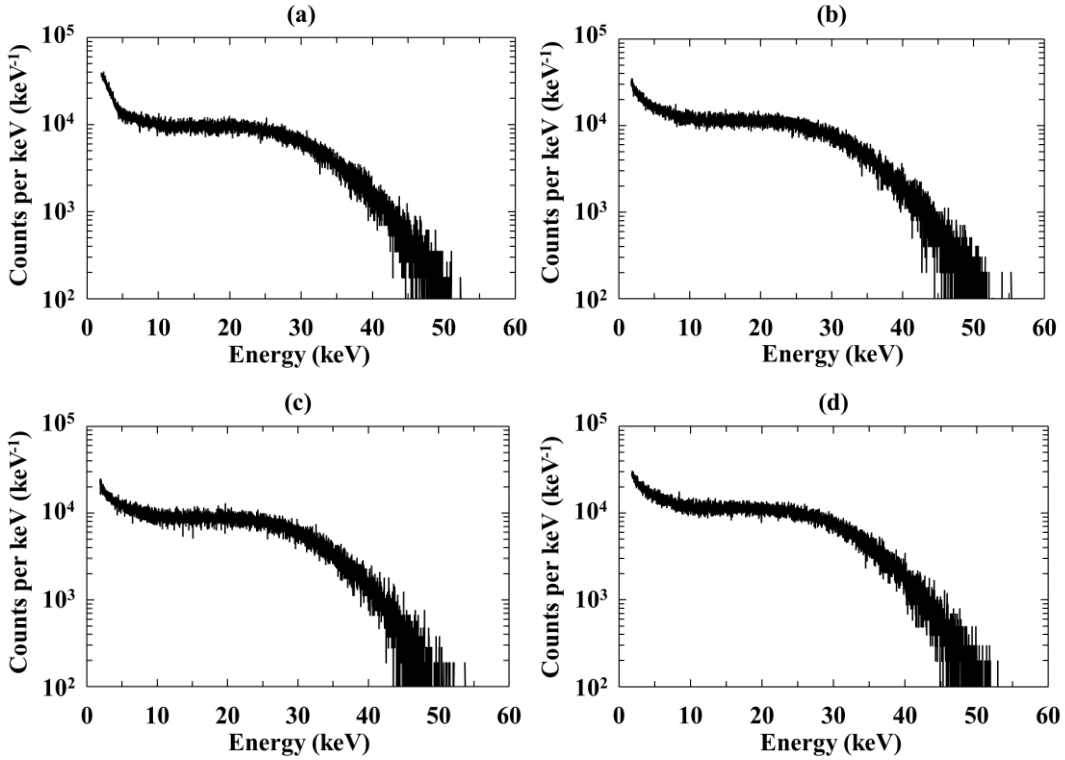

Fig. 4.19. Experimentally measured ^{63}Ni β^- particle spectra obtained using pixel: D1 (a); D2 (b); D3 (c); D4 (d). The accumulated spectra are presented in terms of counts per keV.

The experimentally detected ^{63}Ni β^- particle spectra were qualitatively compared with that predicted to be detected from the simulations. This comparison for pixel D1 is presented in Fig. 4.20. The experimentally measured spectrum was normalised to the mean number of counts detected per channel within the broadly flat 11 keV $\leq E \leq$ 20 keV region of the experimentally measured spectrum. The predicted to be detected spectrum was normalised to the mean number of counts detected per channel within the broadly flat 1 keV $\leq E \leq$ 20 keV region of the predicted to be detected spectrum. Comparable results were obtained for the other pixels. At low energies ($\leq$ 11 keV), the difference between the simulated and measured ^{63}Ni β^- particle spectra of D1 was attributed to the right hand side of the zero energy noise peak tail not being entirely eliminated by the low energy threshold (2 keV).

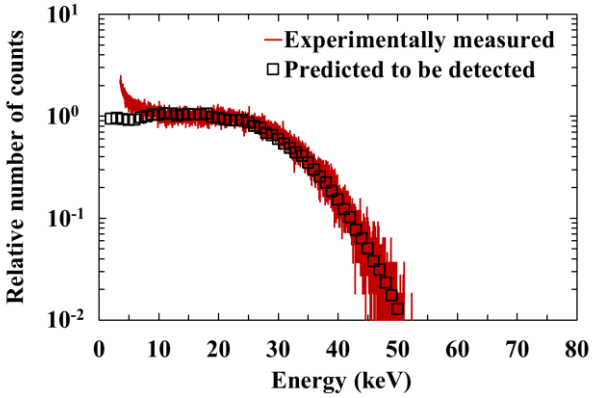

Fig. 4.20. Comparison between the experimentally measured ^{63}Ni β^- particle spectrum using pixel D1 (red line) and that predicted from the simulations (squares).

4.6.4 A method to improve high energy response

Whilst the thickness of the detector's active region could be increased to improve the high energy response of the spectrometer, an alternative approach would be to use multiple thin detectors (e.g. as part of a pixel array) each of which has a different thickness of inactive absorber material in front of the pixel. This may be a useful approach in the case that thin commercial-off-the-shelf (COTS) detectors are being used by researchers who are unable to grow custom structures and procure suitable detectors with thick active layers from external suppliers. For example, in the instance of the presently reported four pixel array, one pixel may have no additional absorber, and the other three pixels may have progressively thicker aluminium layers (e.g. 20 µm, 100 µm, and 500 µm for D2, D3, and D4, respectively) deposited on top of them. A soft electron would be entirely attenuated by such Al layers, and would be thus prevented from reaching the pixel in question. However, for a high energy electron, the Al layer would only attenuate some of that electron's energy, with the remainder available to be absorbed in the pixel. Such Al layers could be tailored to be of appropriate thickness to reduce a portion of the incident spectrum's energy to that which is more readily detected by the thin detectors.

CASINO simulations were conducted in order to identify the suitable Al layer thicknesses for incident electron energies of 100 keV, 200 keV, and 500 keV. Al layers of varying thickness, directly atop the presently reported $Al_{0.2}Ga_{0.8}As$ detecting structure, were simulated at each electron energy of interest, using 4,000 electrons in each case. Two sets of simulations were conducted for each Al layer thickness in order to account for the areas covered and uncovered by the $Al_{0.2}Ga_{0.8}As$ p^+-i-n^+ mesa structure metal contact. They were combined in the appropriate proportions (see **Section 4.6.1**). In the case of an incident electron energy of 100 keV, Al thicknesses of 5 µm, 10 µm, 20 µm, 30 µm, and 40 µm were simulated, see Fig. 4.21. The total number of detected counts from the resulting spectra, given 4,000 incident electrons, were then

compared in order to establish the optimal Al thickness (greatest number of detected counts). Detected counts below an electron energy of 11 keV were not considered due to the mismatch between experimental and simulated results which was reported earlier (see **Section 4.6.3**). The same CASINO settings as **Section 4.6.1** were used.

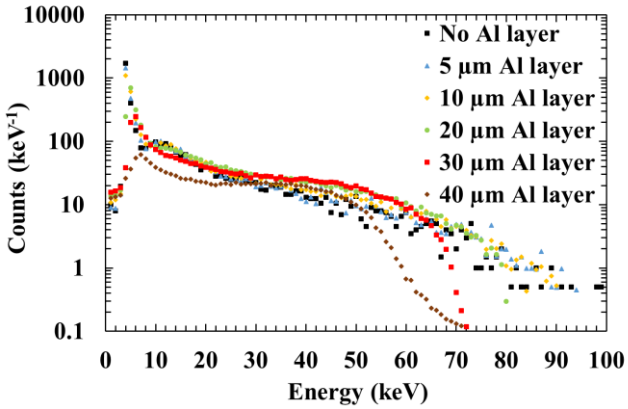

Fig. 4.21. Counts detected as a function of electron energy for a simulated $Al_{0.2}Ga_{0.8}As$ pixel with: no Al layer (black squares); a 5 µm Al layer (blue triangles); a 10 µm Al layer (yellow diamonds); a 20 µm Al layer (green circles); a 30 µm Al layer (red squares); a 40 µm Al layer (brown diamonds).

The resulting simulations showed that the number of counts detected from 4,000 incident 100 keV electrons was increased from 1291 to 1664 when a 20 µm Al layer is introduced. Similarly, the numbers of detected counts was increased from 397 to 944 given 4,000 incident 200 keV electrons, and from 101 to 382 given 4,000 incident 500 keV electrons, with the introduction of 100 µm and 500 µm Al layers, respectively. Fig. 4.22 shows how 20 µm, 100 µm, and 500 µm Al layers placed atop an $Al_{0.2}Ga_{0.8}As$ pixel improves the number of detected counts for the spectrometer. The introduction of Al absorption layers atop the $Al_{0.2}Ga_{0.8}As$ structure was found to increase the E_{abs} of the spectrometer by 22 % (0.1238 ± 0.0020 to 0.1508 ± 0.0024) at 100 keV, 46 % (0.0296 ± 0.0005 to 0.0431 ± 0.0007) at 200 keV, and 20 % (0.0065 ± 0.0001 to 0.0078 ± 0.0001) at 500 keV, respectively.

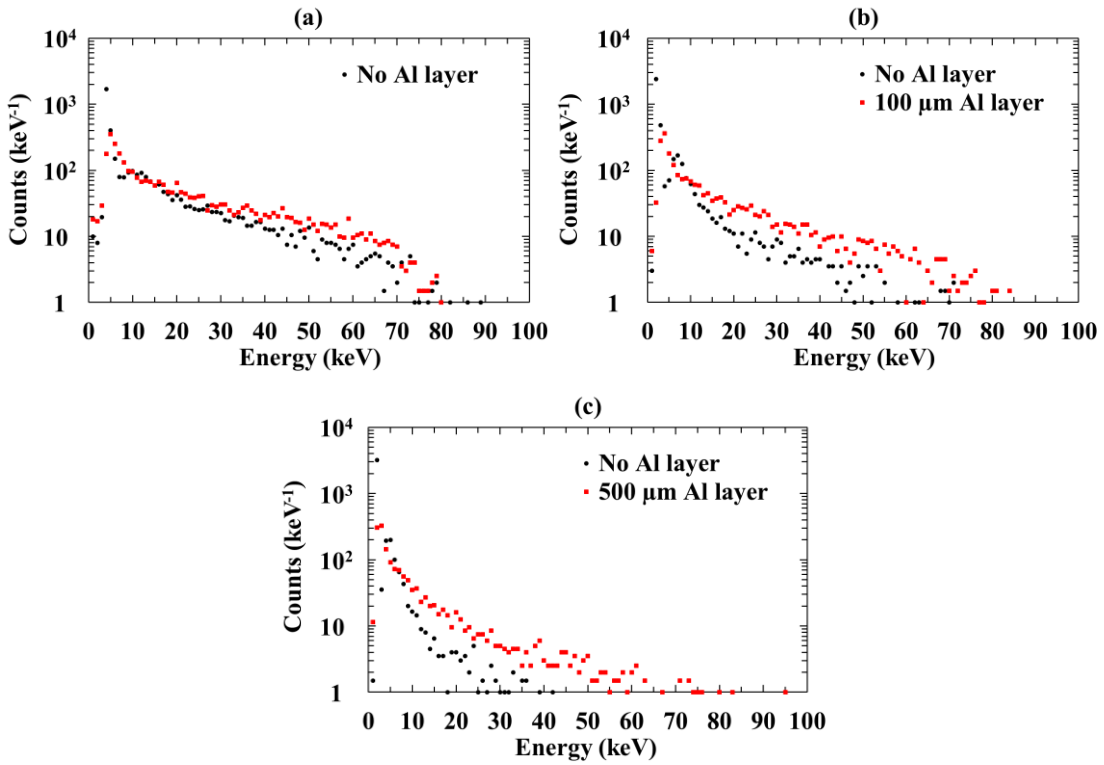

Fig. 4.22. Comparison of detected counts as a function of energy given 4,000 incident electrons of energy: 100 keV (a); 200 keV (b); 500 keV (c), between an $Al_{0.2}Ga_{0.8}As$ pixel with the corresponding Al layer (red squares), and without the Al layer (black squares).

4.6.5 Discussion of space science applications

The above results have demonstrated that this prototype $Al_{0.2}Ga_{0.8}As$ pixel array can be used for spectroscopic particle counting detection of electrons (β^- particles) when coupled to suitable readout electronics. This is the first time $Al_{0.2}Ga_{0.8}As$ has been demonstrated for this application. Previous reports have shown $Al_xGa_{1-x}As$ to be potentially radiation hard (Walker et al., 2017) (Yoshida et al., 1982) (Yamaguchi et al., 1995). Consequently, electron spectrometers with $Al_{0.2}Ga_{0.8}As$ detectors (either as single pixels or pixel arrays) may find use in future space missions to intense radiation environments. The benefits of inherently radiation-hard instrumentation may be demonstrated by considering the JEDI particle spectrometer on board the Juno spacecraft (Mauk et al., 2017). JEDI has an instrument mass of ≈ 1.4 kg plus ≈ 5 kg of radiation shielding (Mauk et al., 2017). If such an instrument was realisable using detectors and electronics of sufficient radiation tolerance that the shielding could be reduced in mass to the extent that the shielding only contributed 50 % of the total instrument mass (i.e. an instrument mass of 1.4 kg plus 1.4 kg of shielding, for the JEDI example), two instruments could be flown within the same mass budget with 0.8 kg spare.

Indeed the development of radiation hard instrumentation, including electron spectrometers, for use in the Jovian system is a pressing matter. The magnetosphere of Jupiter is plasma-rich and of particular interest in contemporary space science. Jupiter's moon Io releases 1 Mg/s of O and S through volcanic eruptions (Grasset et al., 2013). Complex processes involving magnetic field ruptures and plasma instabilities accelerates this material, in addition to Solar particles, to high energies, creating high energy ion and electron populations throughout Jupiter's magnetosphere. Measurements of these electrons and ions, including their associated energy, spatial, and angular distributions, can help studies of the nature and origin of Jupiter's magnetic field, which is the largest and fastest rotating magnetic field in the Solar System after that of the Sun (Grasset et al., 2013).

Whilst the detector array presented here is only a proof-of-concept prototype, it is informative to consider eventual use-cases for such instrumentation in order to direct future development. Since the predicted and measured ^{63}Ni β^- particle spectra were in agreement (see **Section 4.6.3**), a spectrum predicted to be detected within the near-Jupiter radiation environment was also considered. The omnidirectional electron flux (computed by Mauk & Fox (2010)) within the Jovian system, at a radial distance of 8.25 R_J (Jovian equatorial radius, R_J, = 71.4 Mm), was used to represent the soft electron (< 66 keV) radiation environment between the orbits of Io (5.90 R_J) and Europa (9.25 R_J), and is shown in Fig. 4.23. For clarity, and given the range of incident energies for which reported percentages of electron energy absorbed in the active layer of the pixel array were computed (see Fig. 4.17), only electrons with energies in the range 1 keV – 66 keV were included in the prediction of the electron spectrometer's response in the Jovian environment. It should be noted that much higher electron energies (up to MeV energies) are also present within Jupiter's magnetosphere, albeit at reduced abundances. Collection of charge from these higher energy electrons would modify the spectrum detected from that computed here, but nevertheless, it is interesting to study the soft electron portion of the spectrum independently since it is this energy range that is of greatest abundance.

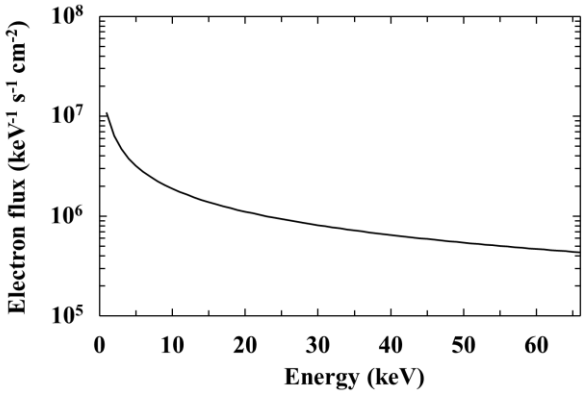

Fig. 4.23. Omnidirectional electron flux predicted at 8.25 R_J radial distance from Jupiter, as a function of energy, and calculated by Mauk & Fox (2010).

To convert the omnidirectional electron flux shown in Fig. 4.23 into the spectrum predicted to be incident on one $Al_{0.2}Ga_{0.8}As$ pixel of the type discussed above (excluding additional Al layers), the flux was halved (thus assuming that the detector is single sided) and multiplied by the area of one pixel (4×10^{-4} cm^2). The electron spectrum predicted to be usefully absorbed in the pixel's active region (assumed to be only the pixel's i layer) was then calculated by considering the structure's E_{abs} (see **Section 4.6.1**) which accounted for energy losses within the dead layers of the pixel (the top Ohmic contact, the p^+ layer, the n^+ layer, and the substrate). Fig. 4.24 shows the spectrum predicted to be incident on the pixel and the spectrum predicted to be detected. The spectrometer's Fano noise, electronic noise, and any incomplete charge collection noise were excluded from the predictions, as were pixel edge effects. Electron energy losses within the top contact and p^+ layers explain the difference between the spectra in Fig. 4.24 at low energies, whereas the thinness of the active region explains the difference at high energies.

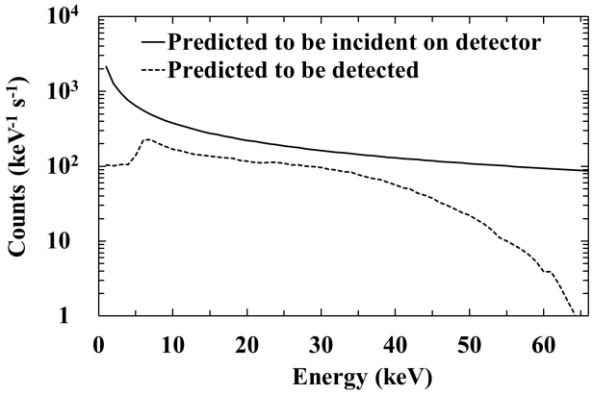

Fig. 4.24. Comparison between the electron spectrum (energy range, 1 keV to 66 keV) predicted to be incident on the detector (solid line) and spectrum expected to be detected (dashed line) at 8.25 R_J from Jupiter. It should be noted that much higher electron energies (up to MeV energies) are also present within Jupiter's magnetosphere, albeit at reduced abundances. Collection of charge from these higher energy electrons would modify the spectrum detected from that computed here.

It is also informative to consider the required spatial resolution for such a spectrometer. For a spectrometer moving on a spacecraft in orbit, the distance travelled in the time taken to collect an adequate (statistically significant) number of counts across the energy range of interest can be the limiting factor. Clearly, the percentage of electron energy absorbed in the active layer and area of the spectrometer's detector each play a part in this. The smallest auroral structures so far imaged at Jupiter are ≈ 80 km wide (Ingersoll et al., 1998). In addition, spacecraft orbiting Jupiter must travel at high speed due to Jupiter's large gravitational well (e.g. JUNO's orbital velocity ≈ 50 km s^{-1} (Mauk et al., 2017)). Therefore, in order to spatially resolve similarly sized features at the spacecraft's orbit, the accumulation time of each spectra needs to be sufficiently short. In the case of JUNO, the electron spectrometer was required to have an accumulation time of < 0.6 s (Mauk et al., 2017). Assuming a spacecraft speed of 50 km s^{-1}, this yields a spatial resolution of 30 km per spectrum. Given a single pixel of the 2 × 2 square pixel photodiode array reported here, and the expected omnidirectional electron flux at 8.25 R_J from Jupiter (8.41×10^7 cm^{-2} s^{-1} within the energy range 1 keV to 66 keV), the total number of counts expected to be detected over an accumulation time of 0.6 s, would be 4.46×10^3 counts per pixel.

Crudely speaking, given a source of constant excitation intensity, the detection of particles constitutes the counting of random events, and obeys the law of Poisson statistics. If the Omnidirectional electron flux predicted at 8.25 R_J radial distance from Jupiter is treated as such (an oversimplification, but useful for present purposes), then the relative statistical precision of the measurement can be approximated as $\approx \frac{1}{\sqrt{I_m t}}$, where I_m (units of s^{-1}) is the counting rate and t

is the real time of detection (Jenkins et al., 1995). The total number of counts per pixel therefore has a relative statistical precision of ≈ 1.5 %. In order to identify and understand the incident electron flux from the detected spectrum, the statistical significance of accumulated counts across the investigated energy range needs to be high (Pfaff et al., 2013) and the electron environment must be modelled.

A further consideration would be the data storage and transmission requirements for such a spectrometer. The $Al_{0.2}Ga_{0.8}As$ devices have previously been found to have an energy resolution of ≈ 800 eV FWHM at 5.9 keV when operated at a temperature of 20 °C (see **Section 4.5.1**). Assuming that the energy resolution broadens at higher energies solely due to Fano noise's energy dependence (Lowe & Sareen, 2014), the expected energy resolution at 66 keV would be 1.1 keV FWHM assuming an electron hole pair creation energy of 4.43 eV (see **Section 3.8**) and a Fano factor of 0.12. A Poissonian probability density function with ≥ 60 channels can be approximated to a Gaussian probability density function (Jenkins et al., 1995). Given the energy resolution of the reported detectors, a suitable channel width would be 25 eV per channel (thus providing 60 channels across three standard deviations of a Gaussian distribution with a FWHM of 1.1 keV). However, counting statistics must be considered; narrower channels result in fewer counts per channel for a given electron population. Considering the simulation results of Fig. 4.24 and the relatively low numbers of detected electrons, binning the spectrum into relatively narrow (e.g. 25 eV wide) channels would result in relatively large statistical uncertainties in the number of count per channel. The number of detected counts could be increased by improving the E_{abs} of the detector, increasing the detector's area, or using more detectors. However, unless this was done, a width of 1 keV per channel (based on the present detector) would be a more practical choice for the environment, assuming the required accumulation time could not be lengthened, thus balancing energy resolution of the detector with better counting statistics. From Fig. 4.24, the maximum number of counts obtained per channel (width = 1 keV) was ≈ 200. It should be noted that the dead-time, the time between each successfully measured count, may affect the number of accumulated counts; the count rate predicted here (4.46×10^3 counts in 0.6 s) is relatively high, and care must be taken to ensure the speed of the readout electronics is sufficient. This demonstrates the need for improvements in spectrometer energy resolution to be combined with improvements in the E_{abs} of the detector, as well as readout electronics speed. For the spectrometer discussed, an MCA with a capacity of 10 bits per channel (up to 1023 counts per channel) would provide adequate scope for greater than average count rates to be experienced by the spectrometer without its accumulation time having to be shortened. Limiting the spectrometer's energy range to extend from 2 keV (the low energy threshold, see **Section 4.6.3**) to 66 keV (high energy threshold), with 64, 10 bit, channels, would mean each spectrum (duration 0.6 s) would require 640 bits. Should lower count rates be expected, channel memory could be

reduced; e.g. for the spectrum shown in Fig. 4.24, 8 bits per channel (up to 255 counts per channel) would be sufficient, requiring 512 bits per spectrum. Assuming 32 bits for labelling each spectrum, but neglecting transmission overheads (e.g. error correction and protocol requirements) an average data transmission rate of ≈ 1120 bits/s would be required. It should be noted that, depending on the desired encoding practice, 10 bit channel data may require padding to 16 bits. This would result in an average data transmission rate of ≈ 1760 bits/s.

4.7 Conclusion

Despite continued efforts, prior to the results reported in this thesis, only single pixel $Al_xGa_{1-x}As$ X-ray spectrometers and β^- particle spectrometers have been reported (see **Section 4.2**). However, for the first time, it has been demonstrated here that yields are now sufficient such that small (2 × 2) $Al_{0.2}Ga_{0.8}As$ mesa pixel arrays can be produced, with good enough quality that they are suitable for photon counting X-ray spectroscopy and direct detection electron spectroscopy.

Uniformity in electrical characteristics (see **Section 4.4**) and measured energy resolution (see **Section 4.5**) across each pixel has been demonstrated, in addition to the best measured energy resolution so far reported for AlGaAs X-ray photodiodes at 20 °C (756 eV ± 30 eV FWHM at 5.9 keV cf. 1.06 keV ± 0.04 keV FWHM at 5.9 keV reported in **Section 3.7**, at 20 °C). As the epitaxial wafer material of the $Al_{0.2}Ga_{0.8}As$ single pixels reported in **Chapter 3** was the same as that used in the present work, the improved energy resolution now reported was attributed in part to subtle improvements in device fabrication and processing techniques. These may have aided in the reduction of leakage current density (8.8 nA cm^{-2} ± 1.0 nA cm^{-2} cf. 44.3 nA cm^{-2} ± 1.4 nA cm^{-2} reported in **Section 3.6.1**, at 100 kV cm^{-1} and 20 °C). Slight modifications to the front-end of the preamplifier may have also contributed to the improved energy resolution through reductions in the dielectric noise contribution (66 e^- rms at 5.9 keV cf. 79 e^- rms at 5.9 keV reported in **Section 3.7.2**, at 100 kV cm^{-1} and 20 °C). It should be noted that the operating conditions of the presently reported spectrometers were not the same as those reported in **Section 3.7**, thus the calculated noise contributions can only be qualitatively compared.

Since the stray dielectric noise of the X-ray spectrometers reported here accounted for 59 e^- rms at 5.9 keV at 20 °C; implementing further ways to improve the front-end electronics, such as directly wirebonding the photodiodes to the input JFETs, could further improve the energy resolution (Bertuccio et al., 1993). As such, the improvement in energy resolution reported here should be seen as an incremental step towards further improving the energy resolution obtained with $Al_xGa_{1-x}As$ X-ray spectrometers.

Although the energy resolutions achieved with the presently reported $Al_{0.2}Ga_{0.8}As$ devices are not yet as good as with some other more developed materials (see **Section 3.9**), it is important to note that useful scientific contributions can still be made by X-ray spectrometers with modest energy resolutions. The D-CIXS (Demonstration of a Compact Imaging X-ray Spectrometer) instrument on SMART-1 for example, which had an energy resolution of 420 eV FWHM at 1.49 keV (Swinyard et al., 2009) having been degraded from 250 eV FWHM at 1.49 keV at launch (Thompson et al., 2009) by radiation damage received during its 15 month journey to the moon (Swinyard et al., 2009) (for reference the Chandrayaan-1 X-ray spectrometer had an energy resolution of 110 eV FWHM at 1.49 keV (Swinyard et al., 2009)), measured Ti Kα (4.51 keV) X-ray fluorescence of material on the lunar surface from orbit for the first time in 2005 (Swinyard et al., 2009)). As such, a photon counting X-ray spectrometer with similar or better energy resolution, that is also tolerant of high temperatures and is radiation hard, would likely find much use in future missions to harsh environments (e.g. the surfaces of the inner planets and the Jovian and Saturnian systems).

The prototype monolithic 2 × 2 square pixel $Al_{0.2}Ga_{0.8}As$ p^+-i-n^+ mesa photodiode array was investigated for its utility as a direct detection electron (β^- particle) detector operating uncooled at 20 °C. The results reported here are the first demonstration of $Al_{0.2}Ga_{0.8}As$ for direct detection electron spectroscopy. The simulated spectra (i.e. those expected to be detected) were found to be in good agreement with those obtained experimentally (see **Section 4.6.3**). Thus, it was shown that each spectrometer could spectroscopically detect electrons from the ^{63}Ni β^- particle source at room temperature (20 °C) without any need for cooling.

As a possible option to improve the high energy response of the reported electron spectrometer, which was relatively thin, inactive Al absorber layers to be placed atop the detecting structure were investigated using Monte Carlo simulations (see **Section 4.6.4**). These simulations showed that the number of counts detected from 4,000 incident 100 keV electrons could be increased from 1291 to 1664 if a 20 μm Al layer was introduced. Similarly, the numbers of counts could be increased from 397 to 944 given 4,000 incident 200 keV electrons, and 101 to 382 given 4,000 incident 500 keV electrons, with the introduction of 100 μm and 500 μm Al layers, respectively. Thus the simulated E_{abs} of the spectrometer (see **Section 4.6.1**) was found to increase by 22 % (0.1238 ± 0.0020 to 0.1508 ± 0.0024) at 100 keV, 46 % (0.0296 ± 0.0005 to 0.0431 ± 0.0007) at 200 keV, and 20 % (0.0065 ± 0.0001 to 0.0078 ± 0.0001) at 500 keV, respectively, when these inactive Al absorption layers were employed.

To inform future development of $Al_{0.2}Ga_{0.8}As$ detectors for space science applications, the electron spectrum predicted to be detected by a spectrometer employing an $Al_{0.2}Ga_{0.8}As$

photodiode of the type described within the near-Jupiter radiation environment was considered. Given a single pixel of the 2 × 2 array reported here, and the expected omnidirectional electron flux at 8.25 R_J from Jupiter (8.41×10^7 cm^{-2} s^{-1} within the energy range 1 keV to 66 keV), the total number of counts expected to be detected over an accumulation time of 0.6 s would be 4.46×10^3 counts per pixel. Assuming a spacecraft speed of 50 km s^{-1}, this accumulation time yields a spatial resolution of 30 km per spectrum, sufficient to investigate the electron environment features of the same size as the smallest auroral structures so far imaged at Jupiter (≈ 80 km wide (Ingersoll et al., 1998)).

Parameter	Value
FWHM at 5.9 keV at 30 °C	773 eV ± 30 eV
FWHM at 5.9 keV at 20 °C	756 eV ± 30 eV
FWHM at 5.9 keV at 0 °C	716 eV ± 30 eV
FWHM at 5.9 keV at -20 °C	722 eV ± 30 eV
Detector leakage current density at full depletion (30 V, 100 kV cm^{-1}) at 20 °C	9.0 nA cm^{-2} ± 1.0 nA cm^{-2}
Detector capacitance density at full depletion (30 V, 100 kV cm^{-1}) at 20 °C	3.51 nF cm^{-2} ± 0.09 nF cm^{-2}
Intrinsic carrier concentration at 20 °C	≈ 4×10^{15} cm^{-3}

Table 4.2. Key results of **Chapter 4** 2 × 2 square pixel $Al_{0.2}Ga_{0.8}As$ p^+-i-n^+ mesa X-ray photodiode (200 μm diameter, 3 μm i layer) measurements.

Chapter 5

2 µm i layer $Al_{0.6}Ga_{0.4}As$ Mesa p^+-i-n^+ detectors

5.1 Introduction

In this chapter, work characterising the X-ray spectroscopic performance of two prototype $Al_{0.6}Ga_{0.4}As$ p^+-i-n^+ circular mesa avalanche photodiodes with different diameters (200 µm and 400 µm) at room temperature is reported. Improved energy resolutions (FWHM at 5.9 keV) as a function of increased applied reverse bias were observed for each detector, achieving 626 eV ± 20 eV at an applied reverse bias of 38 V and 732 eV ± 30 eV at an applied reverse bias of 40 V, for the 200 µm and 400 µm diameter device respectively. In part, the improvement was attributed to avalanche multiplication. The average energy consumed in the generation of an electron hole pair in $Al_{0.6}Ga_{0.4}As$ was experimentally measured and determined to be 4.97 eV ± 0.12 eV at 25 °C ± 1 °C. The experimental methods and techniques used to characterise the devices, along with the findings of the experimental work performed, is presented.

5.2 Background

The potential benefits of $Al_xGa_{1-x}As$ as a material for spectroscopic photon counting X-ray photodiodes has led to the extensive study of $Al_{0.8}Ga_{0.2}As$ (see **Section 1.6.2**) and $Al_{0.2}Ga_{0.8}As$ (see **Chapters 3** and **4**). However, since adjusting the Al fraction leads to changes in material and device characteristics (e.g. reducing the Al fraction leads to a narrower bandgap, an increased linear X-ray absorption coefficient, and a better lattice match with GaAs (see **Section 1.6.2**)), it may be beneficial to tailor the Al fraction of $Al_xGa_{1-x}As$ depending on the operating environment. For example, $Al_{0.6}Ga_{0.4}As$, with a bandgap (E_g = 2.03 eV (Adachi, 1985)) slightly smaller than that of $Al_{0.8}Ga_{0.2}As$ (2.09 eV (Adachi, 1985)), could optimise the material for use in more modestly elevated temperatures (e.g. space missions to the poles of Mercury, where surface temperatures reach 70 °C (Novara, 2002)).

Prior to the results reported in this thesis, there have been no reports in the literature of $Al_{0.6}Ga_{0.4}As$ photodiodes for X-ray photon counting spectroscopy. Instead, research of $Al_{0.6}Ga_{0.4}As$ photodiodes has focussed on the materials avalanche multiplication (see **Section 2.9**) characteristics (Plimmer et al., 2000) (Tan et al., 2001) (Harrison et al., 2002) in an effort to address inconsistencies in the local model (see **Section 2.9.3**) and the increasing limitations in performance of high-power and microwave transistors as device dimensions continue to shrink (Harrison et al., 2002). Thin $Al_{0.6}Ga_{0.4}As$ p^+-i-n^+ photodiodes for example, with avalanche region

thicknesses of 0.026 μm to 0.85 μm, have been reported by Tan et al. (2001) at room temperature. The associated multiplication and excess noise characteristics of these devices were measured over a wide range of internal electric field strengths. The measured excess noise (N_x = 3.3 at M = 15.5, for an avalanche thickness of 0.026 μm (Tan et al., 2001)) was the lowest (at this multiplication factor) of any device grown upon GaAs substrates (Tan et al., 2001).

5.3 Device structure

The $Al_{0.6}Ga_{0.4}As$ p^+-i-n^+ structure was grown by MOVPE on a commercial GaAs n^+ substrate. The layer details of the structure are summarised in Table 5.1. Since it was the first time structures of this material had been grown for this application, and considering the small but significant lattice mismatch between GaAs (the substrate) and $Al_{0.6}Ga_{0.4}As$, only a relatively thin (total 2.6 μm thickness) epitaxial AlGaAs structure was grown. Circular mesa structures of two diameters (200 μm and 400 μm) were fabricated at the EPSRC National Centre for III-V Technologies, Sheffield, UK using 1:1:1 H_3PO_4:H_2O_2:H_2O solution followed by 10 s in 1:8:80 H_2SO_4:H_2O_2:H_2O solution. An Ohmic contact consisting of 20 nm InGe and 200 nm Au was evaporated onto the rear of the substrate, and an Ohmic top contact of 20 nm Ti and 200 nm Au was evaporated onto the p^+ side of the mesa device; the devices were unpassivated. The p^+ metal contact covered 45 % of the 200 μm diameter photodiode's surface and 33 % of the 400 μm diameter photodiode's surface.

Material	Dopant	Dopant type	Thickness (nm)	Doping density (cm^{-3})
GaAs	Zn	p	10	1×10^{19}
$Al_{0.6}Ga_{0.4}As$	Zn	p	500	2×10^{18}
$Al_{0.6}Ga_{0.4}As$			2000	Undoped
$Al_{0.6}Ga_{0.4}As$	Si	n	100	2×10^{18}
GaAs	Si	n	200	2×10^{18}
GaAs n^+ substrate				

Table 5.1. Layer details of the $Al_{0.6}Ga_{0.4}As$ p^+-i-n^+ structure from which the devices were fabricated.

5.4 Room temperature electrical characterisation

5.4.1 Current measurements as a function of applied bias

Current as a function of forward and reverse bias was measured for two (one 200 μm diameter and one 400 μm diameter) $Al_{0.6}Ga_{0.4}As$ p^+-i-n^+ photodiodes under dark conditions. A Keithley

6487 Picoammeter/Voltage Source was used to bias the detectors and measure the current. Fig. 5.1a presents the measured forward current as a function of forward bias and Fig. 5.1b presents the measured reverse leakage current as a function of reverse bias for the 200 µm and 400 µm devices.

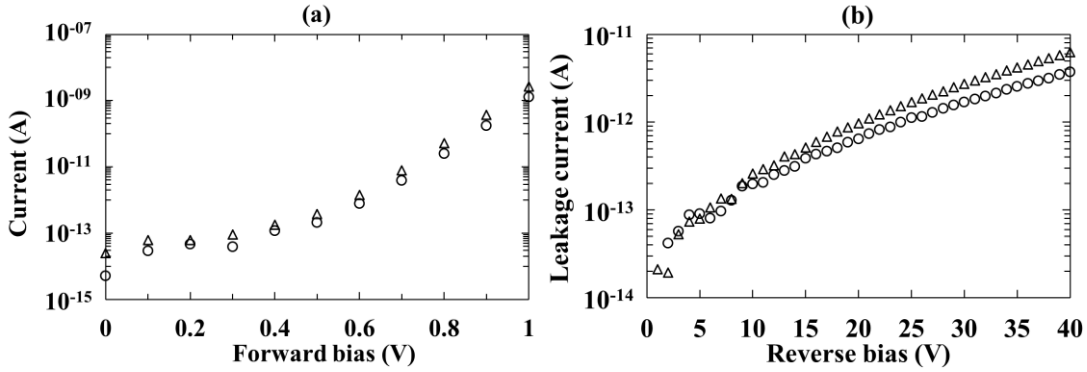

Fig. 5.1. Current as a function of applied forward bias (a) and applied reverse bias (b), for the 200 µm device (circles) and the 400 µm device (triangles) at 20 °C. The associated uncertainties were omitted for clarity.

The maximum forward (1 V) and reverse (40 V) biases were selected to maintain device current at relatively low levels (< 1 nA) to ensure there was no damage to the devices during the characterisation procedure. The leakage current of both devices increased as a function of increased reverse bias magnitude. At the maximum applied reverse bias (40 V), the leakage currents were measured to be 3.7 pA ± 0.4 pA and 6.3 pA ± 0.4 pA for the 200 µm and 400 µm devices, respectively. The uncertainties associated with the current measurements were dominated by the uncertainty associated with the Keithley 6487 Picoammeter/Voltage Source. Assuming the electric field strength, E_f, was uniform and across only the depleted region (implying E_f = 345 kV cm^{-1} and E_f = 361 kV cm^{-1} for the 200 µm and 400 µm devices, respectively, at 40 V) it was expected that the photodiodes were operating in the avalanche regime.

The leakage current density, J_d, of the devices was calculated using the measured leakage current and is presented in Fig. 5.2. At the maximum applied reverse bias (V_R = 40 V; E_f = 345 kV cm^{-1} and E_f = 361 kV cm^{-1} for the 200 µm and 400 µm devices respectively (assuming E_f was uniform and across only the depleted region)), the leakage current densities were 11.9 nA cm^{-2} ± 1.3 nA cm^{-2} and 5.0 nA cm^{-2} ± 0.3 nA cm^{-2} for the 200 µm and 400 µm devices, respectively. The difference in leakage current density between the 200 µm and 400 µm devices indicated a significant surface leakage current component (Owens, 2012).

The best (lowest) leakage current density previously reported for $Al_xGa_{1-x}As$ X-ray photodiodes at room temperature was 2.2 nA cm^{-2}, at E_f = 100 kV cm^{-1} (Barnett et al., 2013b). At the same E_f (equivalent to an applied reverse bias of 5 V for the present devices, assuming E_f was uniform and across only the depleted region), the $Al_{0.6}Ga_{0.4}As$ devices had leakage current densities of 0.3 nA cm^{-2} ± 1.3 nA cm^{-2} and 0.1 nA cm^{-2} ± 0.3 nA cm^{-2} for the 200 µm and 400 µm diameter devices, respectively. The reported leakage current densities were also lower than recently studied GaAs devices: at 20 °C and E_f = 50 kV cm^{-1}, a 200 µm diameter GaAs device with a 10 µm i layer was measured to have a leakage current density of 6 nA cm^{-2} ± 1 nA cm^{-2} (Lioliou et al., 2018). At the same E_f (equivalent to an applied reverse bias of 2 V for the present devices), the $Al_{0.6}Ga_{0.4}As$ devices had leakage current densities of 0.1 nA cm^{-2} ± 1.3 nA cm^{-2} and 1.5 pA cm^{-2} ± 0.3 nA cm^{-2} for the 200 µm and 400 µm devices, respectively.

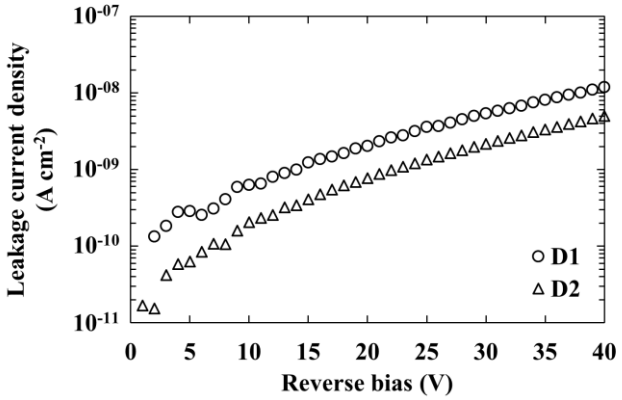

Fig. 5.2. Leakage current density as a function of applied reverse bias for the 200 µm device (circles) and the 400 µm device (triangles) at 20 °C. The associated uncertainties were omitted for clarity.

5.4.2 Capacitance measurements as a function of applied bias

Capacitance as functions of forward and reverse applied bias was measured for both $Al_{0.6}Ga_{0.4}As$ p^+-i-n^+ photodiodes under dark conditions and at a temperature of 20 °C. An HP 4275A LCR Meter (signal magnitude 50 mV rms; frequency 1 MHz) and a Keithley 6487 picoammeter/voltage source were used to measure the capacitance and bias the detectors respectively. The $Al_{0.6}Ga_{0.4}As$ photodiodes were installed in a custom test harness and placed within a TAS Micro MT climatic cabinet for temperature control as per **Section 3.6.1**. National Instruments LabVIEW software was used to automate the characterisation routine. The temperature was set to 20 °C and left for 1 hour before measuring to ensure thermal equilibrium

and stabilisation. Fig. 5.3 presents the capacitance as a function of forward (Fig. 5.3a) and reverse (Fig. 5.3b) bias for the 200 µm and 400 µm devices.

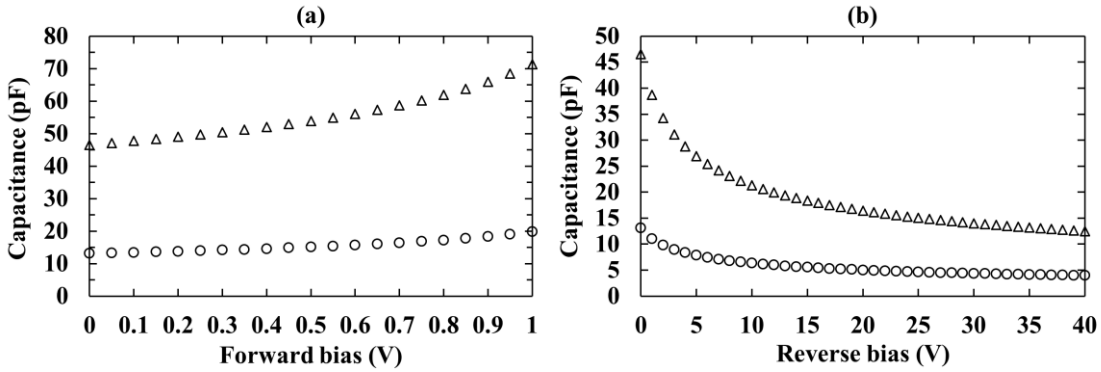

Fig. 5.3. Capacitance as a function of applied forward bias (a) and applied reverse bias (b) for the 200 µm (circles) and 400 µm (triangles) devices, at 20 °C. The empty package capacitance has not been subtracted. The associated uncertainties were smaller than the symbols.

The measured capacitance increased as a function of forward bias for both devices; increasing from 13.13 pF ± 0.02 pF at 0 V to 19.79 pF ± 0.03 pF at 1 V for the 200 µm device, and 46.56 pF ± 0.08 pF at 0 V to 71.32 pF ± 0.11 pF at 1 V for the 400 µm device. Conversely, the devices' capacitances decreased as functions of reverse bias. The capacitance of the 200 µm device reduced from 13.13 pF ± 0.02 pF at 0 V to 3.96 pF ± 0.01 pF at 40 V; the capacitance of the 400 µm device reduced from 46.55 pF ± 0.08 pF at 0 V to 12.51 pF ± 0.06 pF at 40 V. The stated uncertainties included those associated with a single measurement as well as those associated with disconnecting and reconnecting the measured devices to the test harness.

As the devices were measured after packaging, the measured capacitance, C_d, included both the diode capacitance, C_D (units of F), and the package capacitance, C_P (units of F). C_P was removed by assuming a constant capacitance density as a function of device area. The capacitance density of the 200 µm diameter device and the 400 µm diameter device at each applied bias were compared, and the empty package capacitance calculated. A mean average empty package capacitance (1.29 pF ± 0.19 pF (rms deviance)) was calculated for C_P and subsequently subtracted from C_d of each diode as a function of reverse bias. The diode capacitance densities for the 200 µm and 400 µm diameter devices are shown in Fig. 5.4.

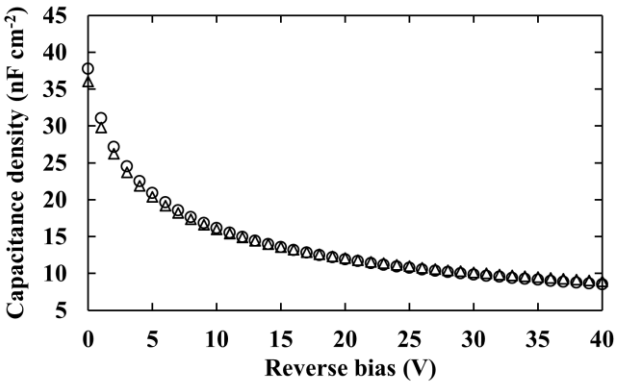

Fig. 5.4. Capacitance density as a function of applied reverse bias for the 200 µm device (circles) and the 400 µm device (triangles) at 20 °C. The associated uncertainties were smaller than the symbols.

The depletion width, W_D, was calculated as per **Section 3.4.2** and has been plotted as a function of applied reverse bias in Fig. 5.5.

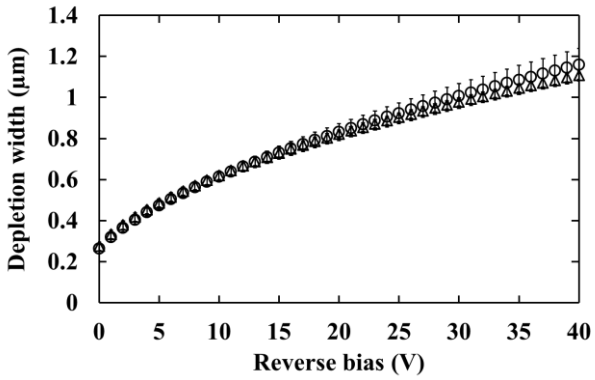

Fig. 5.5. Calculated depletion width for the 200 µm device (circles) and the 400 µm device (triangles) at 20 °C, taking into account the empty package capacitance (1.29 pF).

The depletion width of the 200 µm device increased from 0.26 µm ± 0.02 µm at 0 V to 1.16 µm ± 0.08 µm at 40 V. Similarly, the depletion width of the 400 µm device increased from 0.28 µm ± 0.02 µm at 0 V to 1.11 µm ± 0.02 µm at 40 V. The stated uncertainty of the depletion width includes the uncertainty associated with the depletion layer capacitance and the uncertainty associated with the Debye length of the $Al_{0.6}Ga_{0.4}As$ p^+-i-n^+ photodiodes (0.02 µm) (Stradling & Klipstein, 1991). The results indicated that a further increase in depletion width would be expected if the applied reverse bias was increased beyond 40 V, indicating that the devices were not fully depleted at 40 V reverse bias. This was consistent with the device structure, which has a 2 µm i layer (see Table 5.1).

The carrier concentration of the i layer, N_{eff}, was calculated as per **Section 3.4.2**. The carrier concentration throughout the intrinsic region was calculated to be approximately 4.0×10^{16} cm^{-3} for both devices. The carrier concentration as a function of distance below the p$^+$-i junction for the $Al_{0.6}Ga_{0.4}As$ detectors is shown in Fig. 5.6. Variation in the apparent carrier concentration between the 200 µm and 400 µm devices was within the uncertainty of the measurements.

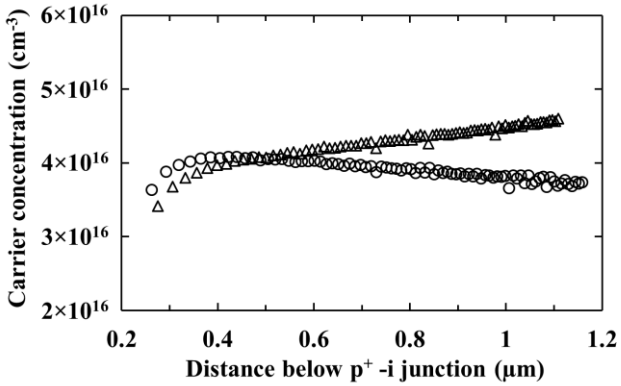

Fig. 5.6. Carrier concentration as a function of distance below the p$^+$-i junction for the 200 µm device (circles) and the 400 µm device (triangles) at 20 °C, taking into account the empty package capacitance (1.29 pF). The associated uncertainties were omitted for clarity.

5.5 Room temperature X-ray spectroscopy

5.5.1 Measurements with an ^{55}Fe radioisotope X-ray source

Each diode was connected, in turn, to the same custom-made low-noise charge-sensitive preamplifier of feedback-resistorless design (see **Section 2.7**). The preamplifier used a Vishay 2N4416A Si JFET as the input transistor. In each case, the preamplifier was connected to an Ortec 572A shaping amplifier and an Ortec 927 ASPEC multi-channel analyser (MCA). An ^{55}Fe radioisotope X-ray source (≈ 157 MBq) emitting characteristic Mn Kα (5.9 keV) and Mn Kβ (6.49 keV) X-rays was placed ≈ 4 mm above each $Al_{0.6}Ga_{0.4}As$ detector in turn. The resultant spectrometers S_{200} (employing the 200 µm diameter photodiode) and S_{400} (employing the 400 µm diameter photodiode) were characterised in turn. Each was installed inside a TAS Micro MT climatic cabinet as per **Section 3.7.1**. The climatic cabinet temperature was set to 20 °C and left for 1 hour in order to ensure thermal equilibrium.

^{55}Fe X-ray spectra were accumulated with S_{200} and S_{400}. The shaping time, τ, of the shaping amplifier was kept at 2 µs throughout the measurements so that direct comparisons could be made between spectra. Since the two detectors had different active areas, the live time limits of each spectrum were set differently: spectra accumulated with S_{200} had a live time limit of 1500 s;

spectra accumulated with S_{400} had a live time limit of 800 s. For S_{200}, spectra were accumulated with the detector operated at reverse biases from 0 V to 40 V in 2 V steps. For S_{400}, spectra were accumulated with the detector operated at reverse biases from 30 V to 40 V in 2 V steps; the photopeak could not be resolved from the so called zero energy noise peak at detector reverse biases < 30V with S_{400}.

The ^{55}Fe X-ray spectra obtained with each spectrometer can be seen in Fig. 5.7. For clarity, not all spectra obtained are plotted; instead, a number of reverse biases have been selected to show the change in spectroscopic response. The form of response is consistent with an avalanche photodiode; this is further exemplified by plotting the change in main (largest) photopeak centroid position (corrected for changes in zero energy noise peak position) as a function of applied detector reverse bias, this is shown in Fig. 5.8. Work on $Al_{0.8}Ga_{0.2}As$ avalanche photodiodes has been reported previously (Barnett, 2011) (Tan et al., 2011) (Gomes et al., 2014) (Barnett et al., 2011a) (Barnett et al., 2011b). The secondary peak observed at the left hand side of the main peak is discussed in **Section 5.5.2**.

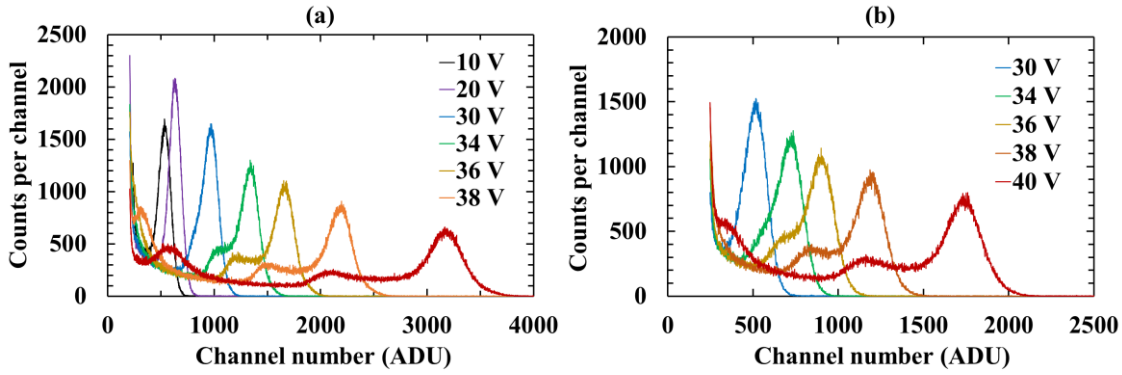

Fig. 5.7. Accumulated ^{55}Fe X-ray spectra obtained with spectrometer S_{200} (a) and spectrometer S_{400} (b). All spectra were accumulated at the same shaping time (2 µs) and at constant temperature (20 °C). The different peaks are distinguished and explained in **Section 5.5.2**.

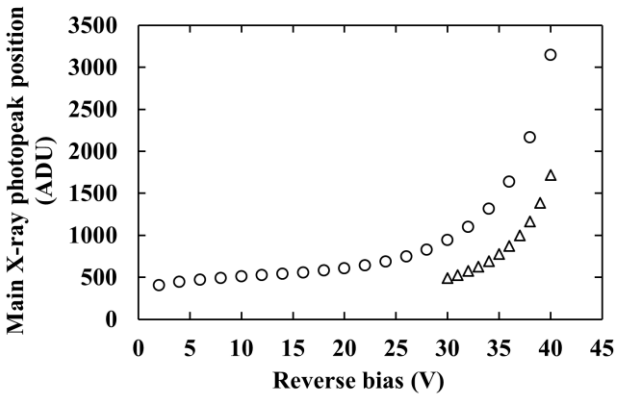

Fig. 5.8. The position of the main (largest) ^{55}Fe X-ray photopeak in each spectrum (corrected for any changes in zero energy noise peak position) as a function of applied detector reverse bias for spectrometer S_{200} (circles) and spectrometer S_{400} (triangles).

Gaussian fitting was applied to the main photopeak from the ^{55}Fe radioisotope X-ray source assuming that it was composed of Mn Kα (5.9 keV) and Mn Kβ (6.49 keV) X-rays from the ^{55}Fe radioisotope X-ray source; the relative emission ratio of these X-rays (Schötzig, 2000), and the relative quantum efficiency of the detector at these energies, were taken into account. Each spectrum was energy calibrated using the position of its zero energy noise peak and the fitted Mn Kα peak, with the assumption of a linear variation of detected and output charge with energy. The FWHM at 5.9 keV was determined for all spectra. Examples of the spectra with the Gaussians fitted are shown in Fig. 5.9 for S_{200} with detector applied biases of 10 V (Fig. 5.9a) and 38 V (Fig. 5.9b). Fig. 5.10 shows the determined energy resolutions (FWHM at 5.9 keV) of the S_{200} and S_{400} spectrometers as functions of applied detector reverse bias.

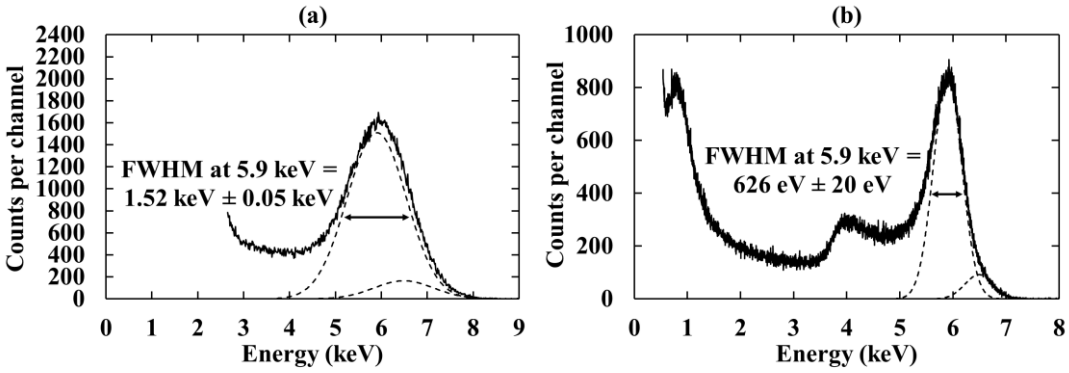

Fig. 5.9. Spectrum accumulated with spectrometer S_{200} at an applied detector reverse bias of 10 V (a) and 38 V (b), when illuminated with an ^{55}Fe radioisotope X-ray source. The dashed lines are the fitted Mn Kα and Mn Kβ peaks.

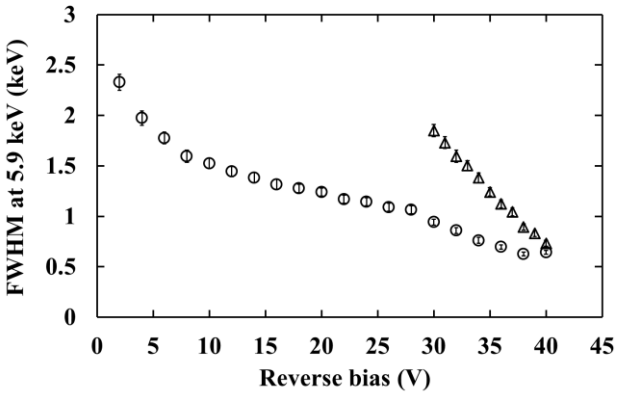

Fig. 5.10. Determined energy resolution (FWHM at 5.9 keV) as a function of applied detector reverse bias for spectrometer S_{200} (circles) and S_{400} (triangles).

The measured energy resolution (FWHM at 5.9 keV) of the presently reported devices was better than any previously reported $Al_xGa_{1-x}As$ X-ray photodiode at room temperature. The best previously reported energy resolution for non-avalanche mode $Al_xGa_{1-x}As$ X-ray detectors was 756 eV ± 30 eV FWHM at 5.9 keV at 20 °C, using square, 200 µm by 200 µm, 3 µm i layer, $Al_{0.2}Ga_{0.8}As$ p^+-i-n^+ mesa X-ray photodiodes (see **Section 4.5.1**). Excluding separate absorption and multiplication region avalanche photodiodes, the best previously reported energy resolution for avalanche mode $Al_xGa_{1-x}As$ X-ray detectors was 1.21 keV FWHM at 5.9 keV at room temperature (Barnett, 2011), using a $Al_{0.8}Ga_{0.2}As$ p^+-p^--n^+ circular device, 200 µm in diameter. Similar energy resolutions have been reported for GaAs/$Al_{0.8}Ga_{0.2}As$ separate absorption and multiplication region avalanche photodiodes (SAM APDs) (1.08 keV FWHM at 5.9 keV at room temperature (Gomes et al., 2014)). The presently reported energy resolution was also improved relative to recent studies of other wide bandgap materials, such as $Al_{0.52}In_{0.48}P$. Non-avalanche mode, 217 µm ± 15 µm and 409 µm ± 28 µm diameter, 6 µm i layer, $Al_{0.52}In_{0.48}P$ p^+-i-n^+ circular mesa X-ray photodiodes were reported to have energy resolutions of 890 eV and 1.05 keV FWHM at 5.9 keV respectively (Zhao et al., 2019). Avalanche mode, 200 µm diameter, $Al_{0.52}In_{0.48}P$ p^+-i-p^--n^+ circular mesa X-ray photodiodes were reported to have an energy resolution of 682 eV FWHM at 5.9 keV (Auckloo et al., 2016). At optimal operating conditions, and at 20 °C, the presently reported spectrometers had a measured energy resolution of 626 eV ± 20 eV (at V_R = 38 V) and 732 eV ± 30 eV (at V_R = 40 V) FWHM at 5.9 keV, for $S_{200µm}$ and $S_{400µm}$ respectively. It should be noted that the energy resolution presently reported is still modest when compared with those measured using GaAs detectors and state-of-the-art Si detectors. For instance, a 5 × 5 GaAs diode array (40 µm i layer) has been previously investigated for X-ray detection, and reported an energy resolution of 266 eV FWHM at 5.9 keV at room temperature when coupled to ultra-low-noise front-end electronics (Owens et al., 2001). A Silicon Drift Detector (SDD) coupled to ultra-low-noise CMOS readout electronics was reported with an

energy resolution of 141 eV FWHM at 5.9 keV at room temperature (Bertuccio et al., 2015), and a Si depleted p channel field effect transistor (DEPFET) detector was reported with an energy resolution of 134 eV FWHM at 5.9 keV at room temperature (Müller-Seidlitz et al., 2016).

5.5.2 Origin of the secondary peak in the obtained X-ray spectra

As can be seen in Fig. 5.7, at high detector reverse bias (≥ 34 V for S_{200}; ≥ 36 V for S_{400}) a secondary peak was present at the left hand side of the main photopeak. The separation between the secondary and main peak increased as the detector reverse bias was increased. Fig. 5.11 shows how the positions of the main and secondary peaks change as functions of applied bias for both spectrometers. A third peak, close to the low energy threshold, was also present in spectra obtained with S_{200} at detector reverse biases ≥ 38 V, and with S_{400} at a detector reverse bias of 40 V. This third peak was hypothesised to be from Al Kα (1.49 keV (Sánchez et al., 2003)) X-rays from detector self-fluorescence; these X-rays became detectable due to improvement in the low energy X-ray performance of the spectrometers at high detector reverse biases as a consequence of the avalanche multiplication.

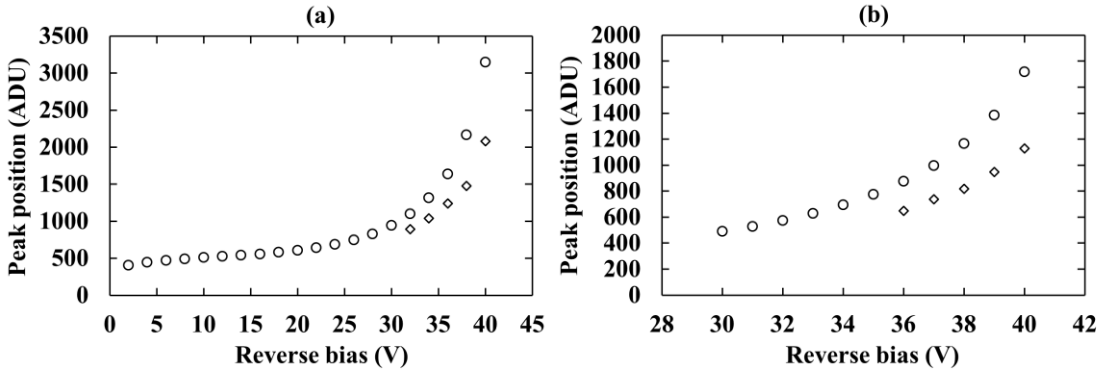

Fig. 5.11. The position of the main (circles) and secondary (diamonds) ^{55}Fe X-ray photopeak in each spectrum (corrected for any changes in zero energy noise peak position) as a function of applied detector reverse bias for spectrometer S_{200} (a) and spectrometer S_{400} (b).

Peaks similar to the secondary peak seen here have also been recorded with SAM APDs made from GaAs-$Al_{0.8}Ga_{0.2}As$ (Gomes et al., 2014) and $Al_{0.52}In_{0.48}P$ (Auckloo et al., 2016). In those cases, the secondary peaks were attributed to holes, created in the n region(s) of the detectors below the avalanche layer, receiving the maximum possible hole initiated avalanche multiplication as they benefitted from the full width of the avalanche region (see **Section 2.9.3**). However, other experimental and theoretical work on $Al_{0.8}Ga_{0.2}As$ p^+-p^--n^+ X-ray avalanche photodiodes indicated that pure hole initiated multiplication of this type played no significant part

in spectrum formation due to loss of the holes (e.g. by recombination) before those charge carriers could reach the avalanche region (Barnett, 2011) (Barnett et al., 2011a).

Furthermore, in the case of the SAM APDs described by Auckloo et al. (2016) and Gomes et al. (2014), the main peak in each spectrum was formed by electrons. These were created by photons absorbed in a low doped absorption region and subsequently transported to a relatively thin avalanche region; they underwent maximum pure electron multiplication since they benefitted from the whole of the width of the avalanche region (see **Section 2.9.3**). This is a different mechanism of formation of main peak than was present in the p^+-p^--n^+ APDs (Barnett et al., 2011a) (Barnett et al., 2011b), where the main peak was formed from both electrons and holes which were created in the p^- layer of the device. This p^- layer was also the avalanche region of that device and consequently charge carriers created there received a mixed multiplication, which would normally be dependent on the position of photon absorption within the layer. However, the doping profile in the particular case of the previously reported p^+-p^--n^+ device was said to be such as to compensate for this position dependence (Barnett, 2011) (Barnett et al., 2011a) (Barnett et al., 2011b); a simulated spectrum showing the morphology which would have been expected without this special doping profile was presented as Fig. 3 in Barnett et al. (2011a).

Those earlier reported p^+-p^--n^+ APDs did show an additional peak, but this was at the right hand (high energy) side of the main peak. This additional peak was shown to be a consequence of electrons created by photons absorbed in the p^+ region of the device diffusing towards the p^- layer and subsequently receiving the maximum pure electron initiated multiplication. It should be noted that, in that case, the only electrons that reached the p^- layer were those created within 0.16 µm of the p^+-p^- junction. Thus, in that case, the 0.16 µm of material close to the p^+-p^- junction acted analogously to the absorption region in the SAM APDs. In the case of the present devices, which are p^+-i-n^+ APDs rather than SAM APDs, the absorption and multiplication regions are not separate. Consequently, a spectrum morphology as per Fig. 3 of Barnett et al. (2011a) was expected to be obtained, assuming there was no contribution from holes created in the device's n^+ layer or the non-depleted portion of its i layer. If there was a contribution from holes created in those regions, the spectrum expected to be accumulated with the present $Al_{0.6}Ga_{0.4}As$ devices would be similar to Fig. 3 of Barnett et al. (2011a) but with a further additional peak (akin to that from the p^+-p^--n^+ device's p^+ layer) but at the low energy side of the main (p^- layer) peak.

However, the morphologies of the spectra obtained with the present devices appear to be more similar to those obtained with the SAM APDs than from the p^+-p^--n^+ APD spectra and earlier modelling. A superficial similarity between the current spectra (e.g. Fig. 5.9b) and Fig. 3 of Barnett et al. (2011a) is noted, but in the present case the depletion region is thicker (1.16 µm

± 0.08 µm and 1.11 µm ± 0.02 µm at V_R = 40 V for the 200 µm and 400 µm diameter devices respectively) than the p^+ region (0.5 µm), and both are relatively thin. Consequently, even if the whole of the p^+ was active, the number of counts from the depletion region should be much greater than the number from the p^+ region. However, the spectrum shape does not indicate this: the number of counts within the saddle between the main and secondary peaks is relatively small compared with the number of counts in the main peak. Consequently, the origin of the spectra morphologies obtained with the present devices is currently unknown. It is noted that this is not the first time that additional peaks of unknown origin have occurred in X-ray APD spectra; the additional peaks in the earlier $Al_{0.8}Ga_{0.2}As$ p^+-p^--n^+ X-ray spectra were reported some years before they were explained (Barnett et al., 2011a).

5.6 Impact ionisation coefficients and multiplication factors

As shown by Fig. 5.7, Fig. 5.8, and Fig. 5.11, the spectroscopic response of the 200 µm and 400 µm diameter devices changed as a function of applied reverse bias in a manner consistent with an avalanche photodiode (see **Section 2.9**). Before determining the apparent multiplication factors, it is important to note that through extensive characterisation, the charge output of the custom-made low-noise charge-sensitive preamplifier used in this work has been found to be sensitive to changes in detector capacitance (≥ 0.2 pF); where a reduction in detector capacitance caused an increase in output voltage. Since the capacitance of the 200 µm and 400 µm diameter devices decreased as a function of applied reverse bias within the investigated range (see Fig. 5.3), the change in spectroscopic response due to the change in capacitance must be understood before the apparent gain due to avalanche multiplication can be calculated.

Since the non-avalanche photopeak of the 400 µm diameter device could not be separated from the so called zero energy noise peak, only the 200 µm diameter device was considered. The 200 µm diameter device was connected to the same custom-made low-noise charge-sensitive preamplifier as used in **Section 5.5.1**. A stabilised tail pulse generator (Berkeley Nucleonics Corporation model BH-1) was connected to the test signal input of the custom preamplifier, such that the change in apparent conversion gain of the preamplifier as a result of change in applied bias of the connected detector could be measured. Spectra were accumulated with the detector operated at reverse biases from 10 V (assumed to be operating in non-avalanche mode) to 40 V in 10 V steps at a shaping time, τ, of 2 µs and a live time limit of 300 s, at 20 °C. The experiment was performed at four different pulse generator amplitudes (test signal input charges) in order to ensure there was no unexpected variation of preamplifier response as a function of pulse generator amplitude; no variation in this regard was detected.

The position of the pulser peak (corrected for any changes in zero energy noise peak position) was found to increase by 17 % ± 1 % as V_R was increased from 10 V to 40 V. Previous investigations of the custom-made preamplifier found no appreciable change in spectral response as a function of detector current for currents ≤ 6 pA. Consequently, the change in pulser peak position reported here was attributed solely to the change in capacitance of the detector. The mean change in conversion factor per unit capacitance was measured to be 6.7 % pF^{-1} ± 0.4 % pF^{-1} (rms deviance). The change in conversion factor due to change in capacitance was subtracted from the measured peak positions (see Fig. 5.11) and can be seen in Fig. 5.12.

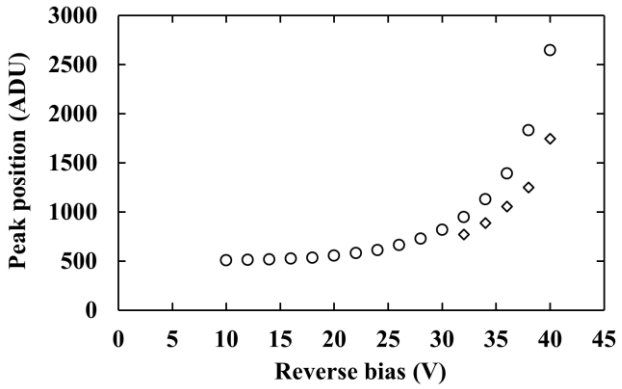

Fig. 5.12. The position of the main (circles) and secondary (diamonds) ^{55}Fe X-ray photopeak in each spectrum (corrected for any changes in detector capacitance and zero energy noise peak position) as a function of applied detector reverse bias for spectrometer S_{200}.

The apparent multiplication factor, *M*, was calculated for the spectrometer S_{200} by calculating the ratio between the fitted primary 5.9 keV peak position at each bias and the fitted primary 5.9 keV peak position at unity gain (M = 1, assumed to be achieved at a reverse bias of 10 V applied to the detector). The same procedure was used for calculating the secondary 5.9 keV peak apparent multiplication factor, assuming unity gain at 10 V applied reverse bias. The apparent multiplication factor for both peaks can be seen in Fig. 5.13.

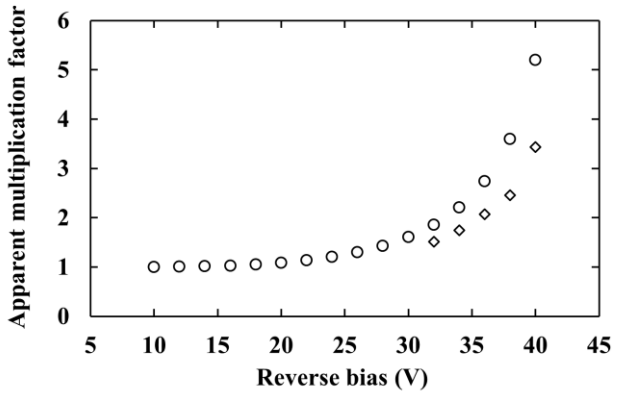

Fig. 5.13. Apparent multiplication factor for the main (circles) and secondary (diamonds) ^{55}Fe X-ray photopeak in each spectrum (corrected for any changes in detector capacitance and zero energy noise peak position) as a function of applied detector reverse bias for spectrometer S_{200}.

Apparent multiplication factors of 5.20 and 3.43 were measured at an applied reverse bias of 40 V for the primary and secondary ^{55}Fe X-ray photopeaks, respectively. The tertiary peak mentioned in **Section 5.5.2** appeared to have the same avalanche multiplication as the secondary peak, assuming that the third peak is indeed a result of Al Kα X-ray fluorescence. The multiplication factors were larger than expected; at 40 V reverse bias and assuming that the electric field strength was uniform and across only the depleted region (see Fig. 5.5), M_e = 1.22, and M_h = 1.18 were calculated given the material's accepted impact ionization coefficients (Plimmer et al., 2000). Given this, the measured relative positions of the peaks were considered in an attempt to establish if there was an alternative 'effective' field strength that would explain the results and maintain the accepted impact ionization coefficients. Two approaches were considered: one starting from the position of the primary peak; one starting from the position of the secondary peak.

The first approach calculated the expected multiplication of the secondary peak given the apparent multiplication of the primary peak. Thus, it was considered that the primary peak may be a consequence of maximum pure electron multiplication; if this was the case then perhaps the secondary peak was from either maximum pure hole multiplication or mixed multiplication. Given the material's accepted impact ionization coefficients (Plimmer et al., 2000), if the primary peak's apparent multiplication factor of 5.20 was a consequence of maximum pure electron multiplication, then the secondary peak's multiplication, M, would be 4.66 if it was a result of maximum pure hole multiplication, or $4.66 < M < 5.20$ if it was a consequence of mixed multiplication. Since the measured multiplication factor of the secondary peak was 3.43, neither explanation in the first case fits the measurements.

The second approach calculated the expected multiplication of the primary peak given the apparent multiplication of the secondary peak. Thus, correspondingly with the first case, if the secondary peak's measured multiplication (3.43) was a consequence of maximum pure hole multiplication then, given the accepted impact ionization coefficients, a primary peak multiplication of 3.80 was expected if it was a consequence of maximum pure electron multiplication, whereas 5.20 was measured experimentally.

Since both approaches indicated that the measured multiplication factors could not be explained by the accepted ratio between the electron and hole impact ionization coefficients, it was considered that it may be informative to calculate the apparent impact ionization coefficients implied by the experimental multiplication factor measurements. With the assumption that the primary peak's multiplication was a result of maximum pure electron multiplication and the secondary peak's multiplication was a result of maximum pure hole multiplication, the apparent impact ionization coefficients were calculated and are presented in Fig. 5.14. Since the secondary peak was only clearly resolved at reverse biases ≥ 32 V, this is the minimum reverse bias for which the apparent impact ionization coefficients could be determined. The values were calculated by assuming the McIntyre local model (see **Section 2.9.2**)

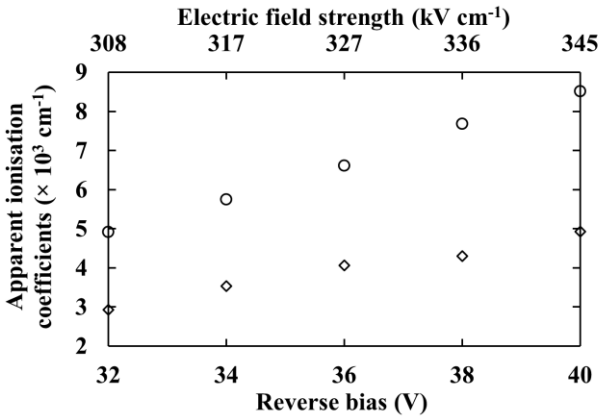

Fig. 5.14. Apparent ionization coefficients for electrons, α, (circles) and holes, β, (diamonds) as a function of applied detector reverse bias for spectrometer S_{200}. The electric field strength, assuming it was uniform and across only the depleted region, has been plotted.

The apparent electron and hole impact ionization coefficients were substantially greater than the generally accepted values reported by Plimmer et al. (2000). For example, at an applied reverse bias of 40 V (E_f = 345 kV cm^{-1}), apparent ionisation coefficients α = 8513 and β = 4930 were measured, whereas the accepted ionisation coefficients at this field strength are α = 930 and β = 742 (Plimmer et al., 2000). The origin of this discrepancy is currently unknown.

5.7 Electron-hole pair creation energy measurements

The electron-hole pair creation energy, ω_{EHP}, at 25 °C ± 1 °C was determined for $Al_{0.6}Ga_{0.4}As$ relative to that of GaAs (ω_{EHP} = 4.19 eV ± 0.03 eV (Bertuccio & Maiocchi, 2002)) as per **Section 3.8**. This method was previously used to determine ω_{EHP} in $Al_{0.2}Ga_{0.8}As$ (see **Section 3.8**), $Al_{0.8}Ga_{0.2}As$ (Barnett et al., 2012b), $Al_{0.52}In_{0.48}P$ (Butera et al., 2018a), and $In_{0.5}Ga_{0.5}P$ (Butera et al., 2018b), using a GaAs reference detector, as well as SiC (Bertuccio & Casiraghi, 2003) and GaAs (Bertuccio & Maiocchi, 2002) using a Si reference detector. Care was taken to ensure that avalanche multiplication did not affect the measurement. The layer structure of the well characterised GaAs p^+-i-n^+ mesa X-ray photodiode (200 µm diameter) (Lioliou & Barnett, 2016) which was used as a reference device is shown in Table 3.2.

The presently reported 200 µm $Al_{0.6}Ga_{0.4}As$ detector and the GaAs reference detector (also 200 µm diameter) were connected in parallel to the same custom-made low-noise charge-sensitive preamplifier of feedback-resistorless design, as that used in **Section 3.8.1**. The ^{55}Fe radioisotope X-ray source was positioned above each detector in turn taking great care not to disturb any other aspect of the apparatus (American National Standards Institute, 1989). The housing, in which the detectors and preamplifier were installed, was continually purged with dry N_2 for the duration of the measurement in order to maintain a dry N_2 environment (< 5 % relative humidity) to eliminate any humidity related effects (Barnett et al., 2013b). The live time limit for each spectrum was 2,000 s. X-ray spectra were accumulated with the GaAs reference detector at its optimum reverse bias of 5 V, and the $Al_{0.6}Ga_{0.4}As$ photodiode at a reverse bias of 10 V. This reverse bias was chosen in order to ensure the detector was operating in non-avalanche mode. The shaping time of the shaping amplifier was set to 10 µs (the optimal shaping time for the dual detector configuration). The temperature of the detector was measured and remained at 25 °C ± 1 °C for the duration of the experiment. The experimental system was identical to that of **Section 3.8.1**.

The spectra obtained with the $Al_{0.6}Ga_{0.4}As$ and GaAs photodetectors were fitted with Gaussians for the Mn Kα (5.9 keV) and Mn Kβ (6.49 keV) emissions of ^{55}Fe in the accepted ratio (Schötzig, 2000), taking into account the detectors' relative detection efficiencies for the Mn Kα and Mn Kβ photons, as shown in Fig. 5.15. Fig. 5.15 presents representative spectra obtained with the $Al_{0.6}Ga_{0.4}As$ and GaAs detectors when they were connected in parallel and illuminated separately; the spectra have been normalised in terms of peak height and are presented within the same figure for the convenience of the reader. Charge calibration was achieved using the positions of the zero energy noise peak of the preamplifier and the 5.9 keV Mn Kα peak observed with the reference GaAs diode, together with the accepted ω_{EHP} value of GaAs (4.19 eV ± 0.03 eV (Bertuccio & Maiocchi, 2002)). The dashed and dotted lines are the fitted Mn Kα and Mn Kβ peaks for the $Al_{0.6}Ga_{0.4}As$ and GaAs detectors respectively.

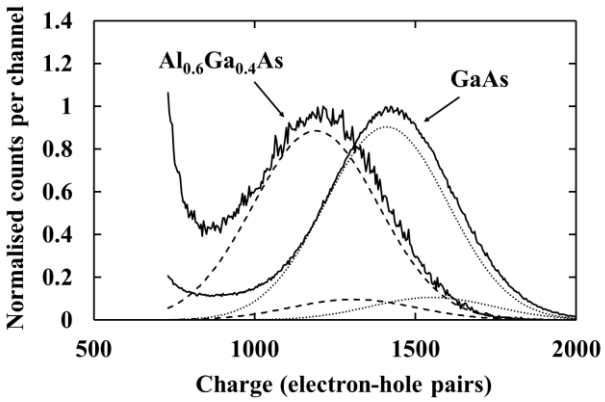

Fig. 5.15. Accumulated spectra at 25 °C ± 1 °C with an ^{55}Fe radioisotope X-ray source placed above the each detector (solid line as indicated). The $Al_{0.6}Ga_{0.4}As$ detector was operated at a reverse bias of 10 V, and with a shaping amplifier shaping time of 10 µs. The GaAs detector was operated at a reverse bias of 5 V and with a shaping amplifier shaping time of 10 µs. The detectors were connected in parallel but illuminated individually in turn; their spectra have been overlaid on the same calibrated charge scale. The spectra have been normalised using their associated centroid peak heights. The Mn Kα and Mn Kβ fitted Gaussian peaks of the $Al_{0.6}Ga_{0.4}As$ detector (dashed lines) and the GaAs reference detector (dotted lines) have also been plotted.

Since the electron-hole pair creation energy of $Al_{0.6}Ga_{0.4}As$ and GaAs (ω_{EHP} = 4.19 eV ± 0.03 eV (Bertuccio & Maiocchi, 2002)) differ, so too does the average number of charge carriers created by the absorption of a photon of energy E (Barnett et al., 2012b) in each material (as shown by the different positions of the peaks' centroids in Fig. 5.15). Therefore, assuming complete charge collection, the electron-hole pair creation energy of $Al_{0.6}Ga_{0.4}As$ can be calculated as per **Section 3.8**. The electron-hole pair creation energy of $Al_{0.6}Ga_{0.4}As$ was found to be 4.97 eV ± 0.12 eV at 25 °C ± 1 °C.

As discussed in **Section 3.8.2**, the measured electron hole pair creation energies of $Al_{0.8}Ga_{0.2}As$ (Barnett et al., 2013a) and $Al_{0.2}Ga_{0.8}As$ (see **Section 3.8**) demonstrated that the Klein relationship between the electron-hole pair creation and bandgap energy is unsatisfactory at least for some materials. Subsequent electron hole pair creation energy measurements of $Al_{0.52}In_{0.48}P$ (Butera et al., 2018a) and $In_{0.5}Ga_{0.5}P$ (Butera et al., 2018b) were also found to lay between the two supposed Klein branches (see **Section 3.8.2**), adding additional weight to the conclusion that the Klein model is unphysical.

The Bertuccio-Maiocchi-Barnett (BMB) relationship (see **Section 3.8.2**) suggests a linear relationship between bandgap and electron-hole pair creation energy which differs from the

"main" and "secondary" Klein branches, and was used to predict (correctly within the associated uncertainties) the electron-hole pair creation energies of $Al_{0.2}Ga_{0.8}As$ (see **Section 3.8**), $Al_{0.52}In_{0.48}P$ (Butera et al., 2018a), and $In_{0.5}Ga_{0.5}P$ (Butera et al., 2018b). The experimental measurements of these materials' electron-hole pair creation energies were then used to refine the BMB relationship, such that

$$\omega_{EHP} = (1.54 \pm 0.08)E_g + (1.89 \pm 0.14). \quad (5.3)$$

From this it can be seen that Eq. 5.3 also correctly predicts an electron-hole pair creation energy for $Al_{0.6}Ga_{0.4}As$ of 5.02 eV ± 0.16 eV at room temperature, which agrees with the experimental value obtained in the current work (4.97 eV ± 0.12 eV). Adding this new value to the dataset, the BMB relationship can be refined to be,

$$\omega_{EHP} = (1.54 \pm 0.07)E_g + (1.89 \pm 0.12). \quad (5.4)$$

The dataset including the new value for $Al_{0.6}Ga_{0.4}As$ is presented in Fig. 5.16.

Strictly speaking, despite the fit of the new datum within the set, the value for the electron-hole pair creation energy determined for $Al_{0.6}Ga_{0.4}As$ should be considered as an upper limit of the parameter in this material, since it cannot be guaranteed that the collection of the charge generated was perfect in its totality.

To demonstrate the inadequacy of the Klein relationship to accurately model the relationship between electron-hole pair creation energy and bandgap, it is informative to consider its predictions for the electron-hole pair creation energy of $Al_{0.6}Ga_{0.4}As$. If $Al_{0.6}Ga_{0.4}As$ were to lie on the main Klein function branch, a value of ω_{EHP} = 6.28 eV would have been expected. If $Al_{0.6}Ga_{0.4}As$ were situated on the secondary Klein function branch, a value of ω_{EHP} = 4.18 eV would have been expected. However, neither of these values agree with the experimentally measured value (4.97 eV ± 0.12 eV). Therefore, $Al_{0.6}Ga_{0.4}As$ is another material that does not fit either of the Klein branches.

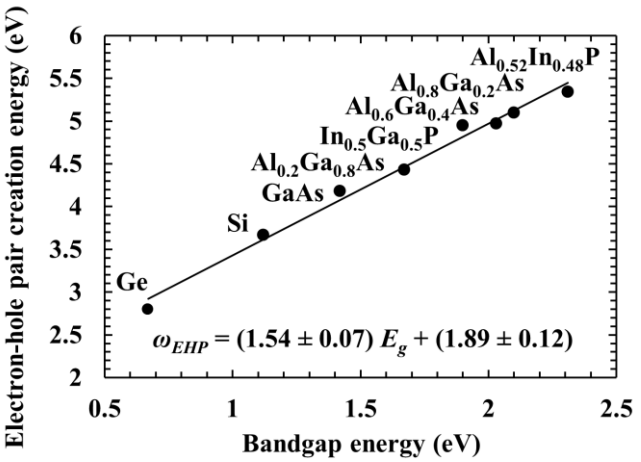

Fig. 5.16. Electron-hole pair creation energies for Ge, Si, GaAs, $Al_{0.2}Ga_{0.8}As$, $Al_{0.6}Ga_{0.4}As$, $Al_{0.8}Ga_{0.2}As$, and $Al_{0.52}In_{0.48}P$ plotted as a function of their respective bandgap energies at ≈ 300 K.

5.8 Conclusion

For the first time, $Al_{0.6}Ga_{0.4}As$ p^+-i-n^+ mesa X-ray photodiodes have been demonstrated to operate as photon counting spectroscopic X-ray detectors at room temperature. The measured energy resolution (FWHM at 5.9 keV) of the presently reported devices (see **Section 5.5.1**) was better than any previously reported $Al_xGa_{1-x}As$ X-ray photodiodes at room temperature (756 eV ± 30 eV FWHM at 5.9 keV at 20 °C (see **Section 4.5.1**)) and comparable to that measured in recent studies of other wide bandgap III-V materials, such as $Al_{0.52}In_{0.48}P$ (e.g. 682 eV FWHM at 5.9 keV at 20 °C (Auckloo et al., 2016)). At optimal operating conditions, and at 20 °C, the presently reported spectrometers had a measured energy resolution of 626 eV ± 20 eV (at V_R = 38 V) and 732 eV ± 30 eV (at V_R = 40 V) FWHM at 5.9 keV, for $S_{200\mu m}$ and $S_{400\mu m}$ respectively.

The spectroscopic response of the 200 µm and 400 µm diameter devices changed as a function of applied reverse bias in a manner consistent with an avalanche photodiode (see **Section 5.5.1**). At high detector reverse bias, secondary and tertiary peaks were present at the left hand side of the main photopeak (see Fig. 5.7). The third peak was hypothesised to be from Al Kα (1.49 keV (Sánchez et al., 2003)) X-rays from detector self-fluorescence (see **Section 5.5.2**). The secondary and main peak were both from the combination of the emissions from the ^{55}Fe radioisotope X-ray source (Mn Kα = 5.9 keV; Mn Kβ = 6.49 keV). The morphologies of the spectra obtained with the present devices appeared similar to those obtained with SAM APDs made from $GaAs/Al_{0.8}Ga_{0.2}As$ (Gomes et al., 2014) and $Al_{0.52}In_{0.48}P$ (Auckloo et al., 2016), in those cases, the secondary peaks were attributed to holes created in the n region(s) of the detectors below the avalanche layer, receiving the maximum possible hole initiated avalanche multiplication. Similarly, in those cases, the main peaks were attributed to electrons created in the p region(s) of

the detectors above the avalanche layer, receiving the maximum possible electron initiated avalanche multiplication. Given the presently reported devices structure however, this was not expected. Even if the whole of the p^+ was active, the number of counts from the depletion region should be much greater than the number from the p^+ region. Consequently, the origin of the spectra morphologies is currently unknown. It is noted that this is not the first time that additional peaks of unknown origin have occurred in X-ray APD spectra; the additional peaks in the earlier $Al_{0.8}Ga_{0.2}As$ p^+-p^--n^+ X-ray spectra were reported some years before they were explained (Barnett et al., 2011a).

The apparent multiplication factors of the primary and secondary ^{55}Fe X-ray photopeaks for the 200 µm $Al_{0.6}Ga_{0.4}As$ device based spectrometer were measured as a function of increasing applied reverse bias (see **Section 5.6**). Values of 5.20 and 3.43 were measured at 40 V applied reverse bias to the detector for the primary and secondary ^{55}Fe X-ray photopeaks, respectively. The apparent impact ionization coefficients, α and β, were calculated assuming that the primary (and secondary) peaks corresponded to events which had received maximum pure electron (and maximum pure hole) initiated avalanche multiplication, respectively. With 40 V reverse bias (E_f = 345 kV cm^{-1}) applied to the detector, apparent ionisation coefficients of α = 8513 and β = 4930 were calculated from the measurements.

The electron-hole pair creation energy for $Al_{0.6}Ga_{0.4}As$ was measured to be 4.97 eV ± 0.12 eV at 25 °C ± 1 °C (see **Section 5.7**). This value agrees with the Bertuccio-Maiocchi-Barnett (BMB) relationship between electron-hole pair creation energy and bandgap, which predicted 5.02 eV ± 0.16 eV for $Al_{0.6}Ga_{0.4}As$ at room temperature, prior to being refined by the new measurement. The new measurement demonstrates that $Al_{0.6}Ga_{0.4}As$ is yet another material whose electron-hole pair creation energy is not accurately predicted by the Klein relationship. The main and secondary Klein branches predict $Al_{0.6}Ga_{0.4}As$ would have an electron hole pair creation energy of 6.28 eV or 4.18 eV, respectively.

Using the experimental measurement of the electron-hole pair creation energy in $Al_{0.6}Ga_{0.4}As$, the BMB relationship was refined such that

$$\omega_{EHP} = (1.54 \pm 0.07)E_g + (1.89 \pm 0.12). \quad (5.5)$$

Although the energy resolution reported (626 eV ± 20 eV FWHM at 5.9 keV for $S_{200\mu m}$ at 20 °C) is modest when compared with those measured using state-of-the-art Si detectors (e.g. 134 eV FWHM at 5.9 keV (Müller-Seidlitz et al., 2016)) and GaAs detectors (e.g. 266 eV FWHM at 5.9 keV (Owens et al., 2001), given the relatively thin i layer thickness (2 µm) of the presently

reported $Al_{0.6}Ga_{0.4}As$ p^+-i-n^+ spectroscopic X-ray photodiodes, the results indicate that $Al_{0.6}Ga_{0.4}As$ is a potentially promising material for photon counting X-ray spectroscopy for space science applications. Indeed, it is hoped in future that the presently reported $Al_{0.6}Ga_{0.4}As$ p^+-i-n^+ spectroscopic X-ray photodiodes will be characterised as a function of temperature in order to assess their performance over the temperature ranges expected of space science missions in which these devices are anticipated to find utility (e.g. exploration of the poles of Mercury, where surface temperatures reach 70 °C (Novara, 2002)).

Parameter	Value
FWHM at 5.9 keV employing 200 µm detector at 20 °C	626 eV ± 20 eV
FWHM at 5.9 keV employing 400 µm detector at 20 °C	732 eV ± 30 eV
ω_{EHP} at 25 °C	4.97 eV ± 0.12 eV
200 µm detector leakage current density (40 V, 345 kV cm^{-1}) at 20 °C	11.9 nA cm^{-2} ± 1.3 nA cm^{-2}
400 µm detector leakage current density (40 V, 345 kV cm^{-1}) at 20 °C	5.0 nA cm^{-2} ± 0.3 nA cm^{-2}
200 µm detector capacitance density (40 V, 345 kV cm^{-1}) at 20 °C	8.55 nF cm^{-2} ± 0.59 nF cm^{-2}
400 µm detector capacitance density (40 V, 345 kV cm^{-1}) at 20 °C	8.94 nF cm^{-2} ± 0.15 nF cm^{-2}
Intrinsic carrier concentration at 20 °C	$\approx 4 \times 10^{16}$ cm^{-3}

Table 5.2. Key results of **Chapter 5** $Al_{0.6}Ga_{0.4}As$ p^+-i-n^+ circular mesa avalanche photodiodes of different diameters (200 µm and 400 µm) measurements.

Chapter 6
GaAs/$Al_{0.8}Ga_{0.2}As$ SAM APD detectors

6.1 Introduction

In this chapter, the X-ray spectroscopic performance of two circular GaAs/$Al_{0.8}Ga_{0.2}As$ separate absorption and multiplication (SAM) avalanche photodiodes (APDs) with different diameters (200 μm and 400 μm), is reported. An energy resolution of 508 eV ± 5 eV FWHM at 5.9 keV was achieved at an apparent avalanche gain, *M*, of 1.1. The results were compared with recently reported non-avalanche GaAs p^+-i-n^+ X-ray photodiodes of the same size and with the same absorption layer thickness, such that changes in performance from the inclusion of an avalanche layer could be evaluated. The experimental methods and techniques, along with the findings of the experimental work, are discussed.

6.2 Background

Whilst $Al_xGa_{1-x}As$ has received attention as a promising alternative for X-ray detection due to the material's ability to be tailored to particular application environments by adjusting the Al fraction (e.g. a reduction in Al fraction reduces the bandgap) (see **Section 1.6.2**). Most work has focused on $Al_xGa_{1-x}As$ p^+-i-n^+ mesa photodiodes, with promising results reported (see **Chapters 3**, **4**, and **5**).

GaAs and $Al_xGa_{1-x}As$ p^+-i-n^+ mesa X-ray detectors (typically operated in non-avalanche mode) show great promise, but the demands they place on their preamplifier electronics are more stringent than those of narrower bandgap materials like Si, because the electron-hole pair creation energies (see **Section 2.4.1**) of GaAs and $Al_xGa_{1-x}As$ are larger (e.g. 4.2 eV for GaAs cf. 3.6 eV for Si (Owens & Peacock, 2004)). Avalanche photodiodes (APDs) potentially reduce those demands by increasing the amount of charge created from the absorption of radiation quanta (see **Section 2.9**). However, the greater operating biases required can cause higher leakage currents which results in more parallel white noise (see **Section 2.8.2.1**).

APDs are widely used in photonic detection systems, most notably within telecommunications (Campbell, 2007) (David & Tan, 2008), to improve response relative to that of conventional p^+-i-n^+ photodiodes (Campbell, 2007). The increased response from such APDs is due to the impact ionisation process, where charge carriers gain enough kinetic energy to create electron-hole pairs during collisions with atoms in the lattice (see **Section 2.9.1**).

The stochastic nature of the impact ionisation process in APDs commonly adds noises (so called the excess noise factor, N_x) to the signal (see **Section 2.9.4**). A local model (McIntyre, 1966) derived expressions for the excess noise factors associated with pure electron initiated mean average multiplication, N_{xe}, and pure hole initiated mean average multiplication, N_{xh} (see Eqs. 2.32a and 2.32b), which predicted poor energy resolutions when the gain was appreciable in X-ray compound semiconductor APDs (Tan et al., 2011). For this reason, it was originally thought that the use of APDs would degrade the resolution of X-ray spectrometers and hence they were not extensively investigated (Fraser, 1989). However, recent studies have improved the understanding of APDs, and showed that the common model of excess noise is not directly applicable at X-ray energies (see **Section 2.9.4**)

The first X-ray SAM APDs were complex staircase-band-structures (Lauter et al., 1995) (Capasso et al., 1983) (Ripamonti et al., 1990). For example, a GaAs/$Al_xGa_{1-x}As$ SAM APD (320 µm × 450 µm active area) was reported to function as an X-ray detector at room temperature, utilising a series of staircase multiplication regions (Lauter et al., 1995); an energy resolution of 900 eV FWHM at 13.96 keV was reported at an avalanche multiplication of 4.1, at room temperature (Lauter et al., 1995). More recent work has concentrated on simpler SAM APD structures (Chia et al., 2003). For example, a GaAs/$Al_{0.8}Ga_{0.2}As$ SAM X-ray APD (430 nm GaAs absorption layer, 220 nm $Al_{0.8}Ga_{0.2}As$ multiplication layer) was reported at room temperature (Gomes et al., 2014); it had an energy resolution of 1.08 keV FWHM at 5.9 keV, at an avalanche multiplication of 3.5.

6.3 Device structure

The GaAs/$Al_{0.8}Ga_{0.2}As$ SAM structure was grown by MOVPE on a commercial GaAs n^+ substrate. The layer details are summarised in Table 6.1. Circular mesa structures (200 µm and 400 µm diameter) were etched using a 1:1:1 H_3PO_4:H_2O_2:H_2O solution followed by 10 s in a 1:8:80 H_2SO_4:H_2O_2:H_2O solution. Ohmic contacts, consisting of 20 nm InGe and 200 nm Au, were evaporated onto the rear of the substrate. Ohmic top contacts, consisting of 20 nm Ti and 200 nm Au, were evaporated onto the p^+ side of the mesa structures. The top contacts covered 45% of the 200 µm diameter diode's faces and 33% of the 400 µm diameter diode's face.

Material	Dopant	Dopant type	Thickness (nm)	Doping density (cm^{-3})
GaAs	Zn	p	10	1×10^{19}
GaAs	Zn	p	200	2×10^{18}
GaAs			10000	Undoped
GaAs	Zn	p	100	2×10^{17}
$Al_{0.8}Ga_{0.2}As$	Zn	p	200	2×10^{17}
$Al_{0.8}Ga_{0.2}As$			100	undoped
$Al_{0.8}Ga_{0.2}As$	Si	n	200	2×10^{18}
GaAs	Si	n	200	2×10^{18}
GaAs n^+ substrate				

Table 6.1. Layer details of the GaAs/$Al_{0.8}Ga_{0.2}As$ SAM structure.

6.4 Room temperature electrical characterisation

6.4.1 Current measurements as a function of applied reverse bias

Leakage current as a function of applied reverse bias was measured for each circular GaAs/$Al_{0.8}Ga_{0.2}As$ SAM photodiode (one 200 µm diameter device and one 400 µm diameter device), using a Keithley 6487 picoammeter/voltage source. Each diode was housed within a custom light tight electromagnetically screened test harness and placed in a TAS Micro MT climatic cabinet for temperature control as per **Section 3.6.1**. National Instruments LabVIEW software was used to automate the characterisation routine. The temperature was set to 20 °C and left for 1 hour before measuring to ensure thermal equilibrium and stabilisation. Fig. 6.1 presents the measured leakage current, I_d, of the packaged devices as a function of applied reverse bias.

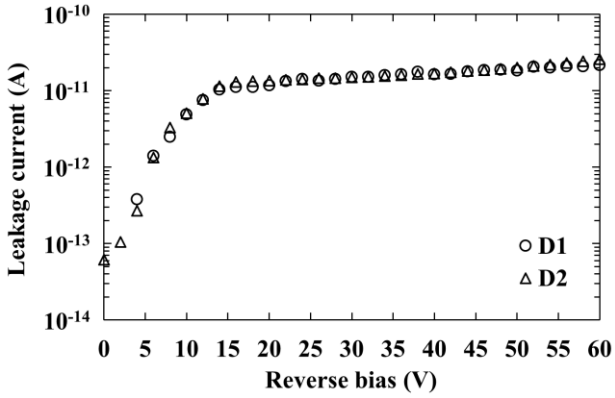

Fig. 6.1. Leakage current as a function of applied reverse bias for the 200 µm diameter device (circles) and the 400 µm diameter device (triangles). The associated uncertainties were omitted for clarity.

The leakage current of both devices increased as a function of increased reverse bias. At the maximum applied reverse bias (60 V), the leakage currents were measured to be 21.6 pA ± 0.8 pA and 25.7 pA ± 0.5 pA for the 200 µm and 400 µm devices, respectively. The uncertainties associated with the current measurements were dominated by the uncertainty associated with a single measurement from the Keithley 6487 Picoammeter/Voltage Source.

In order to determine the corresponding leakage current density, J_d, of the devices, the leakage current associated with the package (and measurement system) was determined by measuring an empty package of identical type. It was found that the empty package's leakage current was smaller than the uncertainty (± 0.4 pA) of the instrument, it was therefore considered negligible. The apparent leakage current density, as shown in Fig. 6.2, of the 400 µm diameter device was improved relative to the 200 µm diameter device (20.4 nA cm^{-2} ± 0.4 nA cm^{-2} for the 400 µm diameter device cf. 68.8 nA cm^{-2} ± 2.7 nA cm^{-2} for the 200 µm diameter device, at the maximum applied reverse bias (60 V). This suggested that the leakage current did not scale with junction area. This was attributed to a non-negligible surface leakage current, possibly due to the devices being unpassivated (Owens, 2012). Contact deposition and wirebonding may have also influenced the leakage current of the detectors.

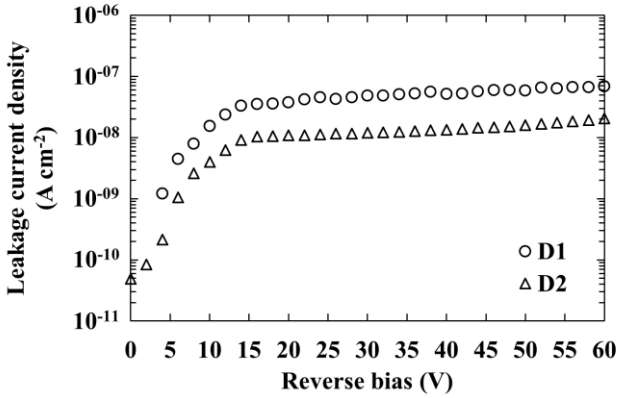

Fig. 6.2. Apparent leakage current density as a function of applied reverse bias at 20 °C for the 200 µm (circles) and 400 µm (triangles) diameter devices. The associated uncertainties were omitted for clarity.

The leakage current densities of the presently reported devices were greater than those measured for recently reported GaAs p^+-i-n^+ mesa X-ray photodiodes (Lioliou et al., 2017). At an internal electric field strength, E_f, of 50 kV cm^{-1} (equivalent to an applied reverse bias of 51 V for the GaAs/$Al_{0.8}Ga_{0.2}As$ devices, assuming E_f was uniform and across only the depleted region), leakage current densities of 61.8 nA cm^{-2} ± 1.5 nA cm^{-2} and 16.4 nA cm^{-2} ± 0.4 nA cm^{-2} were measured for the 200 µm diameter and 400 µm diameter devices respectively. At the same E_f,

leakage current densities of 15 nA cm^{-2} and 6 nA cm^{-2} were measured for the 200 µm and 400 µm GaAs devices respectively, at 20 °C (Lioliou et al., 2017).

6.4.2 Capacitance measurements as a function of applied reverse bias

Capacitance as a function of applied reverse bias was measured for the 200 µm and 400 µm diameter devices using an HP 4275A LCR Meter (signal magnitude 50 mV rms; frequency 1 MHz) and a Keithley 6487 picoammeter/voltage source to bias the detectors. National Instruments LabVIEW software was used to automate the characterisation routine. The environmental conditions were the same as for the leakage current measurements. Fig. 6.3 presents the measured capacitance as a function of reverse bias for (a) the 200 µm diameter device and (b) the 400 µm diameter device.

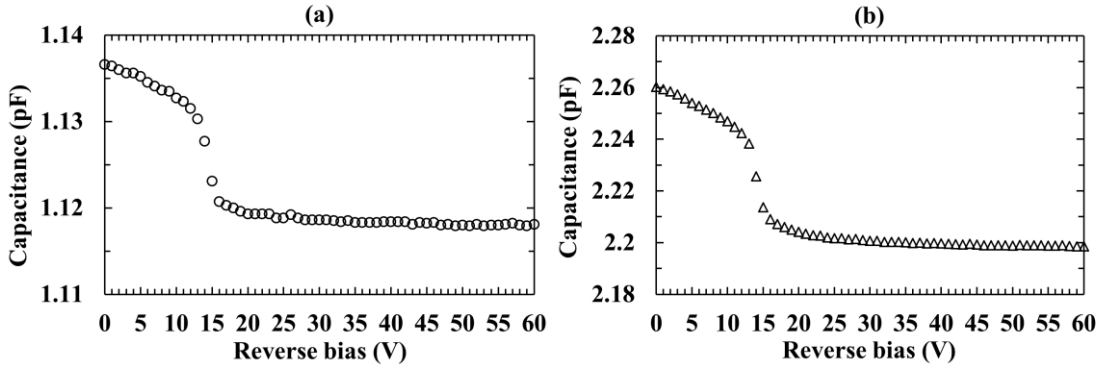

Fig. 6.3. Capacitance as a function of applied reverse bias for the 200 µm diameter device (a) and the 400 µm diameter device (b), at 20 °C. The empty package capacitance, in each case, has not been subtracted. The associated uncertainties were smaller than the symbols.

The measured capacitance of both packaged devices decreased as a function of reverse bias, from 1.14 pF and 2.26 pF at V_R = 0 V for the 200 µm and 400 µm diameter device respectively, to 1.12 pF and 2.20 pF at V_R = 60 V for the 200 µm and 400 µm diameter device respectively. The uncertainty associated with each individual capacitance measurement was ≈ ± 0.03 pF. However, because a set of measurements were taken at the same instrument working conditions (e.g. no variations in electrical connections and temperature), fittings on the experimental data provide a more appropriate uncertainty for relative changes (Butera et al., 2016). Exponential fittings on the measured capacitance for each device were performed as a function of reverse bias. An uncertainty of magnitude < 0.4 fF was estimated. The drop in capacitance across both the 200 µm and 400 µm diameter devices, within the range 13 V ≤ V_R ≤ 16 V, indicated the punch-through voltage (the voltage at which the multiplication region rapidly depletes) was ≈ 14 V (Gomes et al., 2014).

As the devices were measured after packaging, the measured capacitance, C_d, included both the diode capacitance, C_D, and the package capacitance, C_P. C_P was removed by assuming a constant capacitance density as a function of device area. The capacitance density of the 200 µm diameter device and the 400 µm diameter device at each applied reverse bias were compared, and the empty package capacitance calculated. A mean average empty package capacitance (0.76 pF) was calculated for C_P and subsequently subtracted from C_d of each device as a function of reverse bias. The capacitance densities for the 200 µm and 400 µm diameter devices have been plotted in Fig. 6.4.

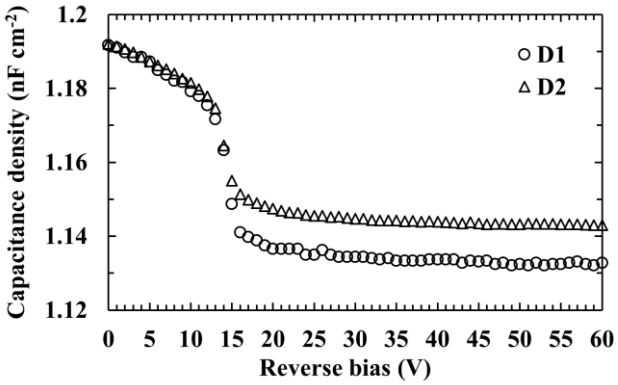

Fig. 6.4. Capacitance density as a function of applied reverse bias for the 200 µm diameter device (circles) and the 400 µm diameter device (triangles), at 20 °C, taking into account the empty package capacitance (0.76 pF). The associated uncertainties were smaller than the symbols.

When the devices were reverse biased, the capacitance was predominantly defined by the depletion layer capacitance, C_{DL} (Sze, 2006). Therefore, the depletion width, W_D, as a function of applied reverse bias could be calculated using Eq. 3.1. For the reported devices, multiple materials (GaAs and $Al_{0.8}Ga_{0.2}As$) influence C_{DL}, with their associated contributions difficult to detangle. As such, in order to calculate W_D, the devices were approximated to be simple GaAs structures (ε = 13.16 (Brozel & Stillman, 1996)). Since ε of $Al_{0.8}Ga_{0.2}As$ (= 10.628 (Adachi, 1993)) is smaller in value, the presently reported W_D should be taken as an upper limit. The Debye length of GaAs (0.06 µm) was also taken into account when calculating the depletion width uncertainty (Stradling & Klipstein, 1991). Fig. 6.5 (a) shows the depletion width as a function of applied reverse bias.

The depletion width increased as a function of applied reverse bias for both devices, increasing from 9.8 µm ± 0.1 µm at V_R = 0 V for the 200 µm and 400 µm diameter device, to 10.3 µm ± 0.1 µm and 10.2 µm ± 0.1 µm at V_R = 60 V for the 200 µm and 400 µm diameter device,

respectively. As was the case in Fig. 6.3, the increase in depletion width across both the 200 µm and 400 µm diameter devices, between 13 V and 16 V, indicated the punch-through voltage. Linear least squares fitting was applied to both devices, and indicated that the devices were fully depleted at $V_R \geq 50$ V.

The quantum detection efficiency of the GaAs/$Al_{0.8}Ga_{0.2}$As SAM APD structure was calculated using the Beer-Lambert law, assuming that the active region was solely confined to the GaAs absorption layer and that it was fully depleted and active. The results can be seen in Fig. 6.5 (b). For photons of 5.9 keV energy, the quantum detection efficiencies of the devices structure presented here were 0.56 in areas not covered by the top contact, and 0.46 in areas covered by the top contact. The weighted quantum efficiency assuming uniform illumination of the devices was 0.52 and 0.53 for the 200 µm and 400 µm diameter detectors, respectively.

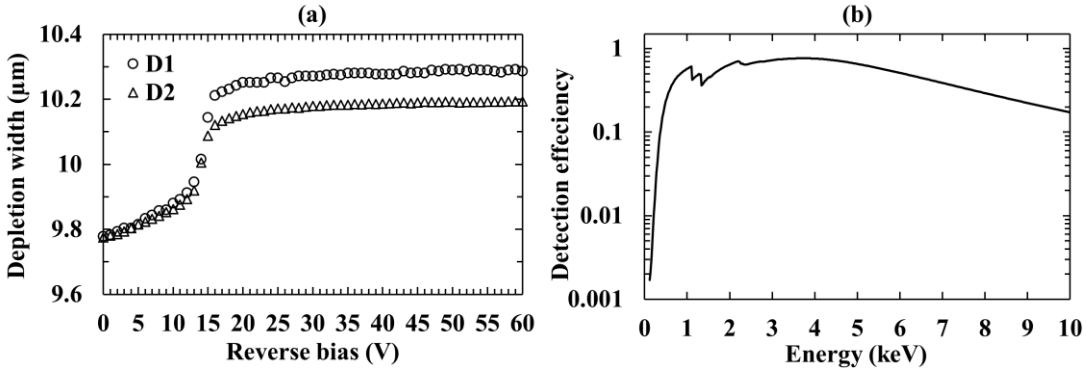

Fig. 6.5. (a) Calculated depletion width as a function of applied reverse bias for the 200 µm diameter device (circles) and the 400 µm diameter device (triangles), at 20 °C. The associated uncertainties were omitted for clarity. (b) Calculated detection efficiency as a function of energy for the GaAs/$Al_{0.8}Ga_{0.2}$As SAM APD structure. The discontinuities are the Al K, Ga L, and As L X-ray absorption edges.

The carrier concentration of the space charge region, N_{eff}, was calculated using the equation for general nonuniform distributions (see **Section 3.4.2**). The carrier concentration reached a minimum of $\approx 7 \times 10^{14}$ cm^{-3} for both devices, at a calculated depletion width ≈ 10 µm. The carrier concentration as a function of calculated depletion width has been plotted for the GaAs/$Al_{0.8}Ga_{0.2}$As detectors in Fig. 6.6. Variation in the apparent carrier concentration between the 200 µm and 400 µm devices was within the uncertainty of the measurements.

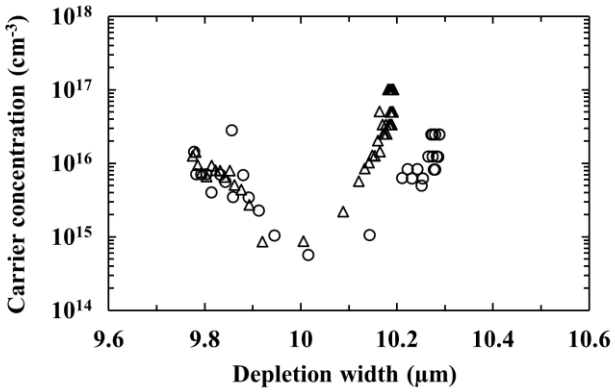

Fig. 6.6. Carrier concentration as a function of calculated depletion width for the 200 μm (circles) and 400 μm (triangles) diameter devices. The associated uncertainties were omitted for clarity.

6.5 Room temperature X-ray spectroscopy

6.5.1 Measurements with an ^{55}Fe radioisotope X-ray source

In order to characterise the X-ray detection performance of the GaAs/$Al_{0.8}Ga_{0.2}As$ SAM APD devices, each detector was connected, in turn, to a custom-made low-noise charge-sensitive preamplifier of feedback-resistorless design (see **Section 2.7**). The preamplifier used a Vishay 2N4416A Si JFET as the input transistor. In each case, the preamplifier was connected to an Ortec 572A shaping amplifier and an Ortec Easy-MCA multi-channel analyser. An ^{55}Fe radioisotope X-ray source (≈ 131 MBq) emitting characteristic Mn Kα (5.9 keV) and Mn Kβ (6.49 keV) X-rays was placed ≈ 4 mm above each GaAs/$Al_{0.8}Ga_{0.2}As$ SAM APD in turn. The resultant spectrometers S_{200} (employing the 200 μm diameter photodiode) and S_{400} (employing the 400 μm diameter photodiode) were installed within a TAS Micro MT climatic cabinet for temperature control as per **Section 3.7.1**. The climatic cabinet temperature was set to 20 °C, and allowed to stabilise for 1 hour before measurements were taken.

Spectra were accumulated for each spectrometer as a function of detector applied reverse bias. The applied reverse bias was initially set to 0 V, then increased in 1 V steps up to 50 V. The reverse bias was increased further in steps of 5 V, up to 60 V. After each voltage change, the system was allowed to stabilise for 5 minutes before taking a measurement. Since the two detectors had different active areas, the live time limits of each spectrum were set differently: spectra accumulated with S_{200} had a live time limit of 100 s; spectra accumulated with S_{400} had a live time limit of 25 s. A shaping time of 0.5 μs was used; this was the best available shaping time for each system. The accumulated ^{55}Fe X-ray spectra for the 200 μm and 400 μm diameter GaAs/$Al_{0.8}Ga_{0.2}As$ SAM APD spectrometers can be seen in Fig. 6.7.

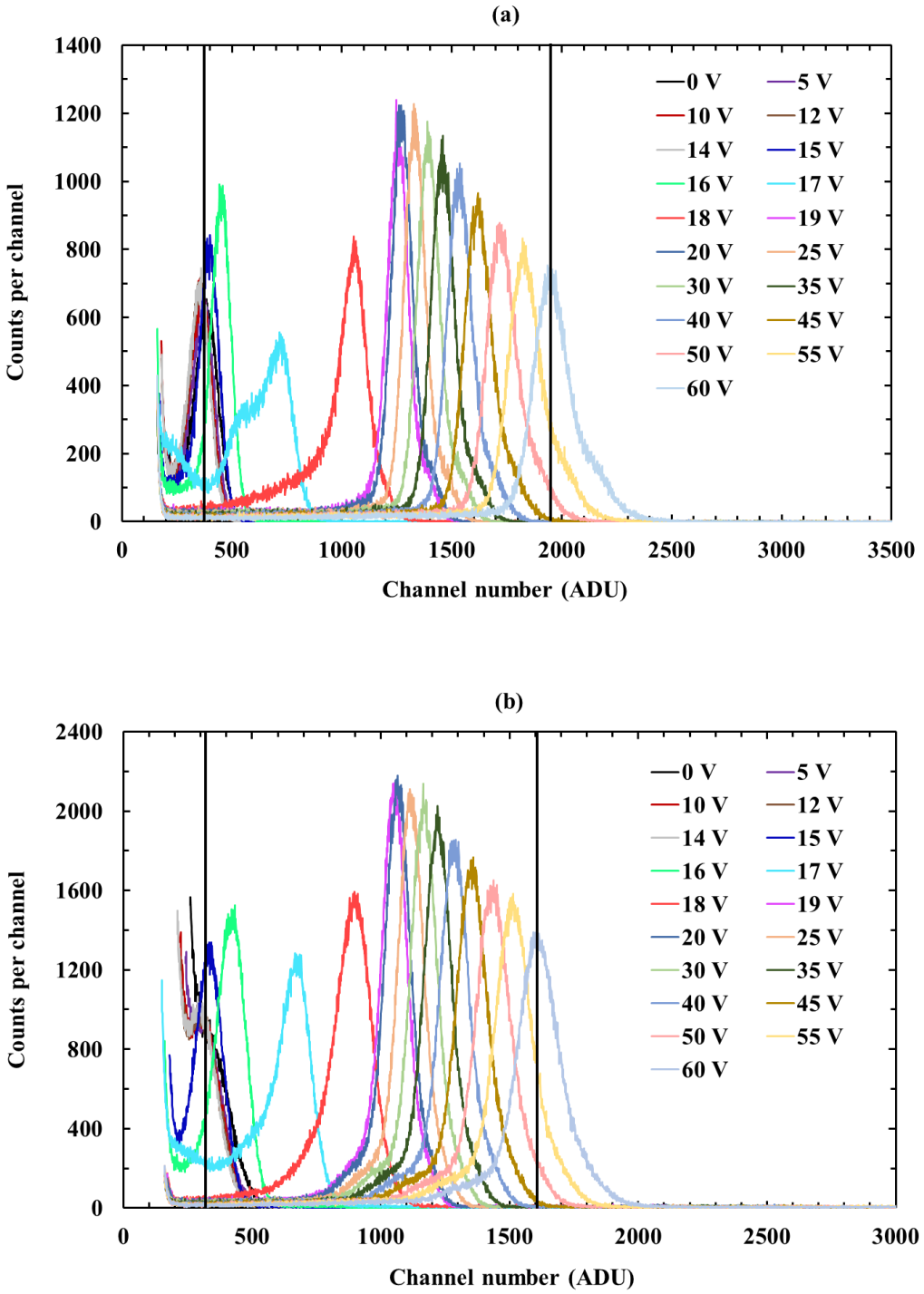

Fig. 6.7. Accumulated ^{55}Fe spectra obtained with S_{200} (a) and S_{400} (b). All spectra were accumulated at the same shaping time (0.5 µs), and at a constant temperature (20 ºC). The vertical black lines indicate the positions of the combined Mn Kα and Kβ X-ray photopeaks from the ^{55}Fe radioisotope X-ray source accumulated with the detectors reverse biased at 0 V and 60 V.

Gaussian fitting was applied to each accumulated spectrum from the ^{55}Fe radioisotope X-ray source (Mn Kα = 5.9 keV; Mn Kβ = 6.49 keV). The relative emission ratio (Schötzig, 2000) and the relative efficiency of the GaAs/$Al_{0.8}Ga_{0.2}As$ SAM APDs at these energies was taken into account in fitting the Mn Kα and Kβ peaks. The Mn Kα and Kβ peaks were not individually resolved by the spectrometer; as such, the peak detected was the combination of the Mn Kα and Kβ lines. The form of spectroscopic response was consistent with a SAM APD; this was further exemplified by plotting the change in 5.9 keV peak centroid position (corrected for changes in zero energy noise peak position and plotted in terms of the MCA's analogue to digital units, ADU, scale) as a function of applied detector reverse bias, as shown in Fig. 6.8.

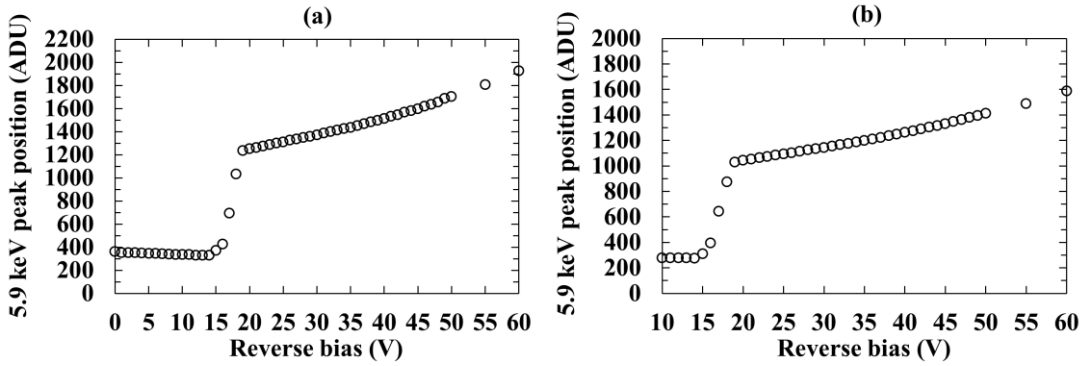

Fig. 6.8. Difference in ADU between the 0 keV position and the centroid of the fitted 5.9 keV peak as a function of applied detector reverse bias, at a shaping time of 0.5 μs, and at 20 ºC for the spectrometers S_{200} (a) and S_{400} (b).

The sharp increase in 5.9 keV peak position between 14 V and 19 V for both the 200 μm and 400 μm diameter devices, as shown in Fig. 6.8, was attributed to an improved charge collection efficiency from reaching the punch-through voltage (see Fig. 6.3). At applied detector reverse biases less than the punch-through voltage, charge carriers cannot readily travel through the $Al_{0.8}Ga_{0.2}As$ junction (see Table 6.1) (Lauter et al., 1995), limiting the charge collection efficiency. The increasing 5.9 keV peak position as a function of applied detector bias beyond 19 V was a result of increases in avalanche multiplication. The apparent multiplication factor, *M*, was calculated for both spectrometers by calculating the ratio between the fitted 5.9 keV peak position at each bias and the fitted 5.9 keV peak position at unity gain (M = 1) and complete charge collection, assumed to be achieved at V_R = 19 V applied to the detector. The apparent multiplication factor as a function of applied detector reverse bias can be seen in Fig. 6.9.

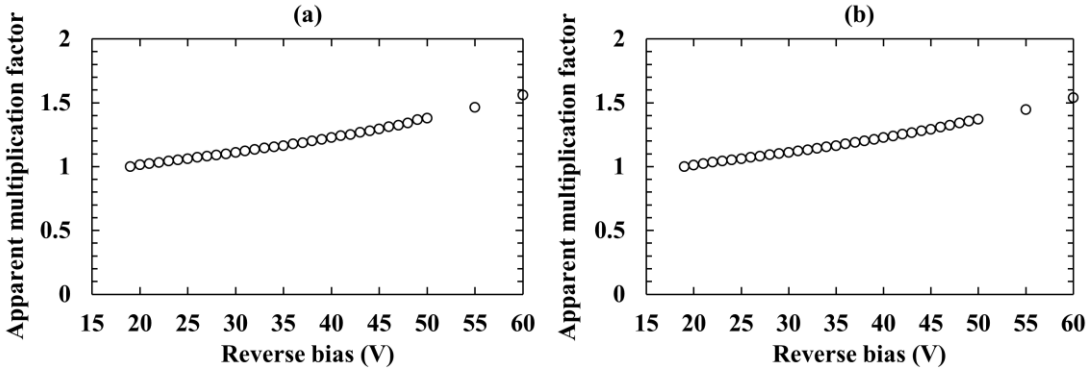

Fig. 6.9. Apparent multiplication factor of the 5.9 keV ^{55}Fe photopeak as a function of applied detector reverse bias for the spectrometers S_{200} (a) and S_{400} (b), at 20 ºC. Unity gain was set to 19 V.

The spectra were energy calibrated using the positions of the so called zero energy noise peak and the fitted Mn Kα (5.9 keV) peak, with the assumption of a linear variation of detected and output charge with energy. The energy resolution (FWHM at 5.9 keV) was then calculated for each accumulated spectrum. Fig. 6.10 presents the energy resolution of each spectrometer as a function of applied detector reverse bias.

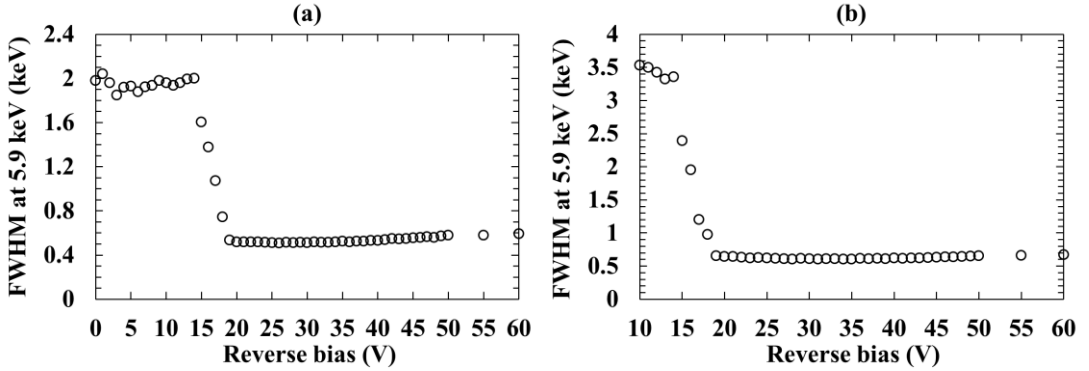

Fig. 6.10. FWHM at 5.9 keV as a function of applied detector reverse bias at a shaping time of 0.5 µs, and at 20 ºC, for the spectrometers S_{200} (a) and S_{400} (b). The associated uncertainties were omitted for clarity.

The improved charge collection efficiency, due to overcoming the punch-through voltage of the detectors, resulted in an abrupt improvement in energy resolution (FWHM at 5.9 keV) of the spectroscopic systems around the punch through voltage, as shown in Fig. 6.10. At V_R = 14 V, the FWHM at 5.9 keV was 2.00 keV ± 0.05 keV and 3.36 keV ± 0.05 keV for the spectrometers S_{200} and S_{400}, respectively. At V_R = 19 V, the FWHM at 5.9 keV was 534 eV ± 5 eV and 653 eV ± 6 eV for S_{200} and S_{400}, respectively. The best measured energy resolution for the spectrometer S_{200} was 508 eV ± 5 eV, achieved at V_R = 26 V, corresponding to an apparent multiplication factor

of 1.1. The best measured energy resolution for the spectrometer S_{400} was 603 eV ± 6 eV, achieved at V_R = 34 V, corresponding to an apparent multiplication factor of 1.2. ^{55}Fe X-ray spectra accumulated with the spectrometers S_{200} and S_{400} can be seen in Fig. 6.11 and Fig. 6.12 respectively.

Both the 200 µm diameter and 400 µm diameter GaAs/$Al_{0.8}Ga_{0.2}As$ SAM APD devices reported here, had improved performance relative to the recently studied GaAs p^+-i-n^+ photodiodes (Lioliou et al., 2017). At 20 ºC, energy resolutions of 690 eV and 730 eV FWHM at 5.9 keV were reported for the 200 µm and 400 µm GaAs p^+-i-n^+ photodiode, respectively (Lioliou et al., 2017). The presently reported spectrometers also had improved performance compared to the previously reported GaAs/$Al_{0.8}Ga_{0.2}As$ SAM APD spectrometers which had a FWHM at 5.9 keV = 1.08 keV at an avalanche gain of M = 3.5 at room temperature (Gomes et al., 2014).

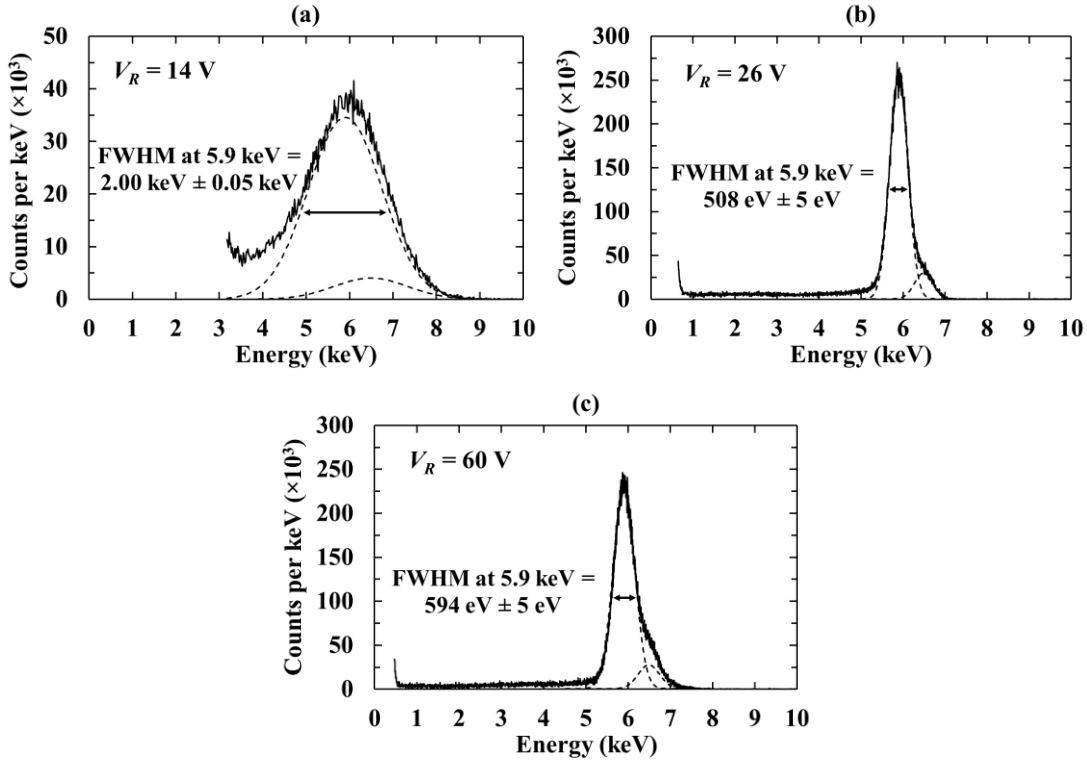

Fig. 6.11. ^{55}Fe X-ray spectra accumulated with the 200 µm diameter detector based spectrometer, at 20 °C, a shaping time of 0.5 µs, and a reverse bias of 14 V (a), 26 V (b), and 60 V (c). The fitted Mn Kα (5.9 keV) and Mn Kβ (6.49 keV) peaks have been plotted (dashed lines). The accumulated spectra have been normalised into counts per keV in order to account for the differing channel widths.

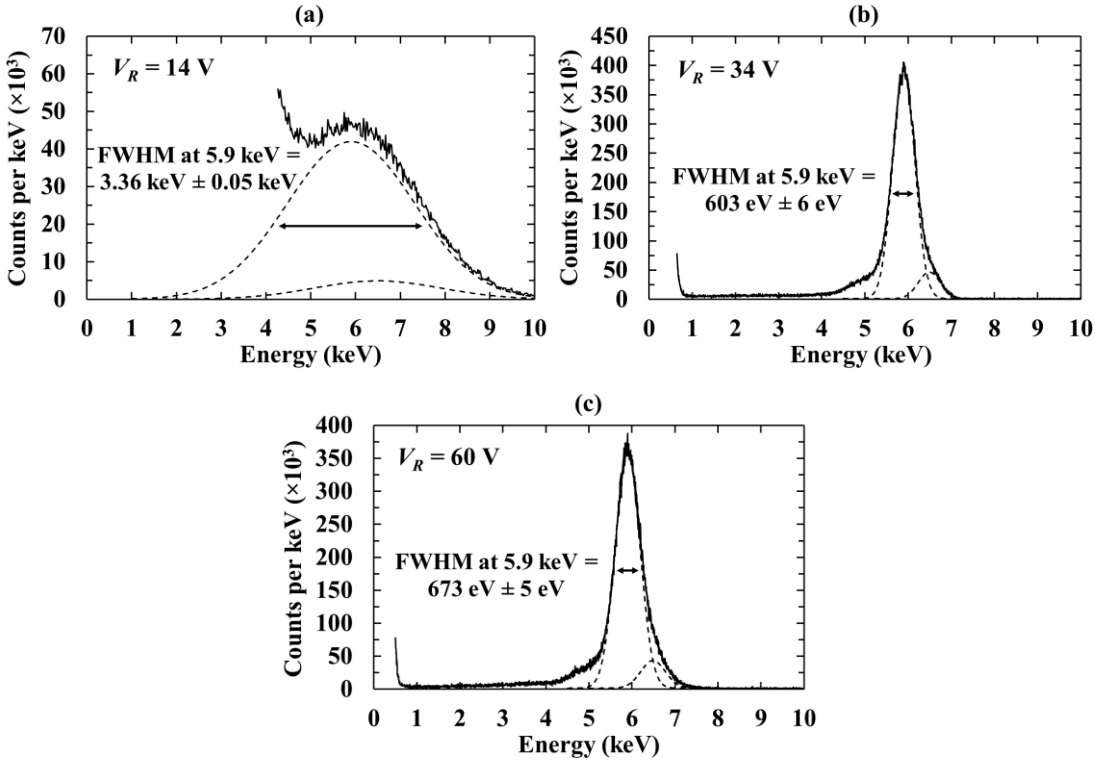

Fig. 6.12. ^{55}Fe X-ray spectra accumulated with the 400 µm diameter detector spectrometer, at 20 °C, a shaping time of 0.5 µs, and a reverse bias of 14 V (a), 34 V (b), and 60 V (c). The fitted Mn Kα (5.9 keV) and Mn Kβ (6.49 keV) peaks have been plotted (dashed lines). The accumulated spectra have been normalised into counts per keV in order to account for the differing channel widths.

6.5.2 Origin of the secondary peak in the obtained X-ray spectra

As could be seen in Fig. 6.12, at sufficiently high applied detector biases ($V_R \geq 17$ V), a small secondary peak appears to the left (low energy) side of the fitted peaks. The secondary peak appears as a shoulder on the main combined peak as they are not resolved from each other. This secondary peak arises as a consequence of the GaAs layer not having a 100% absorption efficiency for the X-ray photons (see Fig. 6.5b); some photons are transmitted through the GaAs layer and absorbed in the $Al_{0.8}Ga_{0.2}As$ layers. This can be proved by consideration of the electron-hole pair creation energies of each material.

Since the electron-hole pair creation energy of $Al_{0.8}Ga_{0.2}As$ (ω_{EHP} = 5.07 eV ± 0.08 eV at 20 °C (Barnett et al., 2013a)) and GaAs (ω_{EHP} = 4.18 eV ± 0.03 eV (Bertuccio & Maiocchi, 2002)) differ, so too does the average number of charge carriers created by the absorption of a photon of energy, E, in each material. Thus it can be demonstrated that the secondary, left shoulder, peak

arises as a consequence of X-ray absorption in the $Al_{0.8}Ga_{0.2}As$ layers by computation of the electron-hole pair creation energy of $Al_{0.8}Ga_{0.2}As$ from the spectra.

The primary and secondary peak of the spectra obtained with S_{400}, with the detector biased at 34 V and 60 V respectively, were fitted with Gaussians for the Mn Kα (5.9 keV) and Mn Kβ (6.49 keV) emissions of ^{55}Fe in the accepted ratio (Schötzig, 2000), taking into account the detectors' relative detection efficiencies for the Mn Kα and Mn Kβ photons, see Fig. 6.13. With the detector biased at 34 V and 60 V, the electron-hole pair creation energy of $Al_{0.8}Ga_{0.2}As$ was found to be 5.04 eV ± 0.08 eV and 5.06 eV ± 0.08 eV respectively, which are in agreement with the accepted value (ω_{EHP} = 5.07 eV ± 0.08 eV at 20 °C (Barnett et al., 2013a)).

The secondary peak, clearly visible as a shoulder in Fig. 6.12 and Fig. 6.13 (400 µm diameter detector), was less visible in Fig. 6.11 (200 µm diameter detector). This was attributed to the size difference between the two investigated detectors; in addition to the front face of the 400 µm diameter detector receiving four times more photons than the 400 µm diameter detector, the not-perfectly-vertical mesa side walls of the detectors (which invariably result in thick wet etched mesa structures) resulted in a proportionally greater volume of $Al_{0.8}Ga_{0.2}As$ cf. GaAs in the 400 µm diameter detector cf. the 200 µm diameter detector.

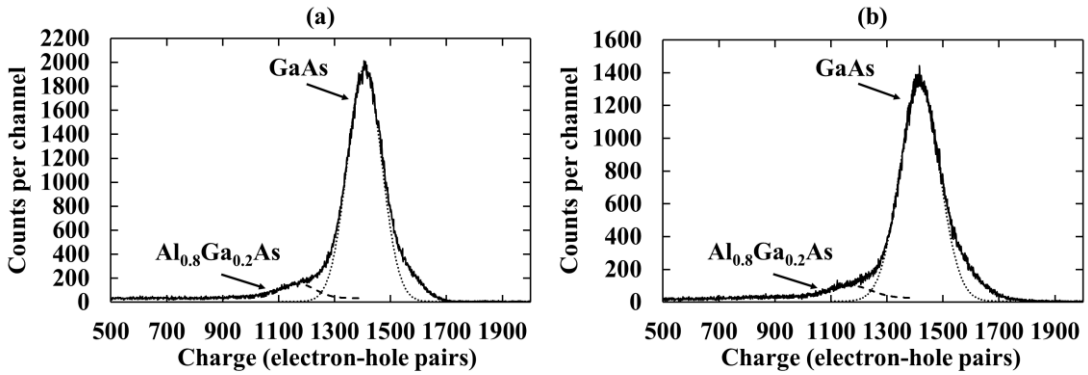

Fig. 6.13. ^{55}Fe X-ray spectra accumulated with S_{400} at a reverse bias of 34 V (a), and 60 V (b). Charge calibration was achieved using the positions of the zero energy noise peak of the preamplifier and the GaAs peak, together with the accepted ω_{EHP} value for GaAs. The dashed and dotted lines are the fitted Mn Kα (5.9 keV) peaks for the $Al_{0.8}Ga_{0.2}As$ and GaAs materials respectively.

6.5.3 Noise analysis

The energy resolution of a semiconductor detector operating in avalanche mode, coupled to a charge sensitive preamplifier, is influenced by four sources of noise: the Fano noise, N_F; the

electronic noise, *A*; incomplete charge collection noise, *R*; the excess noise factor, N_x (see **Sections 2.8** and **2.9.4**).

The Fano noise, assuming that X-ray photons incident on the reported detectors are absorbed only within the GaAs absorption region and that the Fano factor, *F*, of GaAs is 0.12 (Bertuccio et al., 1997), was calculated to be 13 e^- rms at 5.9 keV (128 eV FWHM at 5.9 keV) for the GaAs/$Al_{0.8}Ga_{0.2}As$ SAM APD. Since the measured energy resolution of the reported spectrometers was greater than the calculated fundamental Fano-limited energy resolution, there were clearly significant noise contributions beyond the statistical generation of charge carriers.

The electronic noise components were calculated for the spectrometer S_{200} and the spectrometer S_{400} as per **Section 2.8.2**. The results can be seen in Fig. 6.14. It should be noted that, since the contribution from series white noise depends on the total capacitance load at the gate of the input transistor of the preamplifier, only a lower bound of the value could be established. This is due to the prototype nature of the preamplifier, where, in addition to estimable capacitances, stray capacitances with unknown values are present (see **Section 2.8.2**). Similarly, dielectric noise contributions arising from the detector, JFET and feedback capacitor were readily estimated (Barnett et al., 2015) (Lioliou & Barnett, 2015), but additional noise from other lossy dielectrics in proximity to the preamplifier may have also added to the noise. The series white noise and dielectric noise were thus considered in two parts: known noise contributions and stray noise contributions. Subtracting the expected Fano noise and the electronic noise contributions (parallel white noise, known series white noise (including induced gate drain current noise), known dielectric noise, and $1/f$ noise) from the measured FWHM in quadrature, yields a combination of stray dielectric noise, stray series white noise, incomplete charge collection noise, excess noise, and possibly stray parallel white noise contributions (so called the remaining noise contribution). Changes in detector capacitance were included in the known series white noise and known dielectric noise calculations, whilst the JFET was considered to contribute a constant capacitance (2 pF (Siliconix, 2001)) to both calculations. A constant JFET leakage current (1 pA (Siliconix, 2001)) was included in the known parallel white noise calculation.

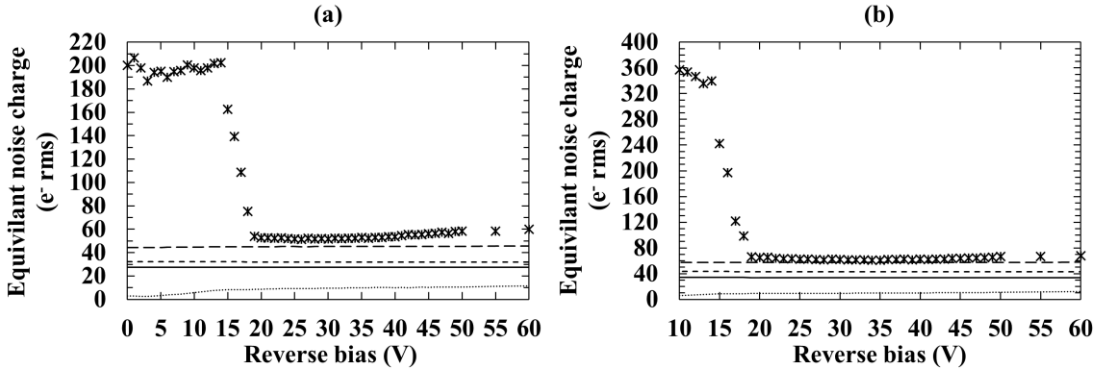

Fig. 6.14. Calculated noise contributions of the spectrometers S_{200} (a) and S_{400} (b) as a function of applied detector reverse bias at a shaping time of 0.5 µs, and at 20 ºC: total noise (stars); sum of the calculated noise contributions (long dashed line); known series white noise (short dashed line); known dielectric noise (solid line); calculated parallel white noise (dotted line).

As can be seen in Fig. 6.14, the total sum of the calculated noise contributions (Fano noise, parallel white noise, known series white noise, known dielectric noise, and 1/*f* noise, added in quadrature) did not account for the measured total noise (FWHM at 5.9 keV) of the 200 µm and 400 µm diameter detector based spectroscopic systems. At an applied detector reverse bias of 10 V, the total noise of each system was 198 e^- rms ± 5 e^- rms, and 357 e^- rms ± 5 e^- rms for S_{200} and S_{400} respectively. At the same applied bias (10 V), the total sum of the calculated noise contributions was 44.7 e^- rms ± 0.4 e^- rms and 57.4 e^- rms ± 0.2 e^- rms, respectively. This discrepancy was attributed in part to incomplete charge collection noise, where charge carriers cannot readily travel through the $Al_{0.8}Ga_{0.2}As$ junction before the punch-through voltage (Lauter et al., 1995) (see **Section 6.5.1**). Stray dielectric noise, stray series white noise, and any stray parallel white noise contributions, arising from the spectroscopic systems, would have also contributed to the measured total noise.

As the applied detector reverse bias was further increased (14 V < V_R < 19 V), the measured total noise (FWHM at 5.9 keV) of both spectrometers improved (reduced). At 19 V applied detector reverse bias, the total noise was 54.0 e^- rms ± 0.5 e^- rms and 66.0 e^- rms ± 0.6 e^- rms for the spectrometers S_{200} and S_{400}, respectively. The total sum of the calculated noise contributions, at the same applied detector reverse bias (19 V), was 45.0 e^- rms ± 0.4 e^- rms and 57.3 e^- rms ± 0.2 e^- rms for the spectrometers S_{200} and S_{400}, respectively. This, in part, indicated a reduction in incomplete charge collection noise as the punch-through voltage (≈ 14 V) was exceeded.

At the optimal applied detector reverse bias for each spectrometer (26 V and 34 V for the spectrometers S_{200} and S_{400} respectively), the measured apparent noise was 51.4 e^- rms ± 0.5 e^- rms and 61.0 e^- rms ± 0.6 e^- rms for the spectrometers S_{200} and S_{400} respectively. The total sum of the

calculated noise contributions, at the same optimal applied detector reverse bias (26 V and 34 V for S_{200} and S_{400} respectively), was 45.1 e^- rms ± 0.4 e^- rms and 57.4 e^- rms ± 0.2 e^- rms for the spectrometers S_{200} and S_{400}, respectively. The apparent decrease in remaining noise contribution between 19 V and the optimal applied detector reverse bias of each spectrometer indicated a net benefit due to avalanche multiplication.

At the maximum investigated applied detector reverse bias (60 V) an apparent noise of 60.1 e^- rms ± 0.5 e^- rms and 68.0 e^- rms ± 0.5 e^- rms was measured for S_{200} and S_{400}, respectively. At the same applied detector reverse bias (60 V), the total sum of the calculated noise contributions was 45.6 e^- rms ± 0.4 e^- rms and 57.9 e^- rms ± 0.2 e^- rms, respectively. The increased discrepancy between the measured apparent noise (FWHM at 5.9 keV) and the total sum of the calculated noise contributions may have arisen from a larger than expected parallel white noise at high biases or from increasing excess noise due to avalanche multiplication.

6.5.4 Improvements in energy resolution due to avalanche multiplication

In order to determine whether avalanche multiplication affected the energy resolution of the reported spectrometers, the measured energy resolution (FWHM at 5.9 keV) was compared to the expected non-avalanche energy resolution of each spectrometer.

The expected non-avalanche energy resolution was calculated by assuming incomplete charge collection noise became negligible at $V_R \geq 19$ V, avalanche multiplication was not present at $V_R \leq 19$ V, and any stray noises contributing to the remaining noise contribution (see **Section 6.5.3**) were independent of applied reverse bias. Given these assumptions, the remaining noise contribution at $V_R = 19$ V for both spectrometers represents the non-avalanche mode remaining noise contribution across the applied reverse bias range ($19 \text{ V} \leq V_R \leq 60$ V). The remaining noise contribution at $V_R = 19$ V was calculated to be 29.8 e^- rms ± 1.1 e^- rms and 32.8 e^- rms ± 1.6 e^- rms for S_{200} and S_{400}, respectively.

Adding in quadrature the remaining noise contribution at $V_R = 19$ V to the calculated known noise contributions at each investigated applied detector reverse bias yields the expected non-avalanche energy resolution as a function of applied reverse bias within the range $19 \text{ V} \leq V_R \leq 60$ V. The expected non-avalanche energy resolution, and measured avalanche energy resolution, at each applied reverse bias for the spectrometers S_{200} and S_{400}, can be seen in Fig. 6.15.

At an applied detector reverse bias of 26 V ($M = 1.1$), an expected non-avalanche energy resolution of 535 eV ± 7 eV FWHM at 5.9 keV was calculated for the spectrometer S_{200}. Given

the same spectrometer and the same applied detector reverse bias (26 V), an energy resolution of 508 eV ± 5 eV was measured. As for the spectrometer S_{400}, at an applied detector reverse bias of 34 V (M = 1.2), an expected non-avalanche energy resolution of 653 eV ± 8 eV FWHM at 5.9 keV was calculated. At the same applied detector reverse bias (34 V), an energy resolution of 603 eV ± 6 eV was measured. As such, it can be concluded that a noticeable benefit from small avalanche multiplication gains (M ≤ 1.4) was measured. This conclusion is further supported by recent results from non-avalanche GaAs p^+-i-n^+ photodiodes, which were near-identical to the devices reported here except that the GaAs detectors did not have an AlGaAs avalanche layer (Lioliou et al., 2017). Where, at 20 ºC, energy resolutions of 690 eV and 730 eV FWHM at 5.9 keV were reported for the 200 µm and 400 µm GaAs p^+-i-n^+ photodiode, respectively (Lioliou et al., 2017).

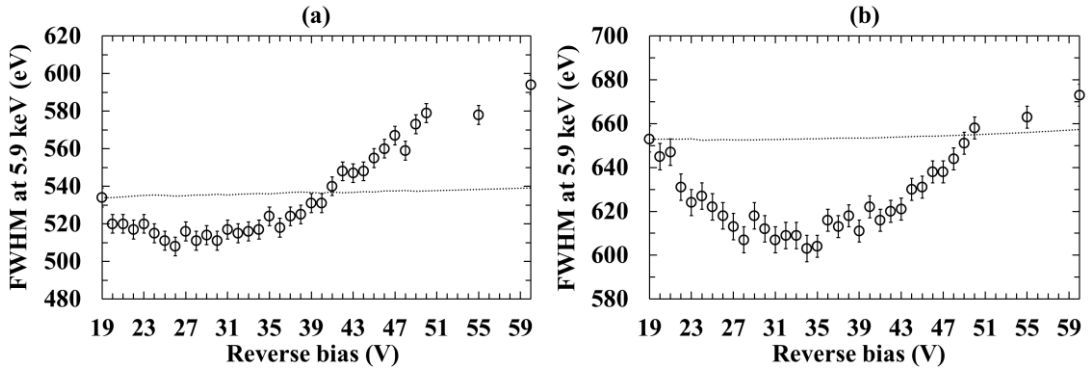

Fig. 6.15. Expected non-avalanche FWHM at 5.9 keV, assuming no incomplete charge collection noise at $V_R \geq 19$ V (dotted line), as a function of applied detector reverse bias to the spectrometers S_{200} (a) and S_{400} (b). The measured FWHM at 5.9 keV (circles) has been included. The associated uncertainties of the expected non-avalanche FWHM at 5.9 keV were omitted for clarity.

6.6 Conclusion

Two circular (one 200 µm diameter and one 400 µm diameter) GaAs/$Al_{0.8}Ga_{0.2}As$ Separate Absorption and Multiplication (SAM) X-ray photodiodes have been electrically characterised at room temperature (20 °C), and investigated for their response to soft X-ray illumination using an ^{55}Fe radioisotope X-ray source (Mn Kα = 5.9 keV; Mn Kβ = 6.49 keV). Each device consisted of a 10 µm thick GaAs absorption layer and a 0.1 µm thick $Al_{0.8}Ga_{0.2}As$ multiplication layer (see Table 6.1 for layer details).

Capacitance measurements indicated a punch-through voltage (the voltage at which the multiplication region rapidly depletes) of ≈ 14 V for both the 200 µm and 400 µm diameter

devices. At the maximum applied reverse bias (60 V) a capacitance of 1.12 pF and 2.20 pF was measured for the 200 µm and 400 µm diameter device respectively, each with an uncertainty of < 0.4 fF. The capacitance measurements indicated that both devices were fully depleted at V_R ≥ 50 V, reporting a depletion width consistent with growth specifications (see Table 6.1).

The best measured energy resolution achieved at 20 °C for the spectrometer S_{200} was 508 eV ± 5 eV FWHM at 5.9 keV, at an applied detector reverse bias of 26 V, corresponding to an apparent multiplication factor of 1.1. The best measured energy resolution at 20 °C for the spectrometer S_{400} was 603 eV ± 6 eV FWHM at 5.9 keV, at an applied detector reverse bias of 34 V, corresponding to an apparent multiplication factor of 1.2. Assuming that energy resolution as a function of incident energy changes only with Fano noise (see **Section 2.4.1**), the energy resolution at 20 °C for the spectrometer S_{200} was calculated to be 494 eV ± 5 eV FWHM at 1 keV, at an applied detector reverse bias of 26 V, and 591 eV ± 5 eV FWHM at 1 keV for the spectrometer S_{400}, at an applied detector reverse bias of 34 V. It should be noted that since avalanche multiplication is occurring within the devices at the specified applied biases, additional energy dependent noise may be present (see **Section 2.9.4**) and could be quantified through experiment.

It was found that further increasing the applied detector reverse bias increased (worsened) the energy resolution (e.g. 594 eV ± 5 eV FWHM at 5.9 keV and 673 eV ± 5 eV FWHM at 5.9 keV for the spectrometers S_{200} and S_{400} respectively, at an applied reverse bias of 60 V). This indicated that any benefits from further increasing avalanche gain were exceeded by increases in excess noise and/or parallel white noise.

In order to determine whether avalanche multiplication affected the energy resolution of the reported spectrometers, the measured energy resolution (FWHM at 5.9 keV) was compared to the expected non-avalanche energy resolution of each spectrometer (see **Section 6.5.4**). The results indicated a noticeable benefit from small avalanche multiplication gains (M ≤ 1.4). At an applied detector reverse bias of 26 V (M = 1.1), an expected non-avalanche energy resolution of 535 eV ± 7 eV FWHM at 5.9 keV was calculated for the spectrometer S_{200}. Given the same spectrometer and the same applied detector reverse bias (26 V), an energy resolution of 508 eV ± 5 eV FWHM at 5.9 keV was measured. Similarly, at an applied detector reverse bias of 34 V (M = 1.2), an expected non-avalanche energy resolution of 653 eV ± 8 eV FWHM at 5.9 keV was calculated for the spectrometer S_{400}. Given the same spectrometer and the same applied detector reverse bias (34 V), an energy resolution of 603 eV ± 6 eV FWHM at 5.9 keV was measured. The results were supported further by a recent study using non-avalanche GaAs p^+-i-n^+ photodiodes which did not have an AlGaAs avalanche layer (Lioliou et al., 2017). At 20 ºC, energy resolutions of

690 eV and 730 eV FWHM at 5.9 keV were reported for the 200 µm and 400 µm GaAs p^+-i-n^+ photodiodes, respectively (Lioliou et al., 2017). The results indicated that introducing a separate AlGaAs multiplication layer may be beneficial to GaAs photodiodes.

The measured energy resolution (FWHM at 5.9 keV) reported here is the best so far reported for GaAs/$Al_xGa_{1-x}As$ SAM APD X-ray spectrometers at room temperature, previously energy resolutions of 1.08 keV FWHM at 5.9 keV (Gomes et al., 2014) and 900 eV FWHM at 13.96 keV (Lauter et al., 1995) have been reported. The measured energy resolution was also better than recently investigated non-avalanche $Al_xGa_{1-x}As$ detector based X-ray spectrometers, where at room temperature, an energy resolution of 756 eV ± 30 eV FWHM at 5.9 keV was reported (see **Section 4.5.1**). It should be noted that the energy resolutions reported here are modest when compared to the best reported results for the best non-avalanche GaAs based X-ray spectrometers (300 eV (Erd et al., 2002) and 266 eV FWHM at 5.9 keV (Owens et al., 2001) at room temperature) and the best Si based X-ray spectrometers (141 eV (Bertuccio et al., 2015) and 134 eV FWHM at 5.9 keV (Müller-Seidlitz et al., 2016)), when those detectors are coupled to ultra-low-noise electronics better than those used for the investigations reported in this thesis.

Although the energy resolutions achieved with GaAs/$Al_xGa_{1-x}As$ SAM APD devices are not yet as good as other more developed materials, it is important to note that useful scientific contributions can still be made by X-ray spectrometers with modest energy resolutions. D-CIXS on SMART-1 (Grande et al., 2003), which measured Ti Kα (4.51 keV) X-ray fluorescence of material on the lunar surface for the first time (Swinyard et al., 2009), had an energy resolution of 420 eV FWHM at 4.5 keV (Swinyard et al., 2009). As such, a photon counting X-ray spectrometer with similar or better energy resolution, that is also radiation hard and temperature tolerant, would likely find utility in future missions to harsh environments.

Parameter	Value
FWHM at 5.9 keV employing 200 µm detector at 20 °C	508 eV ± 5 eV
FWHM at 5.9 keV employing 400 µm detector at 20 °C	603 eV ± 6 eV
200 µm detector leakage current density (60 V, 58 kV cm^{-1}) at 20 °C	68.8 nA cm^{-2} ± 2.7 nA cm^{-2}
400 µm detector leakage current density (60 V, 59 kV cm^{-1}) at 20 °C	20.4 nA cm^{-2} ± 0.4 nA cm^{-2}
200 µm detector capacitance density (60 V, 58 kV cm^{-1}) at 20 °C	1.13 nF cm^{-2} ± 0.10 nF cm^{-2}
400 µm detector capacitance density (60 V, 59 kV cm^{-1}) at 20 °C	1.14 nF cm^{-2} ± 0.13 nF cm^{-2}
Intrinsic carrier concentration at 20 °C	≈ 7×10^{14} cm^{-3}

Table 6.2. Key results of **Chapter 6** GaAs/$Al_{0.8}Ga_{0.2}As$ SAM APDs of different diameters (200 µm and 400 µm) measurements.

Chapter 7
Conclusions and future work

7.1 Conclusions

$Al_xGa_{1-x}As$ photodiodes have been investigated for their suitability as spectroscopic radiation detectors for space science applications.

$Al_{0.2}Ga_{0.8}As$ p^+-i-n^+ circular mesa photodiodes (200 µm diameter, 3 µm i layer) have been demonstrated, for the first time, to function as spectroscopic X-ray photon counting detectors within the temperature range 20 °C to -20 °C, with promising energy resolutions (FWHM at 5.9 keV) reported (see **Chapter 3**). Initial proof of principle measurements at room temperature (20 °C) demonstrated energy resolutions of 1.24 keV ± 0.04 keV FWHM at 5.9 keV for the devices studied (see **Section 3.5.1**). Subsequent noise analysis indicated that the $Al_{0.2}Ga_{0.8}As$ p^+-i-n^+ photodiode based spectroscopic system performance was primarily limited by the performance of the preamplifier electronics rather than the material's inherent properties (see **Section 3.5.2**). Slight modifications to the preamplifier resulted in an improved energy resolution for the $Al_{0.2}Ga_{0.8}As$ p^+-i-n^+ mesa photodiodes (1.06 keV ± 0.04 keV FWHM at 5.9 keV at 20 °C) (see **Section 3.7.1**). The results were comparable to the best previously reported energy resolution for non-avalanche AlGaAs X-ray detectors (1.07 keV FWHM at 5.9 keV at room temperature (Barnett et al., 2010)). The results indicated that, should the detection efficiency (thickness) be increased and the energy resolution improved, $Al_{0.2}Ga_{0.8}As$ radiation detectors may provide a suitable replacement for conventional Si X-ray detectors used within space science missions (e.g. in situ planetary analysis on the Martian and Lunar surface, or planetary remote sensing within the Jovian system), where required temperature control systems and radiation shielding could be reduced or removed entirely, reducing the financial costs and technological complexity of future space science missions.

A prototype 2 × 2 square pixel $Al_{0.2}Ga_{0.8}As$ p^+-i-n^+ mesa photodiode array (each photodiode area 200 µm by 200 µm, 3 µm i layer) was also investigated for its spectroscopic response to X-ray illumination (see **Chapter 4**). Uniformity in electrical characteristics (see **Section 4.4**) and measured energy resolution (see **Section 4.5**) across each pixel was demonstrated within the temperature range 30 °C to -20 °C, in addition to the best measured energy resolution so far reported for AlGaAs non-avalanche X-ray photodiodes at 20 °C (756 eV ± 30 eV FWHM at 5.9 keV (see **Section 4.5.1**)). As the epitaxial wafer material of the $Al_{0.2}Ga_{0.8}As$ photodiodes reported in **Chapter 3** was the same as that used for the 2 × 2 square pixel $Al_{0.2}Ga_{0.8}As$ photodiode

array, the improved energy resolution was attributed in part to subtle improvements in device fabrication and processing techniques. Subtle modifications to the front-end of the preamplifier may have also contributed to the improved energy resolution (see **Section 4.7**). The results demonstrated, for the first time, that device yields are now sufficient such that small (2 × 2) $Al_{0.2}Ga_{0.8}As$ mesa pixel arrays can be produced at a quality suitable for photon counting X-ray spectroscopy.

The prototype 2 × 2 square pixel $Al_{0.2}Ga_{0.8}As$ photodiode array was further investigated for its utility as a direct detection electron (β^- particle) detector, operated uncooled at 20 °C (see **Chapter 4**). Each pixel was illuminated by a ^{63}Ni β^- particle source at room temperature (20 °C) (see **Section 4.6.3**), and theoretical Monte Carlo simulations were performed (see **Section 4.6.2**). The simulated spectra (i.e. those expected to be detected) were found to be in good agreement with those obtained experimentally, demonstrating that each $Al_{0.2}Ga_{0.8}As$ pixel based spectrometer could spectroscopically detect electrons from the ^{63}Ni β^- particle source (see **Section 4.6.3**).

As a possible option to improve the high energy response of the reported $Al_{0.2}Ga_{0.8}As$ photodiode array electron spectrometer, inactive Al absorber layers to be placed atop the detecting structure were investigated using Monte Carlo simulations (see **Section 4.6.4**). These simulations showed that the number of counts detected from 4,000 incident 100 keV electrons could be increased from 1291 to 1664 if a 20 µm Al layer was introduced. Similarly, the numbers of counts could be increased from 397 to 944 given 4,000 incident 200 keV electrons, and 101 to 382 given 4,000 incident 500 keV electrons, with the introduction of 100 µm and 500 µm Al layers, respectively. Thus the simulated E_{abs} of the spectrometer (see **Section 4.6.1**) was found to increase by 22 % (0.1238 ± 0.0020 to 0.1508 ± 0.0024) at 100 keV, 46 % (0.0296 ± 0.0005 to 0.0431 ± 0.0007) at 200 keV, and 20 % (0.0065 ± 0.0001 to 0.0078 ± 0.0001) at 500 keV, respectively, when these inactive Al absorption layers were employed.

To inform future development of $Al_{0.2}Ga_{0.8}As$ detectors for space science applications the electron spectrum predicted to be detected by a spectrometer employing an $Al_{0.2}Ga_{0.8}As$ photodiode, of the type reported in this thesis, within the near-Jupiter radiation environment was considered (see **Section 4.6.5**). Given a single pixel of the reported 2 × 2 array and the expected omnidirectional electron flux at 8.25 R_J from Jupiter (8.41×10^7 cm^{-2} s^{-1} within the energy range 1 keV to 66 keV), the total number of counts expected to be detected over an accumulation time of 0.6 s was 4.46×10^3 counts per pixel.

$Al_{0.6}Ga_{0.4}As$ p^+-i-n^+ circular mesa X-ray photodiodes of different diameters (200 µm and 400 µm) have been demonstrated to operate as photon counting spectroscopic X-ray detectors at room

temperature (20 °C) (see **Chapter 5**). The measured energy resolution (FWHM at 5.9 keV) of the reported devices (see **Section 5.5.1**) was better than any previously reported $Al_xGa_{1-x}As$ X-ray photodiodes at room temperature (756 eV ± 30 eV FWHM at 5.9 keV at 20 °C (see **Section 4.5.1**)), and comparable to that measured in recent studies of other wide bandgap III-V materials, such as $Al_{0.52}In_{0.48}P$ (e.g. 682 eV FWHM at 5.9 keV at 20 °C (Auckloo et al., 2016)). At optimal operating conditions, and at 20 °C, the $Al_{0.6}Ga_{0.4}As$ photodiode based spectrometers had a measured energy resolution of 626 eV ± 20 eV (at V_R = 38 V) and 732 eV ± 30 eV (at V_R = 40 V) FWHM at 5.9 keV, for $S_{200\mu m}$ and $S_{400\mu m}$ respectively (see **Section 5.5.1**).

The spectroscopic response of the 200 µm and 400 µm diameter $Al_{0.6}Ga_{0.4}As$ devices changed as a function of applied reverse bias in a manner consistent with an avalanche photodiode (see **Section 5.5.1**). At high detector reverse bias, secondary and tertiary peaks were present at the left hand side of the main photopeak (see **Section 5.5.2**). The third peak was hypothesised to be from Al Kα (1.49 keV (Sánchez et al., 2003)) X-rays from detector self-fluorescence. The secondary and main peak were both from the combination of the emissions from the ^{55}Fe radioisotope X-ray source (Mn Kα = 5.9 keV; Mn Kβ = 6.49 keV) (see **Section 5.5.2**). The apparent multiplication factors of the primary and secondary ^{55}Fe X-ray photopeaks for the 200 µm $Al_{0.6}Ga_{0.4}As$ device based spectrometer were measured as a function of increasing applied reverse bias (see **Section 5.6**). Values of 5.20 and 3.43 were measured at 40 V applied reverse bias to the detector for the primary and secondary ^{55}Fe X-ray photopeaks, respectively. The apparent multiplication factors were larger than expected, and could not be explained by the accepted ratio between the electron and hole impact ionization coefficients (see **Section 5.6**). As such, the apparent impact ionization coefficients (α and β) were calculated assuming that the primary (and secondary) peaks corresponded to events which had received maximum pure electron (and maximum pure hole) initiated avalanche multiplication. With 40 V reverse bias (E_f = 345 kV cm^{-1}) applied to the detector, apparent ionisation coefficients of α = 8513 and β = 4930 were calculated from the measurements.

The X-ray spectroscopic performance of two circular (one 200 µm diameter and one 400 µm diameter) $GaAs/Al_{0.8}Ga_{0.2}As$ SAM APDs was investigated (see **Chapter 6**). Each device consisted of a 10 µm thick GaAs absorption layer and a 0.1 µm thick $Al_{0.8}Ga_{0.2}As$ multiplication layer (see Table 6.1). The best measured energy resolution achieved at 20 °C for the spectrometer S_{200} was 508 eV ± 5 eV FWHM at 5.9 keV, at an applied detector reverse bias of 26 V, corresponding to an apparent multiplication factor of 1.1. The best measured energy resolution at 20 °C for the spectrometer S_{400} was 603 eV ± 6 eV FWHM at 5.9 keV, at an applied detector reverse bias of 34 V, corresponding to an apparent multiplication factor of 1.2 (see **Section 6.5.1**). Comparisons between the measured noise contributions and the expected non-avalanche noise

contributions indicated that introducing a separate AlGaAs multiplication layer may be beneficial to GaAs based photodiodes (see **Section 6.5.4**). The measured energy resolution (FWHM at 5.9 keV) reported was the best so far reported for GaAs/$Al_xGa_{1-x}As$ SAM APD based X-ray spectrometers at room temperature, where energy resolutions of 1.08 keV FWHM at 5.9 keV (Gomes et al., 2014) and 900 eV FWHM at 13.96 keV (Lauter et al., 1995) have been previously reported.

The electron-hole pair creation energies for $Al_{0.2}Ga_{0.8}As$ and $Al_{0.6}Ga_{0.4}As$ were measured for the first time. The results agreed with previous electron-hole pair creation energy measurements for a number of materials (see **Section 3.8** and **5.7**) that the Klein model (that which describes the empirical relationship between the electron-hole pair creation energy and the bandgap energy) is unphysical. The electron-hole pair creation energy measurements reported here, support the case of the Bertuccio-Maiocchi-Barnett relationship, and were used to further refine the model (see **Section 5.7**).

The work presented in this thesis, including extensive characterisation of the investigated devices, supported calculations, theoretical simulations, and comparisons to previous reports in the literature, advances the state of AlGaAs photodiode radiation detectors for space science applications. Although the reported energy resolutions achieved are modest when compared with other more developed materials (see **Section 3.9**), the results indicate that $Al_{0.2}Ga_{0.8}As$ p^+-i-n^+ photodiodes, $Al_{0.6}Ga_{0.4}As$ p^+-i-n^+ photodiodes, and GaAs/$Al_{0.8}Ga_{0.2}As$ SAM APDs are potentially promising replacements for conventional Si X-ray detectors used within space science missions, should the detection efficiency (active region thickness) be increased and the energy resolution improved. Future space science missions that may benefit from such detectors include those to study the Jovian and Saturnian systems, where spacecraft are exposed to intense radiation, and those to study inner planetary bodies such as Mercury and Venus, which give rise to extreme temperatures (see **Section 1.3**).

7.2 Future work

The results reported in this thesis indicate several avenues for future research regarding the investigated devices, and for improving their suitability for use in space science applications. This section discusses such possibilities and explains how the research would be beneficial.

For each spectroscopic system in which a thorough noise analysis was conducted (see **Sections 3.5.2**, **3.7.2**, **4.5.2**, and **6.5.3**), the unknown noise (stray dielectric noise, stray series white noise, and stray parallel white noise) was found to be significant. From work conducted in the literature

regarding a variety of detector types, notably Silicon Drift Detectors (SDDs) and Depleted Field Effect Transistors (DEPFETs), X-ray energy resolution performance has improved considerably through modifications to the front-end electronics. Recently, the energy resolution of an SDD based X-ray spectrometer has been reduced to near the Fano limit at room temperature (141 eV FWHM at 5.9 keV at 21 °C (Bertuccio et al., 2015) cf. Fano noise limit = 120 eV FWHM at 5.9 keV). Whilst it should be noted that SDDs possess exceptionally low capacitances (< 0.1 pF (Bertuccio et al., 2015)) and consequently low series white noise contributions, should the Fano noise limit be reached for the devices reported in this thesis, they would likely receive wide-spread adoption in many types of space science mission. A particular way in which the dielectric noise of the front-end electronics could be reduced, would be to make the input FET from the same material as the detector, and integrate the input FET onto the same wafer as the detector (Bertuccio et al., 1996).

Radiation doses within the space environment can be substantial (e.g. radiation doses of ≈ 200 krad per day, at a distance of 280 Mm from Jupiter's centre of mass, assuming an isotropic radiation environment, and 4 mm of Al shielding (Atzei et al., 2007)). Such intense radiation can degrade spectroscopic performance (Lindström, 2003) (Hall & Holland, 2010). Indeed, the development of radiation-hard instrumentation for use in the Jovian system is a pressing matter, as the financial cost and technical complexity imposes limits on the frequency of missions to the Jovian system, as well as restricting mission objectives. Reducing instrument radiation shielding and temperature control requirements by using radiation-hard and temperature tolerant semiconductor detectors would help alleviate these restrictions. Although the radiation hardness of $Al_xGa_{1-x}As$ has been studied for other applications (Walker et al., 2017) (Yoshida et al., 1982) (Yamaguchi et al., 1995), it is important to directly study the radiation hardness of the devices reported in this thesis, with a specific view to establishing how their performance as spectroscopic radiation detectors changes with exposure to high doses of radiation. Radiation damage investigations using the photons, charged particles, energy ranges, and fluxes of the radiation environments anticipated within likely forthcoming space science missions (e.g. those to study the interactions between local environments of the Galilean moons) is essential in order to verify the suitability of these detectors, and to accurately determine the likely lifetimes of the spectrometer once deployed to these harsh environments.

The investigation of the spectroscopic responses of the devices reported in this thesis was limited to X-rays of 5.9 keV (Mn Kα) and 6.49 keV (Mn Kβ) energy and β^- particles of ≤ 66 keV energy. Characterisation of the devices at higher energies (e.g. X-rays and γ-rays from ^{241}Am and ^{109}Cd radioisotope X-ray/γ-ray sources, and β^- particles from ^{147}Pm and ^{90}Sr radioisotope β^- particle sources) and lower energies (e.g. from X-ray fluorescence of low *Z*, high purity, metal foils)

would enable study of energy dependent phenomena in the detectors, such as charge trapping and incomplete charge collection noise.

Research finding	Proposed future work	Proposed method
The spectroscopic systems investigated in this thesis possessed significant "unknown" noise contributions (stray dielectric noise, stray series white noise, and stray parallel white noise).	Improve front-end electronics to reduce dielectric noise contributions. Apply novel wafer architectures such as those found in SSDs and DEPFETs to $Al_xGa_{1-x}As$.	Reduce the presently reported stray noise contributions by careful study and reselection of preamplifier components. Design, produce, and integrate an input FET onto the same wafer as the detector.
Although radiation hardness studies of $Al_xGa_{1-x}As$ are available, the radiation hardness of $Al_xGa_{1-x}As$ based radiation detectors cf. other materials is not clear.	The radiation hardness of $Al_xGa_{1-x}As$ detectors should be studied, with a specific view to establishing how their performance as spectroscopic radiation detectors changes with exposure to high doses of radiation.	The $Al_xGa_{1-x}As$ devices used in this thesis should be connected to well understood front-end electronics and illuminated with radiation of a known energy deposition rate, with the spectral performance analysed as a function of energy deposition rate.
Investigation of the spectroscopic responses of the devices in this thesis was limited to X-rays of 5.9 keV and 6.49 keV energy, and β^- particles of energy ≤ 66 keV.	Characterise the devices reported in this thesis at higher and lower energies in order to study energy dependent phenomena.	Investigate spectroscopic performance of the devices in this Thesis using ^{241}Am and ^{109}Cd radioisotope X-ray/γ-ray sources. The use of high-purity X-ray fluorescence calibration samples, excited by X-ray tube, should also be explored.

Table 7.1. Key future work directions and proposed methods that have emerged from the research presented in this Thesis.

References

Adachi, S., 1985, *GaAs, AlAs, and $Al_xGa_{1-x}As$: Material Parameters for use in Research and Device Applications*, Journal of Applied Physics, Vol. 58, pp. 1-29.

Adachi, S., 1993, *Properties of Aluminium Gallium Arsenide*, INSPEC, The Institution of Electrical Engineers, London, UK.

Adriani, O., Barbarino, G.C., Bazilevskaya, G.A., Bellotti, R., Boezio, M., Bogomolov, E.A., Bongi, M., Bonvicini, V., Borisov, S., Bottai, S., Bruno, A., Cafagna, F., Campana, D., Carbone, R., Carlson, P., Casolino, M., Castellini, G., Consiglio, L., De Pascale, M.P., De Santis, C., De Simone, N., Di Felice, V., Galper, A.M., Gillard, W., Grishantseva, L., Jerse, G., Karelin, A.V., Koldashov, S.V., Krutkov, S.Y., kVashnin, A.N., Leonov, A., Malakhov, V., Malvezzi, V., Marcelli, L., Mayorov, A.G., Menn, W., Mikhailov, V.V., Mocchiutti, E., Monaco, A., Mori, N., Nikonov, N., Osteria, G., Palma, F., Papini, P., Pearce, M., Picozza, P., Pizzolotto, C., Ricci, M., Ricciarini, S.B., Rossetto, L., Sarkar, R., Simon, M., Sparvoli, R., Spillantini, P., Stochaj, S.J., Stockton, J.C., Stozhkov, Y.I., Vacchi, A., Vannuccini, E., Vasilyev, G., Voronov, S.A., Wu, J., Yurkin, Y.T., Zampa, G., Zampa, N., and Zverev, V.G., 2011, *Cosmic-ray Electron Flux Measured by the PAMELA Experiment between 1 and 625 GeV*, Physical Review Letters, Vol. 106, Art. No. 201101.

Ahmed, S.N., 2014, *Physics and Engineering of Radiation Detection*, 2nd ed., Elsevier, Oxford, UK.

Akimov, Y.K., 2007, *Silicon Radiation Detectors (Review)*, Instruments and Experimental Techniques, Vol. 50, pp. 1-28.

American National Standards Institute, 1989, *IEEE Standard Test Procedures for Amplifiers and Preamplifiers used with Detectors of Ionizing Radiation*, IEEE Std. 101065-1989.

Andrews, G.B., Zurbuchen, T.H., Mauk, B.H., Malcom, H., Fisk, L.A., Gloeckler, G., Ho, G.C., Kelley, J.S., Koehn, P.L., LeFevere, T.W., Livi, S.S., Lundgren, R.A., and Raines, J.M., 2007, *The Energetic Particle and Plasma Spectrometer Instrument on the MESSENGER Spacecraft*, Space Science Reviews, Vol. 131, pp. 523-556.

Arai, T., Okada, T., Yamamoto, Y., Ogawa, K., Shirai, K., and Kato, M., 2008, *Sulfur Abundance of Asteroid 25143 Itokawa Observed by X-ray Fluorescence Spectrometer Onboard Hayabusa*, Earth, Planets and Space, Vol. 60, pp. 21-31.

Armantrout, G.A., Swierkowski, S.P., Sherohman, J.W., and Yee, J.H., 1977, *What Can Be Expected from High-Z Semiconductor Detectors?*, IEEE Transactions on Nuclear Science, Vol. 24, pp. 121-125.

Athiray, P.S., Narendranath, S., Sreekumar, P., Grande, M., 2014, *C1XS results — First measurement of enhanced sodiumon the lunar surface*, Planetary and Space Science, Vol. 104, pp. 279-287.

Atzei, A., Wielders, A., Stankov, A., and Falkner, P., 2007, *Overview of the ESA Jovian Technology Reference Studies*, ESA/ESTEC Technical Note, Netherlands.

Auckloo, A., Cheong, J.S., Meng, X., Tan, C.H., Ng, J.S., Krysa, A., Tozer, R.C., and David, J.P.R., 2016, *$Al_{0.52}In_{0.48}P$ Avalanche Photodiodes for Soft X-ray Spectroscopy*, Journal of Instrumentation, Vol. 11, Art. No. P03021.

Bambynek, W., Crasemann, B., Fink, R.W., Freund, H.U., Mark, H., Swift, C.D., Price, R.E., and Rao, P.V., 1972, *X-Ray Fluorescence Yields, Auger, and Coster-Kronig Transition Probabilities*, Reviews of Modern Physics, Vol. 44, pp. 716-813.

Barnett, A.M., 2011, *Wide Band Gap Compound Semiconductor Detectors for X-ray Spectroscopy in Harsh Environments*, PhD Thesis, Department of Physics and Astronomy, University of Leicester, Leicester, UK.

Barnett, A.M., Bassford, D.J., Lees, J.E., Ng, J.S., Tan, C.H., and David, J.P.R., 2010, *Temperature Dependence of AlGaAs Soft X-ray Detectors*, Nuclear Instruments and Methods in Physics Research Section A, Vol. 621, pp. 453-455.

Barnett, A.M., Lees, J.E., and Bassford, D.J., 2013a, *Temperature Dependence of the Average Electron-hole Pair Creation Energy in $Al_{0.8}Ga_{0.2}As$*, Applied Physics Letters, Vol. 102, Art. No. 181119.

Barnett, A.M., Lees, J.E., and Bassford, D.J., 2013b, *First Spectroscopic X-ray and Beta Results from a 400 μm Diameter $Al_{0.8}Ga_{0.2}As$ photodiode*, Journal of Instrumentation, Vol. 8, Art. No. P10014.

Barnett, A.M., Lees, J.E., Bassford, D.J., and Ng, J.S., 2012a, *A Varied Shaping Time Noise Analysis of $Al_{0.8}Ga_{0.2}As$ and GaAs Soft X-ray Photodiodes Coupled to a Low-noise Charge Sensitive Preamplifier*, Nuclear Instruments and Methods in Physics Research Section A, Vol. 673, pp. 10-15.

Barnett, A.M., Lees, J.E., Bassford, D.J., and Ng, J.S., 2012b, *Determination of the Electron-hole Pair Creation Energy in $Al_{0.8}Ga_{0.2}As$*, Journal of Instrumentation, Vol. 7, Art. No. P06016.

Barnett, A.M., Lees, J.E., Bassford, D.J., Ng, J.S., Tan, C.H., and Gomez, R.B., 2011a, *Modelling Results of Avalanche Multiplication in AlGaAs Soft X-ray APDs*, Nuclear Instruments and Methods in Physics Research Section A, Vol. 626, pp. 25-30.

Barnett, A.M., Lees, J.E., Bassford, D.J., Ng, J.S., Tan, C.H., and Gomes, R.B., 2011b, *Temperature Dependence of the Avalanche Multiplication Process and the Impact Ionization Coefficients in $Al_{0.8}Ga_{0.2}As$*, Nuclear Instruments and Methods in Physics Research Section A, Vol. 629, pp. 154-156.

Barnett, A.M., Lioliou, G., and Ng, J.S., 2015, *Characterization of Room Temperature AlGaAs Soft X-ray Mesa Photodiodes*, Nuclear Instruments and Methods in Physics Research Section A, Vol. 774, pp. 29-33.

Barth, J.L., Isaacs, J.C., and Poivey, C., 2000, *The Radiation Environment for the Next Generation Space Telescope*, NGST Doc. 570, pp. 1-29.

Benkhoff, J., van Casteren, J., Hayakawa, H., Fujimoto, M., Laakso, H., Novara, M., Ferri, P., Middleton, H.R., and Ziethe, R., 2010, *BepiColombo–Comprehensive Exploration of Mercury: Mission Overview and Science Goals*, Planetary and Space Science, Vol. 58, pp. 2-20.

Bertuccio, G., 2012, *The Silence of the Amps: Integrated Circuits for Very-Low-Noise Processing of Random Signals from Radiation Detectors*, IEEE Solid-State Circuits Magazine, Vol. 4, pp. 36-45.

Bertuccio, G., Ahangarianabhari, M., Graziani, C., Macera, D., Shi, Y., Rachevski, A., Rashevskaya, I., Vacchi, A., Zampa, G., Zampa, N., Bellutti, P., Giacomini, G., Picciotto, A., and Piemonte, C., 2015, *A Silicon Drift Detector-CMOS front-end system for high resolution X-ray spectroscopy up to room temperature*, Journal of Instrumentation, Vol. 10, Art. No. P01002.

Bertuccio, G., Caccia, S., Puglisi, D., and Macera, D., 2011, *Advances in Silicon Carbide X-ray Detectors*, Nuclear Instruments and Methods in Physics Research Section A, Vol. 652, pp. 193-196.

Bertuccio, G., and Casiraghi, R., 2003, *Study of Silicon Carbide for X-ray Detection and Spectroscopy*, IEEE Transactions on Nuclear Science, Vol. 50, pp. 175-185.

Bertuccio, G., and Maiocchi, D., 2002, *Electron-hole Pair Generation Energy in Gallium Arsenide by X-ray and γ-ray Photons*, Journal of Applied Physics, Vol. 92, Art. No. 3.

Bertuccio, G., and Pullia, A., 1993, *A Method for the Determination of the Noise Parameters in Preamplifying Systems for Semiconductor Radiation Detectors*, Review of Scientific Instruments, Vol. 64, pp. 3294-3298.

Bertuccio, G., Pullia, A., and De Geronimo, G., 1996, *Criteria of Choice of the Front-end Transistor for Low-noise Preamplification of Detector Signals at Sub-microsecond Shaping Times for X-ray and γ-ray Spectroscopy*, Nuclear Instruments and Methods in Physics Research Section A, Vol. 380, pp. 301-307.

Bertuccio, G., Pullia, A., Lauter, J., Forster, A., and Luth, H., 1997, *Pixel X-ray Detectors in Epitaxial Gallium Arsenide with High Energy Resolution Capabilities (Fano Factor Experimental Determination)*, IEEE Transactions on Nuclear Science, Vol. 44, Art. No. 1.

Bertuccio, G., Rehak, P., and Xi, D., 1993, *A Novel Charge Sensitive Preamplifier without the Feedback Resistor*, Nuclear Instruments and Methods in Physics Research Section A, Vol. 326, pp. 71-76.

Blake, D. F., Vaniman, D. T., Anderson, R., Bish, D., Chipera, S., Chemtob, S., Crisp, J., Desmarais, D. J., Downs, R., Farmer, J., Gailhanou, M., Ming, D. W., Morris, D., Stolper, E., Sarrazin, P., Treiman, A. H., and Yen, A., 2009, *The CheMin Mineralogical Instrument on the Mars Science Laboratory Mission*, 40th Lunar and Planetary Science Conference, Lunar and Planetary Science XL, The Woodlands, USA.

Blake, D., Vaniman, D., Achilles, C., Anderson, R., Bish, D., Bristow, T., Chen, C., Chipera, S., Crisp, J., Des marais, D., Downs, R.T., Farmer, J., Feldman, S., Fonda, M., Gailhanou, M., Ma, H., Ming, D.W., Morris, R.V., Sarrazin, P., Stolper, E., Treiman, A., and Yen, A., 2012, *Characterization and Calibration of the CheMin Mineralogical Instrument on Mars Science Laboratory*, Space Science Reviews, Vol. 170, pp. 341-399.

Boyle, W.S., and Smith, G.E., 1970, *Charge Coupled Semiconductor Devices*, The Bell System Technical Journal, Vol. 49, pp. 587-593.

Branduardi-Raymont, G., Bhardwaj, A., Elsner, R.F., and Rodriguez, P., 2010, *X-rays From Saturn: A Study with XMM-Newton and Chandra over the Years 2002–2005*, Astronomy and Astrophysics, Vol. 510, Art. No. A73.

Branduardi-Raymont, G., Bhardwaj, A., Elsner, R.F., Gladstone, G.R., Ramsay, G., Rodriguez, P., Soria, R., Waite, J.H., Jr, and Cravens, T.E., 2007, *A Study of Jupiter's Aurorae with XMM-Newton*, Astronomy and Astrophysics, Vol. 463, pp. 761-774.

Brown, W.L., Higinbotham, W.A., Miller, G.L., and Chase, R.L., 1969, *Semiconductor Nuclear-particle Detectors and Circuits: Proceedings of a Conference Conducted by the Subcommittee on Instruments and Techniques, Committee on Nuclear Science*, National Academy of Sciences, Washington, USA.

Brozel, M.R., and Stillman, G.E., 1996, *Properties of Gallium Arsenide*, 3rd ed, The Institution of Electrical Engineers, London, UK.

Brückner, J., Dreibus, G., Rieder, R., and Wänke, H., 2003, *Refined Data of Alpha Proton X-ray Spectrometer Analyses of Soils and Rocks at the Mars Pathfinder Site: Implications for Surface Chemistry*, Journal of Geophysical Research: Planets, Vol. 108, Art. No. E12.

Butera, S., Lioliou, G., Krysa, A.B., and Barnett, A.M., 2017, *InGaP (GaInP) Mesa p-i-n Photodiodes for X-ray Photon Counting Spectroscopy*, Scientific Reports, Vol. 7, Art. No. 10206.

Butera, S., Lioliou, G., Krysa, A.B., and Barnett, A.M., 2018a, *Measurement of the Electron–hole Pair Creation Energy in $Al_{0.52}In_{0.48}P$ using X-ray radiation*, Nuclear Instruments and Methods in Physics Research Section A, Vol. 879, pp. 64-68.

Butera, S., Lioliou, G., Krysa, A.B., and Barnett, A.M., 2018b, *Temperature Characterisation of Spectroscopic InGaP X-ray Photodiodes*, Nuclear Instruments and Methods in Physics Research Section A, Vol. 908, pp. 277-284.

Butera, S., Lioliou, G., Zhao, S., Whitaker, M.D.C., Krysa, A.B., and Barnett, A.M., 2019, *InGaP electron spectrometer for high temperature environments*, Scientific Reports, Vol. 9, Art. No. 11096.

Butera, S., Whitaker, M.D.C., Lioliou, G., and Barnett, A.M., 2016, *AlGaAs ^{55}Fe X-ray Radioisotope Microbattery*, Scientific Reports, Vol. 6, Art. No. 38409.

Campbell, J.C., Dentai, A.G., Holden, W.S., and Kasper, B.L., 1983, *High-performance Avalanche Photodiode with Separate Absorption 'Grading' and Multiplication Regions*, Electronics Letters, Vol. 19, pp. 818-820.

Campbell, J.C., 2007, *Recent Advances in Telecommunications Avalanche Photodiodes*, Journal of Lightwave Technology, Vol. 25, pp. 109-121.

Capasso, F., Won-Tien, T., and Williams, G.F., 1983, *Staircase Solid-state Photomultipliers and Avalanche Photodiodes with Enhanced Ionization Rates Ratio*, IEEE Transactions on Electron Devices, Vol. 30, pp. 381-390.

Casnati, E., Tartari, A., and Baraldi, C., 1982, *An empirical approach to K-shell ionisation cross section by electrons*, Journal of Physics B: Atomic and Molecular Physics, Vol. 15, pp. 155-167.

Catura, R.C., and Smithson, R.C., 1979, *Single Photon X-ray Detection with a CCD Image Sensor*, Review of Scientific Instruments, Vol. 50, pp. 219-220.

Chia, C.K., Ng, B.K., David, J.P.R., Rees, G.J., Tozer, R.C., Hopkinson, M., Airey, R.J., and Robson, P.N., 2003, *Multiplication and Excess Noise in $Al_xGa_{1-x}As$/GaAs Multilayer Avalanche Photodiodes*, Journal of Applied Physics, Vol. 94, Art. No. 4.

Crisp, J.A., Adler, M., Matijevic, J.R., Squyres, S.W., Arvidson, R.E., and Kass, D.M., 2003, *Mars Exploration Rover Mission*, Journal of Geophysical Research: Planets, Vol. 108, Art. No. 8061.

Damerell, C.J.S., 1998, *Charge-coupled Devices as Particle Tracking Detectors*, Review of Scientific Instruments, Vol. 69, Art. No. 4.

David, J.P.R., and Tan, C.H., 2008, *Material Considerations for Avalanche Photodiodes*, IEEE Journal of Selected Topics in Quantum Electronics, Vol. 14, pp. 998-1009.

Drouin, D., Hovington, P., and Gauvin, R., 1997, *CASINO: A New Monte Carlo Code in C Language for Electron Beam Interactions—Part II: Tabulated Values of the Mott Cross Section*, Scanning, Vol. 19, pp. 20-28.

Dunkin, S.K., Grande, M., Casanova, I., Fernandes, V., Heather, D.J., Kellett, B., Muinonen, K., Russell, S.S., Browning, R., Waltham, N., Parker, D., Kent, B., Perry, C.H., Swinyard, B., Perry, A., Feraday, J., Howe, C., Phillips, K., McBride, G., Huovelin, J., Muhli, P., Hakala, P.J., Vilhu, O., Thomas, N., Hughes, D., Alleyne, H., Grady, M., Lundin, R., Barabash, S., Baker, D., Clark, P.E., Murray, C.D., Guest, J., D'uston, L.C., Maurice, S., Foing, B., Christou, A., Owen, C., Charles, P., Laukkanen, J., Koskinen, H., Kato, M., Sipila, K., Nenonen, S., Holmstrom, M., Bhandari, N., Elphic, R., and Lawrence, D., 2003, *Scientific Rationale for the D-CIXS X-ray Spectrometer on board ESA's SMART-1 Mission to the Moon*, Planetary and Space Science, Vol. 51, pp. 435-442.

Dunn, W.R., Branduardi-Raymont, G., Ray, L.C., Jackman, C.M., Kraft, R.P., Elsner, R.F., Rae, I.J., Yao, Z., Vogt, M.F., Jones, G.H., Gladstone, G.R., Orton, G.S., Sinclair, J.A., Ford, P.G., Graham, G.A., Caro-Carretero, R., and Coates, A.J., 2017, *The Independent Pulsations of Jupiter's Northern and Southern X-ray Auroras*, Nature Astronomy, Vol. 1, pp. 758-764.

Economou, T., 2001, *Chemical Analyses of Martian Soil and Rocks Obtained by the Pathfinder Alpha Proton X-ray Spectrometer*, Radiation Physics and Chemistry, Vol. 61, pp. 191-197.

Elsner, R.F., Ramsey, B.D., Waite, J.H., Rehak, P., Johnson, R.E., Cooper, J.F., and Swartz, D.A., 2005, *X-ray Probes of Magnetospheric Interactions with Jupiter's Auroral Zones, the Galilean Satellites, and the Io Plasma Torus*, Icarus, Vol. 178, pp. 417-428.

Erd, C., Owens, A., Brammertz, G., Bavdaz, M., Peacock, A., Lämsä, V., Nenonen, S., Andersson, H., and Haack, N., 2002, *Hard X-ray Test and Evaluation of a Prototype 32×32 Pixel Gallium Arsenide Array*, Nuclear Instruments and Methods in Physics Research Section A, Vol. 487, pp. 78-89.

Evans, R.D., 1955, *The Atomic Nucleus*, McGraw-Hill, New York, USA.

Fano, U., 1947, *Ionization Yield of Radiations. II. The Fluctuation of the Number of Ions*, Physical Review, Vol. 72, Art. No. 1.

Foing, B.H., Heather, D.J., and Almeida, M., 2001, *The Science Goals Of Esa's Smart-1 Mission To The Moon*, Earth, Moon, and Planets, Vol. 85, pp. 523-531.

Fraser, G.W., 1989, *X-ray Detectors in Astronomy*, Cambridge University Press, Cambridge, UK.

Fraser, G.W., Carpenter, J.D., Rothery, D.A., Pearson, J.F., Martindale, A., Huovelin, J., Treis, J., Anand, M., Anttila, M., Ashcroft, M., Benkoff, J., Bland, P., Bowyer, A., Bradley, A., Bridges, J., Brown, C., Bulloch, C., Bunce, E.J., Christensen, U., Evans, M., Fairbend, R., Feasey, M., Giannini, F., Hermann, S., Hesse, M., Hilchenbach, M., Jorden, T., Joy, K., Kaipiainen, M., Kitchingman, I., Lechner, P., Lutz, G., Malkki, A., Muinonen, K., Näränen, J., Portin, P., Prydderch, M., Juan, J.S., Sclater, E., Schyns, E., Stevenson, T.J., Strüder, L., Syrjasuo, M., Talboys, D., Thomas, P., Whitford, C., and Whitehead, S., 2010, *The Mercury Imaging X-ray Spectrometer (MIXS) on Bepicolombo*, Planetary and Space Science, Vol. 58, pp. 79-95.

Fujiwara, A., Kawaguchi, J., Yeomans, D.K., Abe, M., Mukai, T., Okada, T., Saito, J., Yano, H., Yoshikawa, M., Scheeres, D.J., Barnouin-Jha, O., Cheng, A.F., Demura, H., Gaskell, R.W., Hirata, N., Ikeda, H., Kominato, T., Miyamoto, H., Nakamura, A.M., Nakamura, R., Sasaki, S., and Uesugi, K., 2006, *The Rubble-Pile Asteroid Itokawa as Observed by Hayabusa*, Science, Vol. 312, pp. 1330-1334.

Gatti, E., and Rehak, P., 1983, *Concept of a Solid-State Drift Chamber*, Proceedings of DPF Workshop on Collider Detectors: Present Capabilities and Future Possibilities, Lawrence Berkley Lab, Berkley, USA.

Gatti, E., Sampietro, M., Manfredi, P.F., and Speziali, V., 1990, *Suboptimal Filtering of 1/f-noise in Detector Charge Measurements*, Nuclear Instruments and Methods in Physics Research Section A, Vol. 297, pp. 467-478.

Gellert, R., Campbell, J.L., King, P.L., Leshin, L.A., Lugmair, G.W., Spray, J.G., Squyres, S.W., and Yen, A.S., 2009, *The Alpha-Particle-X-ray-Spectrometer (APXS) for the Mars Science Laboratory (MSL) Rover Mission*, 40th Lunar and Planetary Science Conference, The Woodlands, USA.

Gellert, R., Rieder, R., Brückner, J., Clark, B.C., Dreibus, G., Klingelhöfer, G., Lugmair, G., Ming, D.W., Wänke, H., Yen, A., Zipfel, J., and Squyres, S.W., 2006, *Alpha Particle X-Ray Spectrometer (APXS): Results from Gusev Crater and Calibration Report*, Journal of Geophysical Research: Planets, Vol. 111, Art. No. E2.

Gershman, D.J., Raines, J.M., Slavin, J.A., Zurbuchen, T.H., Anderson, B.J., Korth, H., Ho, G.C., Boardsen, S.A., Cassidy, T.A., Walsh, B.M., and Solomon, S.C., 2015, *MESSENGER Observations of Solar Energetic Electrons within Mercury's Magnetosphere*, Journal of Geophysical Research: Space Physics, Vol. 120, pp. 8559-8571.

Gilmore, G., 2008, *Practical Gamma-ray Spectrometry*, 2nd ed., John Wiley & Sons, Chichester, UK.

Gladstone, G.R., Waite Jr, J.H., Grodent, D., Lewis, W.S., Crary, F.J., Elsner, R.F., Weisskopf, M.C., Majeed, T., Jahn, J.M., Bhardwaj, A., Clarke, J.T., Young, D.T., Dougherty, M.K., Espinosa, S.A., and Cravens, T.E., 2002, *A Pulsating Auroral X-ray Hot Spot on Jupiter*, Nature, Vol. 415, pp. 1000-1003.

Glisson, T.H., 2011, *Introduction to Circuit Analysis and Design*, Springer, Netherlands.

Gohil, T., Whale, J., Lioliou, G., Novikov, S.V., Foxon, C.T., Kent, A.J., and Barnett, A.M., 2016, *X-ray Detection with Zinc-Blende (Cubic) GaN Schottky Diodes*, Scientific Reports, Vol. 6, Art. No. 29535.

Golombek, M.P., 1997, *The Mars Pathfinder Mission*, Journal of Geophysical Research: Planets, Vol. 102, Art. No. E2.

Golombek, M.P., Anderson, R.C., Barnes, J.R., Bell, J.F., Bridges, N.T., Britt, D.T., Brückner, J., Cook, R.A., Crisp, D., Crisp, J.A., Economou, T., Folkner, W.M., Greeley, R., Haberle, R.M., Hargraves, R.B., Harris, J.A., Haldemann, A.F.C., Herkenhoff, K.E., Hviid, S.F., Jaumann, R., Johnson, J.R., Kallemeyn, P.H., Keller, H.U., Kirk, R.L., Knudsen, J.M., Larsen, S., Lemmon, M.T., Madsen, M.B., Magalhães, J.A., Maki, J.N., Malin, M.C., Manning, R.M., Matijevic, J., McSween, H.Y., Moore, H.J., Murchie, S.L., Murphy, J.R., Parker, T.J., Rieder, R., Rivellini, T.P., Schofield, J.T., Seiff, A., Singer, R.B., Smith, P.H., Soderblom, L.A., Spencer, D.A., Stoker, C.R., Sullivan, R., Thomas, N., Thurman, S.W., Tomasko, M.G., Vaughan, R.M., Wänke, H., Ward, A.W., and Wilson, G.R., 1999, *Overview of the Mars Pathfinder Mission: Launch through Landing, Surface Operations, Data Sets, and Science Results*, Journal of Geophysical Research: Planets, Vol. 104, Art. No. E4.

Gomes, R.B., Tan, C.H., Meng, X., David, J.P.R., and Ng, J.S., 2014, *GaAs/$Al_{0.8}Ga_{0.2}As$ Avalanche Photodiodes for Soft X-ray Spectroscopy*, Journal of Instrumentation, Vol. 9, Art. No. P03014.

Grande, M., Browning, R., Waltham, N., Parker, D., Dunkin, S.K., Kent, B., Kellett, B., Perry, C.H., Swinyard, B., Perry, A., Feraday, J., Howe, C., McBride, G., Phillips, K., Huovelin, J., Muhli, P., Hakala, P.J., Vilhu, O., Laukkanen, J., Thomas, N., Hughes, D., Alleyne, H., Grady, M., Lundin, R., Barabash, S., Baker, D., Clark, P.E., Murray, C.D., Guest, J., Casanova, I., D'uston, L.C., Maurice, S., Foing, B., Heather, D.J., Fernandes, V., Muinonen, K., Russell, S.S., Christou, A., Owen, C., Charles, P., Koskinen, H., Kato, M., Sipila, K., Nenonen, S., Holmstrom, M., Bhandari, N., Elphic, R., and Lawrence, D., 2003, *The D-CIXS X-ray Mapping Spectrometer on SMART-1*, Planetary and Space Science, Vol. 51, pp. 427-433.

Grasset, O., Dougherty, M.K., Coustenis, A., Bunce, E.J., Erd, C., Titov, D., Blanc, M., Coates, A., Drossart, P., Fletcher, L.N., Hussmann, H., Jaumann, R., Krupp, N., Lebreton, J.P., Prieto-Ballesteros, O., Tortora, P., Tosi, F., and van Hoolst, T., 2013, *JUpiter ICy moons Explorer (JUICE): An ESA Mission to Orbit Ganymede and to Characterise the Jupiter System*, Planetary and Space Science, Vol. 78, pp. 1-21.

Grotzinger, J.P., Crisp, J., Vasavada, A.R., Anderson, R.C., Baker, C.J., Barry, R., Blake, D.F., Conrad, P., Edgett, K.S., Ferdowski, B., Gellert, R., Gilbert, J.B., Golombek, M., Gómez-Elvira, J., Hassler, D.M., Jandura, L., Litvak, M., Mahaffy, P., Maki, J., Meyer, M., Malin, M.C., Mitrofanov, I., Simmonds, J.J., Vaniman, D., Welch, R.V., and Wiens, R.C., 2012, *Mars Science Laboratory Mission and Science Investigation*, Space Science Reviews, Vol. 170, pp. 5-56.

van Grieken, R., and Markowicz, A., 2002, *Handbook of X-ray Spectrometry*, 2nd ed., Marcel Dekker, New York, USA.

Gruner, S.M., Tate, M.W., and Eikenberry, E.F., 2002, *Charge-coupled Device Area X-ray Detectors*, Review of Scientific Instruments, Vol. 73, pp. 2815-2842.

Hakim, N.Z., Saleh, B.E.A., and Teich, M.C., 1990, *Generalized Excess Noise Factor for Avalanche Photodiodes of Arbitrary Structure*, IEEE Transactions on Electron Devices, Vol. 37, pp. 599-610.

Hall, D.J., and Holland, A., 2010, *Space Radiation Environment Effects on X-ray CCD Background*, Nuclear Instruments and Methods in Physics Research Section A, Vol. 612, pp. 320-327.

Hansson, C.T.C., Owens, A., and van Den Biezen, J., 2014, *X-ray, γ-ray and Neutron Detector Development for Future Space Instrumentation*, Acta Astronautica, Vol. 93, pp. 121-128.

Harrison, C.N., David, J.P.R., Hopkinson, M., and Rees, G.J., 2002, *Temperature Dependence of Avalanche Multiplication in Submicron $Al_{0.6}Ga_{0.4}As$ Diodes*, Journal of Applied Physics, Vol. 92, Art. No. 12.

van Heerden, P.J., 1945, *The Crystal Counter: A New Instrument in Nuclear Physics*, PhD Thesis, Rijksuniversiteit Utrecht, Utrecht, Netherlands.

Henke, B.L., Gullikson, E.M., and Davis, J.C., 1993, *X-ray Interactions: Photoabsorption, Scattering, Transmission, and Reflection at E = 50 – 30,000 eV, Z = 1 – 92*, Atomic Data and Nuclear Data Tables, Vol. 54, pp. 181-342.

Holland, A.D., Hutchinson, I.B., Smith, D.R., and Pool, P., 2004, *Proton Damage in the E2V Swept Charge Device*, Nuclear Instruments and Methods in Physics Research Section A, Vol. 521, pp. 393-398.

Hovington, P., Drouin, D., and Gauvin, R., 1997, *CASINO: A New Monte Carlo Code in C Language for Electron Beam Interaction — Part I: Description of the Program*, Scanning, Vol. 19, pp. 1-14.

Howell, R.W., 2008, *Auger Processes in the 21st Century*, International journal of radiation biology, Vol. 84, pp. 959-975.

Huovelin, J., Alha, L., Andersson, H., Andersson, T., Browning, R., Drummond, D., Foing, B., Grande, M., Hämäläinen, K., Laukkanen, J., Lämsä, V., Muinonen, K., Murray, M., Nenonen, S., Salminen, A., Sipilä, H., Taylor, I., Vilhu, O., Waltham, N., and Lopez-Jorkama, M., 2002, *The SMART-1 X-ray Solar Monitor (XSM): Calibrations for D-CIXS and Independent Coronal Science*, Planetary and Space Science, Vol. 50, pp. 1345-1353.

Ingersoll, A.P., Vasavada, A.R., Little, B., Anger, C.D., Bolton, S.J., Alexander, C., Klaasen, K.P., and Tobiska, W.K., 1998, *Imaging Jupiter's Aurora at Visible Wavelengths*, Icarus, Vol. 135, pp. 251-264.

Ishikawa, S.N., Katsuragawa, M., Watanabe, S., Uchida, Y., Takeda, S.I., Takahashi, T., Saito, S., Glesener, L., Buitrago-Casas, J.C., Krucker, S., and Christe, S., 2016, *Fine-pitch CdTe Detector for Hard X-ray Imaging and Spectroscopy of the Sun with the FOXSI Rocket Experiment*, Journal of Geophysical Research: Space Physics, Vol. 121, pp. 6009-6016.

Jenkins, R., Gould, R.W., and Gedcke, D., 1995, *Quantitative X-ray Spectrometry*, 2nd ed., Marcel Dekker, New York, USA.

Johnson, T.V., Yeates, C.M., and Young, R., 1992, *Space Science Reviews Volume on Galileo Mission Overview*, Space Science Reviews, Vol. 60, pp. 3-21.

Joy, D.C., and Luo, S., 1989, *An empirical stopping power relationship for low-energy electrons*, Scanning, Vol. 11, pp. 176-180.

Jun, I., Garrett, H.B., Swimm, R., Evans, R.W., and Clough, G., 2005, *Statistics of the Variations of the High Energy Electron Population Between 7 and 28 Jovian Radii as Measured by the Galileo Spacecraft*, Icarus, Vol. 178, pp. 386-394.

Kalinka, G., 1994, *Entrance Window Structure of a Si (Li) Detector*, Nuclear Instruments and Methods in Physics Research Section B, Vol. 88, pp. 470-484.

Kemmer, J., and Lutz, G., 1987, *New Detector Concepts*, Nuclear Instruments and Methods in Physics Research Section A, Vol. 253, pp. 365-377.

Kemmer, J., Lutz, G., Prechtel, U., Schuster, K., Sterzik, M., Strüder, L., and Ziemann, T., 1990, *Experimental Confirmation of a New Semiconductor Detector Principle*, Nuclear Instruments and Methods in Physics Research Section A, Vol. 288, pp. 92-98.

Klein, C.A., 1968, *Bandgap Dependence and Related Features of Radiation Ionization Energies in Semiconductors*, Journal of Applied Physics, Vol. 39, pp. 2029-2038.

Knoll, G., 2000, *Radiation Detection and Measurement*, 3rd ed., John Wiley & Sons, New York, USA.

Kumagai, O., Kawai, H., Mori, Y., and Kaneko, K., 1984, *Chemical Trends in the Activation Energies of DX Centers*, Applied Physics Letters, Vol. 45, pp. 1322-1323.

Lauter, J., Förster, A., Lüth, H., Müller, K.D., Reinartz, R., 1996, *AlGaAs/GaAs Avalanche Detector Array 1GBit/s X-ray Receiver for Timing Measurements*, IEEE Transactions on Nuclear Science, Vol. 43, pp. 1446-1451.

Lauter, J., Protić, D., Förster, A., and Lüth, H., 1995, *AlGaAs/GaAs SAM Avalanche Photodiode: An X-ray Detector for Low Energy Photons*, Nuclear Instruments and Methods in Physics Research Section A, Vol. 356, pp. 324-329.

Lees, J.E., Bassford, D.J., Ng, J.S., Tan, C.H., and David, J.P.R., 2008, *AlGaAs Diodes for X-ray Spectroscopy*, Nuclear Instruments and Methods in Physics Research Section A, Vol. 594, pp. 202-205.

Levinzon, F.A., and Vandamme, L.K.J., 2011, *Comparison of 1/f Noise in JFETs and MOSFETs with several Figures of Merit*, Fluctuation and Noise Letters, Vol. 10, Art. No. 4.

Lide, D.R., 2005, *CRC Handbook of Chemistry and Physics*, 85th ed., CRC Press, Boca Raton, Florida, USA.

Lindström, G., 2003, *Radiation Damage in Silicon Detectors*, Nuclear Instruments and Methods in Physics Research Section A, Vol. 512, pp. 30-43.

Lioliou, G., 2017, *Wide Bandgap Semiconductor Radiation Detectors for Extreme Environments*, PhD Thesis, Department of Engineering and Informatics, University of Sussex, Sussex, UK.

Lioliou, G., Butera, S., Zhao, S., Whitaker, M.D.C., and Barnett, A.M., 2018, *GaAs Spectrometer for Planetary Electron Spectroscopy*, Journal of Geophysical Research: Space Physics, Vol. 123, pp. 7568-7580.

Lioliou, G., Meng, X., Ng, J.S., and Barnett, A.M., 2016a, *Characterization of gallium arsenide X-ray mesa p–i–n photodiodes at room temperature*, Nuclear Instruments and Methods in Physics Research Section A, Vol. 813, pp. 1-9.

Lioliou, G., Meng, X., Ng, J.S., and Barnett, A.M., 2016b, *Temperature Dependent Characterization of Gallium Arsenide X-ray Mesa p-i-n Photodiodes*, Journal of Applied Physics, Vol. 119, Art. No. 124507.

Lioliou, G., Whitaker, M.D.C., and Barnett, A.M., 2017, *High Temperature GaAs X-ray Detectors*, Journal of Applied Physics, Vol. 122, Art. No. 244506.

Lioliou, G., and Barnett, A.M., 2015, *Electronic Noise in Charge Sensitive Preamplifiers for X-ray Spectroscopy and the Benefits of a SiC Input JFET*, Nuclear Instruments and Methods in Physics Research Section A, Vol. 801, pp. 63-72.

Lioliou, G., and Barnett, A.M., 2016, *Gallium Arsenide Detectors for X-ray and Electron (Beta Particle) Spectroscopy*, Nuclear Instruments and Methods in Physics Research Section A, Vol. 836, pp. 37-45.

Lioliou, G., and Barnett, A.M., 2018, *Prototype GaAs X-ray Detector and Preamplifier Electronics for a Deep Seabed Mineral XRF Spectrometer*, X-Ray Spectrometry, Vol. 47, pp. 201-214.

Liu, Y.-P., Tang, X.-B., Xu, Z.-H., Hong, L., Wang, H., Liu, M., and Chen, D., 2015, *Influences of Planar Source Thickness on Betavoltaics with Different Semiconductors*, Journal of Radioanalytical and Nuclear Chemistry, Vol. 304, pp. 517-525.

Livi, S.A., McNutt, R., Andrews, G.B., Keath, E., Mitchell, D., and Ho, G., 2003, *The Energetic Particles Spectrometers (EPS) on MESSENGER and New Horizons*, Proceedings of the Tenth International Solar Wind Conference, American Institute of Physics, Vol. 679, pp. 838-841.

Lottermoser, B., 2010, *Mine Wastes: Characterisation, Treatment and Environmental Impacts*, 3rd ed., Springer, Berlin, Germany.

Lowe, B.G., and Sareen, R.A., 2007, *A Measurement of the Electron–hole Pair Creation Energy and the Fano Factor in Silicon for 5.9keV X-rays and their Temperature Dependence in the range 80–270K*, Nuclear Instruments and Methods in Physics Research Section A, Vol. 576, pp. 367-370.

Lowe, B.G., and Sareen, R.A., 2014, *Semiconductor X-ray Detectors*, Taylor & Francis Group, Florida, USA.

Luque, A., and Hegedus, S., 2003, *Handbook of Photovoltaic Science and Engineering*, 2nd ed., John Wiley & Sons, New Jersey, US.

Lutz, G., Porro, M., Aschauer, S., Wölfel, S., and Strüder, L., 2016, *The DEPFET Sensor-Amplifier Structure: A Method to Beat 1/f Noise and Reach Sub-Electron Noise in Pixel Detectors*, Sensors, Vol. 16, Art. No. 608.

Mari, R.H., Shafi, M., Aziz, M., Khatab, A., Taylor, D., and Henini, M., 2011, *Electrical Characterisation of Deep Level Defects in Be-doped AlGaAs Grown on (100) and (311)A GaAs Substrates by MBE*, Nanoscale Research Letters, Vol. 6, Art. No. 180.

Matson, D.L., Spilker, L.J., and Lebreton, J.-P., 2002, *The Cassini/Huygens Mission to the Saturnian System*, Space Science Reviews, Vol. 104, pp. 1-58.

Mauk, B.H., and Fox, N.J., 2010, *Electron Radiation Belts of the Solar System*, Journal of Geophysical Research: Space Physics, Vol. 115, Art. No. A12220.

Mauk, B.H., Haggerty, D.K., Jaskulek, S.E., Schlemm, C.E., Brown, L.E., Cooper, S.A., Gurnee, R.S., Hammock, C.M., Hayes, J.R., Ho, G.C., Hutcheson, J.C., Jacques, A.D., Kerem, S., Kim, C.K., Mitchell, D.G., Nelson, K.S., Paranicas, C.P., Paschalidis, N., Rossano, E., and Stokes, M.R., 2017, *The Jupiter Energetic Particle Detector Instrument (JEDI) Investigation for the Juno Mission*, Space Science Reviews, Vol. 213, pp. 289-346.

Mauk, B.H., Williams, D.J., and Eviatar, A., 2001, *Understanding Io's Space Environment Interaction: Recent Energetic Electron Measurements from Galileo*, Journal of Geophysical Research: Space Physics, Vol. 106, Art. No. A11.

Maurer, R.H., and Goldsten, J.O., 2016, *The Van Allen Probes Engineering Radiation Monitor: Mission Radiation Environment and Effects*, Johns Hopkins APL Technical Digest, Vol. 33, pp. 183-193.

Mayer, J.W., 1960, *The Development of the Junction Detector*, IRE Transactions on Nuclear Science, Vol. NS-7, pp. 178-180.

McAdams, J.V., Farquhar, R.W., Taylor, A.H., and Williams, B.G., 2007, *MESSENGER Mission Design and Navigation*, Space Science Reviews, Vol. 131, pp. 219-246.

McComas, D.J., Elliott, H.A., Weidner, S., Valek, P., Zirnstein, E.J., Bagenal, F., Delamere, P.A., Ebert, R.W., Funsten, H.O., Horanyi, M., McNutt, R.L., Moser, C., Schwadron, N.A., Strobel, D.F., Young, L.A., Ennico, K., Olkin, C.B., Stern, S.A., and Weaver, H.A., 2016, *Pluto's Interaction with the Solar Wind*, Journal of Geophysical Research: Space Physics, Vol. 121, pp. 4232-4246.

McLeod, B., Geary, J., Conroy, M., Fabricant, D., Ordway, M., Szentgyorgyi, A., Amato, S., Ashby, M., Caldwell, N., Curley, D., Gauron, T., Holman, M., Norton, T., Pieri, M., Roll, J., Weaver, D., Zajac, J., Palunas, P., and Osip, D., 2015, *Megacam: A Wide-Field CCD Imager for the MMT and Magellan*, Publications of the Astronomical Society of the Pacific, Vol. 127, pp. 366-382.

McIntyre, R.J., 1966, *Multiplication Noise in Uniform Avalanche Diodes*, IEEE Transactions on Electron Devices, Vol. 13, pp. 164-168.

McNutt, R.L., Livi, S.A., Gurnee, R.S., Hill, M.E., Cooper, K.A., Andrews, G.B., Keath, E.P., Krimigis, S.M., Mitchell, D.G., Tossman, B., Bagenal, F., Boldt, J.D., Bradley, W., Devereux, W.S., Ho, G.C., Jaskulek, S.E., Lefevere, T.W., Malcom, H., Marcus, G.A., Hayes, J.R., Moore, G.T., Perry, M.E., Williams, B.D., Wilson, P., Brown, L.E., Kusterer, M.B., and Vandegriff, J.D., 2008, *The Pluto Energetic Particle Spectrometer Science Investigation (PEPSSI) on the New Horizons Mission*, Space Science Reviews, Vol. 140, pp. 315-385.

Meidinger, N., Andritschke, R., Hartmann, R., Herrmann, S., Holl, P., Lutz, G., and Strüder, L., 2006, P*n CCD for Photon Detection from Near-infrared to X-rays*, Nuclear Instruments and Methods in Physics Research Section A, Vol. 565, pp. 251-257.

Mooney, P.M., 1990, *Deep Donor Levels (DX Centers) in III-V Semiconductors*, Journal of Applied Physics, Vol. 67, Art. No. 3.

Müller-Seidlitz, J., Andritschke, R., Bähr, A., Meidinger, N., Ott, S., Richter, R.H., Treberspurg, W., and Treis, J., 2016, *Spectroscopic Performance of DEPFET Active Pixel Sensor Prototypes Suitable for the High Count Rate Athena WFI Detector*, SPIE Astronomical Telescopes and Instrumentation, UK.

Nikjoo, H., Uehara, S., and Emfietzoglou, D., 2012, *Interaction of Radiation with Matter*, CRC Press, Boca Raton, USA.

Novara, M., 2002, *The Bepicolombo ESA Cornerstone Mission To Mercury*, Acta Astronautica, Vol. 51, pp. 387-395.

Okada, T., Shirai, K., Yamamoto, Y., Arai, T., Ogawa, K., Hosono, K., and Kato, M., 2006, *X-ray Fluorescence Spectrometry of Asteroid Itokawa by Hayabusa*, Science, Vol. 312, pp. 1338-1341.

Ortec, 2004, *Model 572A Spectroscopy Amplifier Operating and Service Manual*, Ortec Part No. 785100, Manual Revision D, Advanced Measurement Technology (Ametek), Berwyn, USA.

Ortec, 2014a, *ASPEC-927 Dual Multichannel Buffer User Manual*, Ortec Part No. 931025, Manual Revision C, Advanced Measurement Technology (Ametek), Berwyn, USA.

Ortec, 2014b, *EASY-MCA-8K Digital Gamma-Ray Spectrometer User's Manual*, Ortec Part No. 931044, Manual Revision C, Advanced Measurement Technology (Ametek), Berwyn, USA.

Owens, A., 2012, *Compound Semiconductor Radiation Detectors*, 1st ed., CRC Press, Boca Raton, USA.

Owens, A., 2019, *Semiconductor Radiation Detectors*, 1st ed., CRC Press, Boca Raton, USA.

Owens, A., Bavdaz, M., Peacock, A., Poelaert, A., Andersson, H., Nenonen, S., Sipila, H., Tröger, L., and Bertuccio, G., 2001, *High Resolution X-ray Spectroscopy using GaAs Arrays*, Journal of Applied Physics, Vol. 90, Art. No. 5376.

Owens, A., and Peacock, A., 2004, *Compound Semiconductor Radiation Detectors*, Nuclear Instruments and Methods in Physics Research Section A, Vol. 531, pp. 18-37.

Palmer, P.T., and Limero, T.F., 2001, *Mass Spectrometry in the U.S. Space Program: Past, Present, and Future*, Journal of the American Society for Mass Spectrometry, Vol. 12, pp. 656-675.

Pantazis, T., Pantazis, J., Huber, A., and Redus, R., 2010, *The Historical Development of the Thermoelectrically Cooled X-ray Detector and its Impact on the Portable and Hand-held XRF Industries*, X-Ray Spectrometry, Vol. 39, pp. 90-97.

Pehl, R.H., Goulding, F.S., Landis, D.A., and Lenzlinger, M., 1968, *Accurate Determination of the Ionization Energy in Semiconductor Detectors*, Nuclear Instruments and Methods, Vol. 59, pp. 45-55.

Pell, E.M., 1960, *Ion Drift in an n-p Junction*, Journal of Applied Physics, Vol. 31, Art. No. 2.

Pfaff, R.F., Borovsky, J.E., and Young, D.T., 2013, *Measurement Techniques in Space Plasmas: Fields*, American Geophysical Union, Vol. 103, pp. 1-355.

Plimmer, S.A., David, J.P.R., Rees, G.J., and Robson, P.N., 2000, *Ionization Coefficients in $Al_xGa_{1-x}As$ ($x = 0 – 0.60$)*, Semiconductor Science and Technology, Vol. 15, pp. 692-699.

Potts, P.J., and West, M., 2008, *Portable X-ray Fluorescence Spectroscopy: Capabilities for in situ Analysis*, RSC publishing, Cambridge, UK.

Press, W.H., Teukolsky, S.A., Vetterling, W.T., and Flannery, B.P., 1986, *Numerical Recipes*, Cambridge University Press, Cambridge, UK.

Radeka, V., 1968, *State of the Art of Low Noise Amplifiers for Semiconductor Radiation Detectors*, Proceedings of the International Symposium on Nuclear Electronics, Versailles, France.

Ramo, S., 1939, *Currents Induced by Electron Motion*, Proceedings of the IRE, Vol. 27, pp. 584-585.

Redus, R., Huber, A., Pantazis, J., and Pantazis, T., 2011, *Enhanced Energy Range Thermoelectrically Cooled Silicon X-ray Detectors*, IEEE Nuclear Science Symposium Conference Record, pp. 580-585.

Renker, D., and Lorenz, E., 2009, *Advances in Solid State Photon Detectors*, Journal of Instrumentation, Vol. 4, Art. No. P04004.

Rieder, R., Gellert, R., Brückner, J., Klingelhöfer, G., Dreibus, G., Yen, A., and Squyres, S.W., 2003, *The New Athena Alpha Particle X-ray Spectrometer for the Mars Exploration Rovers*, Journal of Geophysical Research: Planets, Vol. 108, Art. No. E12.

Ripamonti, G., Capasso, F., Hutchinson, A.L., Muehlner, D.J., Walker, J.F., and Malik, R.J., 1990, *Realization of a Staircase Photodiode: Towards a Solid-state Photomultiplier*, Nuclear Instruments and Methods in Physics Research Section A, Vol. 288, pp. 99-103.

Rizzi, M., D'Aloia, M., and Castagnolo, B., 2010, *Semiconductor Detectors and Principles of Radiation-matter Interaction*, Journal of Applied Sciences, Vol. 10, pp. 3141-3155.

Round, H.J., 1907, *A Note on Carborundum*, Electrical World, Vol. 49, pp. 309.

Sah, C., Noyce, R.N., and Shockley, W., 1957, *Carrier Generation and Recombination in p-n Junctions and p-n Junction Characteristics*, Proceedings of the IRE, Vol. 45, pp. 1228-1243.

Sánchez, M., Brunetti, A., and Golosio, B., 2003, *XRAYLIB Tables (X-ray Fluoresence Cross-Section)*, European Synchrotron Radiation Facility, Grenoble, France.

Schindler, K., 2007, *Physics of Space Plasma Activity*, Cambridge University Press, Cambridge, UK.

Schlemm, C.E., Starr, R.D., Ho, G.C., Bechtold, K.E., Hamilton, S.A., Boldt, J.D., Boynton, W.V., Bradley, W., Fraeman, M.E., Gold, R.E., Goldsten, J.O., Hayes, J.R., Jaskulek, S.E., Rossano, E., Rumpf, R.A., Schaefer, E.D., Strohbehn, K., Shelton, R.G., Thompson, R.E., Trombka, J.I., and Williams, B.D., 2007, *The X-Ray Spectrometer on the MESSENGER Spacecraft*, Space Science Reviews, Vol. 131, pp. 393-415.

Schötzig, U., 2000, *Half-life and X-ray Emission Probabilities of ^{55}Fe*, Applied Radiation and Isotopes, Vol. 53, pp. 469-472.

Seward, F.D., and Charles, P.A., 2010, *Exploring the X-ray Universe*, 2nd ed., Cambridge University Press, New York, USA.

Shockley, W., 1938, *Currents to Conductors Induced by a Moving Point Charge*, Journal of Applied Physics, Vol. 9, pp. 635-636.

Shockley, W., 1961, *Problems Related to p-n Junctions in Silicon*, Solid-State Electronics, Vol. 2, Art. No. 1.

Silenas, A., Miller, A., Pozela, J., Pozela, K., Dapkus, L., and Juciene, V., 2011, *Graded-gap $Al_xGa_{1-x}As$ Detector for High Energy Electron Beam Dosimetry*, Nuclear Instruments and Methods in Physics Research Section A, Vol. 633, pp. 62-64.

Silenas, A., Pozela, J., Pozela, K., Dapkus, L., and Juciene, V., 2006, *High Spatial Resolution Graded-gap $Al_xGa_{1-x}As$ X-ray Detector*, Nuclear Instruments and Methods in Physics Research Section A, Vol. 563, pp. 21-23.

Silenas, A., Pozela, J., Smith, K.M., Pozela, K., Jasutis, V., Dapkus, L., and Juciene, V., 2002, *Non-uniformly Doped Graded-gap $Al_xGa_{1-x}As$ X-ray Detectors with High Photovoltaic Response*, Nuclear Instruments and Methods in Physics Research Section A, Vol. 487, pp. 54-59.

Siliconix, 2001, *2N4416/2N4416A/SST4416 N-Channel JFETs*, Data Sheet, 70242 S-04028, Rev. F, Vishay Electronic GmbH, Selb, Germany.

Spanovich, N., Smith, M.D., Smith, P.H., Wolff, M.J., Christensen, P.R., and Squyres, S.W., 2006, *Surface and Near-surface Atmospheric Temperatures for the Mars Exploration Rover Landing Sites*, Icarus, Vol. 180, pp. 314-320.

Spieler, H., 2005, *Semiconductor Detector Systems*, Oxford University Press, New York, USA.

Starr, R.D., Schlemm, C.E., Ho, G.C., Nittler, L.R., Gold, R.E., and Solomon, S.C., 2016, *Calibration of the MESSENGER X-Ray Spectrometer*, Planetary and Space Science, Vol. 122, pp. 13-25.

Stephens, S.K., 2018, *Juno at Jupiter: The Mission and its path to unveiling Secrets of the History of the Solar System*, 2018 IEEE Aerospace Conference, IEEE, Montana, USA.

Stern, S.A., Bagenal, F., Ennico, K., Gladstone, G.R., Grundy, W.M., McKinnon, W.B., Moore, J.M., Olkin, C.B., Spencer, J.R., Weaver, H.A., Young, L.A., Andert, T., Andrews, J., Banks, M., Bauer, B., Bauman, J., Barnouin, O.S., Bedini, P., Beisser, K., Beyer, R.A., Bhaskaran, S., Binzel, R.P., Birath, E., Bird, M., Bogan, D.J., Bowman, A., Bray, V.J., Brozovic, M., Bryan, C., Buckley, M.R., Buie, M.W., Buratti, B.J., Bushman, S.S., Calloway, A., Carcich, B., Cheng, A.F., Conard, S., Conrad, C.A., Cook, J.C., Cruikshank, D.P., Custodio, O.S., Dalle Ore, C.M., Deboy, C., Dischner, Z.J.B., Dumont, P., Earle, A.M., Elliott, H.A., Ercol, J., Ernst, C.M., Finley, T., Flanigan, S.H., Fountain, G., Freeze, M.J., Greathouse, T., Green, J.L., Guo, Y., Hahn, M., Hamilton, D.P., Hamilton, S.A., Hanley, J., Harch, A., Hart, H.M., Hersman, C.B., Hill, A., Hill, M.E., Hinson, D.P., Holdridge, M.E., Horanyi, M., Howard, A.D., Howett, C.J.A., Jackman, C., Jacobson, R.A., Jennings, D.E., Kammer, J.A., Kang, H.K., Kaufmann, D.E., Kollmann, P., Krimigis, S.M., Kusnierkiewicz, D., Lauer, T.R., Lee, J.E., Lindstrom, K.L., Linscott, I.R., Lisse, C.M., Lunsford, A.W., Mallder, V.A., Martin, N., McComas, D.J., McNutt, R.L., Mehoke, D., Mehoke, T., Melin, E.D., Mutchler, M., Nelson, D., Nimmo, F., Nunez, J.I., Ocampo, A., Owen, W.M., Paetzold, M., Page, B., Parker, A.H., Parker, J.W., Pelletier, F., Peterson, J., Pinkine, N., Piquette, M., Porter, S.B., Protopapa, S., Redfern, J., Reitsema, H.J., Reuter, D.C., Roberts, J.H., Robbins, S.J., Rogers, G., Rose, D., Runyon, K., Retherford, K.D., Ryschkewitsch, M.G., Schenk, P., Schindhelm, E., Sepan, B., Showalter, M.R., Singer, K.N., Soluri, M., Stanbridge, D., Steffl, A.J., Strobel, D.F., Stryk, T., Summers, M.E., Szalay, J.R., Tapley, M., Taylor, A., Taylor, H., Throop, H.B., Tsang, C.C.C., Tyler, G.L., Umurhan, O.M., Verbiscer, A.J., Versteeg, M.H., Vincent, M., Webbert, R., Weidner, S., Weigle, G.E., White, O.L., Whittenburg, K., Williams, B.G., Williams, K., Williams, S., Woods, W.W., Zangari, A.M., and Zirnstein, E., 2015, *The Pluto System: Initial Results from its Exploration by New Horizons*, Science, Vol. 350, Art. No. AAD1815.

Soga, T., 2006, *Handbook of Photovoltaic Science and Engineering*, 2nd ed., Elsevier, Amsterdam, Netherlands.

Stoneham, A.M., 1981, *Non-radiative Transitions in Semiconductors*, Reports on Progress in Physics, Vol. 44, pp. 1251-1295.

Stradling, R.A., and Klipstein, P.C., 1991, *Growth and Characterisation of Semiconductors*, 1st ed., IOP Publishing Ltd, Bristol, UK.

Street, R.A., 2000, *Technology and Applications of Amorphous Silicon*, Springer-Verlag, Berlin, Germany.

Strüder, L., Briel, U., Dennerl, K., Hartmann, R., Kendziorra, E., Meidinger, N., Pfeffermann, E., Reppin, C., Aschenbach, B., Bornemann, W., Bräuninger, H., Burkert, W., Elender, M., Freyberg, M., Haberl, F., Hartner, G., Heuschmann, F., Hippmann, H., Kastelic, E., Kemmer, S., Kettenring, G., Kink, W., Krause, N., Müller, S., Oppitz, A., Pietsch, W., Popp, M., Predehl, P., Read, A., Stephan, K.H., Stötter, D., Trümper, J., Holl, P., Kemmer, J., Soltau, H., Stötter, R., Weber, U., Weichert, U., Von Zanthier, C., Carathanassis, D., Lutz, G., Richter, R.H., Solc, P., Böttcher, H., Kuster, M., Staubert, R., Abbey, A., Holland, A., Turner, M., Balasini, M., Bignami, G.F., La Palombara, N., Villa, G., Buttler, W., Gianini, F., Lainé, R., Lumb, D., and Dhez, P., 2001, *The European Photon Imaging Camera on XMM-Newton: The pn-CCD Camera*, Astronomy and Astrophysics, Vol. 365, pp. 18-26.

Swierkowski, S.P., and Armantrout, G.A., 1975, *Prognosis for High-Z Semiconductor Detectors*, IEEE Transactions on Nuclear Science, Vol. 22, pp. 205-210.

Swinyard, B.M., Joy, K.H., Kellett, B.J., Crawford, I.A., Grande, M., Howe, C.J., Fernandes, V.A., Gasnault, O., Lawrence, D.J., Russell, S.S., Wieczorek, M.A., and Foing, B.H., 2009, *X-ray Fluorescence Observations of the Moon by SMART-1/D-CIXS and the First Detection of Ti Kα from the Lunar Surface*, Planetary and Space Science, Vol. 57, pp. 744-750.

Szatkowski, J., Płaczek-Popko, E., Sierański, K., and Hansen, O.P., 1999, *Deep Hole Traps in Be-doped $Al_{0.5}Ga_{0.5}As$ Layers Grown by Molecular Beam Epitaxy*, Journal of Applied Physics, Vol. 86, Art. No. 3.

Sze, S.M., 2006, *Physics of Semiconductor Devices*, 3rd ed., John Wiley & Sons, New Jersey, USA.

Tan, C., David, J.P.R., Plimmer, S.A., Rees, G.J., Tozer, R.C., and Grey, R. 2001, *Low Multiplication Noise Thin $Al_{0.6}Ga_{0.4}As$ Avalanche Photodiodes*, IEEE Transactions on Electron Devices, Vol. 48, pp. 1310-1317.

Tan, C.H., Gomes, R.B., David, J.P.R., Barnett, A.M., Bassford, D.J., Lees, J.E., and Ng, J.S., 2011, *Avalanche Gain and Energy Resolution of Semiconductor X-ray Detectors*, IEEE Transactions on Electron Devices, Vol. 58, pp. 1696-1701.

Taylor, F., and Grinspoon, D., 2009, *Climate Evolution of Venus*, Journal of Geophysical Research: Planets, Vol. 114, Art. No. E00B40.

Thompson, A., Attwood, D., Gullikson, E., Howells, M., Kim, K.J., Kirz, J., Kortright, J., Lindau, I., Liu, Y., Pianetta, P., Robinson, A., Scofield, J., Underwood, J., Williams, G., and Winick, H., 2009, *X-Ray Data Booklet (Center for X-Ray Optics and Advanced Light Source)*, Lawrence Berkeley National Laboratory, Berkeley, USA.

Treis, J., Andricek, L., Aschauer, F., Heinzinger, K., Herrmann, S., Hilchenbach, M., Lauf, T., Lechner, P., Lutz, G., Majewski, P., Porro, M., Richter, R.H., Schaller, G., Schnecke, M., Schopper, F., Soltau, H., Stefanescu, A., Strüder, L., and De Vita, G., 2010, *MIXS on BepiColombo and its DEPFET Based Focal Plane Instrumentation*, Nuclear Instruments and Methods in Physics Research Section A, Vol. 624, pp. 540-547.

Tsang, W.T., 1985, *Semiconductors and Semimetals*, Academic Press, London, UK.

Tsoulfanidis, N., and Landsberger, S., 2015, *Measurement and Detection of Radiation*, 4th ed., CRC Press, Boca Raton, USA.

Tsuji, K., Injuk, J., and van Grieken, R., 2004, *X-ray Spectrometry: Recent Technological Advances*, John Wiley & Sons, Chichester, UK.

Vasavada, A.R., Grotzinger, J.P., Arvidson, R.E., Calef, F.J., Crisp, J.A., Gupta, S., Hurowitz, J., Mangold, N., Maurice, S., Schmidt, M.E., Wiens, R.C., Williams, R.M.E., and Yingst, R.A., 2014, *Overview of the Mars Science Laboratory Mission: Bradbury Landing to Yellowknife Bay and Beyond*, Journal of Geophysical Research: Planets, Vol. 119, pp. 1134-1161.

Vasilescu, G., 2005, *Electronic Noise and Interfering Signals*, Springer-Verlag, Berlin, Germany.

Walker, A.W., Heckelmann, S., Tibbits, T., Lackner, D., Bett, A.W., and Dimroth, F., 2017, *Radiation Hardness of AlGaAs n-i-p Solar Cells with Higher Bandgap Intrinsic Region*, Solar Energy Materials and Solar Cells, Vol. 168, pp. 234-240.

Wermes, N., Andricek, L., Fischer, P., Heinzinger, K., Herrmann, S., Karagounis, M., Kohrs, R., Kruger, H., Lutz, G., Lechner, P., Peric, I., Porro, M., Richter, R.H., Schaller, G., Schnecke-Radau, M., Schopper, F., Soltau, H., Struder, L., Trimpl, M., Ulrici, J., and Treis, J., 2004, *New Results on DEPFET Pixel Detectors for Radiation Imaging and High Energy Particle Detection*, IEEE Transactions on Nuclear Science, Vol. 51, pp. 1121-1128.

White, J.F., 1982, *Microwave Semiconductor Engineering*, van Nostrand Reinhold, New York, USA.

Williams, D.B., and Carter, B.C., 2009, *Transmission Electron Microscopy: A Textbook for Materials Science*, 2nd ed., Springer, New York, USA.

Williams, D.J., McEntire, R.W., Jaskulek, S., and Wilken, B., 1992, *The Galileo Energetic Particles Detector*, Space Science Reviews, Vol. 60, pp. 385-412.

Yada, T., Fujimura, A., Abe, M., Nakamura, T., Noguchi, T., Okazaki, R., Nagao, K., Ishibashi, Y., Shirai, K., Zolensky, M.E., Sandford, S., Okada, T., Uesugi, M., Karouji, Y., Ogawa, M., Yakame, S., Ueno, M., Mukai, T., Yoshikawa, M., and Kawaguchi, J., 2013, *Hayabusa-returned Sample Curation in the Planetary Material Sample Curation Facility of JAXA*, Meteoritics & Planetary Science, Vol. 49, pp. 135-153.

Yamaguchi, M., 1995, *Radiation Resistance of Compound Semiconductor Solar Cells*, Journal of Applied Physics, Vol. 78, Art. No. 3.

Yoshida, S., Mitsui, K., Oda, T., and Yukimoto, Y., 1982, *Comparison of High Energy Proton Radiation Damages on AlGaAs/GaAs and Si Solar Cells*, Japanese Journal of Applied Physics, Vol. 21, pp. 27-31.

Young, L.A., Stern, S.A., Weaver, H.A., Bagenal, F., Binzel, R.P., Buratti, B., Cheng, A.F., Cruikshank, D., Gladstone, G.R., Grundy, W.M., Hinson, D.P., Horanyi, M., Jennings, D.E., Linscott, I.R., McComas, D.J., McKinnon, W.B., McNutt, R., Moore, J.M., Murchie, S., Olkin, C.B., Porco, C.C., Reitsema, H., Reuter, D.C., Spencer, J.R., Slater, D.C., Strobel, D., Summers, M.E., and Tyler, G.L., 2008, *New Horizons: Anticipated Scientific Investigations at the Pluto System*, Space Science Reviews, Vol. 140, pp. 93-127.

Younglove, B.A., and Olien, N.A., 1985, *Tables of Industrial Gas Container Contents and Density for Oxygen, Argon, Nitrogen, Helium, and Hydrogen*, National Institute of Standards and Technology, Gaithersbury, Maryland, USA.

Zhang, C., Lechner, P., Lutz, G., Porro, M., Richter, R., Treis, J., Strüder, L., and Nan Zhang, S., 2006, *Development of DEPFET Macropixel Detectors*, Nuclear Instruments and Methods in Physics Research Section A, Vol. 568, pp. 207-216.

Zhao, S., Lioliou, G., and Barnett, A.M., 2018a, *X-ray Spectrometer with a Low-cost SiC Photodiode*, Nuclear Instruments and Methods in Physics Research Section A, Vol. 887, pp. 138-143.

Zhao, S., Lioliou, G., Butera, S., Whitaker, M.D.C., and Barnett, A.M., 2018b, *Electron Spectroscopy with a Commercial 4H-SiC Photodiode*, Nuclear Instruments and Methods in Physics Research Section A: Accelerators, Spectrometers, Detectors and Associated Equipment, Vol. 910, pp. 35-40.

Zhao, S., Butera, S., Lioliou, G., Krysa, A.B., and Barnett, A.M., 2019, *AlInP Photodiode X-ray Detectors*, Journal of Physics D: Applied Physics, Vol. 52, Art. No. 225101.

Zheng, X.G., Yuan, P., Sun, X., Kinsey, G.S., Holmes, A.L., Streetman, B.G., and Campbell, J.C., 2000, *Temperature Dependence of the Ionization Coefficients of $Al_xGa_{1-x}As$*, IEEE Journal of Quantum Electronics, Vol. 36, pp. 1168-1173.